

Characterisation of GaAsBi/GaAs Multiple Quantum Wells for Photovoltaic Applications

FAEZAH HARUN



A thesis submitted for the degree of Doctor of Philosophy

Semiconductor Materials and Devices Group
Department of Electronic and Electrical Engineering
The University of Sheffield

February 2020

Acknowledgements

In the name of God, the Most Gracious, the Most Merciful.

I would like to thank my supervisor, Professor John David for his endless guidance and supervision on me throughout my PhD years. I also would like to express my gratitude to Professor Tan Chee Hing, my second supervisor for his useful comments and advices. Special thank you to Professor Jo Shien Ng for helping me a lot for women's support from the department. I would also like to thank my Bismide team, especially Dr. Robert Richards for his valuable feedback and discussions, Dr. Thomas Rockett, Dr. Zhize Zhou, Liu Yuchen, Riduwan Nawawi, Nick Bailey and Nada Adham for being good company during the study. Special thanks to Impact Ionisation officemates; Aina, Akeel, Ben, Cheong, Leh Woon, Liang, Shiyu, Simon, Xiao, Xinxin and Xinyi; for many cups of tea and good friendship. Thank you so much to all EEE departmental staff for helping out in every aspect to finish my study especially Mrs Hilary Levesley for assisting me with the non-technical parts for my PhD.

I would like to express my appreciation to my sponsor, Majlis Amanah Rakyat (MARA) and my employer, Universiti Kuala Lumpur (UniKL) for their financial support throughout my study in Sheffield. I am grateful to have my fellow Malaysian friends in Sheffield; especially Aisyah, Yanti, Huda, Diyana, Liyana, Rabiatul, Syeda Exaty, Farahwahida and many more for the encouragement and good time. Thank you too, to my bestfriends in Malaysia; Athirah, Nadirah and Fatihah for the comfort and virtual hugs.

I am forever indebted to my beloved parents and mother in-law, Mr Harun, Mrs Zaiton and Mrs Siti Maradziyah, as well as my family members for their endless support from Malaysia. It means so much to me.

Finally, special gratitude to my darling husband, Muhd Saifuddin Salleh who sacrifices so much and for his never-ending patience, love and kindness during our life together. Thank you and I love you. To our kids, Adam and Athifah; you both are our greatest blessings in life.

List of Publications

Journal papers

1. A. R. Mohmad, F. Bastiman, C. J. Hunter, **F. Harun**, D. F. Reyes, D. L. Sales, D. Gonzalez, R. D. Richards, J. P. R. David, B. Y. Majlis. *Bismuth concentration inhomogeneity in GaAsBi bulk and quantum well structures*. Semicond. Sci. Technol. 30 (2015) 094018, July 2015.
2. R. D. Richards, **F. Harun**, J. S. Cheong, A. Mellor, N. P. Hylton, T. Wilson, T. Thomas, N. J. Ekins-Daukes, J. P. R. David. *GaAsBi: An alternative to InGaAs based multiple quantum well photovoltaics* (June 2016) Proceedings paper: 2016 IEEE 43th Photovoltaic Specialists Conference (PVSC)
3. T. B. O. Rockett, R. D. Richards, Y. Gu, **F. Harun**, Y. Liu, Z. Zhou, J. P. R. David. *Influence of growth conditions on the structural and opto-electronic quality of GaAsBi..* Journal of Crystal Growth 477, 139-143 (2017)
4. R. D. Richards, A. Mellor, **F. Harun**, J. S. Cheong, N. P. Hylton, T. Wilson, T. Thomas, J.S. Roberts, N. J. Ekins-Daukes, J. P. R. David. *Photovoltaic characterisation of GaAsBi/GaAs multiple quantum well devices*. Solar Energy Materials and Solar Cells, December 2017
5. R. D. Richards, T. B. O. Rockett, M. R. Nawawi, **F. Harun**, A. Mellor, T. Wilson, C. Christou, S. Chen, J. P. R. David, *Light-biased IV characteristics of a GaAsBi/GaAs multiple quantum well pin diode at low temperature*, Semiconductor Science and Technology 33, 094008 (2018)

Oral and poster presentations

1. **F. Harun**, T. B. O. Rockett, A. R. Mohmad, R. D. Richards, Z. Zhou, F. Bastiman, J. P. R. David. *Polarised Photoluminescence Study of GaAsBi grown by Molecular Beam Epitaxy*. UK Semiconductors 2015 Conference, Sheffield Hallam University, Sheffield, UK. 1-2 July 2015.
2. R. D. Richards, C. J. Hunter, F. Bastiman, Z. Zhou, **F. Harun**, T. B. O. Rockett, J. P. R. David. *GaAsBi LEDs emitting at 1,200nm*. UK Semiconductors 2015 Conference, Sheffield Hallam University, Sheffield, UK. 1-2 July 2015.
3. T. B. O. Rockett, **F. Harun**, A. R. Mohmad, R. D. Richards, F. Bastiman, J. P. R. David, B. Y. Majlis. *Investigation of Ordering in GaAsBi through PL Polarization Effects*. 6th International Workshop on Bismuth Containing Semiconductor, University of Wisconsin-Madison, USA. 19-22 July 2015.
4. **F. Harun**, R. D. Richards, J. S. Cheong, A. Mellor, N. P. Hylton, T. Wilson, T. Thomas, N. J. Ekins-Daukes, J. P. R. David. *GaAsBi Based Multiple Quantum Well Photovoltaics*. Semiconductor and Integrated Optoelectronics (SIOE) 2016, Cardiff University, Cardiff, UK. – 5-7 April 2016.
5. T. B. O. Rockett, R. D. Richards, **F. Harun**, Y. Gu, Z. Zhou, J. P. R. David. *Optimising the structural and optical quality of GaAsBi*. UK Semiconductors 2016 Conference, Sheffield Hallam University, Sheffield, UK, 6th July 2016.
6. Z. Zhou, R. D. Richards, Y. Gu, T. B. O. Rockett, **F. Harun**, Y. Liu, J. S. Cheong, A. Baharuddin, J. P. R. David. *Investigation of Photo-multiplication in GaAsBi Diodes*. 7th International Workshop on Bismuth Containing Semiconductors, Shanghai, China, 24-27 July 2016.
7. T. B. O. Rockett, R. D. Richards, **F. Harun**, Y. Gu, Z. Zhou, J. P. R. David. *Optimising the opto-electronic properties of GaAsBi*. 7th International Workshop on Bismuth Containing Semiconductors, Shanghai, China, 24-27 July 2016.

8. T. B. O. Rockett, R. D. Richards, **F. Harun**, Y. Gu, Z. Zhou, J. P. R. David. *Optimizing the Opto-Electronic Properties of GaAsBi by Tuning Growth Conditions*. 19th International Conference on Molecular Beam Epitaxy, 4-9 September 2016.
9. **F. Harun**, J. S. Cheong, J. S. Ng, R. D. Richards, and J. P. R. David. *Absorption and Franz Keldysh Electroabsorption in InGaAs/InP*. Semiconductor and Integrated Optoelectronics (SIOE) 2017, Cardiff University, Cardiff, UK. – 18-20 April 2017.
10. T. B. O. Rockett, R. D. Richards, Y. Gu, **F. Harun**, Y. Liu, Z. Zhou, J. P. R. David. *Opto-electronic measurements of GaAsBi PIN diodes*. Semiconductor and Integrated Optoelectronics (SIOE) 2017, Cardiff University, Cardiff, UK. – 18-20 April 2017.
11. R. D. Richards, T. B. O. Rockett, Y. Liu, **F. Harun**, J. S. Roberts, J. P. R. David. *Making progress in photovoltaics: Can dilute bismides fill the 1 eV band gap gap?*, Wroclaw University of Science and Technology, Wroclaw, Poland, 11th May 2017.
12. R. D. Richards, T. B. O. Rockett, Y. Liu, **F. Harun**, J. P. R. David. *Hole trapping in GaAsBi/GaAs MQWs: Lessons from dilute nitrides*. UK Semiconductors 2017 Conference, Sheffield Hallam University, Sheffield, UK, 12th July 2017.
13. T. B. O. Rockett, R. D. Richards, Y. Gu, **F. Harun**, Y. Liu, Z. Zhou, J. P. R. David, *Electroluminescence and current-voltage measurements of GaAsBi PIN diodes*. 8th International Workshop on Bismuth Containing Semiconductors, Marburg, Germany, 25th July 2017.
14. Z. Zhou, R. D. Richards, Y. Liu, T. B. O. Rockett, **F. Harun**, J. P. R. David. *The investigation of photo-multiplication in GaAsBi diodes*. 8th International Workshop on Bismuth Containing Semiconductors, Marburg, Germany, 25th July 2017.
15. **F. Harun**, R. D. Richards, A. Ray, and J. P. R. David. *GaAsBi MQW device performance at solar concentrator temperatures*. Semiconductor and Integrated Optoelectronics (SIOE) 2018, Cardiff University, Cardiff, UK. – 27-29 March 2018.

16. Y. Liu, R. D. Richards, T. B. O. Rockett, **F. Harun**, Y. Gu, J. P. R. David.
Electroluminescence study of GaAsBi devices of different growth conditions. UK Semiconductors 2018 Conference, Sheffield Hallam University, Sheffield, UK, 4th July 2018.

17. T. B. O. Rockett, R. D. Richards, Y. Liu, **F. Harun**, Z. Zhou, Y. Gu, J. P. R. David.
GaAsBi/GaAs multiple quantum wells with up to 120 periods. 9th International Workshop on Bismuth Containing Semiconductors, Kyoto, Japan, 18th July 2018.

Abstract

The incorporation of bismuth (Bi) into GaAs creates many potentials in different areas of technology such as telecommunications, spintronics and photovoltaics applications. The ability for GaAsBi to reach 1 eV bandgap is highly anticipated in solar cells industry as an alternative to replace InGaAs in achieving higher efficiency multi-junction solar cells. Although it is known that the growth of Bi-based material is challenging, the characterisations of this material device will help in providing its properties and open up opportunity for improvement and development.

A series of GaAsBi/GaAs multiple quantum well p-i-n diodes was grown using molecular beam epitaxy and the material characterisations are presented in this thesis. From the electrical characterisations, the current-voltage measurements of the devices demonstrate good diode behaviours with clear differences in dark current value between strained and strain-relaxed devices. Meanwhile, the reverse bias current-voltage measurements show the dominance of reverse leakage current for all devices.

The devices also experience hole trapping in the valence band, causing poor carrier extractions when light is absorbed during photocurrent measurements. Carrier enhancement can be achieved by applying slight reverse bias when the measurement was taken. Besides that, the absorption coefficient of the devices was confirmed to be similar with other work. Finally, the device's performance under solar illuminator is lower compared to InGaAs/GaAsP strained-balanced multiple-quantum well device due to its poor value of open-circuit voltage and it has higher bandgap offset compared to GaAs.

Overall, these results suggest than GaAsBi/GaAs multiple quantum well(s) do have a lot of room for improvement especially on growth, structure and strain level of the material. If these components can be catered, GaAsBi can be a competitive alternative for 1 eV junction in multiple junction solar cells.

Table of Contents

Acknowledgements	2
List of Publications	3
Abstract	7
Table of Contents	8
Chapter 1: Introduction	11
1.1 Solar Cell for Renewable Energy	11
1.1.1 Renewable and Non-Renewable Energy	11
1.1.2 Solar Energy	12
1.1.3 Solar Cells	13
1.2 Technology and Demands in Solar Cell Industry	14
1.2.1 First Generation Solar Cells	15
1.2.2 Second Generation Solar Cells	16
1.2.3 Third Generation Solar Cells	16
1.3 1 eV Material System	20
1.3.1 Rainbow of Choices	20
1.3.2 GaAsBi for Device Sources and Detectors	22
1.4 Thesis Overview	25
1.5 References	26
Chapter 2: Background Theory	32
2.1 Band Structure in Semiconductors	32
2.1.1 Atoms and their Electronic States	32
2.1.2 Energy Bands in Semiconductors	33
2.2 Crystalline Semiconductor	34
2.2.1 The Fermi Level	34
2.2.2 The p-n Junction	36
2.2.3 Diode Equation	39
2.3 Photo-carrier Generation and Recombination	41
2.3.1 Absorption of Light	41
2.3.2 Emission of Light	44
2.3.3 Semiconductor Opto-Electronic Devices	46
2.3.4 Solar Cells	47
2.4 III-V Semiconductor Material Systems	49
2.4.1 Lattice Structure Formation	49
2.4.2 Vegard's Law	50
2.4.3 Band Anticrossing Model	52
2.4.4 Valence Band Anti-Crossing Model	52

2.5	Multiple Quantum Well Structures	55
2.5.1	Multiple Quantum Wells	55
2.5.2	Strain and Strain Relaxation	58
2.6	Summary	60
2.7	References	61
 Chapter 3: Experimental Methodology		65
3.1	Growth: Molecular Beam Epitaxy	65
3.2	Optical Characterisation	66
3.2.1	Photoluminescence	66
3.3	Device Fabrication	68
3.4	Electrical Characterisation	73
3.4.1	Dark Current-Voltage	73
3.4.2	Current-Voltage under Illumination	75
3.4.3	Capacitance-Voltage	76
3.5	Opto-electronic characterisation	77
3.5.1	Photocurrent	77
3.6	Summary	80
3.7	References	81
 Chapter 4: Electrical Characterisation of GaAsBi/GaAs MQW Devices		82
4.1	Introduction	82
4.2	Previous Work on STC-3X	84
4.3	Capacitance-Voltage (C-V) Measurement	88
4.4	Current-Voltage (I-V) Measurement	94
4.4.1	Forward dark (I-V) Measurement	94
4.4.2	Reverse Dark (I-V) Measurement	100
4.5	Summary	106
4.6	References	107
 Chapter 5: Opto-Electronic Characterisation of GaAsBi/GaAs MQW Devices		110
5.1	Introduction	110
5.2	Photocurrent Measurements	110
5.2.1	Measurement testing	110
5.2.2	Photocurrent measurements	114
5.3	I-V under Illumination	130

5.4	Summary	136
5.5	References	137
Chapter 6: Conclusions and Future Work		140
6.1	Conclusions	140
6.2	Future Work	142
6.3	References	143
Appendices		144
Appendix A: FD05D Responsivity Graph		144
Appendix B: C-V and CA-V for STC-3X and QT1879 devices		145
Appendix C: Doping profile for STC-3X and QT1879 devices		147
Appendix D: Forward bias I-V and J-V for STC-3X devices		149
Appendix E: Reverse bias J-V for STC-3X devices		151
Appendix F: Photocurrent of STC-3X devices taken with different filters		153
Appendix G: Photocurrent of STC-3X devices taken at different biases		156
Appendix H: Responsivity and absorption coefficient (with Urbach fitting) of STC-3X devices		159
Appendix I: Solar Simulator Spectrum		165

Chapter 1: Introduction

1.1 Solar Cell for Renewable Energy

1.1.1 Renewable and Non-Renewable Energy

Demand in industry to have a long-lasting energy supply to humankind is leading to a very intense research and study on many renewable and non-renewable resources. A race between renewable energy such as sunlight, wind and tides and non-renewable energy like natural gas, oil and coal in becoming the main energy source to the world has become very competitive. In addition to that, debates between professionals on switching from current non-renewable energy source to renewable energy source becomes more frequent for the past few years. This is due to the limitation that we have from the non-renewable resources especially oil and natural gas. It takes a very long time to be replenished and usually leave behind by-products such as carbon dioxide (CO₂), carbon monoxide (CO) and lead that cause damages to the environment. The burning of fossil fuels especially leads to the formation of CO₂ which climatologist believe to be the main reason for global warming issue.

There are several advantages of renewable energy compared to non-renewable energy. They are sustainable and never runs out. It can be quickly replenished over time too. Besides that, they are clean as they produce little or no waste products, unlike the by-product of fossil fuels like carbon dioxide, sulphur dioxide and other chemical pollutants that can harm the environment. With these benefits, it gives a very little impact to the environment and avoid greenhouse effect leading to global warming. The operating cost for energy generation is lower in a long run too. This is applied to a non-moving renewable technology such as photovoltaic panel due to less maintenance needed. Somehow, other renewable energy requires a high maintenance cost. For example, wind turbine normally runs in a harsh environment and corrode easily which require regular servicing to keep everything working efficiently. The renewable energy projects also can bring economic benefits because most projects are located outside main city like solar energy collection A new spacious area will be open and this require more local services.

However, the renewable energy is facing the difficulty in generating same quantities of energy as large as traditional fossil fuel generators. One of the best solutions is to have a balance of many different power sources. Reliability is also another disadvantage of renewable energy.

The unpredictable and inconsistency of natural resources makes it difficult to estimate how much energy production. If the resources are unavailable, the capacity to generate energy from them also will be unavailable. For this thesis, the interest is on solar energy as a potential renewable energy resource and other alternatives of renewable energy will not be discussed after this.

1.1.2 Solar Energy

Solar energy is one of the highly anticipated renewable energy that can replace fossil fuel energy and non-renewable energy. This is due to its ability to directly convert the solar energy consist of light and heat into other type of energy such as electricity. The Sun radiates a large amount of energy every day and the planet absorb some of it. The remainder however, is dissipated when it is reaching the Earth or being reflected back out into the space. The focus will be on the photovoltaics cells that convert light energy to electricity. Meanwhile, solar thermal technology, where heat energy is used is not studied here.

The advantages of solar energy are; it is limitless, it reduces the use of fossil fuels and most importantly, non-polluting. In avoidance to global warming, these characteristics of solar energy is very promising and demanding. However, depending on the location of the collection point, day of the year and time of the day, the amount of energy collected will vary. The average annual solar irradiance around the world shows that the irradiation reached the Earth mostly at near the equator. It is also an unreliable technology during the night or on cloudy weather. Besides that, the technology to date is expensive and require a large surface to collect a useful amount of solar energy. Despite the drawback, solar energy has been commercially available for more than 15 years especially in the major markets lead by Germany with 31% of the total photovoltaic market, followed by Italy and China and the number of installations are seven times more than in 2010's.[1]

Commonly, solar energy is used for space and terrestrial applications. Space applications are operated with concentrated cells. Cost also is not the main issue as long as the efficiency can be increased by minimising the weight of the optics used. Vice versa, for terrestrial applications, cost is the main issue. If the cost is higher than the cell's energy recovery, it will not be worthwhile to use it.

The Sun has the original surface temperature of $\sim 5,800$ K and its characteristic can be approximated by a blackbody spectrum peaking at visible wavelength. With the known size of the Sun and the distance between the Sun and the Earth, the spectral irradiance or intensity can be determined by calculating it using Planck's law. Figure 1.1 shows the blackbody spectrum at 5,800 K normalised to a total power density of the sunlight spectrum when it reaches outside the atmosphere (AM0) and after it reaches the earth (AM1.5) which are $1,366.1 \text{ W.m}^{-2}$ and $1,000 \text{ W.m}^{-2}$, respectively.[2]

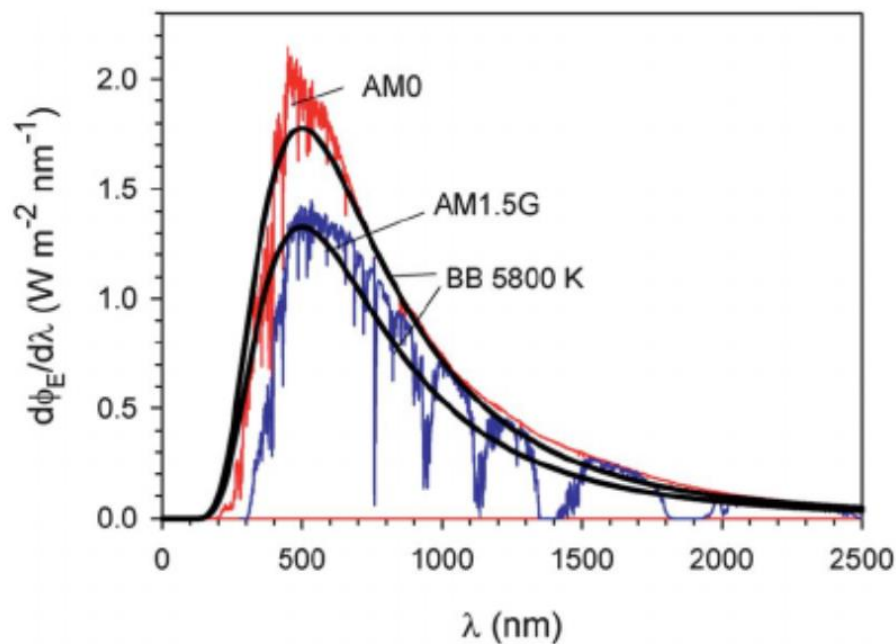


Figure 1.1: Normalised blackbody (BB) spectra indicated with black lines compared to the solar spectrum at the top of atmosphere (red line) and at sea level (blue line). Image taken from [2].

1.1.3 Solar Cells

The theoretical maximum efficiency of a solar cell can be calculated from Carnot efficiency, which is the operation of heat engine between two temperatures.[3] In this case, it is between the temperature of the Sun and the Earth. It is shown that the efficiency of solar cell can never be 100% because of the finite difference between the Sun's temperature and the solar cell. There are also other loss mechanisms that affect and actually reduce the efficiency of the solar cells.

Two main losses caused by the solar cell are the transmission losses and thermalisation losses. For a solar cell with specific bandgap, any photon below the bandgap will not be absorbed by the cell causing transmission losses. Meanwhile, thermalisation losses occur when the photon above the bandgap generate electron-hole pairs and they thermalised to the band edges. There are needs in balancing these two losses because changing the bandgap will decrease the effect of one, while increasing the effect of another. Therefore, it is important to optimise the value of bandgap to achieve maximum efficiency of the solar cell. In depth discussion on solar cell processes can be found in Section 2.3.5.

1.2 Technology and Demands in Solar Cell Industry

This sub-section is to understand the general concept of the different generations and current demand in industry for solar cells. Solar cell technology has been classified to three main groups, known as the three generations of solar cells. First generation solar cells consist of single junction solar cells made of silicon. Second generation cells are made of organic cells and thin-films. The third-generation cells are the research goal, consisting of advanced technology-related such as hot carrier solar cells, intermediate band solar cells, multi-junction solar cells and multiple quantum wells solar cells. The different generations have different efficiencies and production costs.[4-6]

Figure 1.2 shows the three generations of solar cells and their comparison in term of cost and efficiency. The horizontal axis represents the cost of the solar module. By including the cost of packaging and mounting, the cost can be twice the value. In addition to that, the dotted slopes indicate the cost per unit power. The steeper the slope of dotted line, the cheaper it can get. Meanwhile, the vertical axis is the theoretical percent efficiency of the solar cell. The horizontal dashed line is the Shockley-Queisser limit line. It is the power conversion limit from radiation into electrical power achievable by single junction solar cell which starts from 31% and can be up to 41% depending on the concentration ratio. Besides that, thermodynamic limit of a solar cell (which is not shown on the figure) is between 67-87%. This parameter is used to determine the power conversion limit for third generation solar cells, depending on the concentration ratio too.[7]

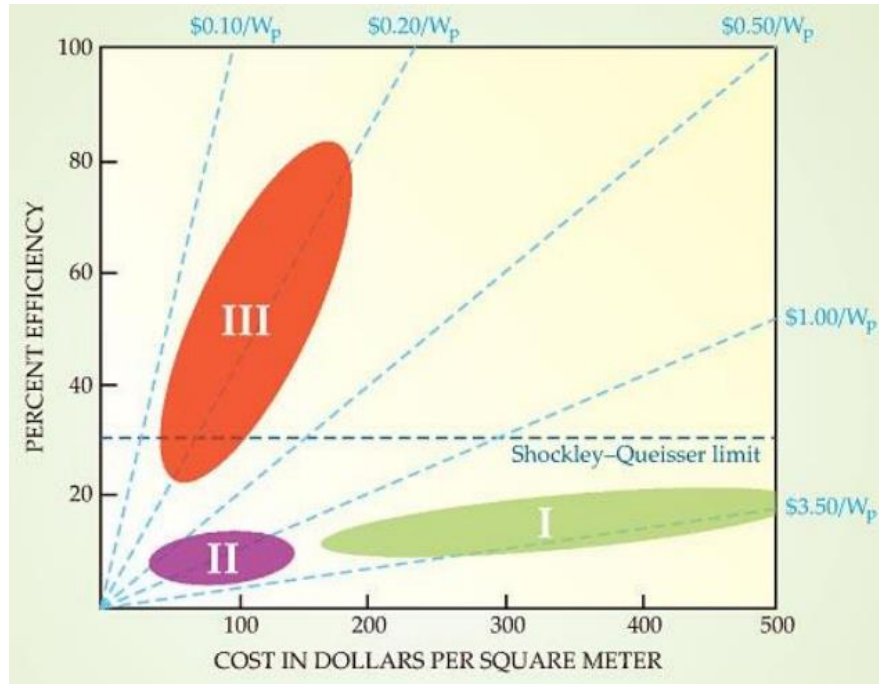


Figure 1.2: Three generations of solar cells with the representation of cost per square meter and percent efficiency. Dashed lines with different gradient value show the cost per unit of efficiency, where the third-generation solar cells show the smallest value compared to the other two generations. Image taken from [8].

1.2.1 First Generation Solar Cells

First generation solar cells are made of different type of silicon and they make up almost 85% of the current commercial market.[9] However, they lose the efficiency at higher operating temperatures. As seen in Figure 1.2, the cost in dollar per square meter is larger compared to other generations while their efficiency is limited by the Shockley-Queisser limit. For example, a high purity single silicon crystal wafer is generally made by the Czochralski process, which is an expensive process due to batch process involving high temperature, long times and mechanically slicing wafers from the ingot.

1.2.2 Second Generation Solar Cells

Second generation solar cells include thin films and organic solar cell. The materials are cheaper than first generation solar cells because they use less quality material, fewer processing steps and manufacturing technology is simpler. However, the efficiency is limited. Thin films such as amorphous silicon cells, nanocrystalline silicon and cadmium telluride (CdTe) are light-weighted and flexible thus of great interest for application on portable photovoltaic, window tinting and building material. Besides that, organic solar cells can be deposited through spray coating. The drawback of this coating is performance degradation over time due to reaction with water and oxygen from the surroundings. According to big companies that invested in this technology such as First Solar and Venture Capital Firms, it is more challenging to obtain CdTe. This is because, although it has good efficiency at a competitive price, the nature of the material is harmful and toxic. More researches are needed to increase the operating efficiency as well as mitigating the hazard from the material.[10]

1.2.3 Third Generation Solar Cells

Third generation solar cells have the ability to dramatically improve the percent efficiency while maintaining low costs. There is a lot of ongoing research under solar companies and universities to find the best method to improve and actually exceed the single junction efficiency. For examples, research on nanotubes antennas are successfully developed and tested in the laboratories at MIT.[11] Prototypes of silicon wire photovoltaic cells are also developed at CalTech.[12] The designs used in this generation are generally made of carrier multiplication technique, hot carrier cells, multi-junction cells or tandem and multiple quantum well solar cells.

Carrier multiplication technique

Carrier multiplication is a process where a single photon absorption will lead to the excitations of multiple electrons from valance band to conduction band. In theory, one photon is able to create one electron-hole pair across the band gap. For a material with carrier multiplication, high energy photons can excite more than one electron across the band gap and therefore, increase the solar cell efficiency.[13]

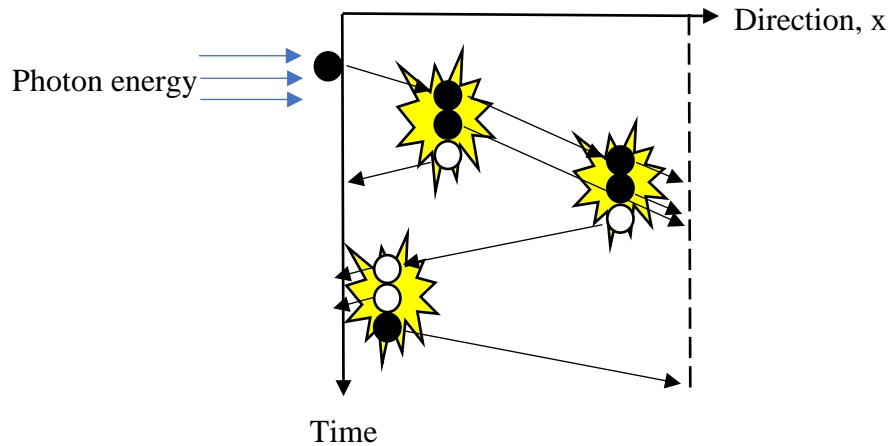


Figure 1.3: Carrier multiplication technique by using impact ionisation process initialised by an electron gaining photon energy. Electrons (black circle) are swept to positive x -direction while holes (white circle) drift to negative x -direction.

Hot carrier cells

Hot carrier cells has the special design that allows the material contact to be energy-selective so that the high energy carriers or ‘hot carriers’ can be collected before they lost most of their energy as heat. As the result, the energies are not lost due to thermalisation like how conventional solar cell normally works.

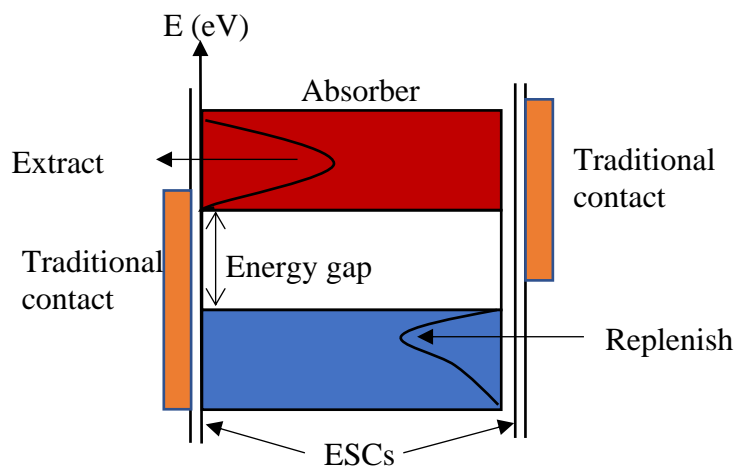


Figure 1.4: Band diagram of hot carrier solar cells. The ‘hot carriers’ remain in the absorber and are extracted through the narrow band energy ESCs before they thermalised to the band edges. ESCs is the energy selective contacts.[14]

Figure 1.4 shows the illustration for a typical band diagram of a hot carrier cell.[14] Hot carriers transfer their energy to the material very fast, normally sub-picosecond times. To address this

challenge, an optimal configuration and design structure is needed to ensure this method is competitive compared to other third generation solar cell structure.[15]

Multi-junction cells

Another current development in third generation solar cell is multi-junction solar cells. A number of semiconductor material systems with different bandgap value to each other are stacked together to allow photon absorption and collection at different part of the solar spectrum. By using this method, thermalisation and sub-band gap transmission losses can be minimised. Therefore, the limiting efficiency can be maximised. This type of solar cell can be monolithically grown or mechanically stacked for it to be operated. Each design has its own technological challenge that limits the efficiency.

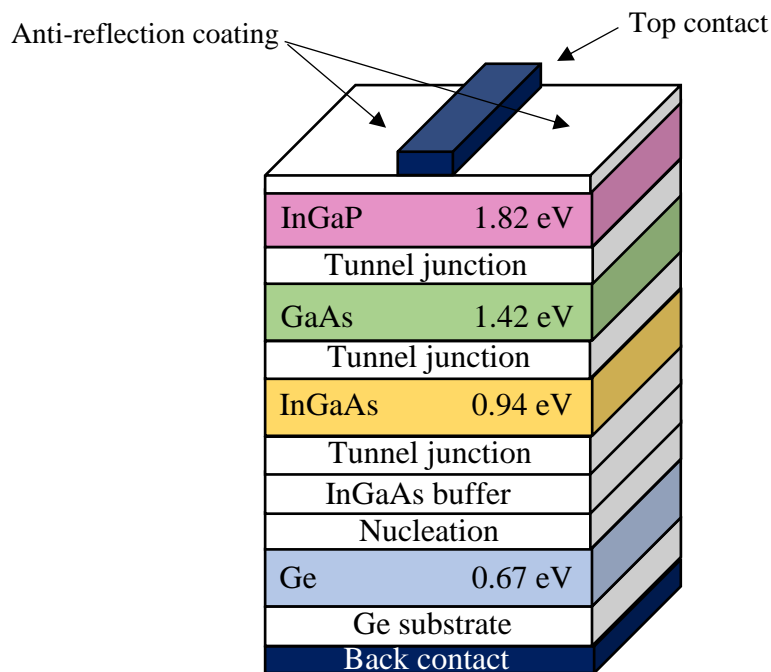


Figure 1.5: 4-junction InGaP/GaAs/InGaAs/Ge terrestrial concentrator solar cell cross section.

Figure 1.5 shows the cross section of a commercial 4-junctions solar cell. Unlike mechanical stack of multi-junction solar cell, the epitaxial growth of multi-junction solar cells requires different material to be deposited on top of each other with the highest band gap material at top surface and lowest band gap material is at the bottom. This is because the material will be transparent to the photons that will be absorbed in the lower bandgap material underneath it. In addition to that, it is limited by the sub-cell that generates the lowest current. Therefore, the

current value of each of the designed junctions has to be equal, this is known as ‘current matching’. This can be achieved by the optimisation of the depletion width of the solar cells and careful choice of semiconductors to adjust the amount of absorption in each junction

The maximum limiting efficiency of a multi-junction solar cell is usually determined by the number of junction and the matching of the lattice structures. Theoretically, high number of junctions will increase the maximum efficiency as it can cover wider range of solar spectrum. For example, under 1,000 x AM1.5 solar spectrum; single junction solar cell has maximum theoretical efficiency of 37% and a 36-junction solar cell increases the theoretical efficiency up to 72%. [16] For infinite number of junctions, the theoretical efficiency for the solar cell is 86.8%. [17] However, it is not easy to obtain matched junctions. This is because, strains introduced to the layers will increase and may reduce the efficiency of the solar cell. Current highest efficiency for multi-junction solar cell reported by National Renewable Energy Laboratory (NREL) is a 6-junction AlGaInP/AlGaAs/GaAs/InGaAs/InGaAs/InGaAs metamorphic solar cell with 47.1 ± 2.6 % solar conversion efficiency and 39.2% 1-Sun global efficiency. [18, 19]

Multiple quantum well solar cells

The remainder of this thesis will cover mainly about multiple quantum well (MQW) semiconductor structure and the outline here is for completeness. Extensive discussion on MQW solar cell will be in Chapter 2. The incorporation of MQW into multi-junction solar cells is one of the methods to alter the absorption edge of the junctions. Basically, photons with energy equal to the ground state of the wells are absorbed, producing carriers. With the built-in field in the junction, the carriers that sit at the ground state of the well will be thermally excited out of the wells and are collected producing the photocurrent. [20]

1.3 1 eV Material System

1.3.1 Rainbow of Choices

The efficiency of multiple junction solar cells is predicted to be at the optimum value by placing a 1 eV junction lattice-matched material system in a three-junction solar cell or replacing InGaAs on top of Ge for a four-junction solar cell.[21-23] The modelling of ideal three- and four-junction solar cell has been studied by Kurtz *et al.* showing the theoretical efficiencies calculated for both space and terrestrial applications. The 1 eV-material as the fourth junction inserted to the multi-junction solar cells also has been predicted to achieve more than 50% efficiencies under concentration.[24] Since there is no binary III-V material with this bandgap, it is necessary to look for a suitable semiconductor material where the band gap can be adjusted.

One of the ways to achieve strain compensating structures while trying to achieve 1 eV bandgap is by the application of strain-balanced material structure such as InGaAs/GaAsP MQWs.[25-28] However, InGaAs/GaAsP MQW has bandgap down to 1.28 eV only before the mismatch strain is introduced. Another way is by replacing Ge bottom layer from the InGaP/InGaAs/Ge design with InGaAs or CuInSe₂ (both with 1 eV bandgap), and it is expected to see higher efficiency solar cell from the structure.

Besides that, inverted metamorphic (IMM) layers from III-V materials also have the potential to increase the efficiency of solar cells. The IMM layers work by growing the lattice-matched top junctions on the substrate first before the lowest bandgap layer. After the growth, a handle is mounted to the layer and the substrate is removed by using etching procedure. By using this process, it can reduce the level of defects, preserve the device quality from the metamorphic layer and increase the efficiency. The drawback from this technology is, the processing requirement of IMM device is more complex than the conventional solar cells.[29-31]

In addition to that, the incorporation of dilute nitride only into GaAs has the capability to extend the emission wavelength and reduce the bandgap by 125 meV/% of nitrogen(N).[32] The interaction between the conduction band and the nitrogen resonant level leads to the reduction of the conduction band minimum thus, contribute to this large bandgap reduction. The optical bowing coefficient for GaAsN is on the order of 10 eV and strongly dependent on the nitrogen composition.[33] This coefficient value is large compared to the typical bowing coefficient for

other material systems such as InGaAs, GaAsSb and InGaSb which are on the order of 0.1 eV and independent of composition.

Incorporation of nitrogen into InGaAs producing a 1 eV junction of InGaAsN, also has been done by Friedman *et al.*[34] The maximum output power obtained by the device can reach between 61% to 66% from the ideal power but the internal quantum efficiency is very low. Incorporating ~3% nitrogen and ~8% antimony into GaAs forming GaAsNSb with a bandgap of 1 eV and also lattice-matched with GaAs also has been studied by several groups. [35, 36] This composition introduces no or very little strain into the solar cell junctions but the performance may be limited by the surface recombination of the junction and diffusion length of the device. One of the challenges while dealing with the incorporation of dilute nitride is the high quality nitride is very difficult to grow due to large difference in lattice constant and thermal expansion coefficient.[37] Photoluminescence efficiency, minority carrier diffusion length and electron mobility are greatly affected by the nitrogen incorporation because it is normally grown at lower growth temperature compared to other semiconductor devices.

Another material system that potentially becomes a way to achieve 1 eV energy bandgap is the combination of bismuth (Bi) and nitrogen into GaAs to create GaAsBiN. Sweeney *et al.* predict the potential that GaAsBiN has by using band anti-crossing theory modelling.[38, 39] The addition of bismuth to GaAs leads to an interaction with the valence band and addition of nitrogen leads to an interaction with the conduction band. Therefore, by introducing small percentage of both elements into GaAs, a lattice-matched system with a large bandgap reduction below the GaAs bandgap can be achieved.

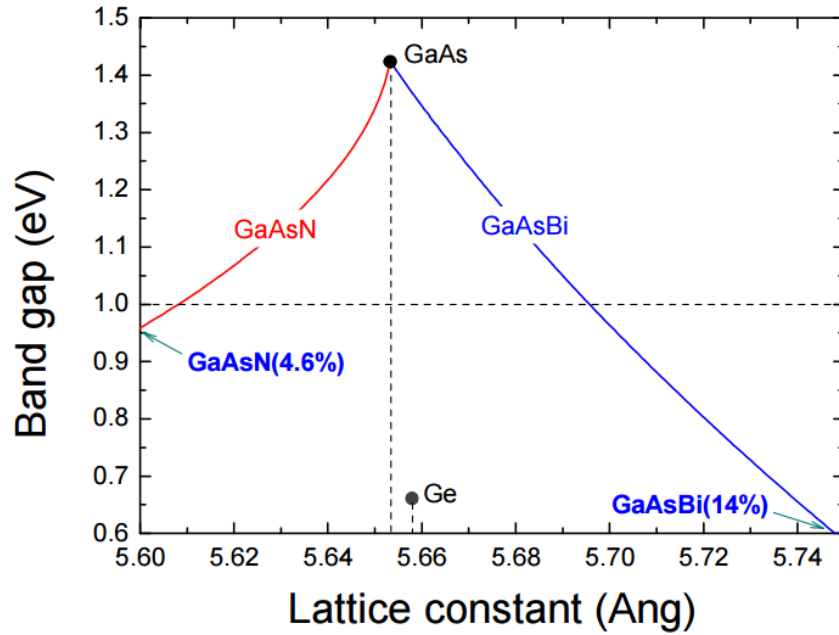


Figure 1.6: Bandgap bowing for GaAsN and GaAsBi. Image taken from [39].

From Figure 1.6, by balancing both elements, it is expected to result in lower strain value because it can be lattice-matched with GaAs when combining them in a quad-alloy. There are other publications on the theoretical model calculation, band structure and first principle calculations of band anti-crossing modelling too, such as by Nacer *et al.* [40] and Habchi *et al.* [41]. Although there are not many publications on the actual growth of this material system due to its highly-challenging growth condition, Yoshimoto *et al.* successfully did the growth of GaAsBiN using a Molecular Beam Epitaxy machine for the first time in 2004 [42] and its optical properties were published in 2006 [43] and 2007 [44].

1.3.2 GaAsBi for Device Sources and Detectors

For the past decades, bismuth is gaining a lot of interest in electronics industry especially from III-V semiconductor alloy group and are seen to be a promising material for developing new optoelectronic devices. Bismuth incorporated material systems are relatively new research compared to other compounds. A small fraction of bismuth introduced to an alloy is proven to have the ability to reduce the energy bandgap of a material allowing it to operate at longer wavelength and suitable for high speed electronics application. The semiconductor bandgap decreases by a rate of ~ 84 meV/ % bismuth compared to other element such as indium and antimony with reduction of 16 meV/% and 21 meV/%, respectively.[32] In comparison with

nitrogen, bismuth shows interaction at valence band (i.e increase in the valence band maximum) and expected to maintain the electron mobility at conduction band. [45]

Several groups have reported bismuth incorporated in many III-V semiconductor materials such as InAsBi [46], InSbBi [47], GaSbBi [48] and others. In this report, we are concentrating the incorporation of bismuth in GaAs to achieve a bandgap of at least 1 eV from the original GaAs bandgap of 1.42 eV. In the late 90's, K Oe (1998) from Japan is the first to successfully incorporate 2.4% of bismuth into GaAs.[49] Further investigation of GaAsBi can be found in [50] and [51] stating the temperature insensitive characteristic when bismuth is incorporated into GaAs. Tixier *et al.* published the first paper on the growth of GaAsBi epilayers by using the MBE machine and the author was able to incorporate the bismuth content up to 3.1% at low substrate temperature down to 380°C. As the result, the PL peak energy is reduced as the bismuth content is increased. [32]

The continuation of S Tixier's paper was published by S Francoeur (2003) from the same group.[52] The author is the first to talk about bandgap dependency of GaAsBi with bismuth content up to 3.6% and has the opposite opinion with K Oe (1998) about the sensitivity of the bandgap of GaAsBi to temperature compared to GaAs. The same author also talked about the bismuth impurities in GaAs and provide evidence that GaAsBi is an isoelectronic alloy.[53] Isoelectronic impurity can create noticeable localised states in the band gap when the alloy is at low temperature with low concentration. Other work on optimising the growth of GaAsBi was also reported in [54-56].

Other research on GaAsBi used as LEDs and lasers have been published too. This material can form the active region in these light-emitting structures either through electroluminescence (EL) or photoluminescence (PL). Moreover, the relative temperature independency of the energy bandgap makes it suitable for semiconductor lasers because the emitted wavelength is nearly constant when the temperature varies.[49] The characterisations of GaAsBi LED emitting at 987 nm have been reported by R.B Lewis *et al* on 2009.[57] The recombination mechanisms of the LEDs were later reported by the same group stating that the emission efficiency of the device reduces as the temperature increase due to the domination of non-radiative recombination in the LEDs.[58] Besides that, Ludewig *et al.* has reported the work on electrically pumped GaAsBi of Bi=2.2% single quantum well laser grown by MOVPE [59]

and the absorption coefficient of GaAsBi layers grown at different temperature specifically for optoelectronic terahertz devices has been investigated by Bertulis *et al.*[60] Extensive characterisations from GaAsBi has been extensively done by other groups too such as in [61] and [62].

Other than device source-type material, GaAsBi also is of interest as a detector such as for mid-infrared photosensitive detectors although not much on solar cell-based applications. The industry demand to increase the efficiency in the triple-junction InGaP/GaAs/Ge solar cell could be increased by adding fourth junction with a 1eV bandgap. A simulation study was conducted to prove that it easy to achieve this desired bandgap by putting around 6% of Bi into GaAs with only 0.7% strain on GaAs.[63, 64] It has a significantly lower strain compared to growing 1 eV $\text{In}_{0.27}\text{Ga}_{0.73}\text{As}$ on GaAs, which was 1.9%.[30] Hunter *et al.* has reported the electrical and absorption characteristics of GaAsBi/GaAs bulk diode in the near infrared with 6% Bi.[65]

The early study of InGaAs/GaAs MQW strained-devices have been studied.[66] It shows that the devices can be grown up to a certain critical thickness with acceptable level of strain. The material is later improved by introducing strain-balancing process, producing InGaAs/GaAsP MQW for multijunction solar cells.[25] Since Bi has the ability to reduce the bandgap value with less strain level, this becomes the vision for GaAsBi MQW to replace InGaAs for a triple or quad-junction solar cells. It is also suggested that well numbers have to be more than 50 to maximise absorption in photovoltaic applications.[67] The highest number of wells for GaAsBi/GaAs MQW that has been reported before this work is 24 wells.[68]

In this work, the electrical and opto-electronic properties of strained GaAsBi/GaAs MQW devices are studied. The electrical characterisations including current-voltage measurements and capacitance-voltage measurements have been performed. Besides that, the opto-electronic characterisations such as photocurrent measurements and illuminated current-voltage measurements have been done too. A strain-balanced material system is used to compare the material quality of the devices.

1.4 Thesis Overview

This chapter in summary has outlined the interest in the Sun as a source of renewable energy, different generations of solar cells available to date and the needs in 1 eV junction solar cells. In this thesis, optical, electrical and opto-electronic characterisations of MQW p-i-n diodes containing undoped GaAsBi wells with GaAs barrier layers are explored to study the potential of GaAsBi for solar cell applications for 1eV junction in a multi-junction solar cell.

Chapter 2 gives an overview on the theoretical concepts of III-V semiconductors and solar cells. This includes the formation of semiconductor band structure and how diode equation works. Then, the III-V lattice structure formation is also discussed including the effects of adding bismuth. Lastly, the concept of the MQW is explained with the effect of strain and strain relaxation on the structure.

Then, Chapter 3 will focus on the experimental methods used to obtain all the scientific data in this thesis. The optical characterisation specifically on the photoluminescence setup are discussed and followed by the device fabrication process to attain the electrical contact on the material. Then, the setup for electrical characterisations including current-voltage (I-V) and capacitance-voltage (C-V) measurements and opto-electronic characterisations focusing on the photocurrent measurement and I-V measurement under illumination are explained.

The result on electrical characterisations of the devices at room temperature is discussed in Chapter 4. First, previous work reported including optical and structural characterisations by people from the same group as the author is presented. Then, the C-V measurement with doping profile, I-V under dark condition measurement in forward and reverse bias for the devices were presented. The ideality factor and other I-V parameters are tabulated and discussed later in the chapter.

After that, Chapter 5 is the discussion on the opto-electronic characterisations which comprises photocurrent measurements and I-V measurements using a solar simulator. These results are important to identify the potential for GaAsBi as a solar cell and also to understand this material system before it is introduced into strain balanced structures.

Lastly, Chapter 6 summarises all of the work done in this report and outlines the suggestions for possible future work.

1.5 References

- [1] N. Nhede, "2020 Global Solar Installations to be 7 Times More than 2010's," ed. Smart Energy International, 2020.
- [2] P. K. Nayak, G. Garcia-Belmonte, A. Kahn, J. Bisquert, and D. Cahen, "Photovoltaic Efficiency Limits and Material Disorder," *Energy & Environmental Science*, Article vol. 5, no. 3, pp. 6022-6039, Mar 2012, doi: 10.1039/c2ee03178g.
- [3] R. D. Knight, *The Limit of Efficiency- Physics for Scientists and Engineers: A Strategic Approach*. 2008.
- [4] M. T. Kibria, A. Ahammed, S. M. Sony, F. Hossain, and S.-U. Islam, "A Review: Comparative Studies on Different Generation Solar Cells Technology," in *International Conference on Environmental Aspects of Bangladesh*, 2014.
- [5] S. W. Glunz, R. Preu, and D. Biro, "Crystalline Silicon Solar Cells: State-of-the-Art and Future Developments," in *Comprehensive Renewable Energy, Vol 1: Photovoltaic Solar Energy*, W. VanSark and A. Sayigh Eds. Amsterdam: Elsevier Science Bv, 2012, pp. 353-387.
- [6] M. A. Green, "Third Generation Photovoltaics: Solar Cells for 2020 and Beyond," *Physica E-Low-Dimensional Systems & Nanostructures*, Article; Proceedings Paper vol. 14, no. 1-2, pp. 65-70, Apr 2002, Art no. Pii s1386-9477(02)00361-2, doi: 10.1016/s1386-9477(02)00361-2.
- [7] G. Conibeer, "Third-generation Photovoltaics," *Materials Today*, Article vol. 10, no. 11, pp. 42-50, Nov 2007, doi: 10.1016/s1369-7021(07)70278-x.
- [8] M. A. Green, "Third Generation Concepts for Photovoltaics," *Proceedings of 3rd World Conference on Photovoltaic Energy Conversion, Vols a-C*, Proceedings Paper pp. 50-54, 2003.
- [9] G. W. Crabtree and N. S. Lewis, "Solar Energy Conversion," ed: American Institute of Physics, 2007, pp. 37-42.
- [10] Stevan. "Website: Solar Facts and Advice." Alchemie Limited Inc. (accessed 2018).
- [11] A. Trafton, "Solar Funnel- New Antenna Made of Carbon Nanotubes could Make Photovoltaic Cells more Efficient by Concentrating Solar Energy," ed. MIT News, 2010, pp. <http://news.mit.edu/2010/solar-antenna-0913>.
- [12] L. Oliwenstein, "Caltech Researchers Create Highly Absorbing, Flexible Solar Cells with Silicon Wire Arrays," ed. Caltech- Division of Chemistry and Chemical Engineering, 2010, pp. <http://www.cce.caltech.edu/news-and-events/news/caltech-researchers-create-highly-absorbing-flexible-solar-cells-silicon-wire-arrays-1597>.
- [13] M. Wolf, R. Brendel, J. H. Werner, and H. J. Queisser, "Solar Cell Efficiency and Carrier Multiplication in $\text{Si}_{(1-x)}\text{Ge}_x$ Alloys," *Journal of Applied Physics*, Article vol. 83, no. 8, pp. 4213-4221, Apr 1998, doi: 10.1063/1.367177.

- [14] G. Conibeer *et al.*, "Hot Carrier Solar Cell Absorbers: Materials, Mechanisms and Nanostructures," in *Conference on Next Generation Technologies for Solar Energy Conversion V*, San Diego, CA, Aug 19-20 2014, vol. 9178, BELLINGHAM: Spie-Int Soc Optical Engineering, in Proceedings of SPIE, 2014, doi: 10.1117/12.2067926. [Online]. Available: <Go to ISI>://WOS:000348035200001
- [15] D. König *et al.*, "Hot Carrier Solar Cells: Principles, Materials and Design," *Physica E-Low-Dimensional Systems & Nanostructures*, Article; Proceedings Paper vol. 42, no. 10, pp. 2862-2866, Sep 2010, doi: 10.1016/j.physe.2009.12.032.
- [16] C. H. Henry, "Limiting Efficiencies of Ideal Single and Multiple Energy-Gap Terrestrial Solar-Cells," *Journal of Applied Physics*, Article vol. 51, no. 8, pp. 4494-4500, 1980, doi: 10.1063/1.328272.
- [17] N. V. Yastrebova, "High-Efficiency Multi-Junction Solar Cells: Current Status and Future Potential," ed. Centre for Research in Photonics, University of Ottawa, April 2007.
- [18] M. A. Green, E. D. Dunlop, D. H. Levi, J. Hohl-Ebinger, M. Yoshita, and A. W. Y. Ho-Baillie, "Solar Cell Efficiency Tables (Version 54)," *Progress in Photovoltaics*, Article vol. 27, no. 7, pp. 565-575, Jul 2019, doi: 10.1002/pip.3171.
- [19] J. F. Geisz *et al.*, "Six-junction III-V Solar Cells with 47.1% Conversion Efficiency under 143 Suns Concentration," *Nature Energy*, Article vol. 5, no. 4, pp. 326+, Apr 2020, doi: 10.1038/s41560-020-0598-5.
- [20] N.J.Ekins-Daukes *et al.*, "Physics of Quantum Well Solar Cells," presented at the SPIE - The International Society for Optical Engineering, 2009.
- [21] D. Derkacs, R. Jones-Albertus, F. Suarez, and O. Fidaner, "Lattice-Matched Multijunction Solar Cells Employing a 1 eV GaInNAsSb Bottom Cell," *Journal of Photonics for Energy*, Article vol. 2, p. 8, 2012, Art no. 021805, doi: 10.1117/1.jpe.2.021805.
- [22] D. J. Friedman and S. R. Kurtz, "Breakeven Criteria for the GaInNAs Junction in GaInP/GaAs/GaInNAs/Ge Four-Junction Solar Cells," *Progress in Photovoltaics*, Article vol. 10, no. 5, pp. 331-344, Aug 2002, doi: 10.1002/pip.430.
- [23] D. B. Jackrel, S. R. Bank, H. B. Yuen, M. A. Wistey, and J. S. Harris, "Dilute Nitride GaInNAs and GaInNAsSb Solar Cells by Molecular Beam Epitaxy," *Journal of Applied Physics*, Article vol. 101, no. 11, p. 8, Jun 2007, Art no. 114916, doi: 10.1063/1.2744490.
- [24] S. R. Kurtz, D. Myers, J. M. Olson, and Ieee, "Projected Performance of Three- and Four-Junction Devices using GaAs and GaInP," in *26th IEEE Photovoltaic Specialists Conference*, Anaheim, Ca, Sep 29-Oct 03 1997, NEW YORK: Ieee, in Ieee Photovoltaic Specialists Conference, 1997, pp. 875-878, doi: 10.1109/pvsc.1997.654226. [Online]. Available: <Go to ISI>://WOS:000072313700210

- [25] N. J. Ekins-Daukes *et al.*, "Strain-balanced GaAsP/InGaAs Quantum Well Solar Cells," *Applied Physics Letters*, Article vol. 75, no. 26, pp. 4195-4197, Dec 1999, doi: 10.1063/1.125580.
- [26] N. J. Ekins-Daukes *et al.*, "Strained and Strain-Balanced Quantum Well Devices for High-Efficiency Tandem Solar Cells," *Solar Energy Materials and Solar Cells*, Article vol. 68, no. 1, pp. 71-87, Apr 2001, doi: 10.1016/s0927-0248(00)00346-9.
- [27] S. J. Ma, H. Sodabanlu, K. Watanabe, M. Sugiyama, and Y. Nakano, "Strain-Compensation Measurement and Simulation of InGaAs/GaAsP Multiple Quantum Wells by Metal Organic Vapor Phase Epitaxy using Wafer-Curvature," *Journal of Applied Physics*, Article vol. 110, no. 11, p. 5, Dec 2011, Art no. 113501, doi: 10.1063/1.3663309.
- [28] H. Sodabanlu, Y. P. Wang, K. Watanabe, M. Sugiyama, and Y. Nakano, "Growth of InGaAs/GaAsP Multiple Quantum Well Solar Cells on Mis-Orientated GaAs Substrates," *Journal of Applied Physics*, Article vol. 115, no. 23, p. 5, Jun 2014, Art no. 233104, doi: 10.1063/1.4884678.
- [29] H. Yoon *et al.*, "Progress of Inverted Metamorphic III-V Solar Cell Development at Spectrolab," in *33rd IEEE Photovoltaic Specialists Conference*, San Diego, CA, May 11-16 2008, NEW YORK: Ieee, in IEEE Photovoltaic Specialists Conference, 2008, pp. 82-87. [Online]. Available: <Go to ISI>://WOS:000273995000019
- [30] J. F. Geisz *et al.*, "40.8% Efficient Inverted Triple-Junction Solar Cell with Two Independently Metamorphic Junctions," *Applied Physics Letters*, Article vol. 93, no. 12, p. 3, Sep 2008, Art no. 123505, doi: 10.1063/1.2988497.
- [31] A. W. Walker, F. Bouchard, A. H. Trojnar, and K. Hinzer, "Inverted Metamorphic III-V Triple-Junction Solar Cell with a 1 eV CuInSe₂ Bottom Subcell," *International Journal of Photoenergy*, Article p. 10, 2014, Art no. 913170, doi: 10.1155/2014/913170.
- [32] S. Tixier *et al.*, "Molecular Beam Epitaxy Growth of GaAs_{1-x}Bi_x," *Applied Physics Letters*, Article vol. 82, no. 14, pp. 2245-2247, Apr 2003, doi: 10.1063/1.1565499.
- [33] S. H. Wei and A. Zunger, "Giant and Composition-Dependent Optical Bowing Coefficient in GaAsN Alloys," *Physical Review Letters*, vol. 76, no. 4, pp. 664-667, Jan 22 1996, doi: 10.1103/PhysRevLett.76.664.
- [34] D. J. Friedman, J. F. Geisz, S. R. Kurtz, and J. M. Olson, "1-eV Solar Cells with GaInNAs Active Layer," *Journal of Crystal Growth*, Article; Proceedings Paper vol. 195, no. 1-4, pp. 409-415, Dec 1998, doi: 10.1016/s0022-0248(98)00561-2.
- [35] A. Gubanov, V. Polojarvi, A. Aho, A. Tukiainen, N. V. Tkachenko, and M. Guina, "Dynamics of Time-Resolved Photoluminescence in GaInNAs and GaNAsSb Solar Cells," *Nanoscale Research Letters*, Article vol. 9, p. 4, Feb 2014, Art no. 80, doi: 10.1186/1556-276x-9-80.

- [36] T. Thomas *et al.*, "GaNASb 1-eV Solar Cells For Use in Lattice-Matched Multi-Junction Architectures," *2014 Ieee 40th Photovoltaic Specialist Conference (Pvsc)*, Proceedings Paper pp. 550-553, 2014.
- [37] J. S. Harris, "GaInNAs Long-Wavelength Lasers: Progress and Challenges," *Semiconductor Science and Technology*, Article vol. 17, no. 8, pp. 880-891, Aug 2002, doi: 10.1088/0268-1242/17/8/317.
- [38] S. J. Sweeney and S. R. Jin, "Bismide-Nitride Alloys: Promising for Efficient Light Emitting Devices in the Near- and Mid-Infrared," *Journal of Applied Physics*, Article vol. 113, no. 4, p. 6, Jan 2013, Art no. 043110, doi: 10.1063/1.4789624.
- [39] S. J. Sweeney, K. Hild, S. R. Jin, and Ieee, "The Potential of GaAsBiN for Multi-Junction Solar Cells," in *39th IEEE Photovoltaic Specialists Conference (PVSC)*, Tampa, FL, Jun 16-21 2013, NEW YORK: Ieee, in IEEE Photovoltaic Specialists Conference, 2013, pp. 2474-2478. [Online]. Available: <Go to ISI>://WOS:000340054100561
- [40] S. Nacer, A. Aissat, and K. Ferdjani, "Band Gap and Band Offsets of GaNASBi Lattice Matched to GaAs Substrate," *Optical and Quantum Electronics*, Article vol. 40, no. 9, pp. 677-683, Jul 2008, doi: 10.1007/s11082-008-9255-0.
- [41] M. M. Habchi, A. Ben Nasr, A. Rebey, and B. El Jani, "Electronic Band Structure Calculation of GaNASBi Alloys and Effective Mass Study," *Infrared Physics & Technology*, Article vol. 61, pp. 88-93, Nov 2013, doi: 10.1016/j.infrared.2013.07.012.
- [42] M. Yoshimoto *et al.*, "New Semiconductor GaNASBi Alloy Grown by Molecular Beam Epitaxy," *Japanese Journal of Applied Physics Part 2-Letters & Express Letters*, Article vol. 43, no. 7A, pp. L845-L847, Jul 2004, doi: 10.1143/jjap.43.1845.
- [43] M. Yoshimoto, W. Huang, G. Feng, and K. Oe, "New Semiconductor Alloy GaNASBi with Temperature-Insensitive Bandgap," *Physica Status Solidi B-Basic Solid State Physics*, Article; Proceedings Paper vol. 243, no. 7, pp. 1421-1425, Jun 2006, doi: 10.1002/pssb.200565270.
- [44] M. Yoshimoto, W. Huang, G. Feng, Y. Tanaka, and K. Oe, "Molecular-Beam Epitaxy of GaNASBi Layer for Temperature-Insensitive Wavelength Emission," *Journal of Crystal Growth*, Article; Proceedings Paper vol. 301, pp. 975-978, Apr 2007, doi: 10.1016/j.jcrysgro.2006.11.118.
- [45] K. Alberi, O. D. Dubon, W. Walukiewicz, K. M. Yu, K. Bertulis, and A. Krotkus, "Valence Band Anticrossing in GaBi_xAs_{1-x}," *Applied Physics Letters*, Article vol. 91, no. 5, p. 3, Jul 2007, Art no. 051909, doi: 10.1063/1.2768312.
- [46] H. Okamoto and K. Oe, "Growth of Metastable Alloy InAsBi by Low-Pressure MOVPE," *Japanese Journal of Applied Physics Part 1-Regular Papers Brief Communications & Review Papers*, Article; Proceedings Paper vol. 37, no. 3B, pp. 1608-1613, Mar 1998, doi: 10.1143/jjap.37.1608.

- [47] B. Joukoff and Jeanloui.Am, "Growth of InSb_{1-x}Bi_x Single-Crystals By Czochralski Method," *Journal of Crystal Growth*, Article vol. 12, no. 2, pp. 169-&, 1972, doi: 10.1016/0022-0248(72)90047-4.
- [48] S. K. Das, T. D. Das, S. Dhar, M. de la Mare, and A. Krier, "Near Infrared Photoluminescence Observed in Dilute GaSbBi Alloys Grown by Liquid Phase Epitaxy," *Infrared Physics & Technology*, Article vol. 55, no. 1, pp. 156-160, Jan 2012, doi: 10.1016/j.infrared.2011.11.003.
- [49] K. Oe and H. Okamoto, "New Semiconductor Alloy GaAs_{1-x}Bi_x Grown by Metal Organic Vapor Phase Epitaxy," *Japanese Journal of Applied Physics Part 2-Letters & Express Letters*, Article vol. 37, no. 11A, pp. L1283-L1285, Nov 1998, doi: 10.1143/jjap.37.11283.
- [50] K. Oe, "Characteristics of Semiconductor Alloy GaAs_{1-x}Bi_x," *Japanese Journal of Applied Physics Part 1-Regular Papers Short Notes & Review Papers*, Article vol. 41, no. 5A, pp. 2801-2806, May 2002, doi: 10.1143/jjap.41.2801.
- [51] K. Oe and H. Asai, "Proposal on a Temperature-Insensitive Wavelength Semiconductor Laser," *Ieice Transactions on Electronics*, Article vol. E79C, no. 12, pp. 1751-1759, Dec 1996.
- [52] S. Francoeur, M. J. Seong, A. Mascarenhas, S. Tixier, M. Adamcyk, and T. Tiedje, "Band Gap of GaAs_{1-x}Bi_x, 0 < x < 3.6%," *Applied Physics Letters*, Article vol. 82, no. 22, pp. 3874-3876, Jun 2003, doi: 10.1063/1.1581983.
- [53] S. Francoeur, S. Tixier, E. Young, T. Tiedje, and A. Mascarenhas, "Bi Isoelectronic Impurities in GaAs," *Physical Review B*, Article vol. 77, no. 8, p. 5, Feb 2008, Art no. 085209, doi: 10.1103/PhysRevB.77.085209.
- [54] X. Lu, D. A. Beaton, R. B. Lewis, T. Tiedje, and M. B. Whitwick, "Effect of Molecular Beam Epitaxy Growth Conditions on the Bi Content of GaAs_{1-x}Bi_x," *Applied Physics Letters*, Article vol. 92, no. 19, p. 3, May 2008, Art no. 192110, doi: 10.1063/1.2918844.
- [55] A. J. Ptak *et al.*, "Kinetically Limited Growth of GaAsBi by Molecular-Beam Epitaxy," *Journal of Crystal Growth*, Article vol. 338, no. 1, pp. 107-110, Jan 2012, doi: 10.1016/j.jcrysgr.2011.10.040.
- [56] A. R. Mohmad *et al.*, "Effects of Rapid Thermal Annealing on GaAs_{1-x}Bi_x Alloys," *Applied Physics Letters*, vol. 101, no. 1, Jul 2 2012, Art no. 012106, doi: 10.1063/1.4731784.
- [57] R. B. Lewis, D. A. Beaton, X. F. Lu, and T. Tiedje, "GaAs_{1-x}Bi_x Light Emitting Diodes," *Journal of Crystal Growth*, Article vol. 311, no. 7, pp. 1872-1875, Mar 2009, doi: 10.1016/j.jcrysgr.2008.11.093.
- [58] N. Hossain *et al.*, "Recombination Mechanisms and Band Alignment of GaAs_{1-x}Bi_x/GaAs Light Emitting Diodes," *Applied Physics Letters*, Article vol. 100, no. 5, p. 3, Jan 2012, Art no. 051105, doi: 10.1063/1.3681139.

- [59] P. Ludewig *et al.*, "Electrical Injection Ga(AsBi)/(AlGa)As Single Quantum Well Laser," *Applied Physics Letters*, Article vol. 102, no. 24, p. 3, Jun 2013, Art no. 242115, doi: 10.1063/1.4811736.
- [60] K. Bertulis *et al.*, "GaBiAs: A Material for Optoelectronic Terahertz Devices," *Applied Physics Letters*, Article vol. 88, no. 20, p. 3, May 2006, Art no. 201112, doi: 10.1063/1.2205180.
- [61] B. Pursley, M. Luengo-Kovac, G. Vardar, R. S. Goldman, and V. Sih, "Spin Lifetime Measurements in GaAsBi Thin Films," *Applied Physics Letters*, Article vol. 102, no. 2, p. 4, Jan 2013, Art no. 022420, doi: 10.1063/1.4781415.
- [62] T. Fuyuki, R. Yoshioka, K. Yoshida, and M. Yoshimoto, "Long-Wavelength Emission in Photo-Pumped GaAs_{1-x}Bi_x Laser with Low Temperature Dependence of Lasing Wavelength," *Applied Physics Letters*, Article vol. 103, no. 20, p. 4, Nov 2013, Art no. Unsp 202105, doi: 10.1063/1.4830273.
- [63] M. Usman, C. A. Broderick, A. Lindsay, and E. P. O'Reilly, "Tight-Binding Analysis of the Electronic Structure of Dilute Bismide Alloys of GaP and GaAs," *Physical Review B*, Article vol. 84, no. 24, p. 13, Dec 2011, Art no. 245202, doi: 10.1103/PhysRevB.84.245202.
- [64] T. Thomas *et al.*, "Requirements for a GaAsBi 1eV Sub-cell in a GaAs-based Multi-junction Solar Cell," *Semiconductor Science and Technology*, Article vol. 30, no. 9, p. 6, Sep 2015, Art no. 094010, doi: 10.1088/0268-1242/30/9/094010.
- [65] C. J. Hunter *et al.*, "Absorption Characteristics of GaAs_{1-x}Bi_x/GaAs Diodes in the Near-Infrared," *Ieee Photonics Technology Letters*, vol. 24, no. 23, pp. 2191-2194, Dec 1 2012, doi: 10.1109/lpt.2012.2225420.
- [66] R. Grey, J. P. R. David, P. A. Claxton, F. G. Sanz, and J. Woodhead, "Relaxation of Strain within Multilayer InGaAs/GaAs Pseudomorphic Structures," *Journal of Applied Physics*, Note vol. 66, no. 2, pp. 975-977, Jul 1989, doi: 10.1063/1.343478.
- [67] D. B. Bushnell *et al.*, "Effect of Well Number on the Performance of quantum-Well Solar Cells," *Journal of Applied Physics*, Article vol. 97, no. 12, p. 4, Jun 2005, Art no. 124908, doi: 10.1063/1.1946908.
- [68] Y. Tominaga, Y. Kinoshita, G. Feng, K. Oe, and M. Yoshimoto, "Growth of GaAs_{1-x}Bi_x/GaAs Multi-Quantum Wells by Molecular Beam Epitaxy," *Physica Status Solidi C - Current Topics in Solid State Physics, Vol 5, No 9*, Proceedings Paper vol. 5, no. 9, pp. 2719-2721, 2008, doi: 10.1002/pssc.200779214.

Chapter 2: Background Theory

2.1 Band Structure in Semiconductors

2.1.1 Atoms and their Electronic States

In quantum mechanics, every individual atom consists of electron occupies discrete energy levels. The electrons in solids also have to obey the Pauli exclusion principle where only one electron (with particular angular momentum, magnetic quantum number and direction of spin values) is allowed to moves around the atom's nucleus in a quantum state, and it will occupy the lowest available energy level. Figure 2.1 shows the electron energy in one atom where the potential energy functions as a barrier to bind the electrons to the nucleus. The lower states' electrons are more strongly bound to the nucleus.

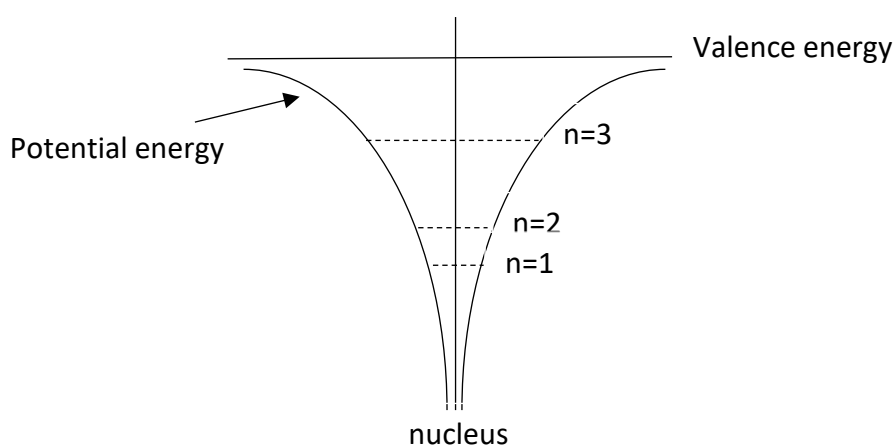


Figure 2.1: 1-D model of electron energy in one atom where n is the level of the electron. Lower n -level has stronger force attached to the nucleus. As the number of n increase, the electrons are more loosely bound to the nucleus.

When the atoms are brought together in a solid, the interaction between atoms causes their orbitals to overlap. To avoid the atoms disobeying the Pauli exclusion principle, the energy levels 'splits', change its levels and this lowers the potential energy barrier. As the number of atoms increases, more 'splitting' will occur between the atoms and this will form an energy band structure for the material.

2.1.2 Energy Bands in Semiconductors

Energy band structure are formed when there is a valence band and a conduction band separated by a value of energy gap, called as the band gap. The band gap is the forbidden gap or level between valence band and conduction band where no electrons are allowed to exist. The valence band is the highest filled band of any atom in which electrons are bound to atoms, while in the conduction band electrons are free to move after they are excited from the valence band. Depending on the value of energy gap that appears between these two bands, there are three categories to distinguish the material type which are metal, insulator and semiconductor.

Metals Valence and conduction bands overlap and electrons are free to move to higher empty levels. At 0 K, they remain conductive because the conduction band is partially filled with moving electrons. Good conductors such as copper (Cu), gold (Au), iron (Fe) and Aluminium (Al) are used mostly in electrical circuits and systems.

Insulators Insulators have relatively large bandgap compared to metals and semiconductors. They require a large amount of energy to excite electrons from the valence band to the conduction band. Examples of insulators are sodium chloride (NaCl), Aluminium oxide (Al_2O_3) and diamond (C) they are normally used as dielectrics in capacitors or act as insulation between conductors.

Semiconductors Semiconductors fall in a category between insulators and metals. At 0 K, a pure semiconductor behaves as an insulator and as temperature increases, there is a finite possibility that some of the electrons in valence band are excited to the conduction band. Electrons that are bound in valence band may obtain enough energy sourced from heat or light and the bound electrons will break free and can be excited to the conduction band. Silicon (Si), germanium (Ge), Gallium Arsenide (GaAs) and Indium Phosphide (InP) are semiconductor materials that are widely used in transistors, diodes, microprocessors etc. This chapter will extensively discuss semiconductors. Figure 2.2 shows the band structure in crystalline solids for different classes of material as discussed above.

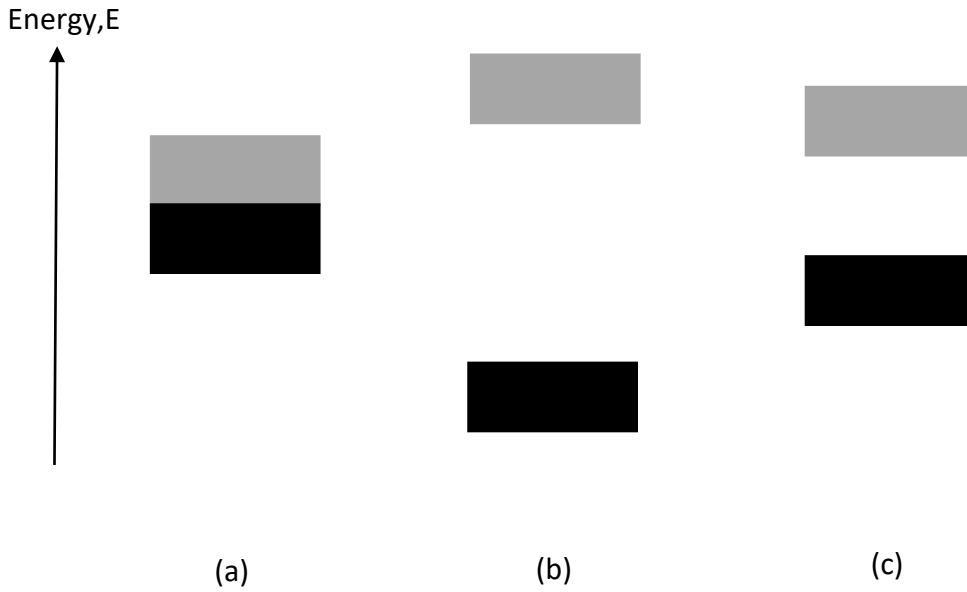


Figure 2.2: Simplified band structure for (a) metal, (b) insulator and (c) semiconductor. Grey blocks indicate conduction band and black blocks indicate valence band. The gap between these two blocks shows how much energy is needed to move an electron from valence band to conduction band.

2.2 Crystalline Semiconductor

2.2.1 The Fermi Level

Fermi-Dirac function is a statistical method to define a distribution function and behavior of electrons in term of a probability value. This is because it is more applicable to find the average behavior instead of calculating the real value of motions. Fermi level, E_F is related to the value of probability of an electron state of energy, E being occupied and it has values between zero and one. The probability function can be obtained by using the equation below,

$$P(E) = \frac{1}{1 + \exp\left(\frac{E - E_F}{kT}\right)} \quad (\text{Equation 2.1})$$

where Boltzmann constant, $k = 1.38 \times 10^{-23} \text{ JK}^{-1}$ and T is the temperature in Kelvin.

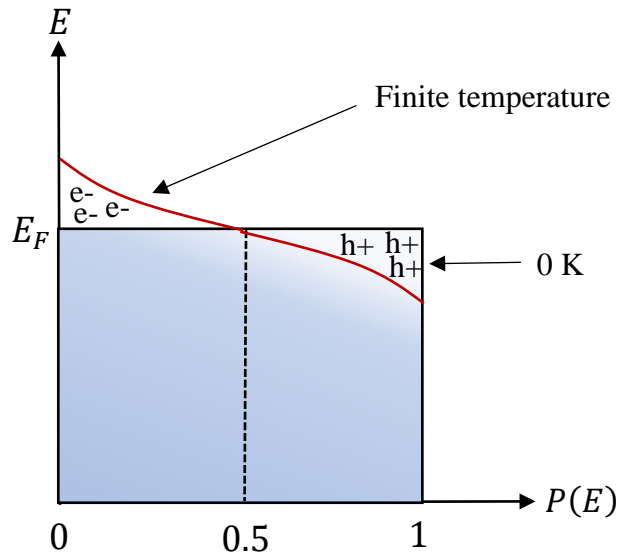


Figure 2.3: Fermi-Dirac probability for electron-hole pairs at 0 K (black line) and at finite temperature (red line) where some electron (e^-) near E_F acquire enough thermal energy and have $E > E_F$ leaving behind holes (h^+).

As seen in Figure 2.3, at 0K, the probabilities of an electron occupying a level above and below E_F are zero and one, respectively and as the temperature increases, the probability of electrons having energy more than fermi level ($E > E_F$) will increase. In an intrinsic semiconductor, E_F is halfway between the valence band and the conduction band as every free electron leave behind a free hole.

E_F can be modified by introducing external atoms into the lattice structure. Depending on the number of electrons in the outermost shell of an element, the external atoms, often referred to as the dopant can be categorised into two types, donor and acceptor. A donor or n-type dopant has more electrons in the outer shell than the atom it is introduced to while an acceptor or p-type dopant has less electrons. The energy levels of donor or acceptor are usually very close to the conduction band or valence band, respectively. As the dopant gains enough energy, they are able to donate an electron (hole) to the conduction band (valence band) and the carriers are free to move. In summary, Figure 2.4 shows the band diagram for intrinsic semiconductor, n-type semiconductor and p-type semiconductor.

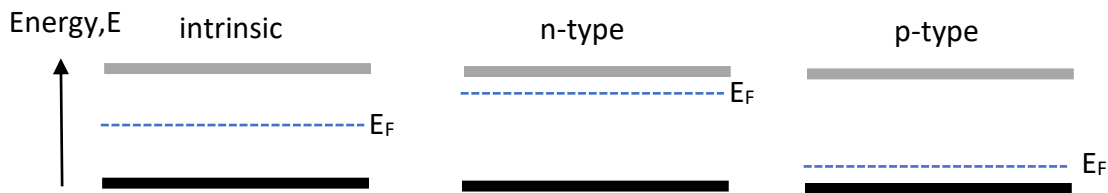


Figure 2.4: Band diagram for intrinsic, n-type and p-type semiconductor. Blue dashed line indicates the fermi level position between the conduction band and valence band.

2.2.2 The p-n Junction

A p-n diode is a construction of a semiconductor diode where a p-type semiconductor and an n-type semiconductor are brought together side by side to form a junction. In reality, it is not possible to do bring them together side by side because the bonds at the interface will not join perfectly to each other. This is different when the layer structures of a device are produced by the process of growth or diffusion of the layers on top of each. This p-n junction explanation is aimed to understand the physics behind it and how they interact “upon contact”.

There are four major components of carrier or current flow that exist in the junction. They are majority hole current from p, J_{hp} , minority hole current from n, J_{hn} , majority electron current from n, J_{en} and minority electron current from p, J_{ep} . These currents flow according to its way to restore equilibrium in the junction, where these current components sum to form a total current of zero. The majority carriers (J_{hp} or J_{en}) from each side will flow across the junction into the empty states on the opposite side resulting in diffusion current. As the electrons leave the n-region, they leave behind positive donor charges and as holes leave the p-region, they leave negative acceptor charges. As the results, an electric field is built up across the junction due to these charges and this causes a drift current due to minority carriers (J_{hn} or J_{ep}) flowing in opposite direction to the diffusion flow. The electric field will keep building up until the net current is zero; where the diffusion current is equal to drift current and the E_F of p-type and n-type is aligned. Note that the E_F level is now the same for both junctions. Figure 2.5 shows the p-n junction when they are brought together and at zero bias voltage.

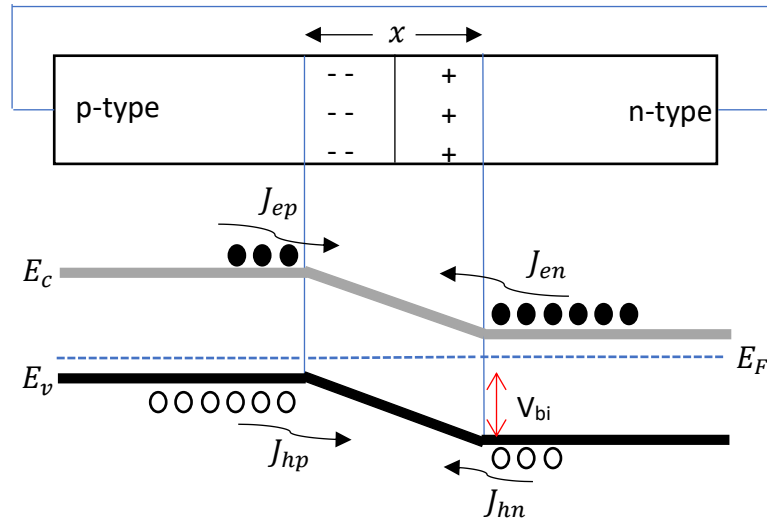


Figure 2.5: *p-n junction upon contact and at zero bias voltage. The arrows show the direction of carrier flow. E_c and E_v are the conduction band and valence band, respectively. The majority carriers, J_{hp} and J_{en} allows diffusion current and the minority carriers, J_{hn} and J_{ep} contribute to drift current at the junction.*

The state of equilibrium in the p-n junction can be altered by applying an external bias voltage, V across the junction. As seen in Figure 2.6 (a), by applying forward bias into the device, more majority carriers are allowed to flow across the junction because the depletion width is decreased as the total built-in potential, V_{bi} is reduced. As a result, the diffusion current is dominating the total diode current and is no longer equal to the drift current.

On the other hand, applying reverse bias allows the V_{bi} value to be increased, increasing the energy barrier and not allowing the majority carriers to flow through it. Therefore, no diffusion current is flowing across the junction. Very small minority carriers flow across the junction and are swept by the electric field. The carriers gain energy from thermal generation of electron-hole pairs in or near the depletion region in reverse bias, therefore they depend primarily on temperature. The process is shown in Figure 2.6 (b).

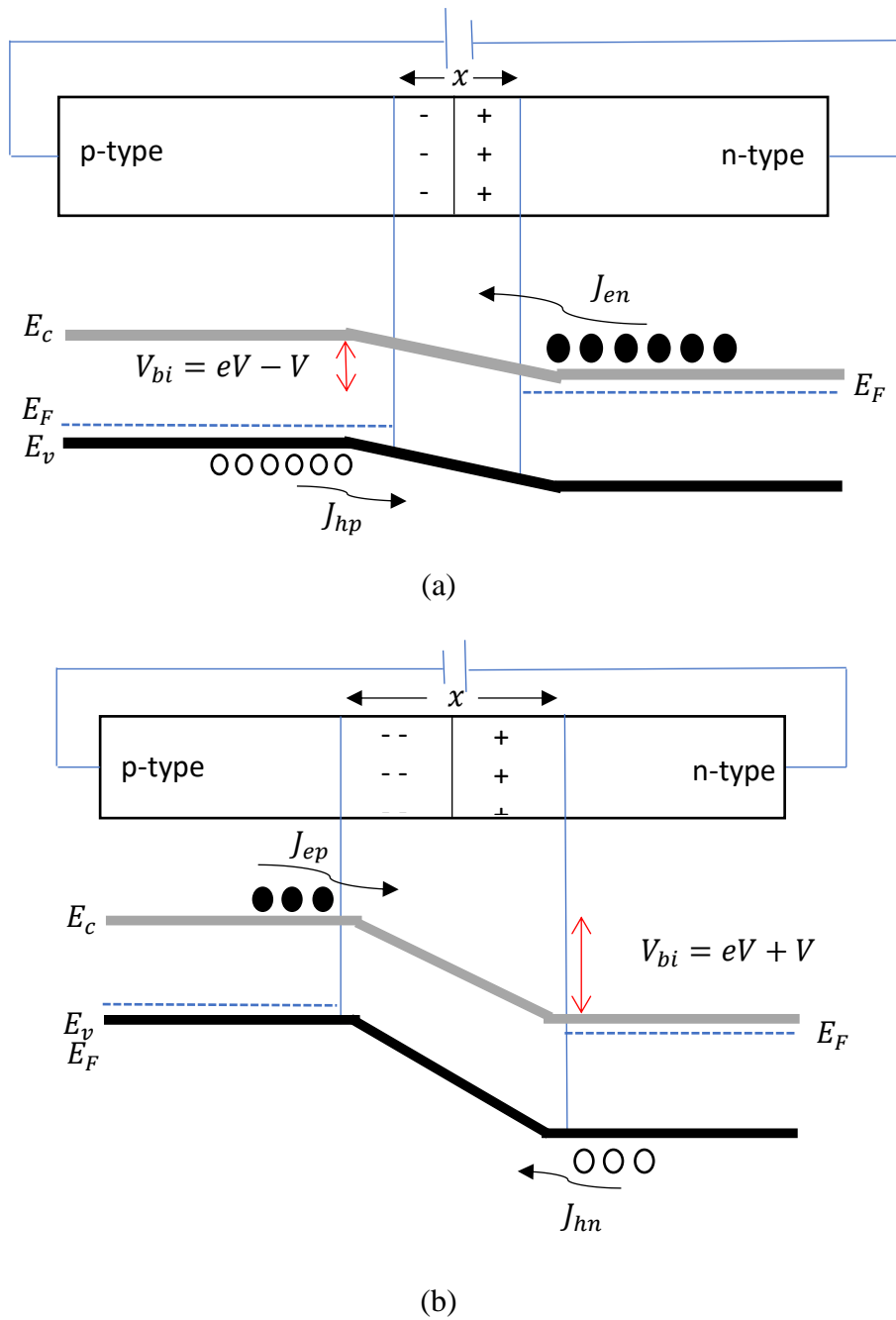


Figure 2.6: (a) p-n junction under forward and (b) p-n junction under reverse bias. Note that under these conditions, the fermi level is discontinuous.

2.2.3 Diode Equation

The exponential current-voltage equation of an ideal diode is called the Shockley equation or known as the diode equation. The ideality of this equation is based on a few assumptions. First, the built-in potential and applied voltages are only supported inside the depletion layer and anything outside that is assumed to be neutral. Secondly, the Boltzmann approximation of the carrier concentration throughout the depletion layer is valid. Besides that, it is assumed that the injected minority carrier concentrations are small compared to the majority carrier concentrations. Lastly, electron and hole currents are constant throughout the depletion layer as no generation-recombination current is present inside the layer.[1]

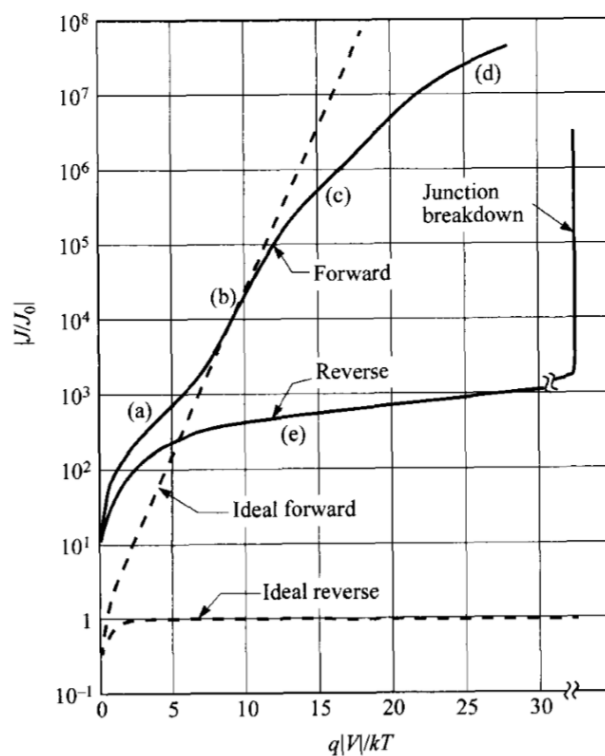


Figure 2.7: Current-Voltage characteristics of a practical Silicon diode. Image taken from [1]. Different components indicate different mechanism is dominating the I-V characteristics of the diode.

Practically, the current-voltage characteristics consist of several parts where at higher voltage value, in both forward and reverse; the current value deviates from ideal diode equation. Figure 2.7 shows the current-voltage characteristics for both ideal and practical Si diodes in forward

and reverse bias. It can be seen that a non-linear curve in forward bias is obtained from the practical Si diode due to different component. (a) shows generation-recombination current region takes place, (b) the domination of diffusion current, (c) is the high-injection region where minority carrier concentrations start to become comparable to majority carrier concentrations, (d) is when series resistance effect comes in. Meanwhile, (e) is the reverse leakage current due to generation-recombination and surface effects.[1]

The diode equation is generally presented as shown in Equation 2.2,

$$J_d = J_o \left[\exp \left(\frac{qV}{nkT} \right) - 1 \right] \quad (\text{Equation 2.2})$$

where J_d is the forward diode current flow through the junction, J_o is the saturation current across the junction, q is the electron charge = 1.6×10^{-19} C, V is the bias voltage applied, n is the ideality factor, k is Boltzmann's constant and T is the temperature in Kelvin. The diode equation from Equation 2.2 also can be re-written as Equation 2.3 due to the presence of a series resistance, R_s , if any.

$$J_d = J_o \left[\exp \left(\frac{q(V - J_f R_s)}{nkT} \right) \right] \quad (\text{Equation 2.3})$$

where J_f is the value of forward dark current. R_s will cause a voltage drop when the current is sufficiently high and it lowers the effective applied voltage across the diode. This problem can be mitigated by having a heavy doped cladding layer or metal deposition on semiconductor to obtain a low resistance ohmic contact. More explanation of the formulation of the diode equation will be given in Chapter 4.

Apart from p-n diode, another diode of interest is a p-i-n diode. The difference between these two diodes is p-i-n diode has an intrinsic or undoped semiconductor region in between p-type semiconductor and n-type semiconductor. This is to provide alternative working characteristics that cannot be achieved by using a p-n junction. For example, by having the intrinsic layer in the diode, the quantum efficiency of the diode can be increase. Besides that, its breakdown voltage also increased and can be used for high-voltage application. The p-i-n diode follow the diode equation at low frequency signals and behave like a perfect resistor at high frequency signals.[2]

2.3 Photo-carrier Generation and Recombination

2.3.1 Absorption of Light

Absorption of light is a way to allow carriers to move from valence band to free conduction band region creating current other than thermal excitation process. When light is radiated on the diode, the photons of similar or greater than the bandgap energy of the diode is being absorbed. Equation 2.4 is the relationship between the photon energy, E and wavelength of light, λ ,

$$E = \frac{hc}{\lambda} \quad (\text{Equation 2.4})$$

where h is Planck's constant and c is the speed of light. Figure 2.8 shows the illustration of carrier absorption and collection after the electron-hole pairs are created when photon falls onto a p-i-n diode. Absorption process is straightforward in i-region, or the carriers from the p or n regions have to diffuse into i-region before the charges are swept and creating electric current.

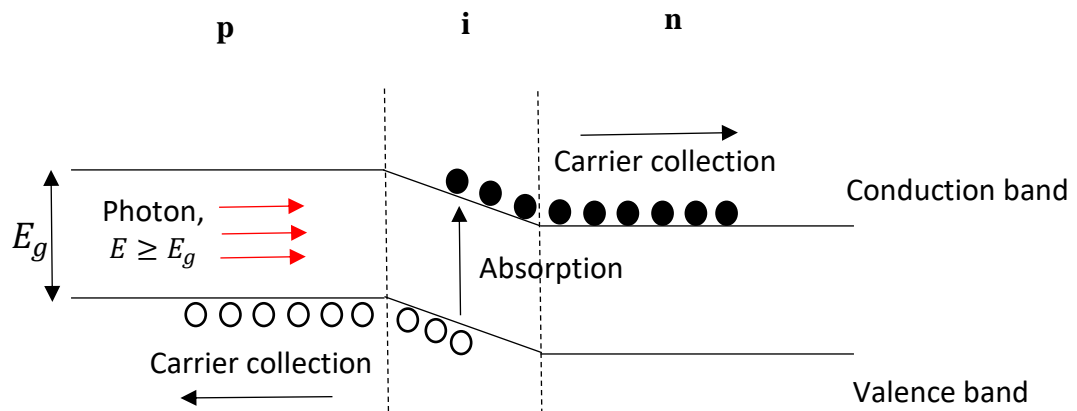
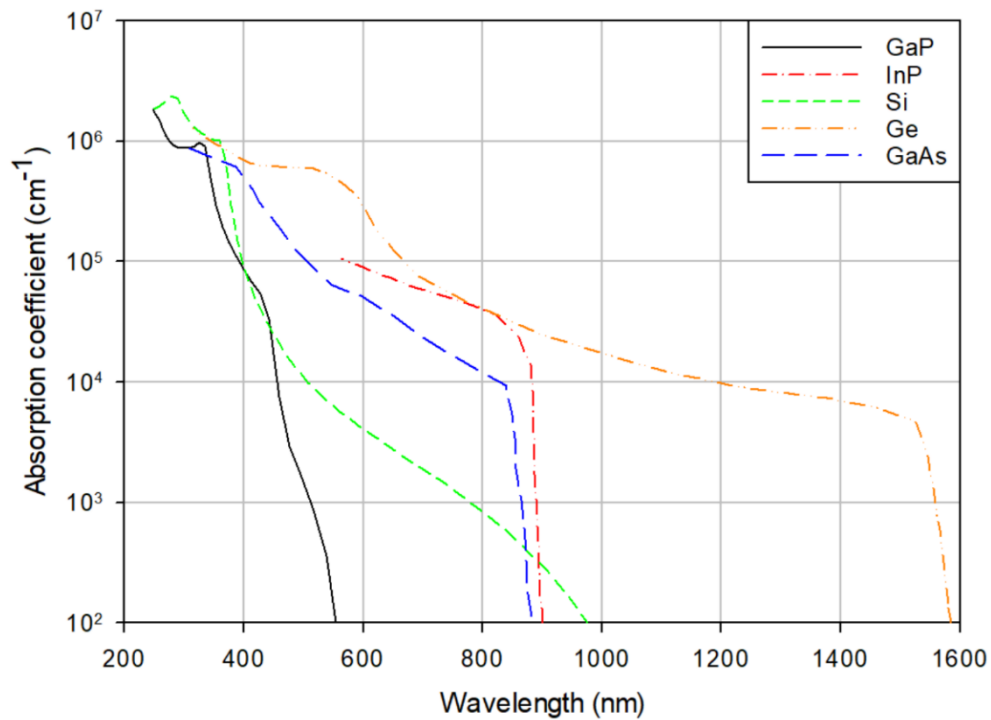


Figure 2.8: Photon absorption and carrier collection process in a p-i-n diode under when photon energy is applied to it.

Light that travels into the diode before its being absorbed is determined by the value of absorption coefficient, α . Different material has different α value; low α means poor absorption by the diode, and vice versa. Figure 2.9 shows the α for several semiconductor materials at room temperature. From the figure, it is shown that the value of α is not always constant and depends greatly on wavelength. Each material has its own wavelength cut-off, λ_c and any absorption at wavelength longer than λ_c is too small to give a comparable value of α due to insufficient energy to excite an electron from valence band to conduction band.



*Figure 2.9: Absorption coefficients for Ge, Si and various III-V semiconductor materials.
(Data adapted from [1])*

Figure 2.10 shows the absorption of light mechanism for a direct and indirect bandgap material. Absorption of light in a direct bandgap material allows simple promotion with negligible momentum change of carriers from valence band maximum to conduction band minimum due to its properties of having lowest point of conduction band that aligns with the highest point of the valence band in k-space. Meanwhile, an indirect bandgap material requires phonon energy and interaction with lattice to have a change in momentum in order to promote carriers from valence band to conduction band. Therefore, the probability of photons being absorbed in direct bandgap materials is higher than in indirect bandgap materials because the electron-hole pairs are generated without the momentum energy assisted from phonon.

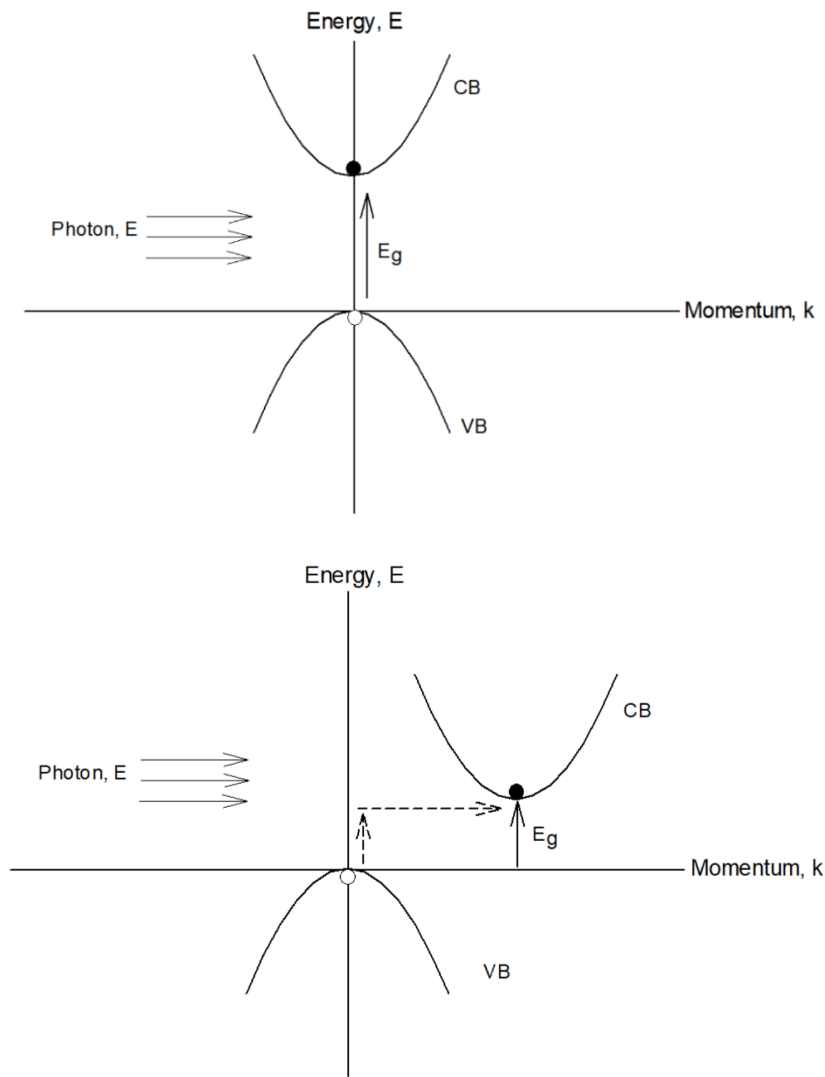


Figure 2.10: E - k diagram for a direct (top) and indirect (bottom) bandgap semiconductor.

The relationship between α and energy bandgap, E_g in direct and indirect bandgap material are given in Equation 2.5 and 2.6, respectively,

$$\alpha = A(E - E_g)^{1/2} \quad \text{(Equation 2.5)}$$

$$\alpha = A(E - E_g)^2 \quad \text{(Equation 2.6)}$$

where A is a constant.

2.3.2 Emission of Light

In contrary to the absorption of light, emission of light occurs when the electrons in the conduction band recombine with the holes in valence band emitting photons. The electron-hole pair created from the absorbed light will undergo scattering events and recombine at the energy band corresponds to the material bandgap. As the result, a photon with energy equal to the energy bandgap of the material is emitted. This is called radiative recombination process and it is usually happening in direct bandgap semiconductors. Non-radiative recombination also can happen in a semiconductor where potential energy is converted to other form of energy instead of photons. The radiative and non-radiative recombination processes in a classical semiconductor determine the intensity of light emission. The dominance of carrier recombination mechanism(s) can be described by the rate equation as shown in Equation 2.7 [1],

$$\frac{dn}{dt} = G - \frac{n}{\tau_{nr}} - Bnp \quad (\text{Equation 2.7})$$

where G is the carrier generation rate, τ_{nr} is the non-radiative recombination lifetime, B is the radiative recombination coefficient and n and p are electron and hole concentrations, respectively.

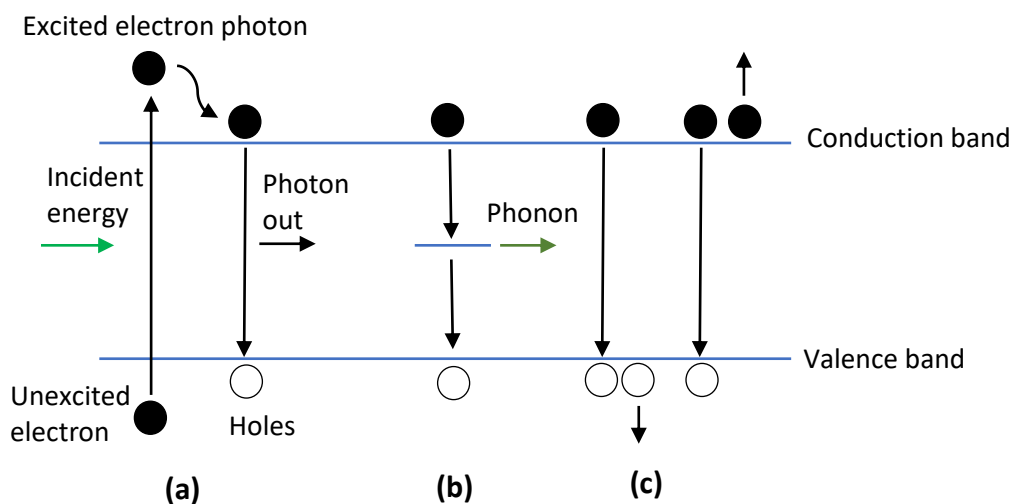


Figure 2.11: Different type of recombination processes. Process (a) is a radiative band to band recombination, (b) recombination through defects and (c) Auger recombination. (b) and (c) are the examples of non-radiative recombination.

From Figure 2.11 (a), the energy absorption from the incident energy such as light source, injected currents or heat energy will cause the electron in the valence band to be excited to the conduction band and creates an electron-hole pair. The high energy electron in conduction band then will undergo scattering, losses energy and it will sit at the lowest band state. When the electron reaches this location, it will recombine with the available hole and release a photon equal to energy bandgap.

Other than radiative band-to-band recombination, other type of recombination processes may occur inside the band that are non-radiative, which means no photons are given out from the recombination. They are able to recombination through defect states and Auger recombination. Figure 2.11 (b) shows the defect states recombination or also known as Shockley-Read-Hall (SRH) recombination. The recombination via defect states will release energy in form of heat or lattice vibration. It can occur when there are growth defects in the materials such as dislocations of atoms, point defects or impurities presence during the growth such as carbon and oxygen.

There are different Auger recombination processes that can occur in a material band depending on the nature of the transition and the carrier concentration. The processes such as direct Auger or phonon-assisted Auger recombination occur when there is a three-body collision event. Figure 2.11 (c) shows a direct Auger recombination. This type of recombination occurs when the electron recombines with the hole in valence band but the energy released is not in the form of a photon. The energy is transferred to or absorbed by a third carrier. Another electron or hole can be excited to a higher level in the conduction band or deeper in the valence band, respectively. The highly excited carrier then sits at the edge of the conduction band or the valence band after the excess energy is lost in form of phonons. This type of recombination usually occurs when high numbers of carriers are created when a high incident energy is absorbed.

2.3.3 Semiconductor Opto-Electronic Devices

In this work, the application of the diode equation to semiconductor opto-electronic devices (working as emitters and detectors, specifically in solar cell applications) is discussed. Generally, semiconductor emitter devices such as LEDs and lasers work by injecting electrons and holes across the band structure semiconductor junction under forward bias, where they will recombine with the majority carriers. The recombination process produces photons of energy that is equal to the bandgap and emission occurs. For LED, spontaneous emission from InAs which has wavelength of 3,800 nm is used for environmental monitoring and GaN with blue ultraviolet wavelength of 340-590 nm is applied for DVD player reader. Meanwhile, laser has a feedback mechanism that amplifies stimulated emission when threshold current is met. The photons created are also identical in energy, coherent with each other and therefore the laser's emitted linewidth is narrower than that of an LED. For examples, InGaP-based laser pointers generate red light.

For semiconductor detector devices like photodiode and solar cell, they work by absorbing the light that falls onto the diode and create electron-hole pairs producing electrical current. The minimum energy needed to create the pair is equal to the band gap of the semiconductor. A photodiode is widely used as sensors and detectors due to its small size, fast response time and low power consumption. Different types of photodiodes such as p-i-n, avalanche and Schottky photodiodes are designed to work in reverse bias condition. Besides that, solar cell also can be treated as a photodiode due to its ability to convert light into photocurrent. The difference between normal photodiode and solar cell is that solar cell operates in forward bias condition. In-depth explanation about solar cell is discussed in the next sub-section. Figure 2.12 shows the region of operation for opto-electronic devices at four different I-V quadrants.

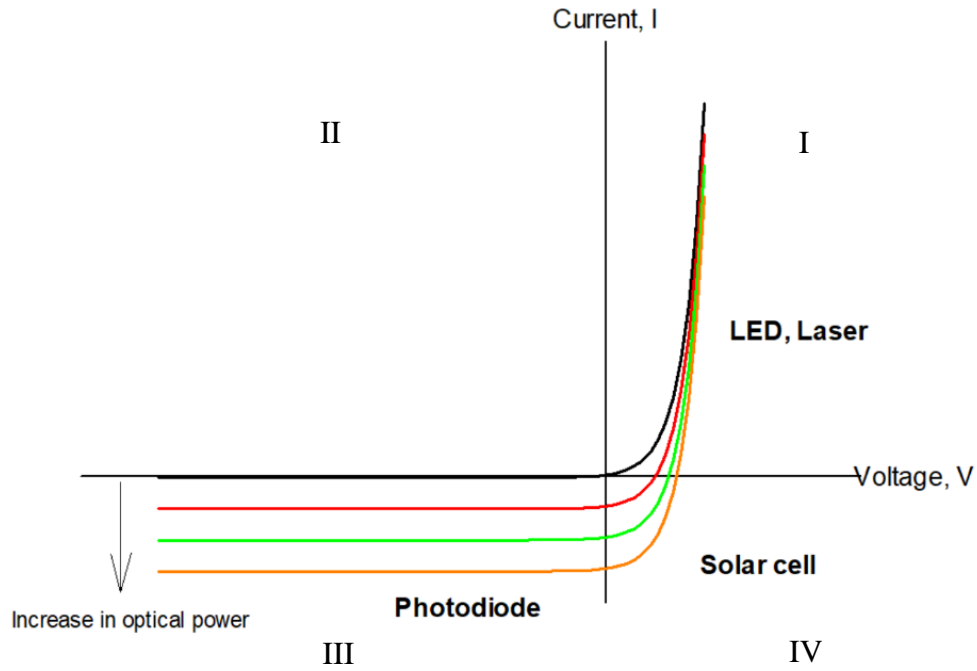


Figure 2.12: Different quadrants of operating region for all opto-electronic devices mentioned above. The second quadrant in the figure is the unphysical region for any electronic device and nothing works in the region.

2.3.4 Solar Cells

In a full closed-circuit diode, the photocurrent, I_L generates voltage and forward biases the diode. Then, a forward diode current begins to flow in the opposite direction to the photocurrent. The total current can be expressed as follows,

$$I = I_d - I_L \quad (\text{Equation 2.8})$$

$$I = I_0 \left[\exp\left(\frac{eV}{nkT}\right) - 1 \right] - I_L \quad (\text{Equation 2.9})$$

By knowing the value of dark current from I_d , the actual I_L created by the devices can be determined. The simplified solar cell equivalent circuit is as shown in Figure 2.13, showing the opposite direction of both currents.

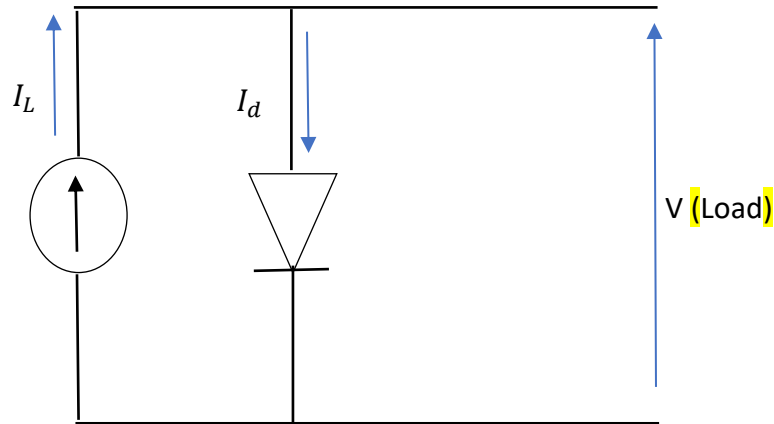


Figure 2.13: Equivalent circuit of an ideal solar cell under illumination.

There are two main parameters that involve in determining the solar cell characteristic for a diode; short circuit current, I_{SC} and open circuit voltage, V_{OC} . From Equation 2.9, assuming that dark current at zero bias is absent, total current is equal to I_L only and its value increase proportionally with light intensity. Meanwhile, V_{OC} is the value of voltage when I_d and I_L value is the same, or simply expressed as when the total current is zero. The typical operating region for a solar cell falls at the fourth quadrant of I-V characteristics.

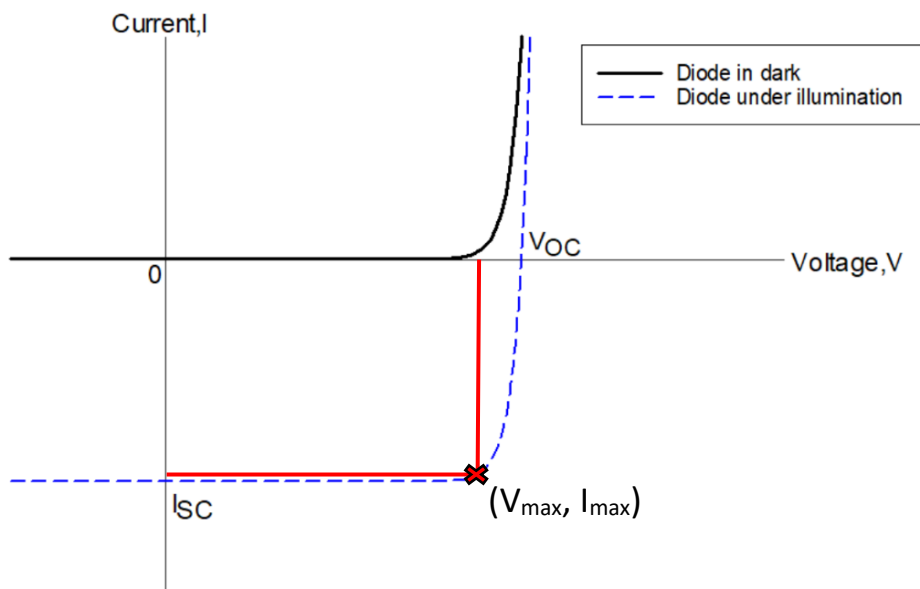


Figure 2.14: I-V characteristics for diode under dark condition and under illumination. At reverse voltage, the current is constant and forward current increase exponentially with voltage. V_{max} and I_{max} are the maximum voltage and maximum current of the solar cell, respectively.

Figure 2.14 shows the I-V characteristics comparison for an ideal diode in dark condition and under illumination. The magnitude of I_L created depends on the intensity of the light that falls onto the diode. If the intensity is higher, the I-V curve is shifted downwards and the values of V_{OC} and I_{SC} is increased. Ideally, the value of maximum voltage, V_{max} and maximum current, I_{max} from the solar cell power output have to be very close to V_{OC} and I_{SC} , respectively. The measure of this quality is called as the fill factor (FF) which is a ratio of the maximum power output and the “ideal” power output.

$$P_{max} = I_{max} \times V_{max} \quad (\text{Equation 2.10})$$

$$\text{Fill factor} = \frac{V_{max} \times I_{max}}{V_{OC} \times I_{SC}} \quad (\text{Equation 2.11})$$

2.4 III-V Semiconductor Material Systems

As mentioned in previous chapter, single junction silicon is widely used in solar cell industry and at the same time, multi-junction solar cell consists of different layer of material systems are fast-developed to compete with the readily available technology. In this section, we will focus on the development of III-V semiconductor material as one of the potential next generation technologies for solar cells.

2.4.1 Lattice Structure Formation

Group →	III	IV	V
Period ↓			
2	B	C	N
3	Al	Si	P
4	Ga	Ge	As
5	In	Sn	Sb
6	Tl	Pb	Bi

Figure 2.15: Simplified periodic table of group III, IV and V.

Figure 2.15 shows the simplified periodic table and elements in group III, IV and V (renamed as 13, 14 and 15 as reported in [3]) which is the group of interest in this report. Every semiconductor material will have its unique energy bandgap value and lattice constant.

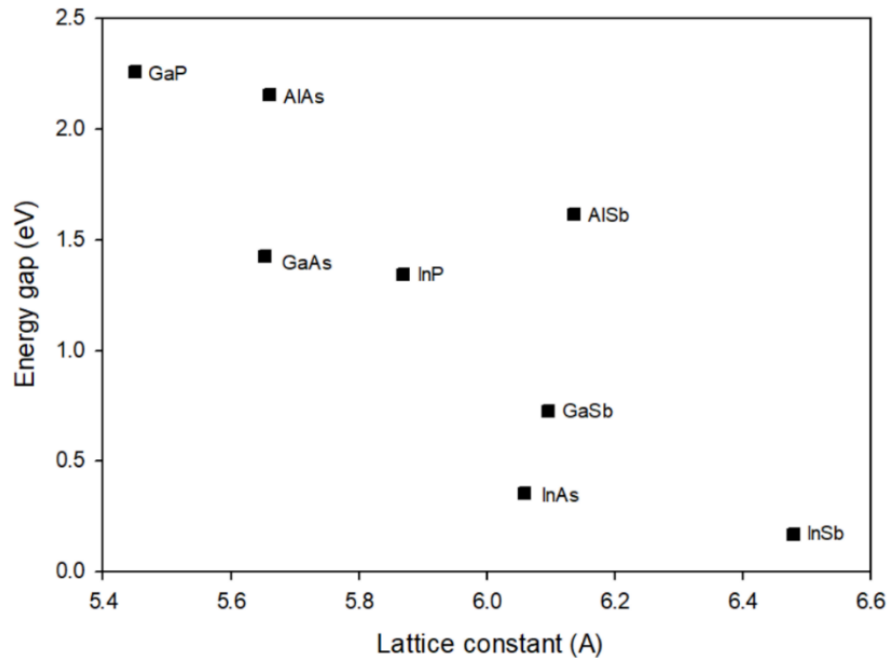


Figure 2.16: Lattice constant and energy bandgap value for several III-V semiconductors.

The bandgaps and lattice constants for several binary III-V semiconductors that are commonly studied are shown in Figure 2.16. Lattice constant is a physical parameter used to measure the unit cells of a material in a crystal lattice. Most of III-V semiconductors are a diamond lattice or called zinc blende structure, which is basically a face-centred-cubic lattice structure with two atoms in the base. For example, GaAs is a combination of gallium and arsenic sublattices. Due to the equal in length for all three axes in this structure (from its volume), let say a , b and c ; the lattice constant value can be referred as one vector value only i.e a . In other word, the lattice constant is independent of direction.

2.4.2 Vegard's Law

In semiconductor-device applications, it is possible to create a ternary compound by alloying two materials with different band gaps and lattice constants. Figure 2.17 shows the alloying lines formed when combining two binary semiconductors creating direct or indirect bandgap material. As long as it matches the lattice structure, atoms dislocation can be avoided hence electrical defects can be minimalised. In addition to that, a good heterostructure junction can

still be grown even if the lattice constant is not matched as long as the layer thickness is below the maximum layer thickness to hold the interface and avoid relaxation.

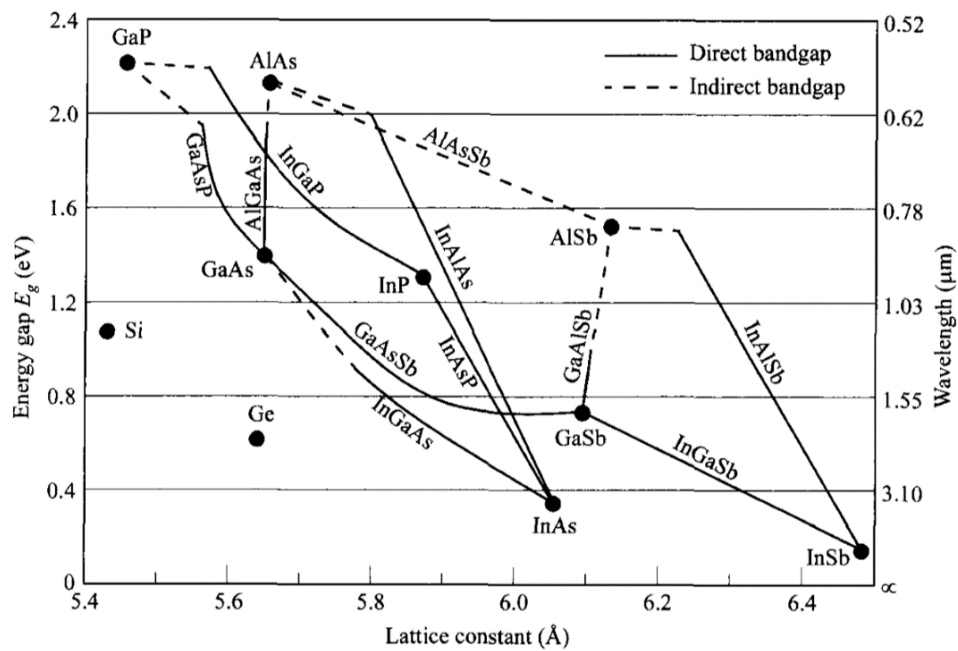


Figure 2.17: Lattice constant diagram for III-V semiconductors with the addition to the ternary alloying lines. Solid and dashed lines represent direct and indirect bandgap materials, respectively. (Image taken from [1])

Vegard's Law is a linear dependency of a lattice constant for a semiconductor compound on the alloy composition.[4] The advantages of adding more element(s) into a binary compound is that more semiconductor compound with different energy bandgap and lattice constant can be tailored to suits the demand in any applications needed. For example, from Figure 2.17, for GaAs; its lattice constant increase as antimony (Sb), aluminium (Al) or indium (In) is added into the compound and decrease as phosphorus (P) is added. The energy bandgap also changes with changes in the element composition. It is common to use subscripts to denote the percentage or ration of the element concentrations for formed compound i.e $A_xB_{1-x}C$, where x is a value between zero and one. An empirical approximation of a semiconductor bandgap energy based on Vegard's Law can be expressed as follows:

$$E_{ABC} = xE_{AC} + (1 - x)E_{BC} + x(1 - x)b \quad (\text{Equation 2.10})$$

where E_{ABC} is the bandgap of the ternary semiconductor, E_{AC} and E_{BC} are the bandgaps of the end binary compounds AC and BC , respectively, and b is the bowing parameter. Bowing parameter is a parabolic term that scales the curvature correction needed to form the energy bandgap of a semiconductor. There are also unexpected changes in some of the alloying lines where the curve is reconstructed due to a change from direct to indirect bandgap material.

2.4.3 Band Anticrossing Model

For some combinations of III-V group, Vegard's Law is not practical. This is due to high value of bowing parameter and Equation 2.10 could not predict the bandgap value adequately. To mitigate this deviation from this linearity law, several approaches and theoretical explanations have been made including dielectric modelling, density functional theory and scaling rule.[5-8] The most recent modelling called two-level band anti-crossing (BAC) was proposed when introducing nitrogen into a host binary compound due to its highly mismatched alloy properties, for example, introducing nitrogen into GaAs.[9, 10] The value of the bowing coefficient calculated for GaAsN is 25 eV which is very big compared to typical value for ternary compound, about less than 1 eV.[11] The coefficient value also varies with nitrogen composition unlike most ternary alloys. BAC model assumes that the localised nitrogen states interact with the conduction band of GaAs. This model is then later proposed to other highly mismatch alloys too such as GaNP.[12, 13]

2.4.4 Valence Band Anti-Crossing Model

To form GaAsBi, the binary III-V compound needed are GaAs and GaBi. GaBi is found to be a semimetal element that has never been fabricated and only theoretically investigated. From the theoretical calculations, it is predicted that GaBi is a semimetal with a bandgap of -0.224eV [14] and a lattice constant of 6.324 Å.[15] The bandgap is a negative value due to the band gap inversion where the bottom of the conduction band is lower than the top of valence band.

Introduction of bismuth into GaAs producing GaAsBi shows reduction in band-gap value as reported in [16] and research studies show that the localised bismuth states have close interaction with the valence band and comparatively little interaction with the conduction band.[17]

As the pattern in bandgap reduction for GaAsBi shows a large bowing similar to GaAsN, the BAC model can be adopted into the calculation and called as the valence band anti-crossing (VBAC) model. The splitting occurs at the valence band forming two sub-bands, higher energy band edge, E_+ and lower energy band edge, E_- where E_+ is the new valence band maximum. The valence band energies can be presented by the equations below,

$$E_{\pm}(GaAsBi) = \frac{E_v(GaAs) + E_{Bi} \pm \sqrt{(E_v(GaAs) - E_{Bi})^2 + 4xC_{Bi}^2}}{2} \quad (\text{Equation 2.11})$$

$$E_v(GaAs) = -\frac{\hbar^2 k^2}{2m^*} \quad (\text{Equation 2.12})$$

where $E_v(GaAs)$ is the valence band maximum (VBM) energy for GaAs, E_{Bi} is the Bi level energy, x is the Bi fraction, C_{Bi} is the coupling between the Bi level and the GaAs VBM, \hbar is the Planck constant, k is the momentum in wavevector and m^* is the effective mass of hole. By using the value of C_{Bi} of 1.6 eV and E_{Bi} of 0.4 eV below the VBM of GaAs from [17], a calculated VBAC model can be plotted as shown in Figure 2.18.

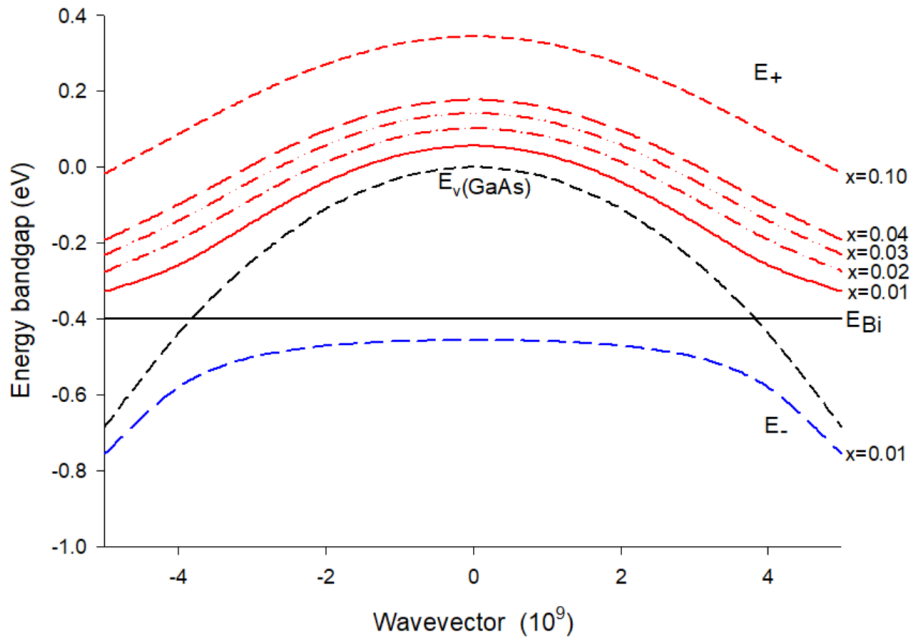


Figure 2.18: The calculated valence band structure of GaAsBi using the VBAC model for different Bi fraction. The VBM of GaAsBi increases as more Bi is introduced to the structure therefore reducing the bandgap.

A simulation study on bulk GaAsBi has been conducted to prove that it is achievable to obtain 1 eV bandgap by putting around 6% of Bi into GaAs with only 0.7% strain on GaAs.[18] It has a significantly lower strain compared to growing similar bandgap for $\text{In}_{0.27}\text{Ga}_{0.73}\text{As}$ on GaAs, which produces 1.9% strain.[19] Simulated performance for single junction GaAsBi solar cell also has been calculated and is compared to a Ge solar cell. The GaAsBi cell produces less I_{SC} but better V_{OC} value compared to Ge cell. This paper however, uses Vegard's Law instead of VBAC modelling to define the bandgap of the material system.[20]

Besides that, a theoretical calculation done by Khanom *et al.* shows that the efficiency for quad-junction solar cell including GaAsBi junction with 6% Bi can achieve up to 52.2% at AM1.5G (global) and 56.7% at AM1.5D (direct) under 1SUN condition. The calculation assumes no losses from reflection, grid coverage and series resistance.[21] Another simulation study has been done by Thomas *et al.*[22] GaAsBi bulk n-p structure with 6% bismuth is able to gain sufficient current to match the other sub-cells but the background doping and minority carrier transport could be the drawback for achieving its maximum efficiency.

Referencing to the absorption coefficient value for bulk GaAsBi from [23], GaAsBi bulk layer need to be 1.9 μm thick to obtain a current matched quad-junction cell. However, this may be highly challenging to achieve due to the fundamental limit of high background doping caused by low growth temperature required by GaAsBi. InGaAs bulk device will also need about the same thickness as GaAsBi for a current-matched junction, assuming that the absorption coefficient value is the same. To achieve the desired thickness, InGaAs requires more In percentage and therefore induce higher level of strain in the structure. To mitigate this problem, a multiple quantum wells structure can be applied to delay the onset dislocation by growing the material below its critical thicknesses. This application will be discussed in the next section.

2.5 Multiple Quantum Well Structures

2.5.1 Multiple Quantum Wells

Semiconductors with different energy bandgap value can form a heterojunction semiconductor when they are grown together. One of the applications of heterojunction is to form a quantum well. The growth of a quantum well consists of a well ‘sandwiched’ between two barriers where the energy bandgap of the barrier, $E_{barrier}$ is higher than energy bandgap of the well, E_{well} . Several identical wells grown in between barriers are called as multiple quantum wells (MQW).

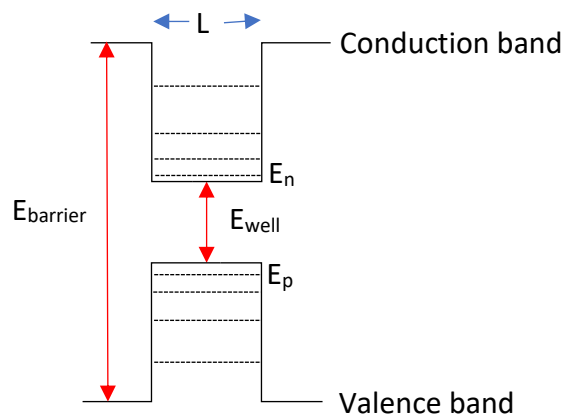


Figure 2.19: Illustration of quantum well with difference in barrier energy bandgap and well energy bandgap. L is the well width. The lines in the wells indicate different quantisation energy in conduction and valence band.

Figure 2.19 shows the illustration of a quantum well where the well has lowest energy for electron well and highest energy for a hole well. Different with bulk, where the electrons/holes are free to move in the conduction/valence band in all directions (3-D), the electrons and holes are confined in a two-dimensional (2-D) system in a quantum well. The carrier confinement energy in a quantum well exists when the well width, L is small and becomes comparable to the de Broglie wavelength of the carriers. De Broglie wavelength, λ_b can be determined as,

$$\lambda_b = h/p \quad (\text{Equation 2.13})$$

where h is the Planck constant and p is the momentum of the carriers. The carriers in quantum well also can be treated as bound particles or as wavefunctions. In a classical theory; for bound particles, the carriers can have any energy as long as it is within the well. However, as

wavefunctions, only certain wavelengths are possible. This is called as quantisation where the energy is no longer continuous and the carriers only have discrete energy value within the well. The quantisation energy in conduction band, E_n can be determined by Equation 2.14,

$$E_n = \frac{n^2 h^2}{8mL^2} \quad (\text{Equation 2.14})$$

where $n = 1, 2, 3 \dots$ is the quantisation level, h is the Planck constant, m is the effective mass of electron, L is the well width. The same equation is used for quantisation effect for holes, E_p in valence band and only effective mass value is different. As the well width becomes smaller, the quantisation energy within the well becomes larger. Unlike MQWs, superlattice structure has a very thin barrier and the wavefunctions of the wells can overlap. Due to the ease in tunnelling process between the wells, the electrons in superlattice can delocalised. Superlattice structure however, will not be further explained in this work.

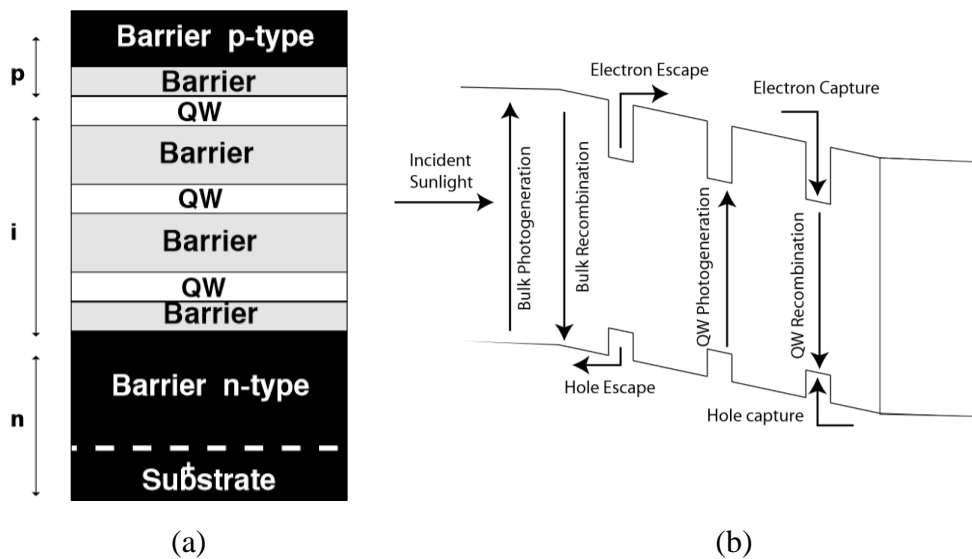


Figure 2.20: (a) shows the layer structure of multiple quantum well p-i-n; (b) band diagram for the quantum well p-i-n solar cell. Carriers generation, recombination, escape and capture processes occur at the same time. Images taken from [24].

Figure 2.20 (a) shows the quantum well p-i-n layer structure. Depending on the thickness of barrier and well thickness, different amount of carrier(s) will be collected and it brings to the efficiency of the solar cells. Figure 2.20 (b) shows the band diagram for the quantum well p-i-n solar cell. From this diagram, several processes occur at the same time which are photogeneration and recombination processes for both barrier and quantum well, together with the carrier capture and escape. At room temperature, most of the quantum well solar cells experience the carrier capture and escape processes faster than the competing recombination processes. All carriers generated in a quantum well are assumed to escape and contribute to the photocurrent.[24]

By introducing quantum well(s) into the device structure, the effective bandgap for energy absorption can be altered while carrier energies are maintained at the same time during carrier extraction. This was proposed by Barnham *et al.* in 1990 where the value of short-circuit current, I_{SC} and open-circuit voltage, V_{OC} can be decoupled if quantum wells are introduced into the cell.[25] The same author also shows an early investigation on AlGaAs/GaAs MQW solar cells where the photo-generated carrier escape from the well resulted in increase of the output current, hence increase the efficiency compared to the control cells without the wells formed from the barrier material.[26] Another research detailing on the electroluminescence (EL) measurements performed in both experiment and modelling for single quantum well shows a reduction in quasi Fermi level due to the thermally assisted escape of carriers that is irreversible as opposed to the study in Araujo *et al.*[27] and Ramey *et al.*[28].[29]

This irreversible carrier escape from the quantum well allows better maximum efficiency enhancement compared to bulk cells. Previous study on strained MQW p-i-n device such as GaAsP/InGaAs show an increase in photocurrent collected compared to bulk structures hence improving the efficiency. However, the electric field across the MQW is incapable of sweeping all carriers to create photocurrent if the background doping is too high.[24, 30] Specifically on GaAsBi/GaAs MQW p-i-n devices, the investigation of growth and characterisations have been taking place since 2008 by several groups such as in [31-34].

2.5.2 Strain and Strain Relaxation

Strain in Bulk Structure

The relative size of the lattice constant between two materials determine the quality of the overall material quality. If the lattice constants are match or very similar, for example $\text{Al}_x\text{Ga}_{1-x}\text{As}$ and GaAs heterojunctions, the strain introduced in the lattice structure will be very small. For heterojunctions with different value of lattice constants, strain is introduced to the structure during the growth process. Strain value in bulk structure can be interpreted as in Equation 2.15,

$$\text{Strain, } \varepsilon = \frac{\alpha_L - \alpha_S}{\alpha_S} \quad (\text{Equation 2.15})$$

where α_L is the lattice constant of the grown layer and α_S is the lattice constant of the substrate.

There are two types of strain, compressive and tensile. If α_L is greater than α_S , it is compressive strain or positive strain constant and vice versa falls to tensile strain, the negative strain constant. Depending on the thickness of the layer growth on the substrate, there will be a critical thickness for a given strain. Passing this critical thickness point will cause misfit dislocations in the lattice, strain relaxation takes place, which affects the quality of the semiconductor in a negative way, mainly linked to an increase in forward dark current.[35] Drigo *et al.* in his paper observed misfit dislocations of InGaAs/GaAs single heterostructures and agrees with Matthews-Blakeslee critical thickness value as seen in Figure 2.21. However, there is a presence of second critical thickness where further strain relaxation occurs.[36]

Several other studies on critical thickness of heterostructure layers and the substrates have been done too, with some of them agree with Matthews-Blakeslee critical thickness [37, 38] and some disagree stating that the critical thickness can actually be exceeded before relaxation occurs on the structure by using growth interrupt technique where the operation of dislocation multiplication mechanisms can be prevented.[39-41] The arguments are understandable because different experiment techniques have different sensitivities, either showing individual or average dislocations from the material.

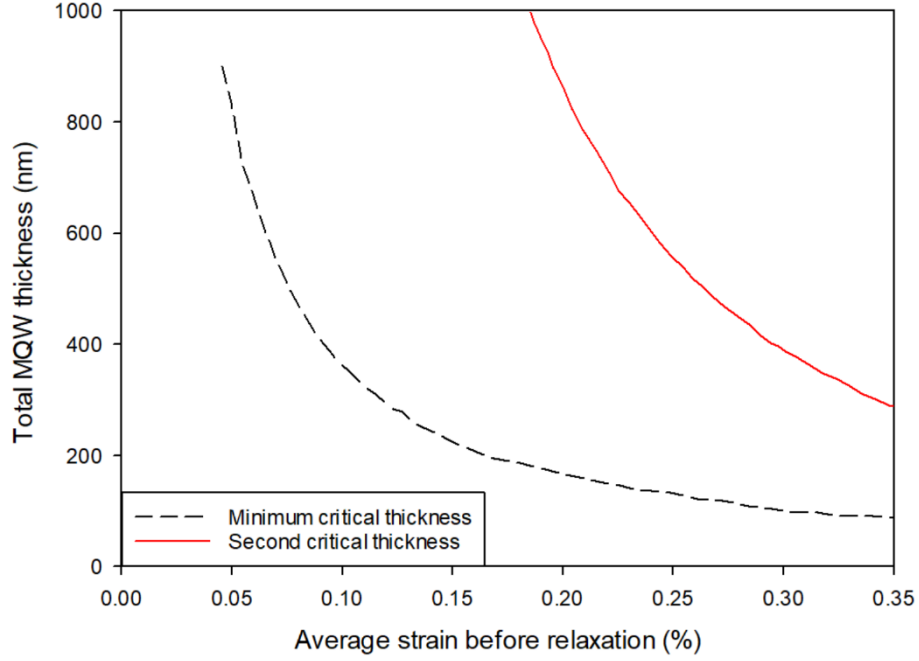


Figure 2.21: The total MQW thickness in the *i*-region against average strain value. The Matthews-Blakeslee critical thickness for the onset of dislocation propagation shown in black dashed line [35] and second critical thickness before strain relaxation occurs according to a fit by Drigo *et al.* is shown in red solid line [36]. Figure is adapted from [42]

Strain in MQW Structure

Strain and strain relaxation study on GaAs/InGaAs MQWs p-i-n diodes has been performed by Griffin *et al.* showing a clear relationship between level of dark line density and forward dark current density with the strain involved where both phenomena show similar trends with respect to the strain percentages. They are dependent on the dislocations density instead of the *i*-region thickness.[42] The modified Equation 2.15 to fit the average strain, ϵ_{avg} value for MQW structure is given by equation below,

$$\epsilon_{avg} = \frac{\alpha_L - \alpha_S}{\alpha_S} \cdot \frac{nt_X}{nt_X + (n-1)t_b} \quad (\text{Equation 2.16})$$

where n is the number of wells, t_X is the thickness of well and t_b is the thickness of the barrier.[42]

Strain Balancing

The idea of having alternate compressive and tensile materials grown on a same substrate creating a strained balanced quantum well and barrier layers is the main aim for the research in quantum well solar cells. Ideally, infinite number of wells can be grown due to the strain free structure, thus making zero-defect growth a possibility and it can provide better tuning of the sub-cells of multi-junction solar cells. As a result, different band-gap semiconductors can be incorporated as junctions in a solar cell without dislocations and a high open-circuit voltage can be maintained. However, the discussion on multiple quantum well bismuth-based system in this thesis will be solely on the strained materials. It is very useful to understand the mechanism of strained materials first before strained-balance materials are studied.

2.6 Summary

In conclusion, this chapter talks about the background theory of the work done in this thesis. First, the band structures of semiconductor specifically on crystalline semiconductor is introduced. Then, the electron distribution function and behaviour are explained. This include the change in distribution level when external atoms are introduced and how the bandgap behaves when two different doping type semiconductors are brought together at zero and with bias. From that, the ideal Shockley diode equation is presented based on current-voltage characteristics of a material.

Besides that, this chapter explains the process of a photocarrier generation and recombination, including the absorption and emission of light in III-V semiconductor material. In addition to that, the applications in semiconductor opto-electronic devices including LED, laser and solar cells are discussed. The development of III-V material systems is explained afterwards, focusing on the lattice structure and different ways to alter the bandgap by manipulating the elements in the system. The incorporation of Bismuth into GaAs allows bandgap engineering and its value is determined by using Valence Band Anti-Crossing model. Lastly, the applications of multiple quantum well structure for solar cell are discussed. This include the calculation of strain in bulk and MQW structure.

2.7 References

- [1] S. M. Sze and K. K. Ng, *Physics of Semiconductor Devices*, Third Edition ed. New Jersey: John Wiley & Sons, Inc, 2007.
- [2] B. Doherty, "MicroNotes: PIN Diode Fundamentals ", ed. Watertown, MA: Microsemi Corp.
- [3] E. Fluck, "New Notations in The Periodic Table," *Pure and Applied Chemistry*, Article vol. 60, no. 3, pp. 431-436, Mar 1988, doi: 10.1351/pac198860030431.
- [4] L. Vegard, "The Constitution of the Mixed Crystals and the Filling of Space of the Atoms," *Zeitschrift Fur Physik*, Article vol. 5, pp. 17-26, Apr-Jul 1921, doi: 10.1007/bf01349680.
- [5] J. A. Vanvechten and T. K. Bergstresser, "Electronic Structures of Semiconductor Alloys," *physical review b-solid state*, article vol. 1, no. 8, pp. 3351+, 1970, doi: 10.1103/physrevb.1.3351.
- [6] e. d. jones *et al.*, "Band Structure of $\text{In}_x\text{Ga}_{1-x}\text{As}_{1-y}\text{N}_y$ Alloys and Effects of Pressure," *Physical Review B*, Article vol. 60, no. 7, pp. 4430-4433, Aug 1999, doi: 10.1103/PhysRevB.60.4430.
- [7] S. H. Wei and A. Zunger, "Predicted Band-Gap Pressure Coefficients of all Diamond and Zinc-Blende Semiconductors: Chemical Trends," *Physical Review B*, Article vol. 60, no. 8, pp. 5404-5411, Aug 1999, doi: 10.1103/PhysRevB.60.5404.
- [8] Y. Zhang, A. Mascarenhas, H. P. Xin, and C. W. Tu, "Scaling of Band-Gap Reduction in Heavily Nitrogen Doped GaAs," *Physical Review B*, Article vol. 63, no. 16, p. 4, Apr 2001, Art no. 161303, doi: 10.1103/PhysRevB.63.161303.
- [9] W. Shan *et al.*, "Band Anticrossing in GaInNAs Alloys," *Physical Review Letters*, Article vol. 82, no. 6, pp. 1221-1224, Feb 1999, doi: 10.1103/PhysRevLett.82.1221.
- [10] S. H. Wei and A. Zunger, "Giant and Composition-Dependent Optical Bowing Coefficient in GaAsN Alloys," *Physical Review Letters*, vol. 76, no. 4, pp. 664-667, Jan 22 1996, doi: 10.1103/PhysRevLett.76.664.
- [11] I. Vurgaftman, J. R. Meyer, and L. R. Ram-Mohan, "Band Parameters for III-V Compound Semiconductors and their Alloys," *Journal of Applied Physics*, Review vol. 89, no. 11, pp. 5815-5875, Jun 2001, doi: 10.1063/1.1368156.
- [12] W. Walukiewicz *et al.*, "Interaction of Localized Electronic States with the Conduction BAND: BAND ANTICROSSING in II-VI Semiconductor Ternaries," *Physical Review Letters*, Article vol. 85, no. 7, pp. 1552-1555, Aug 2000, doi: 10.1103/PhysRevLett.85.1552.
- [13] W. Shan *et al.*, "Nature of the Fundamental Band Gap in $\text{GaN}_x\text{P}_{1-x}$ Alloys," *Applied Physics Letters*, Article vol. 76, no. 22, pp. 3251-3253, May 2000, Art no. Pii [s0003-6951(00)01922-7], doi: 10.1063/1.126597.

- [14] J. Yoshida, T. Kita, O. Wada, and K. Oe, "Temperature Dependence of GaAs_{1-x}Bi_x Band Gap Studied by Photoreflectance Spectroscopy," *Japanese Journal of Applied Physics Part 1-Regular Papers Short Notes & Review Papers*, Article vol. 42, no. 2A, pp. 371-374, Feb 2003, doi: 10.1143/jjap.42.371.
- [15] Y. Zhang, A. Mascarenhas, and L. W. Wang, "Similar and Dissimilar Aspects of III-V Semiconductors Containing Bi versus N," *Physical Review B*, Article vol. 71, no. 15, p. 4, Apr 2005, Art no. 155201, doi: 10.1103/PhysRevB.71.155201.
- [16] S. Tixier *et al.*, "Molecular Beam Epitaxy Growth of GaAs_{1-x}Bi_x," *Applied Physics Letters*, Article vol. 82, no. 14, pp. 2245-2247, Apr 2003, doi: 10.1063/1.1565499.
- [17] K. Alberi, O. D. Dubon, W. Walukiewicz, K. M. Yu, K. Bertulis, and A. Krotkus, "Valence Band Anticrossing in GaBi_xAs_{1-x}," *Applied Physics Letters*, Article vol. 91, no. 5, p. 3, Jul 2007, Art no. 051909, doi: 10.1063/1.2768312.
- [18] M. Usman, C. A. Broderick, A. Lindsay, and E. P. O'Reilly, "Tight-Binding Analysis of the Electronic Structure of Dilute Bismide Alloys of GaP and GaAs," *Physical Review B*, Article vol. 84, no. 24, p. 13, Dec 2011, Art no. 245202, doi: 10.1103/PhysRevB.84.245202.
- [19] J. F. Geisz *et al.*, "40.8% Efficient Inverted Triple-Junction Solar Cell with Two Independently Metamorphic Junctions," *Applied Physics Letters*, Article vol. 93, no. 12, p. 3, Sep 2008, Art no. 123505, doi: 10.1063/1.2988497.
- [20] A. Zayan, M. Stevens, T. E. Vandervelde, and Ieee, "GaAsBi Alloys for Photovoltaic and Thermophotovoltaic Applications," in *43rd IEEE Photovoltaic Specialists Conference (PVSC)*, Portland, OR, Jun 05-10 2016, NEW YORK: Ieee, in IEEE Photovoltaic Specialists Conference, 2016, pp. 2839-2843. [Online]. Available: <Go to ISI>://WOS:000399818702198
- [21] S. Khanom *et al.*, "Simulation Study of Multijunction Solar Cell Incorporating GaAsBi," in *5th IEEE-Region-10 Humanitarian Technology Conference (R10-HTC)*, BUET, Dhaka, BANGLADESH, Dec 21-23 2017, NEW YORK: Ieee, in IEEE Region 10 Humanitarian Technology Conference, 2017, pp. 432-435. [Online]. Available: <Go to ISI>://WOS:000426969400098
- [22] T. Thomas *et al.*, "Requirements for a GaAsBi 1eV Sub-Cell in a GaAs-based Multi-Junction Solar Cell," *Semiconductor Science and Technology*, Article vol. 30, no. 9, p. 6, Sep 2015, Art no. 094010, doi: 10.1088/0268-1242/30/9/094010.
- [23] C. J. Hunter *et al.*, "Absorption Characteristics of GaAs_{1-x}Bi_x/GaAs Diodes in the Near-Infrared," *Ieee Photonics Technology Letters*, vol. 24, no. 23, pp. 2191-2194, Dec 1 2012, doi: 10.1109/lpt.2012.2225420.
- [24] N.J.Ekins-Daukes *et al.*, "Physics of Quantum Well Solar Cells," in *SPIE - The International Society for Optical Engineering*, 2009, vol. 7211, doi: 10.1117/12.816946.

- [25] K. W. J. Barnham and G. Duggan, "A New Approach to High-Efficiency Multi-Band-Gap Solar-Cells," *Journal of Applied Physics*, Article vol. 67, no. 7, pp. 3490-3493, Apr 1990, doi: 10.1063/1.345339.
- [26] K. Barnham *et al.*, "Quantum Well Solar Cells," *Applied Surface Science*, Article; Proceedings Paper vol. 113, pp. 722-733, Apr 1997, doi: 10.1016/s0169-4332(96)00876-8.
- [27] G. L. Araujo and A. Marti, "Absolute Limiting Efficiencies for Photovoltaic Energy-Conversion," *Solar Energy Materials and Solar Cells*, Article vol. 33, no. 2, pp. 213-240, Jun 1994, doi: 10.1016/0927-0248(94)90209-7.
- [28] S. M. Ramey and R. Khoie, "Modeling of Multiple-Quantum-Well Solar Cells including Capture, Escape, and Recombination of Photoexcited Carriers in Quantum Wells," *Ieee Transactions on Electron Devices*, Article vol. 50, no. 5, pp. 1179-1188, May 2003, doi: 10.1109/ted.2003.813475.
- [29] N. J. Ekins-Daukes *et al.*, "Radiative Currents in Quantum-Well Solar Cells," *Physica E*, Article; Proceedings Paper vol. 2, no. 1-4, pp. 171-176, Jul 1998, doi: 10.1016/s1386-9477(98)00037-x.
- [30] D. B. Bushnell *et al.*, "Effect of Well Number on the Performance of Quantum-Well Solar Cells," *Journal of Applied Physics*, Article vol. 97, no. 12, p. 4, Jun 2005, Art no. 124908, doi: 10.1063/1.1946908.
- [31] Y. Tominaga, Y. Kinoshita, K. Oe, and M. Yoshimoto, "Structural Investigation of GaAs_(1-x)Bi_(x)/GaAs Multiquantum Wells," *Applied Physics Letters*, Article vol. 93, no. 13, p. 3, Sep 2008, Art no. 131915, doi: 10.1063/1.2993343.
- [32] Y. Tominaga, K. Oe, and M. Yoshimoto, "Temperature-Insensitive Photoluminescence Emission Wavelength in GaAs_{1-x}Bi_x/GaAs Multiquantum Wells," *Physica Status Solidi C: Current Topics in Solid State Physics, Vol 8, No 2*, Proceedings Paper vol. 8, no. 2, p. 3, 2011, doi: 10.1002/pssc.201000520.
- [33] Y. I. Mazur *et al.*, "Optical Evidence of a Quantum Well Channel in Low Temperature Molecular Beam Epitaxy Grown Ga(AsBi)/GaAs Nanostructure," *Nanotechnology*, Article vol. 22, no. 37, p. 6, Sep 2011, Art no. 375703, doi: 10.1088/0957-4484/22/37/375703.
- [34] Y. I. Mazur *et al.*, "Effects of Spatial Confinement and Layer Disorder in Photoluminescence of GaAs_{1-x}Bi_x/GaAs Heterostructures," *Journal of Physics D-Applied Physics*, Article vol. 46, no. 6, p. 8, Feb 2013, Art no. 065306, doi: 10.1088/0022-3727/46/6/065306.
- [35] J. W. Matthews and A. E. Blakeslee, "Defects in Epitaxial Multilayers .1. Misfit Dislocations," *Journal of Crystal Growth*, Article vol. 27, no. DEC, pp. 118-125, 1974, doi: 10.1016/0022-0248(74)90424-2.
- [36] A. V. Drigo *et al.*, "On the Mechanisms of Strain Release in Molecular-Beam-Epitaxy-Grown In_xGa_{1-x}As/GaAs Single Heterostructures," *Journal of Applied Physics*, Article vol. 66, no. 5, pp. 1975-1983, Sep 1989, doi: 10.1063/1.344335.

- [37] P. L. Gourley, R. M. Biefeld, and L. R. Dawson, "Elimination of Dark Line Defects in Lattice-Mismatched Epilayers through Use of Strained-Layer Superlattices," *Applied Physics Letters*, Article vol. 47, no. 5, pp. 482-484, 1985, doi: 10.1063/1.96099.
- [38] I. J. Fritz, S. T. Picraux, L. R. Dawson, T. J. Drummond, W. D. Laidig, and N. G. Anderson, "Dependence of Critical Layer Thickness on Strain for $\text{In}_x\text{Ga}_{1-x}\text{As}/\text{GaAs}$ Strained-Layer Superlattices," *Applied Physics Letters*, Article vol. 46, no. 10, pp. 967-969, 1985, doi: 10.1063/1.95783.
- [39] P. J. Orders and B. F. Usher, "Determination of Critical Layer Thickness in $\text{In}_x\text{Ga}_{1-x}\text{As}$ GaAs Heterostructures by X-ray-Diffraction," *Applied Physics Letters*, Article vol. 50, no. 15, pp. 980-982, Apr 1987, doi: 10.1063/1.98004.
- [40] R. People, "Physics and Applications of $\text{Ge}_x\text{Si}_{1-x}/\text{Si}$ Strained-Layer Heterostructures," *Ieee Journal of Quantum Electronics*, Article vol. 22, no. 9, pp. 1696-1710, Sep 1986, doi: 10.1109/jqe.1986.1073152.
- [41] D. J. Lockwood, M. W. C. Dharmawardana, W. T. Moore, and R. L. S. Devine, "Raman-Scattering Study of Folded Acoustic Phonons in $\text{GaAs}/\text{In}_x\text{Ga}_{1-x}\text{As}$ Strained-Layer Superlattices," *Applied Physics Letters*, Article vol. 51, no. 5, pp. 361-363, Aug 1987, doi: 10.1063/1.98441.
- [42] P. R. Griffin *et al.*, "Effect of Strain Relaxation on Forward Bias Dark Currents in $\text{GaAs}/\text{InGaAs}$ Multiquantum Well P-I-N Diodes," *Journal of Applied Physics*, Article vol. 80, no. 10, pp. 5815-5820, Nov 1996, doi: 10.1063/1.363574.

Chapter 3: Experimental Methodology

3.1 Growth: Molecular Beam Epitaxy

Molecular Beam Epitaxy (MBE) growth is a type of epitaxial growth process that involves the deposition of a molecular beam of element(s) onto a crystalline surface. This film deposition technique was designed at Bell Laboratories, New Jersey and demonstrated the first GaAs layer grown on a GaAs substrate in 1971.[1] The elemental deposition in MBE is done under ultrahigh-vacuum (UHV) condition and it has a method of live-monitoring of the growth layer to see its growth rate by using a camera installed onto the machine.

Figure 3.1 shows the schematic diagram of the MBE machine used to grow all the samples characterised in this report.

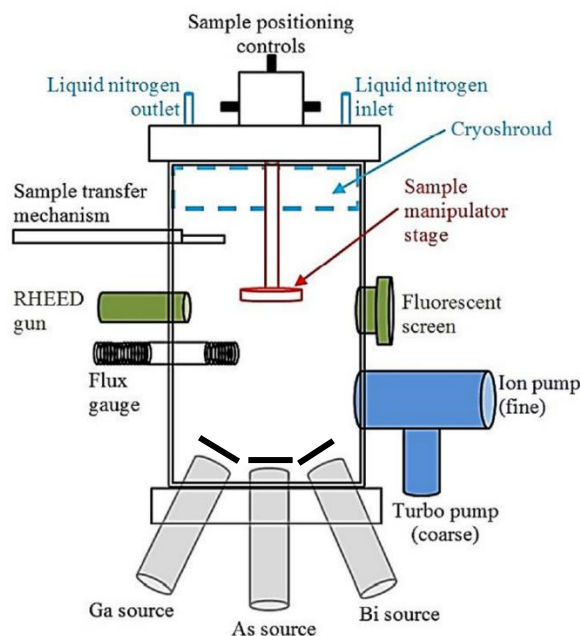


Figure 3.1: Schematic diagram of the MBE machine. Image taken from [2].

Several source crucibles containing different elements including Ga, As and Bi are used to grow GaAsBi samples. Each crucible has its own shutter that is used to allow or block the molecular beam by opening or closing the source's crucible, respectively. The beam of each element is produced by maintaining the temperature of the crucible at certain temperature to evaporate the elements in the crucibles.

Different type of substrates will need different heating profile for a given surface temperature. For example, a doped substrate contains higher electron density therefore it requires lower heater element current value than an undoped substrate to reach the desired temperature. It is essential to work closely with the growers to know the growth conditions and layer structure for every sample. This is because, the characteristics of the samples and devices are interrelated with how they were grown. The growth of devices in this work was performed by the STM-MBE growth team from the University of Sheffield.

3.2 Optical Characterisation

3.2.1 Photoluminescence

Luminescence is an emission of light by a material or substance due to chemical reactions, light energy injection, electronic injection or temperature variation and has been described in section 2.3.2. Photoluminescence (PL) is a phenomenon that involve the process of energy absorption from a light source normally a laser, hence the word ‘photo’, followed by emission of light due to the carrier recombination process.

It is a technique used for investigating the quality of a semiconductor material, specifically through bulk electronic transitions and electronic transitions at defects.[3] PL is very useful because it is a non-destructive process that can identify material properties of the material such as the energy bandgap and inhomogeneity- indicated by the full width at half maximum (FWHM). From the energy bandgap value, Bi percentage incorporated into the structure can be estimated too. It is also useful to identify the transition of carriers intrinsically and at defects, whether the carriers are actively recombining and creating emission when excited by photons or whether other features dominate the recombination. One of the disadvantages of PL is that, it cannot directly measure the non-radiative recombination intensity in a device.

Figure 3.2 shows the schematic diagram of the experimental setup used for PL measurements. The laser used as the excitation source is a continuous-wave 532 nm diode-pumped solid state (DPSS) laser with a maximum output power of 2 W at 532 nm and 10 mW at its second order wavelength, 1,064 nm. The spot size for the laser used is ~250 μm . The higher order excitation laser is filtered out by using a 350-550 nm bandpass filter to allow only 532 nm wavelength to pass through. The laser beam is passed through the chopper, which is set to a frequency of 180 Hz to produce an alternating laser signal. This frequency is chosen to avoid any unwanted

interference from voltage main supply, which is a multiple of 50 Hz to affect the source signal. At room temperature, the test sample is placed on an X-Y-Z stage for an accurate positioning and focusing.

For low temperature PL measurements, the sample is placed in a closed-cycle helium compressor system that can go down to ~15 K. This system consists of a cryostat fitted with a cold finger plate connected to a temperature controller. The cryostat body also mounted to an X-Y-Z stage for sample positioning. A helium compressor, vacuum pump and water supply are the components used to create a low-pressure environment allowing low temperature PL measurements to be conducted. The sample is placed on the cold-plate with vacuum grease because this type of adhesive is thermally conducting and avoids air being trapped under the sample during the low-pressure operation of the cryostat chamber.

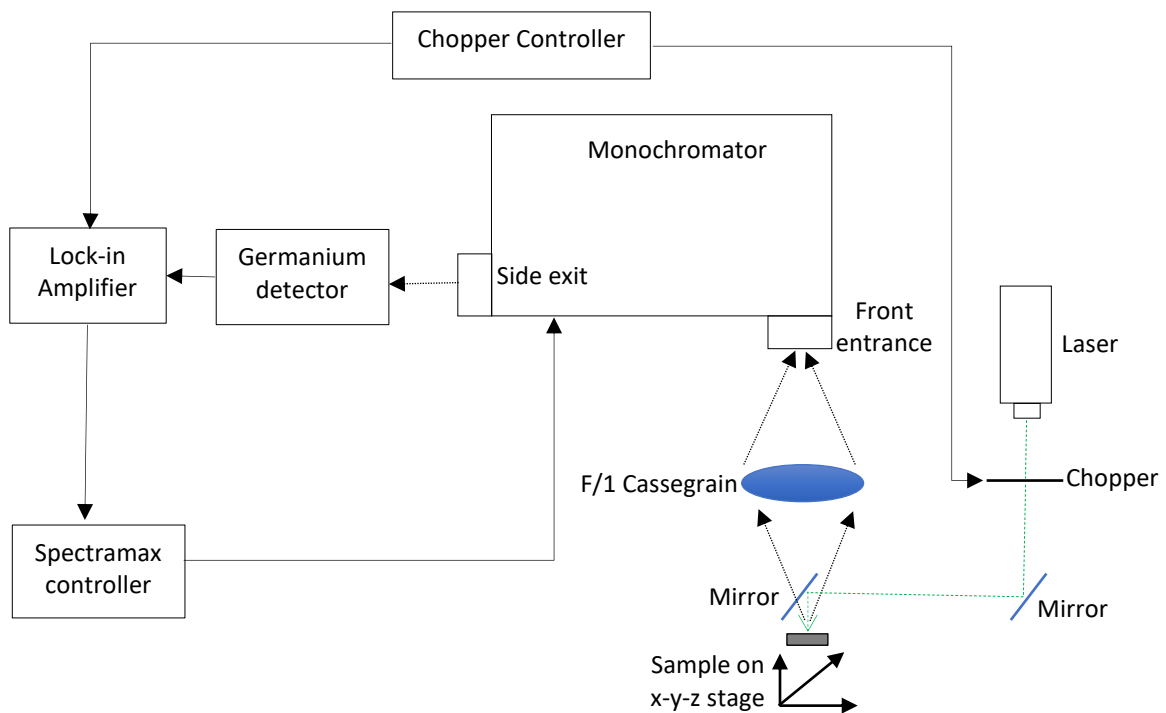


Figure 3.2: The schematic diagram of photoluminescence setup.

When the excitation laser beam hits the sample, the luminescence signal emitted by the sample is collected by the F/1 Cassegrain lens. Note that the lens has to be aligned with the monochromator's optical axis for maximum signal collection. The signal collected is then focused and enter the front entrance of the monochromator. The monochromator used in this setup is a Horiba iHR550 spectrometer. It has three grating options; (1) 1,200 grooves/mm, (2)

900 grooves/mm and (3) 600 grooves/mm with blazes at 330 nm, 850 nm and 1,500 nm, respectively. For this work, a 1mm entrance and exit slit size is set and grating 2 is used because the wavelength range of interest is between 800 and 1,600 nm.

The PL signals are detected by a 77 K operated-germanium (Ge) detector that can detect signal up to 1,700 nm. To reach this temperature, liquid nitrogen is supplied to cool the detector. The signal detected is read by the lock-in amplifier (LIA) that is used as a phase-sensitive detection method matched with the chopper frequency to eliminate the unwanted noise and signals from surrounding light sources. Various neutral density (ND) filters are used to attenuate any strong PL signal intensity detected. A software called Spectramax is used to control the scanning and tabulation of data from the LIA. The optimisation of the setup during experimental works are regularly performed to minimise errors and for optimum calibration.

3.3 Device Fabrication

Device fabrication in this work is a process of depositing metal contacts onto the sample surfaces to form positive and negative electrical connections. This is necessary in order to perform the device electrical testing. A standard process for p-i-n diodes is applied to all of the devices in this work.[4] This includes sample preparation, metallisation, photolithography and etching process.

3.3.1 Sample Preparation

Sample cleaving For p-i-n structures, it is important to identify which side is the epitaxial or top contact and which is the back side before the cleaving process to ensure correct fabrication process. The substrate used in this study is one-sided polished GaAs and epitaxial layer were grown on top of the polished ones, therefore it is easier to identify the epitaxial layer. Firstly, the 11.8 x 11.4 mm size material is placed on a clean filter paper, epitaxial side up. The sample is hold firmly by using a tweezer, then a small line is made starting about 2mm from the edge of the sample and scribe towards the edge by using a diamond scribe. The sample is turned over onto a clean filter paper and the body of the scribe is used to apply pressure in a rolling action above the scribe mark. The sample can be cleaved easily by using this method due to its lattice properties. For this step, a large amount of dust may be produced and it can cause scratching of the surface. Therefore, it is a good practice to work in an extracted

fume cupboard and to use a new filter paper for each stage of cleaving. The other half is kept unprocessed for other characterisations, if needed.

3.3.2 Sample cleaning

Sample cleaning is applied to samples to remove any dirt, dust or grease that may left on the samples during cleaving process or other fabrication steps. Initial sample cleaning and routine cleaning requires similar solvents. The only difference is that for initial cleaning, cotton bud can be used because there are no patterns on the unfabricated sample surface. Meanwhile, routine cleaning is applied when the sample has surface patterns. The use of cotton bud at routine cleaning will cause damage to the pattern and introduce more dirt.

Initial cleaning:

First the sample is boiled in iso-clean n-butyl acetate for about 30 seconds. Then, the sample is taken out and placed on a clean filter paper. Cotton bud is used to firmly wipe the surface with technique from centre towards the edge. The process is repeated for all four directions around the sample. After that, the sample is blow dry using nitrogen gun and checked under a microscope to identify the cleanliness of it. It is important to not apply too much pressure onto the sample when cleaning as it can cause more particles introduced on the surface or may cause damage and break to the surface.

Routine cleaning:

The cleaning sequence for the sample is as follows; first, it is boiled in n-butyl acetate for 30 seconds, in acetone for 30 seconds and in isopropyl alcohol (IPA) for 30 seconds. Then, the sample is taken out from the IPA and placed on a clean filter paper. By using the nitrogen gun, the sample is blow dry by using the nitrogen gun as described before. These steps are known as 'three stage cleaning' because three solvents are required to do the cleaning.

3.3.3 Sample Metallisation

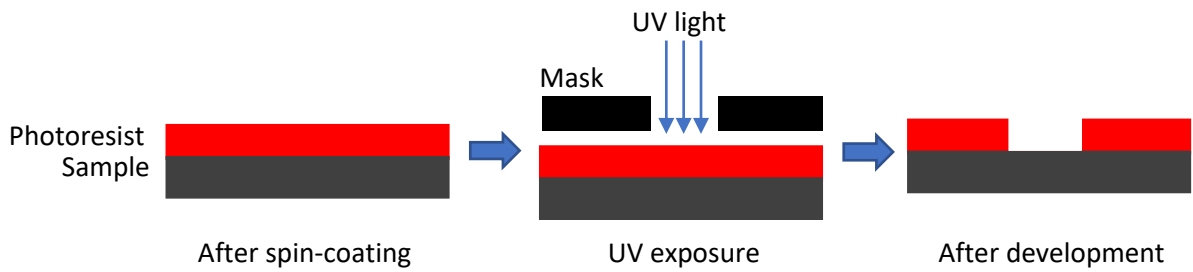
In order to run electrical characterisations to the sample, sample metallisation is the crucial step to begin with. Top and back contact are important to ensure there are current flow from positive side to negative side- creating a close loop flow of electrons. The metals are loaded in a coil basket and deposited onto the sample by using evaporation process using a high vacuum evaporator. Evaporation process needs to be in vacuum condition to ensure no oxidation occurs to the surface and helps in better deposition of the metal contacts.

Back Contact The metallisation on the back surface of the sample is done to create an ohmic contact. After cleaning the back contact, alloying of the n-type back contact is done by using Indium (In) and Germanium (Ge) and then coated by Gold (Au) following the recipe of In/Ge/Au of 10mg/10mg/200mg. This step is followed by the heating treatment or called as annealing process at 420°C for 90 seconds by using a pre-heated furnace with nitrogen gas flow replacing the air in the furnace tube.

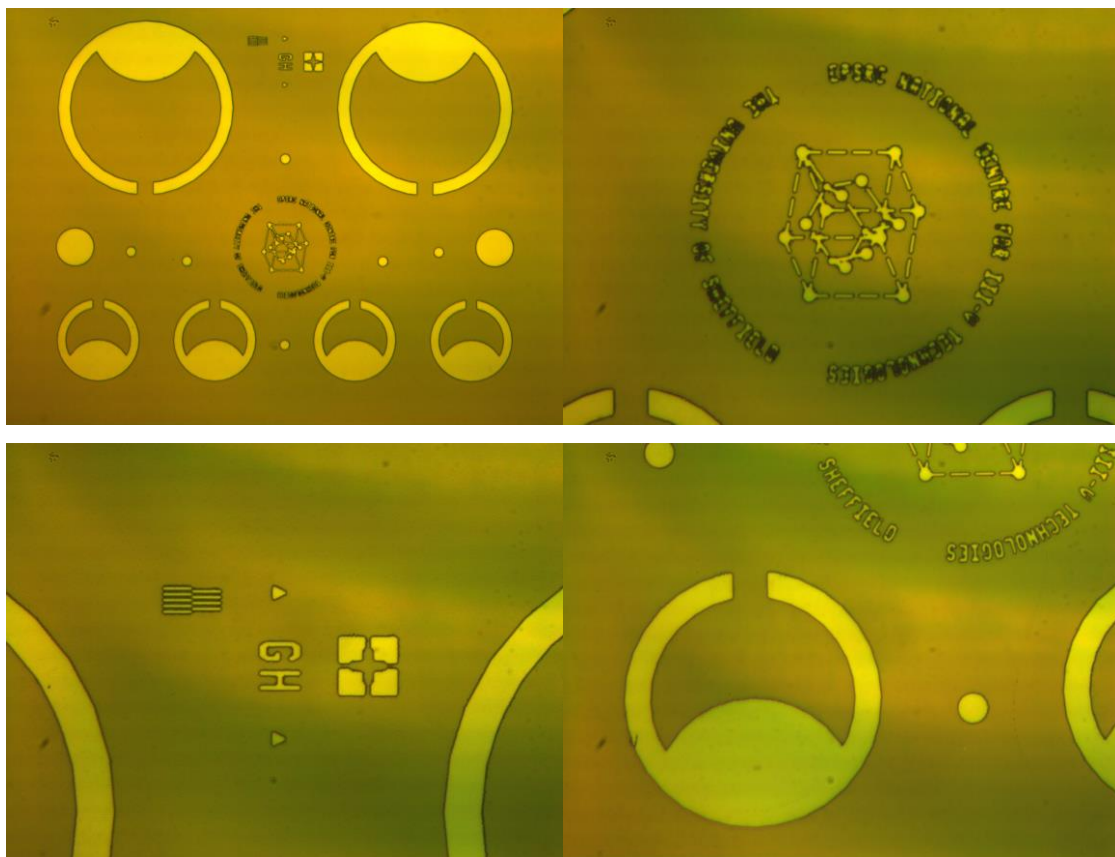
Top Contact Mesa pattern is chosen for this set of samples to maximise the optical absorption from the devices. The patterns are ‘printed’ by using ultraviolet (UV) photolithography process done in a yellow room. Steps for photolithography process are as follow:

The sample is placed on a glass slide with wax to ensure a better grip while handling the sample. Then, dehydration bake of the sample is done at 100°C for one minute. After that, a few drops of photoresists are used and the sample is spin-coated at a speed of 4000rpm for 30 seconds to achieve 2 µm resist thickness. Then, the sample is soft baked at 100°C for one minute to harden the resist. The next step is to give exposure of UV light into the coated sample by using a Karl-Suss mask aligner for 10 seconds to create patterns on the sample. The sample is in close contact with the mask surface to obtain accurate repeated pattern onto the device. After that, development process is done. The sample is dipped in the developer solution for one minute and rinsed with de-ionised water. This is to remove all the unwanted photoresist that have been exposed to the UV light and only leave the non-exposed photoresist where the pattern is on for the metallisation process.

Figure 3.3 (a) shows the steps of photolithography process and Figure 3.3 (b) shows several images of sample after photolithography process taken under microscope.



(a)



(b)

Figure 3.3: (a) Photolithography process for the samples and (b) Images of a sample after photolithography process.

The metallisation of top contact requires a p-type contact and it is done by using a combination of Au and zinc (Zn) in the evaporator. A thin trace of Au about 5 nm is alloyed followed by 10 mg of Zn and 200 nm of Au. After the metallisation process is completed, the photoresist with metal on it is removed by using acetone. This process is called lift-off process. As photoresist is reactive towards acetone, it will dissolve in the solvent and eventually lift off the unwanted metal coating it too and leaving only metal contact on the desired pattern. Once this step is completed, annealing process is done at 360°C for 90 seconds.

3.3.4 Device Isolation

Device isolation is required to define the mesa pattern and provide isolation of the contacts from one another. This can be achieved by applying the second stage photolithography and etching process

1) Second Stage Photolithography

This process is similar with the first photolithography process described above. The sample is cleaned and covered with photoresist except the type of mask is different. The mask used in this process covers the area that form the devices and only the photoresist around the mesa pattern is removed. The alignment of the mask onto the device pattern in this step is crucial to ensure that etching process afterwards is done accurately. There are alignment markings that help to align the mask pattern onto the device pattern. After the exposure and development process, the sample is etched.

2) Etching

Etching process is a process to ‘cut’ the p-i-n devices individually to form many test devices on one sample. Etching done in this work uses universal etchant consists of hydrobromic acid (HBr), acetic acid (CH₃COOH) and potassium dichromate (K₂Cr₂O₇) with 1:1:1 ratio that is freshly prepared. This is because, the etch rate of the mixture will decrease over time and the process will not be consistent. Etching time for this step is chosen depending on the depth needed to ‘cut’ the device layer. For this work, it is needed to etch from the top p-type layers down to the n-type layer to ensure accuracy in testing the devices. To determine the depth of the sample surface, a surface profiler is used. After the desired depth is obtained, the photoresist that covers the devices can be removed by using acetone. Routine cleaning is applied and the device characterisations can be done afterwards. The image of final device

under the microscope after it went through all the device fabrication processes is shown in Figure 3.4.

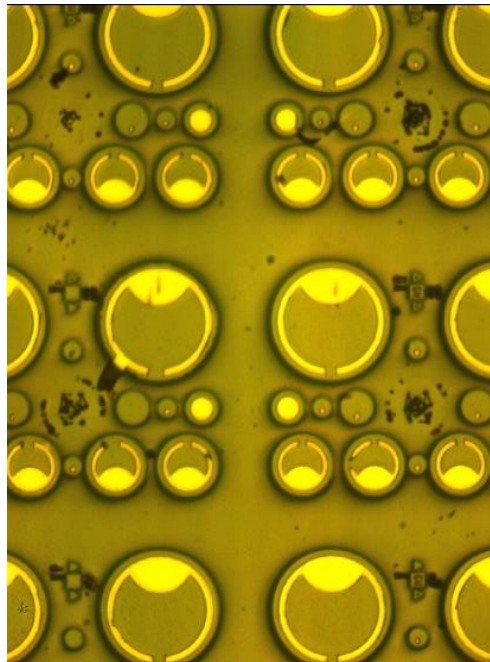


Figure 3.4: p-i-n diode image under microscope after undergoing etching process. A black ring surrounds the diode shows that there is a different in height from the floor of the mesa, indicating etching process has happened.

3.4 Electrical Characterisation

3.4.1 Dark Current-Voltage

One of the fundamental ways to discover the diode behaviour of a material system is by using current-voltage (I-V) technique on the device. This measurement is straightforward, applying a voltage or current to a device and measuring the current or potential drop across it, respectively. Ohm's law is the simplest representation of an I-V curve with a linear relationship between voltage and current. I-V measurement is performed to determine the quality of the device as a diode. Dark current traces of the devices were measured by using the I-V setup, in which a pico-ammeter was used to supply the voltage and measure the current flow. Different sized mesa devices, (200, 100 and 50 μm radii) were measured to calculate the current densities for each device. If the current density is independent of the device radius, the current domination is from bulk current. If the density is different for each diode size, it is affected by the edge leakage current through the less resistive path at the mesa edge.

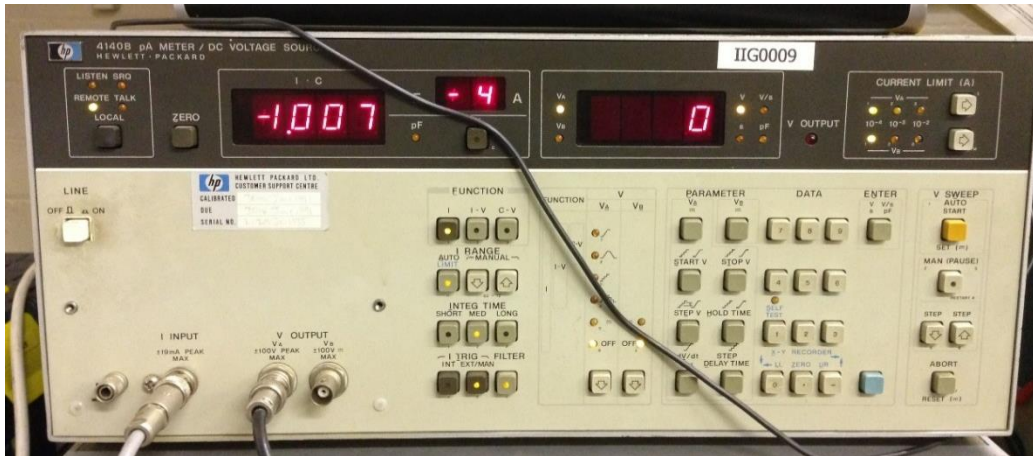


Figure 3.5: HP-4140B pico-ammeter/ DC voltage source.

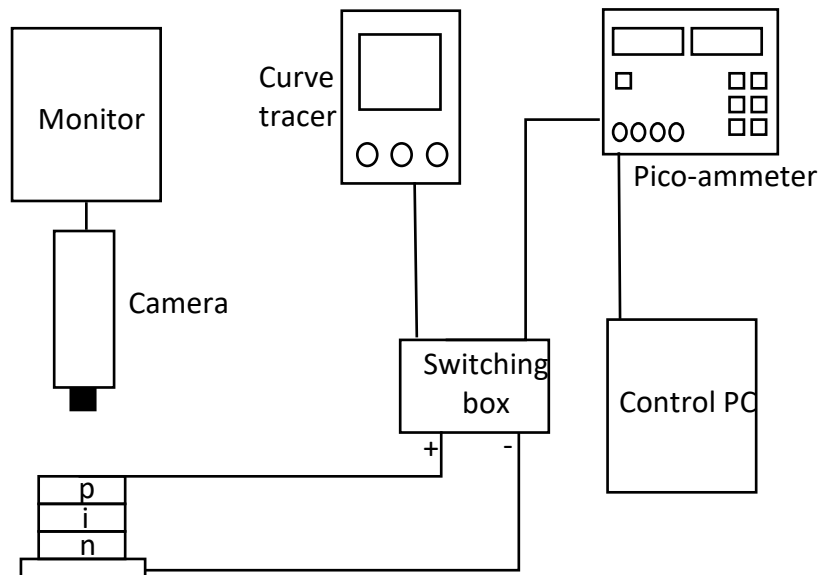


Figure 3.6: Schematic diagram of the I-V measurement setup.

Room temperature forward and reverse bias dark I-V measurements were taken by using a Hewlett-Packard HP4140B pico-ammeter and controlled by software on a PC connected through a GPIB cable. A curve tracer is used in the setup to manually check the connection of the diode before taking the actual measurement. Figure 3.5 and 3.6 show the pico-ammeter used to obtain I-V data in this work and the schematic diagram of the setup used for I-V measurements, respectively.

Several precaution methods were applied while taking I-V measurement to ensure the accuracy of the data taken. First, the measurements were carried out in a dark room to prevent optical

generation of carriers contributed by ambient light. The measurement scans were current limited to avoid overshoot of the current or breakdown damage of the device while taking the forward and reverse bias measurements, respectively. Besides that, high resistance coaxial cables of more than $1T\Omega$ were used in the setup to minimise the potential difference between core and out shield that can result in significant leakage current. Lastly, a vibration-free setup table were used to reduce the noise level while taking the measurements.

3.4.2 Current-Voltage under Illumination

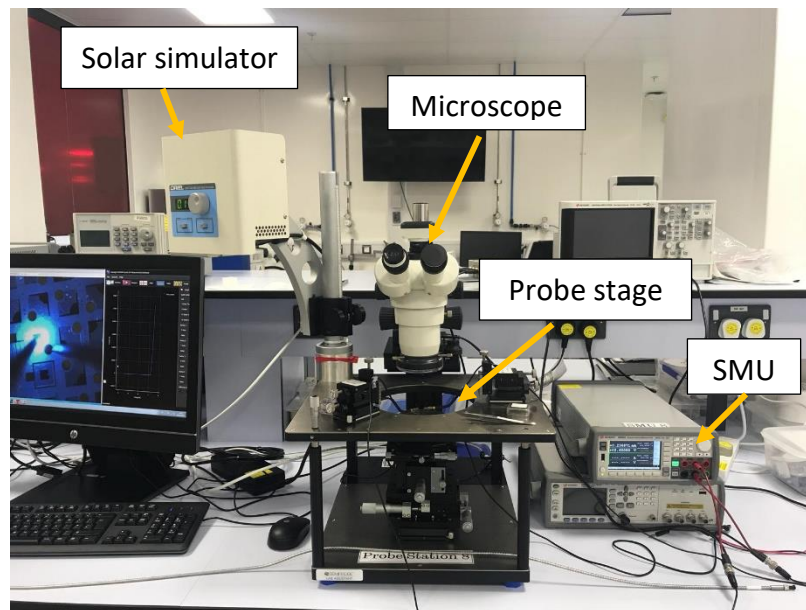


Figure 3.7: I-V under illumination (with solar simulator) setup in the cleanroom

I-V measurement under illumination was performed to study the performance of a diode as a solar cell. The setup as shown in Figure 3.7 has a probe stage comprising a pair of probe arms to connect the positive and negative terminals of the diodes. An LED-based solar simulator with a 2×2 -inch illumination area is placed on top of the probe stage to directly emit illumination onto the diode. It is a close-matched AM1.5 spectrum with wavelength range of 400 to 1,100 nm and has a maximum power density of 110 mW/cm^2 equivalent to 1.1 SUN. To optimise the illumination, the solar simulator has a head rotation of 360° to move the low power red laser ($<1\text{ mW}$) used for alignment purposes. For safety reasons, any reflections and light from the illuminator are avoided by the system operators.

3.4.3 Capacitance-Voltage

Capacitance-voltage (C-V) measurements were performed on diodes with different radii by biasing the diodes with a DC voltage using an HP 4275A LCR meter. The LCR meter, shown in Figure 3.8 is a test instrument to obtain various parameters for a diode such as inductance, capacitance, resistance and others by measuring the effective impedance across the diode.



Figure 3.8: LCR meter used for C-V measurement.

The capacitance value for the devices is modelled and obtained by using Equation 3.1,

$$C = \frac{I_{AC}}{2\pi f V_{AC}} \quad (\text{Equation 3.1})$$

where I_{AC} is the AC test signal set by the LCR meter, V_{AC} is the AC voltage through the device and f is the frequency of the test signal. The ideal phase angle difference of 90° is desired between I_{AC} and V_{AC} based on the principle of current leading voltage in a purely capacitive circuit. For this work, most of the data collected have a phase angle between 85° and 90° .

There are two types of equivalent circuit models that can be chosen from the equipment; parallel and series circuit mode. By choosing the right equivalent circuit mode, accurate readings of capacitance can be achieved. Unless the resistance value is zero, the reactance value can be different for the devices. Due to having capacitance $<1,000$ pF for this set of devices, any equivalent circuit mode can be used because the difference is negligible. For data consistency, parallel circuit mode is chosen throughout the measurements. Besides that, the AC

test signal used for the measurement also has to be sufficiently large to be measured accurately by the AC voltmeter but small compared to the DC voltage supply. Another way to obtain an accurate capacitance value is by using a high value of test frequency to reduce the reactance of capacitor. The value of the AC test signal and frequency used for C-V measurements in this work is 60 mV and 100 kHz, respectively.

3.5 Opto-electronic characterisation

3.5.1 Photocurrent

The photocurrent measurement setup is shown in Figure 3.9. The light source is a 100 W white tungsten lamp and it is spectrally dispersed through a monochromator which is controlled by a software system in a PC. The selected wavelength is focused at the exit slit of the monochromator and mechanically chopped at 180 Hz. At the the same time, the chopping frequency is fed to an LIA as a phase locking signal. The diode is also connected in series with a load resistor. Besides that, the LIA must be in parallel with the load resistor to ensure that only the voltage drop across resistor is fed to the LIA. Depending on the dark current value, different values of load resistor can be used during the measurement. The phase sensitive locking technique from LIA amplifies the photocurrent signal and at the same time suppresses the noise level and dark current. It helps filter out the dark current down to nanoamps and only photocurrent signal is detected. Therefore, only the photocurrent generated by the diode will be displayed in the control PC.

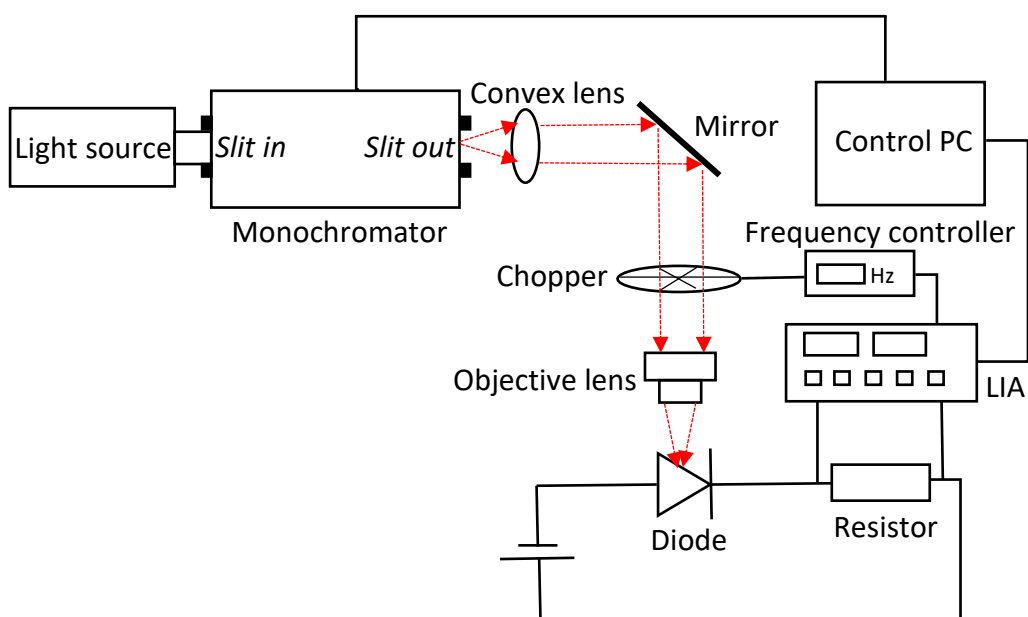


Figure 3.9: The schematic diagram of photocurrent setup used for measurements.

The arbitrary units of the photocurrent spectrum displayed on the control PC is the conversion of the LIA reading that reads the voltage drop across the resistor. Depending on the sensitivity set on the LIA, the accuracy and precision of the actual photocurrent can be controlled. Equation 3.2 shows the relationship between the conversion value of the LIA and the voltage drop across the diode while Equation 3.3 is the photocurrent calculation, which is simply a modification of Ohm's Law, $V = IR$. [5]

$$LIA \text{ reading } (V) = \frac{Conversion}{10} \times Sensitivity \quad (\text{Equation 3.2})$$

$$I_{ph} = \frac{LIA \text{ reading } (V)}{0.45 \times R} \quad (\text{Equation 3.3})$$

where I_{ph} is the photocurrent value. From photocurrent data, the responsivity of the devices as a function of wavelength can be determined. It is a method of identifying the detection efficiency of a device and a high value of responsivity is desired when designing a photovoltaic cell. The value is obtained by correcting the photocurrent to the system response by using a calibrated photodiode. In general, it is the ratio of photocurrent with incident light intensity at a particular wavelength and is defined as in Equation 3.4,

$$R = \frac{I_{ph}}{P} \quad (\text{Equation 3.4})$$

where R is the responsivity and P is the incident monochromatic light power on the device under test.

The actual power for each monochromatic light in the spectrum that falls onto the measured device has to be determined because its power is different with the power from the light source. This is due to the light passing the monochromator, lenses and mirrors resulting in the attenuation of power for different wavelengths. A commercial photodiode (PD) is used to obtain the optical power at each wavelength. The PD's photocurrent is measured and its extrapolated responsivity taken from the datasheet are used to calculate the power. From Equation 3.4, the optical power at each wavelength can be obtained, as shown in Equation 3.5,

$$P_{(PD)} = \frac{I_{ph(PD)}}{R_{(PD)}} \quad (\text{Equation 3.5})$$

In this work, an InGaAs FD05D 250 μm radius-sized calibrated photodiode is used due to its similarity in range of wavelength detection and active window area. The FD05D photodiode responsivity graph is placed in Appendix A. To work out the responsivity of the device, several considerations need to be taken while estimating the power that falls onto it. First, the active window area for the devices in this work is 70% of its total area due to the metal contact on top of it. In addition to that, the ratio of area between 250 μm radius-sized FD05D and the 200 μm radius-sized devices is 0.64. Therefore, the total incident power, P received by the devices is,

$$P = 0.7 \times 0.64 \times P_{(PD)} \quad (\text{Equation 3.6})$$

$$P = 0.45 \times P_{(PD)} \quad (\text{Equation 3.7})$$

The value of incident power obtained can be used to calculate the responsivity of the measured devices by using Equation 3.4.

Monochromator The monochromator used in this setup is a Horiba Scientific iHR320 monochromator. It is a Czerny-Turner monochromator where the polychromatic light source is focused after the entrance slit by a collimating mirror. The collimated light is then refracted by the diffraction grating to extract individual wavelengths and focused again using a concave mirror before it passes the exit slit. Depending on the angle of the grating, θ , a given wavelength can be selected. Figure 3.10 shows the general schematic diagram of a Czerny-Turner monochromator for the extraction of a single wavelength for photocurrent measurement.

Similar to PL setup, the F-number of the light source has to match the F-number of the collimating lenses to give a maximum signal to the devices. The diffraction grating surface has saw-tooth shaped grooves with a periodic distance. Choosing the correct grating allows maximum throughput for the chosen wavelength range. A grating is classified by its number of grooves per unit length, with a specified optimum operating wavelength (blaze wavelength). In this work, the monochromator is set at 600 groove/mm grating with blaze wavelength of 1,000 nm. The usable wavelength range of this grating is 667 nm to 1,500 nm. This follows the 2/3-3/2 rule of blazed grating, which directly defines the wavelengths range with reasonable

efficiency as having the lower limit and upper limit of $2/3$ and $3/2$ of λ_{blazed} , respectively, any wavelength outside this range will have a reduced efficiency.[6]

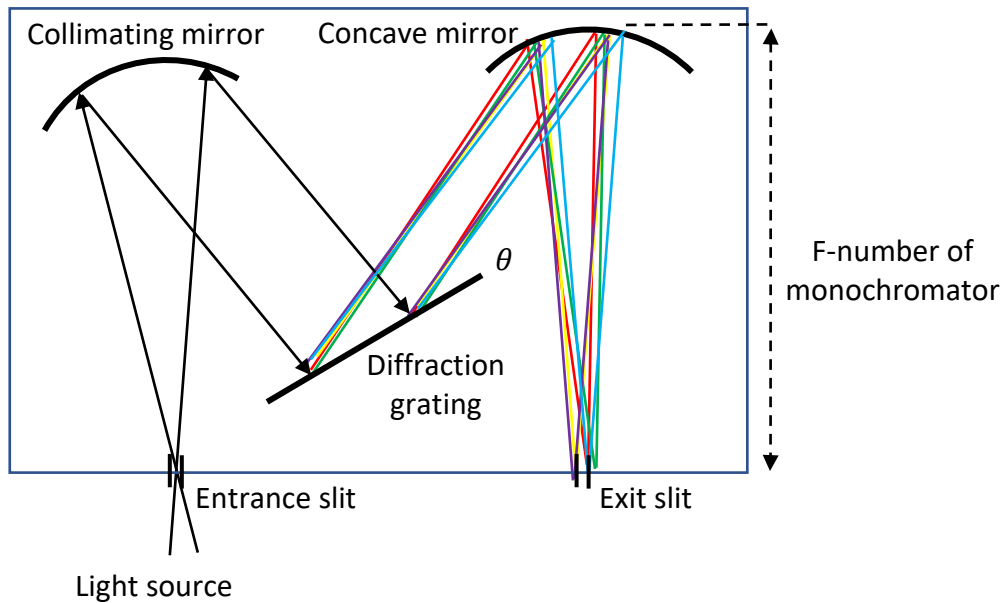


Figure 3.10: Schematic diagram of a Czerny- Turner monochromator

3.6 Summary

In summary, this chapter discuss all the procedures and methodology to obtain experimental data and result discussion. First, the growth procedures are briefly explained although the author is not involved directly with the growth of the devices. Then, photoluminescence measurements procedures at room temperature and low temperature are explained for the completeness of the thesis. After that, the device fabrication processes to create metal contact on the devices are explained. The processes follow the standard fabrication processing guideline recommended by the facility's cleanroom.

For data collection, the electrical characterisation methodology include current-voltage(I-V) in dark condition and capacitance-voltage(C-V) are discussed. Then, the opto-electronic characterisation for photocurrent measurements and I-V under illumination of solar simulator are explained too. Careful measures are taken in order to achieve highly accurate data and ensure optimisation during the data collection.

3.7 References

- [1] A. Y. Cho, "Film Deposition by Molecular-Beam Techniques," *Journal of Vacuum Science & Technology*, Article vol. 8, no. 5, pp. S31-&, 1971, doi: 10.1116/1.1316387.
- [2] A. R. B. Mohmad, "Growth and Characterisation of GaAsBi," ed: University of Sheffield; 2013, 2013.
- [3] E. C. Lightowers, R. A. Stradling and P. C. Klipstein, Eds. *Growth and Characterisation of Semiconductors*. Bristol IOP Publishing Ltd., 1990.
- [4] A. Walker, "EEE6060 - Semiconductor Device Processing for RTP students (Laboratory Sheet)," ed. University of Sheffield, 2009.
- [5] S. R. S. Inc., "Model SR830 DSP Lock-In Amplifier," ed. California, US, 1993.
- [6] A. Al-Azzawi, *Photonics: Principles and Practices*. CRC Press, 2006.

Chapter 4: Electrical Characterisation of GaAsBi/GaAs MQW Devices

4.1 Introduction

Electrical characterisation of a material system is used to understand the current-voltage (I-V) relationship, which is very important in designing a solar cell. From diode modelling it is shown that by adding Bi to GaAs for a 1 eV bandgap, it can potentially allow higher multi-junction solar cell efficiency.[1] However, in practice the growth conditions for Bi-incorporation into the layer are challenging. Low growth temperature causes defects and mid-band traps, thus affecting the quality of the material.[2] As the result, the dark I-V of the devices increases, reduces their efficiency as solar cells. According to Beaton *et al.*, as the percentage of Bi incorporation increases, the carrier mobility in the device is decreased.[3, 4] The carrier mobility value is also lower compared to the GaAs mobility reported by Adachi *et al.*[3, 4]

Several works on dark current density of GaAsBi have been reported. Rockett *et al.* shows that the saturation current density, J_0 is more affected by the defects related to the growth temperature compared to the Bi related defects. By lowering the growth temperature, a higher Bi percentage can be incorporated to GaAs. However, the minority carrier lifetime is decreased due to a higher rate of defect-assisted recombination, which increases the dark current density.[5]

A GaAsBi/GaAs multiple quantum wells (MQW) p-i-n diode series consisting of 7 devices was grown on (100) GaAs n-type substrates by a molecular beam epitaxy (MBE) machine. Each device has a different number of fixed thickness quantum wells, 8nm of GaAsBi with the same 3% bismuth content. For the rest of this work, the devices will be called the STC-3X devices. While maintaining the total i-region thickness, the GaAs barrier thickness varies with the number of wells. The STC-3X devices structure consists of a 200 nm n-type GaAs buffer followed by a 200 nm n-type $\text{Al}_{0.3}\text{Ga}_{0.6}\text{As}$ cladding layer and 620 nm of undoped i-region GaAsBi/GaAs MQWs. Then, a 600 nm p-type $\text{Al}_{0.3}\text{Ga}_{0.6}\text{As}$ cladding layer is grown on top of it followed by a 10 nm p+ GaAs cap. AlGaAs cladding layers are added to the structure to improve the thermal stability of the devices.[6] The detailed growth specifications and protocol used for these devices have been discussed in [7] and [8]. The schematic diagram of device structures is shown in Figure 4.1.

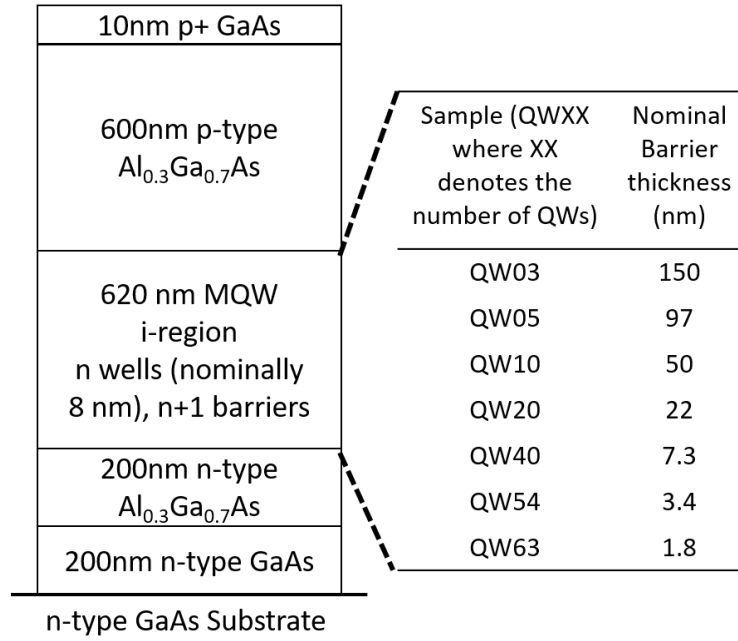


Figure 4.1: Structure of the STC-3X devices characterised in this work.

So far, there is no report on the electrical characterisations of GaAsBi/GaAs quantum wells specifically on the dark current density value in forward and reverse bias. In this chapter, the electrical characterisation of STC-3X series is investigated in detail. The characterisation techniques include capacitance-voltage (C-V) and I-V under dark condition and the results are discussed below.

First, for electrical characterisations to be conducted, a series of fabrication processes were performed on the devices to allow positive and negative terminal connections. The devices comprise repeating patterns of mesa structures with radii of 200 μm , 100 μm , 50 μm and 25 μm and the patterns can be referred to as “cells”. The cells allow electrical contacts on the devices for testing with different option of sizes and mesa pattern. Since electrical testing can cause damage and degradation to the structure, it is useful to have many cells so that if one is not working or short-circuited, there are still other cells that can be used for testing. This is also to ensure uniformity when characterising the devices by sequentially testing different cells. In this work, more than five cells of each size are measured for every device and the best results are plotted in the result section.

The results obtained from the STC-3X devices are compared with those from a strain-balanced InGaAs/GaAsP MQW from Quantasol- named QT1897 the structure of which is shown in Figure 4.2. This device is used as a comparison to the STC-3X devices due to its ideal properties- almost zero strain, as is desired for lattice matched solar cell devices.

0.22 μm p+ Zn GaAs
43 nm $\text{Al}_{0.8}\text{Ga}_{0.2}\text{As}$ 2×10^{18} p+ C
0.4 μm 2×10^{18} p+ GaAs
i-region 1.67 μm MQW (65 periods) 17.4nm GaAsP (barrier), 8.3nm InGaAs (well)
2 μm 4×10^{17} n GaAs
0.3 μm buffer n+ GaAs
GaAs n+ substrate

Figure 4.2: Diagram shows the layer structure of QT1879, an InGaAs/GaAsP strain-balanced MQW consisting of 65 wells with thickness of 8.3 nm each.

4.2 Previous Work on STC-3X

There are several early works on the structural and optical of this set of devices. They include room temperature PL, Nomarski surface profiling, X-Ray diffraction, reciprocal space mapping and transmission electron microscopy (TEM).[8, 9]. A brief explanation about the reported work is discussed here. The room temperature PL from the STC-3X devices has been reported in [8] and is shown in Figure 4.3.

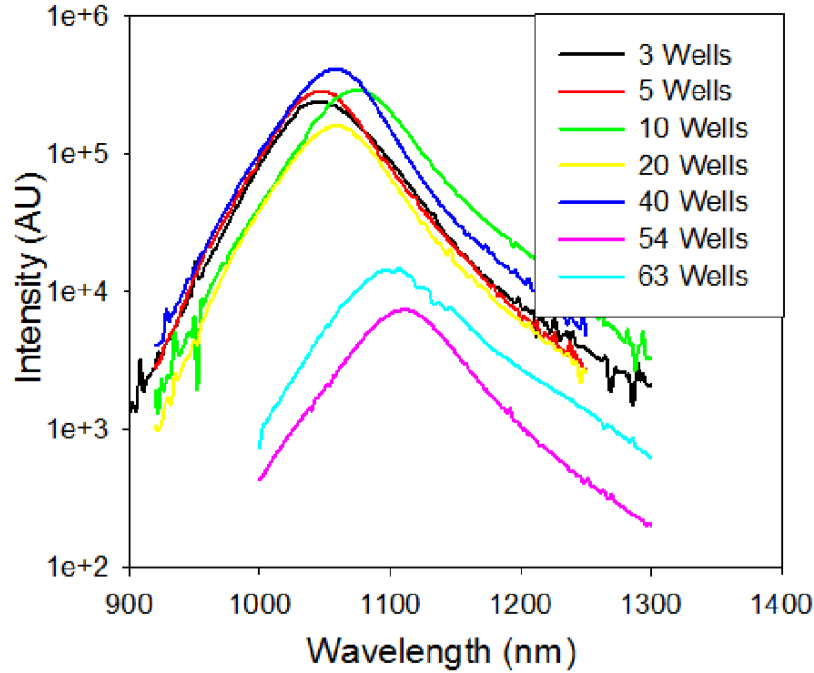


Figure 4.3: Room temperature PL for the STC-3X devices.

In summary, there are two distinct regions within the samples as shown in Figure 4.3. One region is for QW03 up to QW40, which are considered to be strained, and another region including QW54 and QW63 where the devices have undergone strain relaxation. QW54 and QW63 show a reduction in PL intensity of about two orders of magnitude compared to the other devices. The peak positions are also slightly redshifted, about 56 meV although they are expected to have similar peak position due to having the same bismuth content. This condition happened due to lattice relaxation in the devices and/or the loss of carrier confinement due to having very thin barriers which may not maintain effective quantum confinement. The slight variation in peak energies for the samples between QW03 to QW40 is due to small parameter variations occurring during growth process, in terms of atomic fluxes, background pressure and ambient temperature. They are broadly consistent around a bandgap of 1.11 to 1.15 eV for the strained devices.

In addition to that, extensive PL characterisations have been done for STC-3X including low temperature PL, power dependent PL and temperature dependent PL. However, the work was not concluded in the result chapters. This is because the electrical and opto-electronic characterisations have become priority for this thesis.

The presence of two regions for these devices are supported by the TEM and Nomarski images. The TEM images show a consistent period of quantum wells for all the devices, with a higher defect density for QW54 and QW63 compared to the strained devices. The defects for these two devices are more noticeable at the interfaces between AlGaAs cladding layer and the MQW region, suggesting strain relaxation, but they are absent between QW03 and QW40. The calculated well thicknesses as determined from the PL peak energy and the average Bi content (from the XRD fitting) are also different from the estimated thicknesses from TEM images. Figure 4.4 are the TEM images from QW 20 and QW63 to compare the defect levels between strained and strained-relaxed devices in STC-3X series.

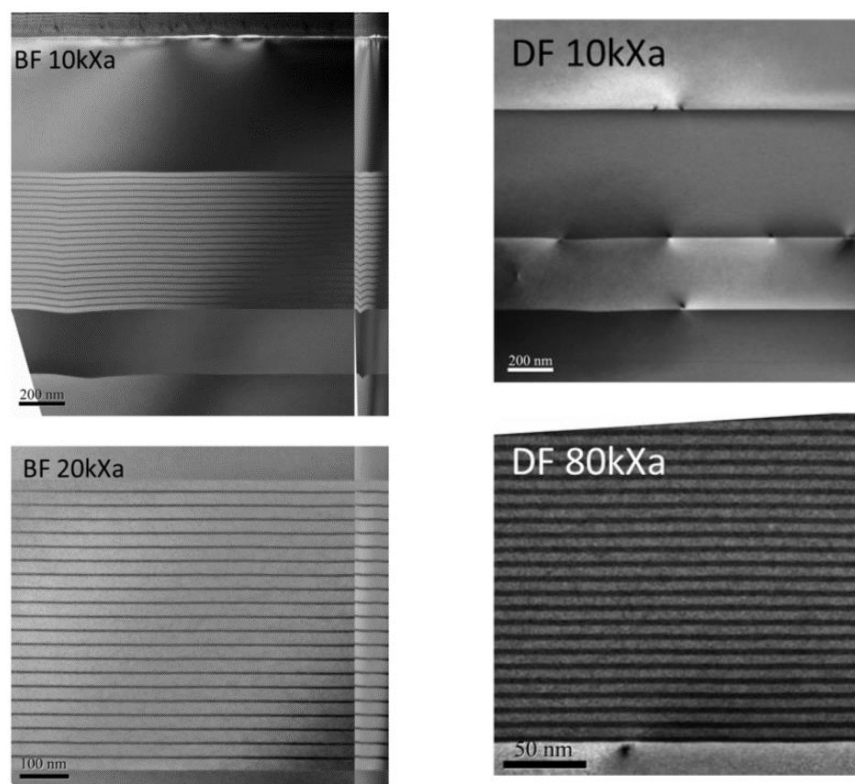


Figure 4.4: TEM images from QW20 (left) and QW63 (right). Bright field (BF) and dark field (DF) measurement types were employed for this technique.

The defects seen in the TEM images shows that contamination on the sample surfaces already present prior to growth. However, QW20 shows no dislocations at the MQW region interface, while QW63 shows dislocation densities at the lower MQW interfaces indicate that the MQW region has relaxed. Furthermore, the interface between the MQW region and the upper AlGaAs cladding layer also suggests that AlGaAs cladding has relaxed to the relaxed MQW region.[9]

Nomarski images from the devices show signs of sub-surface structural damage termed crosshatching. Depending on the appearance of the damage lines, the causes can be due to poor substrate preparation such as surface cleaning or oxide removal [10] or also can be caused by a new structure formed during the rearrangement of the atoms during growth (relaxation). For QW03 to QW20, the surface damage lines were random and non-orthogonal, QW40 did show some relaxation-induced crosshatching and QW54 and QW63, the crosshatching becomes significant and straight density of damage lines can be seen.

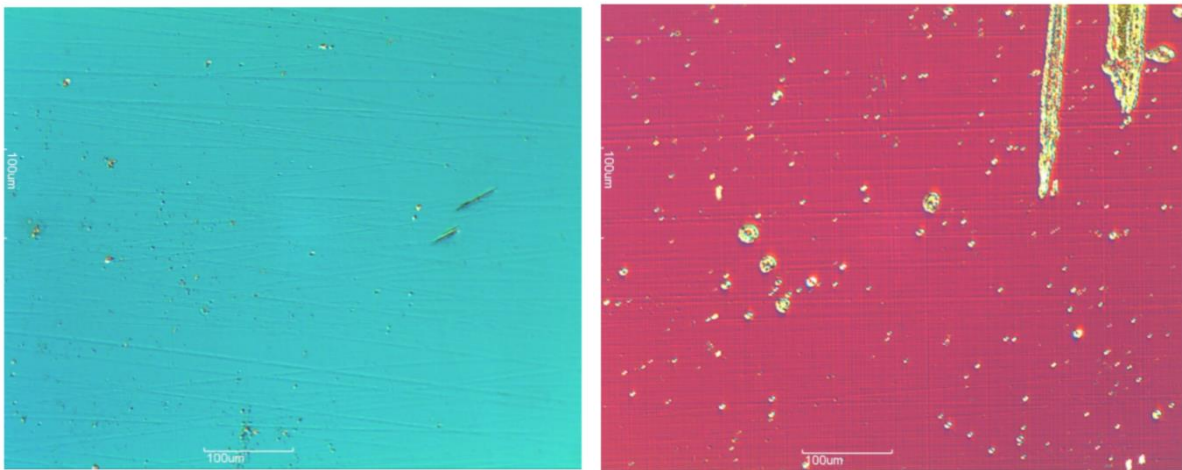


Figure 4.5: Nomarski surface profiles for QW20 (left) and QW63 (right).

Figure 4.5 shows the Nomarski images for QW20 and QW63. From the figure, QW20 shows surface damage features that coming from the pre-growth process. The visible lines on the surface are random and non-orthogonal. Meanwhile, high density metallic droplets and structured-orthogonal grids formation can be seen from QW63, showing significant contamination on the surface suggests strain relaxation has occur.

In conclusion, GaAsBi/GaAs MQW p-i-n diodes have been successfully grown by MBE. The STC-3X devices show good structural quality and strain relaxation were detected for samples more than 40 wells evidenced by the high-density crosshatching from Nomarski images, visible dislocations imaged by TEM and intensity attenuation and peak redshift of the PL spectra.

Figure 4.3, 4.4 and 4.5 are the figures taken from [9] with permission and courtesy from the original author, Dr. Robert D. Richards.

4.3 Capacitance-Voltage (C-V) Measurement

Room temperature C-V measurements were performed on all STC-3X devices and QT1879 by using an LCR meter, as mentioned in Chapter 3.4.3. From C-V data, the unintentional background doping density and thickness in the i-region of the devices can be determined. This is done by fitting the data with the one-dimensional Poisson equation as discussed later in this chapter. The measurements were also repeated on smaller sized cell with radius of 100 μm to ensure the capacitance values are scaling with the device's junction area.

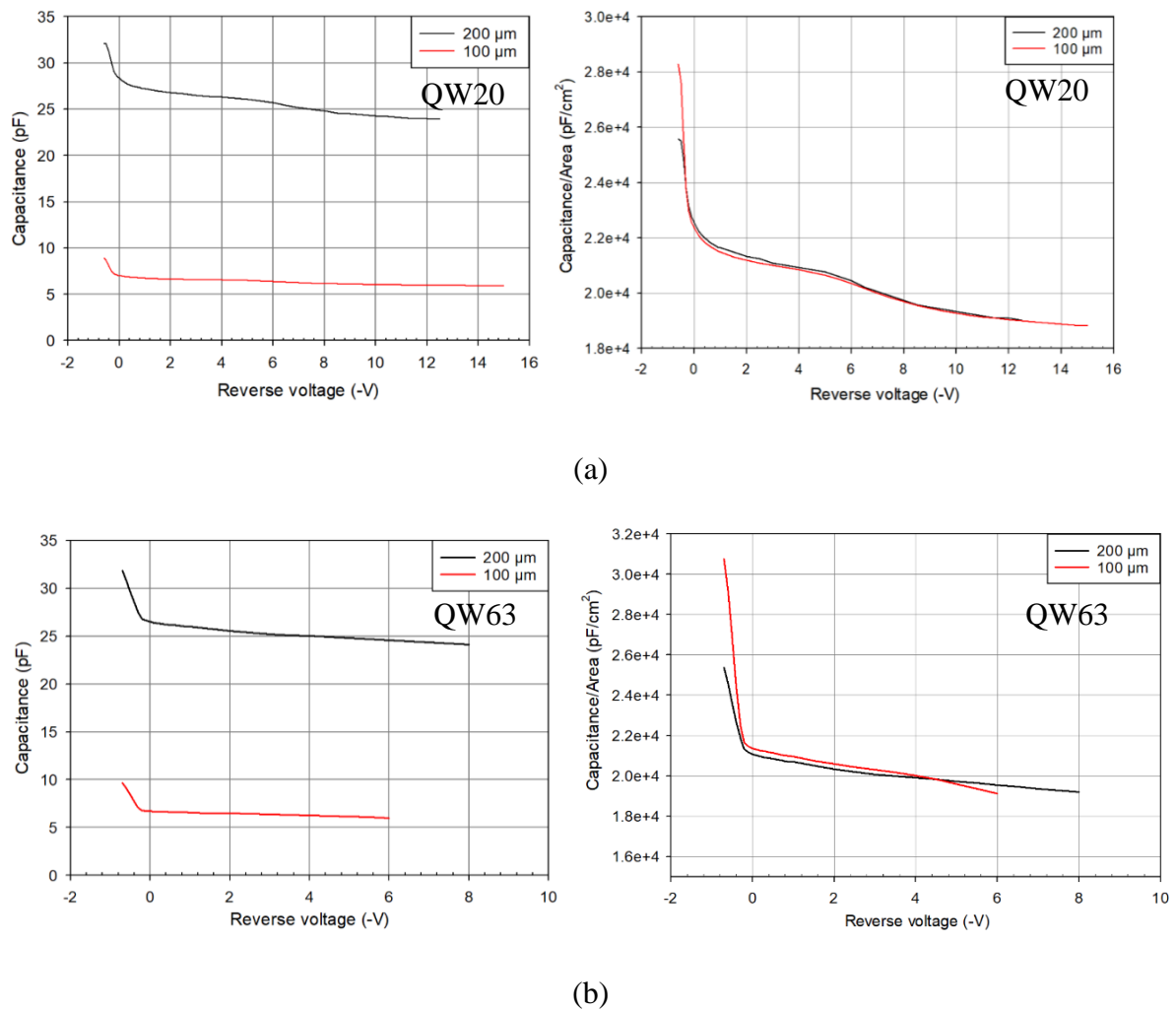


Figure 4.6: The C-V and CA-V of (a) QW20 and (b) QW63.

Figure 4.6 shows the C-V and capacitance per unit area with respect to voltage (CA-V) for 200 μm and 100 μm radius-sized cells of QW20 and QW63. These two devices are chosen due to their characteristics as strained and strain-relaxed devices in the STC-3X series for comparison. It is assumed that other devices that were not mentioned here would show a similar trend to

these measurements, unless stated. Similar figures for the rest of the devices (QW03, QW05, QW10, QW40 and QW54) are placed in Appendix B. From the figure, it is shown that the value of CA-V for both QW20 and QW63 scale with area despite their differences as strained and strain-relaxed devices. This confirms that bulk capacitance is dominating the measurement and other parasitic effects such as stray capacitance or shunt resistance are very small and not affecting the capacitance of the devices.

Figure 4.7 shows the CA-V of the STC-3X and QT1879 devices. Slight forward bias and reverse bias are applied to the devices during the measurements. The value of reverse voltage must not be close to the breakdown voltage value because it can cause a large current to flow across the diode and will cause the phase angle to deviate. As a result, the capacitance measurement will be less accurate. Therefore, the C-V measurements for STC3X devices were performed up to -15 V only after it was confirmed that very small capacitance differences are collected towards higher reverse voltages. Meanwhile, C-V for QT1879 was measured up to -20 V. The value of applied forward bias voltage was also kept below built-in voltage for similar reasons as in the reverse voltage case. For this, the forward bias voltage value is up to 0.5 V only.

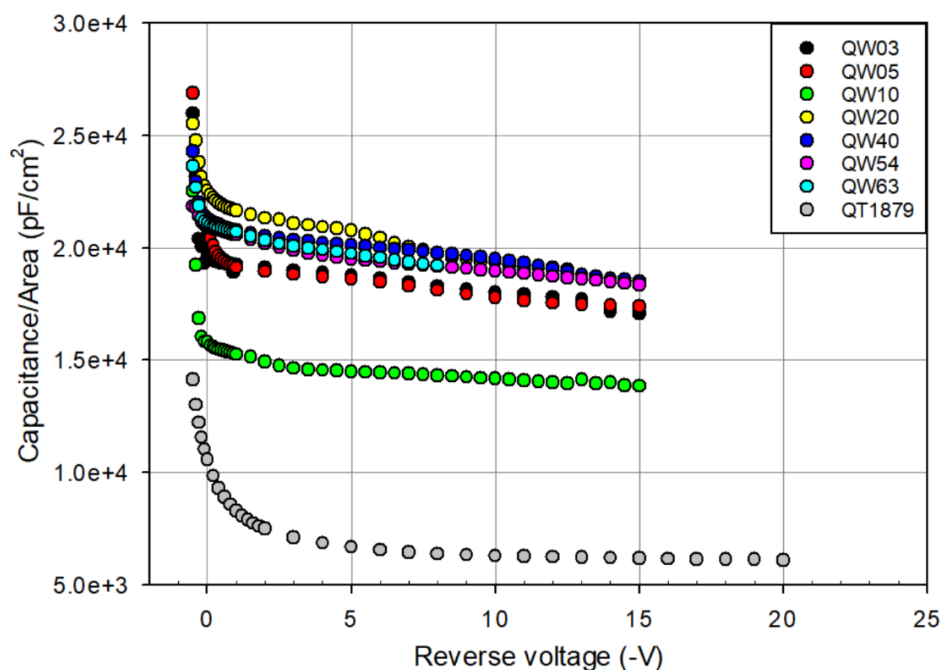


Figure 4.7: CA-V of STC-3X and QT1879.

As the forward voltages are applied, the capacitance value increases rapidly. Here, the capacitance value may not be as accurate as when the reverse bias is applied, due to the fluctuation in phase angle during the measurement. A decrease of capacitance value for all devices can be seen from the zero bias to ~ -2 V before they become fairly constant. This is because the depletion region in the cladding layers increases slightly as a small reverse bias is applied. The doping profile of a device can be tabulated from the C-V data by finding the doping density and depletion width of its i-region.[11] First, the doping density can be calculated by using the expansion of Poisson's equation,

$$\frac{d^2V}{dx^2} = \frac{dEF}{dx} = \frac{\rho}{\varepsilon} = \frac{qN}{\varepsilon} \quad (\text{Equation 4.1})$$

where V is the voltage applied, EF is the electric field at the junction, N is the doping density, ε is the material dielectric constant, ρ and q are the charge density and the electron charge, respectively. N can be presented as acceptor doping density, N_A or donor doping density, N_D depending whether the junction is p-/n+, or p+/n-, respectively. By integrating EF with respect to depletion width, x ; the expression is as follows,

$$EF = \frac{qN_A}{\varepsilon_1} x_p = \frac{qN_D}{\varepsilon_2} x_n \quad (\text{Equation 4.2})$$

From the well-known capacitance equation, the x value for the doping profile can be calculated.

$$C = \frac{\varepsilon_0 \varepsilon_r A}{x} \quad (\text{Equation 4.3})$$

where A is the area of the device, ε_0 is the dielectric constant, ε_r relative constant of the material. In addition, the value of x also can be presented as,[11]

$$x = \sqrt{\frac{2\varepsilon_0 \varepsilon_r (V_{bi} \mp V)}{qN_D}} \quad (\text{Equation 4.4})$$

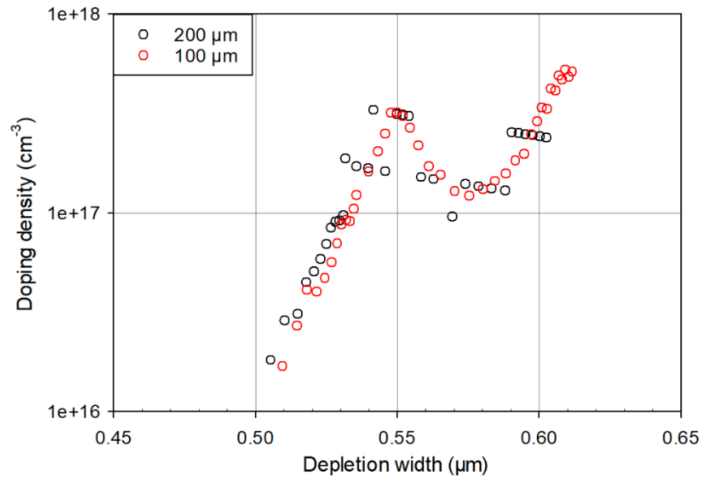
where V_{bi} is the built-in voltage, assuming that the junction is heavily doped on one side, in this case heavily n-doped. By combining Equation 4.3 and 4.4 into,

$$\frac{1}{C^2} = \frac{2}{\epsilon_0 \epsilon_r A^2 q N_d} (-V) + \frac{2V_{bi}}{\epsilon_0 \epsilon_r A^2 q N_d} \quad (\text{Equation 4.5})$$

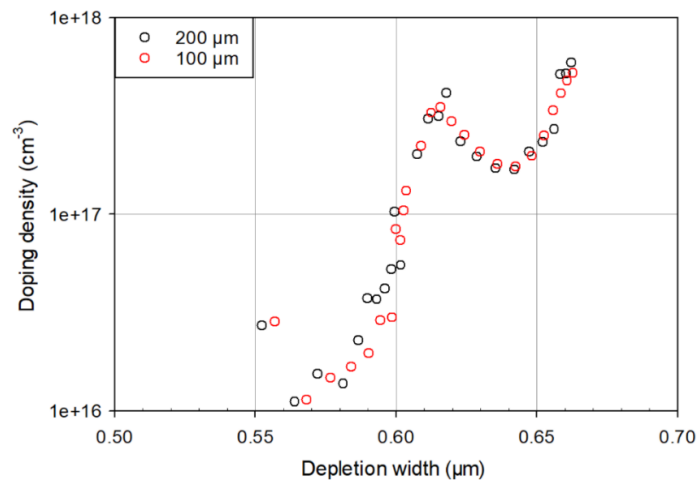
this equation becomes a linear function. Differentiating $\frac{1}{C^2}$ with respect to its voltage from Equation 4.5, the doping density value can be calculated.

$$N_d = \frac{2}{\epsilon_0 \epsilon_r e A^2} \left(\frac{dV}{d(1/C^2)} \right) \quad (\text{Equation 4.6})$$

From here, the plotting of N_d against x acquires the estimated thickness of the undoped region in the device; for a p-i-n structure.



(a)



(b)

Figure 4.8: Doping profile of (a) QW20 and (b) QW63.

The doping profile for QW20 and QW63 at different sized cells are shown in Figure 4.8. The ϵ_r used in this work is 12.9, similar to ϵ_r for GaAs. From the figures, different sized cells for each device show similar background doping density values and the i-region depletion width is within the estimated i-region thickness from the growth specifications. Figures of doping profile of different sized cells for other MQW devices are placed in Appendix C.

From the figure, a peak appears in both data in the middle of their profiles. The peak with higher apparent doping density value is caused by the band discontinuities that are usually seen in a heterojunction structure where different energy bandgaps are involved. This is due to charge accumulation at the smaller bandgap material interface with larger bandgap material. Here, the carriers from the doped AlGaAs cladding layer accumulate at the first undoped GaAs barrier in the i-region of the structure.

This condition is also seen in GaAs/AlGaAs MQW structures.[12] For a solar cell, a sufficiently large depletion width is desired to ensure a high rate of carrier collection. For example, InGaAsN has more than 1 μm depletion width for a 1 eV bandgap material.[13] This helps carrier collection and improves the short circuit current. A large depletion width can be achieved by decreasing the background doping to a range of between $10^{14} - 10^{15} \text{ cm}^{-3}$, which is a challenge for GaAsBi devices as they require low growth temperature.

Figure 4.9 shows the doping profile of STC-3X and QT1879 devices tabulated from the C-V data measured at reverse bias in this work. The sharp increase with a measured thickness of between 0.55-0.64 μm of the doping densities agree with the intended thickness for i-region of these devices which is 0.62 μm for most of the devices. A small variation between measured and intended thickness of the devices may be caused by dopant diffusion that occurs during the growth. However, QW10 shows a wider estimated depletion width compared to other STC-3X with $w = \sim 0.75 \mu\text{m}$. The 20 nm difference from the rest of the devices is due to the slight difference in growth condition. QW10 is reported to contain a thicker first barrier than other barriers due to an error in growth recipe programming, causing the thicker width.[9]

The measured doping densities for STC-3X devices are all roughly the same, within the range of $1.5 \times 10^{16} \text{ cm}^{-3}$ to $5.5 \times 10^{16} \text{ cm}^{-3}$. The background doping density values for this work are similar to previous work done by the same group, with density values of $1.2 \times 10^{16} \text{ cm}^{-3}$ [14] and $5 \times 10^{16} \text{ cm}^{-3}$ [15] for 2.1-3.4% and 6% Bi content, respectively. The value of background doping

is higher compared to other MQW devices reported such as the InGaAs MQWs reported in [16] with $\leq 3 \times 10^{15} \text{ cm}^{-3}$ background doping. Other than Bi-based growth conditions, the impurities in the growth chamber and arsenic cell outgassing can also be the factors contributing to the higher doping. It is still not clear what the type of background doping in this work, but there are several reports on undoped GaAsBi with p-type background doping [17, 18] and n-type background doping [14].

Meanwhile, the doping profile of QT1879 shown is not fully depleted at 0 V. The doping density value is roughly one order of magnitude lower than STC-3X devices and the value gradually increases as the reverse bias increases until it reaches about $\sim 1.87 \mu\text{m}$. Due to the thick depletion width in the structure, it requires more potential to fully deplete the i-region. Besides that, the depletion width is 200 nm thicker than its intended thickness which is 1.67 μm .

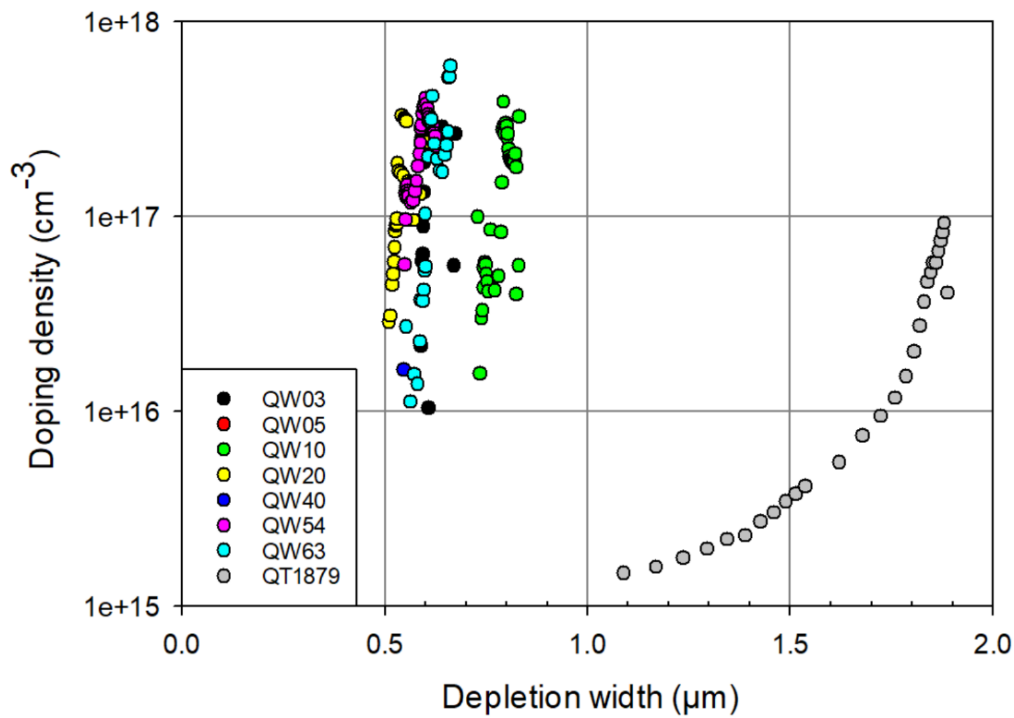


Figure 4.9: Doping profile of STC-3X and QT1879 estimated from C-V curves. All the STC-3X devices are fully depleted at zero bias and the measured depletion widths agree with the intended i-region thickness. QW10 shows thicker width due to having different material recipe programming set during growth. Meanwhile, QT1879 shows thicker depletion width due to having thicker i-region thickness.

4.4 Current-Voltage (I-V) Measurement

4.4.1 Forward dark (I-V) Measurement

This sub-section will focus on forward bias I-V characterisation performed in dark conditions. Figure 4.10 shows the data of the forward dark current, I and dark current density, J of QW20 and QW63 plotted as functions of voltage. The measurements were done on several 200, 100 and 50 μm radius-sized cells. The raw I-V and J-V graphs with different sizes for other devices are placed in Appendix D.

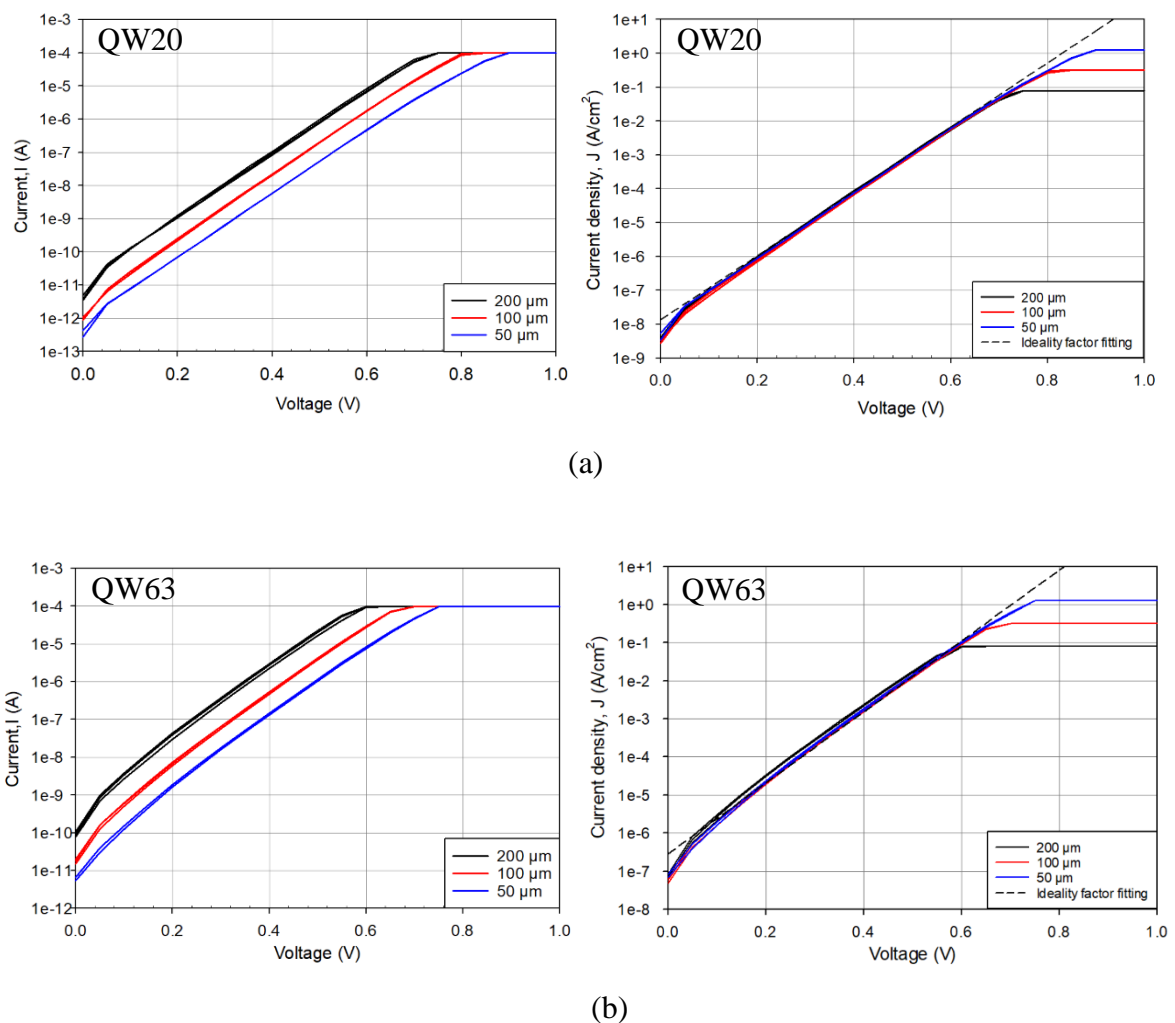


Figure 4.10: I-V (left) and J-V (right) forward bias for (a) QW20 and (b) QW63 at three different cell areas. 0.1 mA is the compliance limit set on the picoammeter during the measurements.

The forward current densities from the figures show good area scaling and are consistent throughout the measurements, indicating that a bulk, rather than surface, dark current mechanism was dominating for each device. The constant regions of the dark current at high voltage for both devices are due to the setting of the current compliance which is 100 μA . This compliance is set to ensure no overheating or overshoot of current due to high injection during the measurements that can cause damage to the cell. The dashed line shown in the J-V graph for both devices is the ideality factor fitted to the current density, showing that a consistent value is achieved for each sized-devices. The discussion on ideality factor will be discussed later in this section.

The J-V measurements on all STC-3X devices and QT1879 at room temperature are shown in Figure 4.11. Here, GaAs is used as another control device to compare the dark current value when no Bi is introduced into GaAs. The measurements were done on GaAs bulk devices grown by the same group labelled as STF86 and STF87 for 0.2 μm and 1.6 μm i-region thicknesses, respectively. In addition to that, J-V data from a GaAs solar cell with a low J_o value taken from Kurtz *et al.* is also extracted and plotted for comparison.[19]

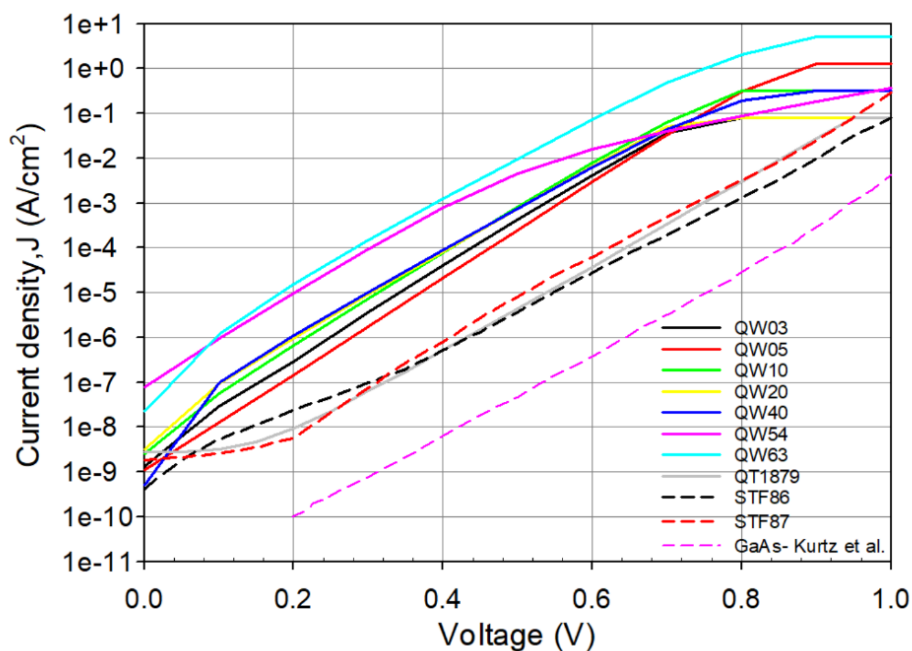


Figure 4.11: Forward J-V measurements for all STC-3X devices and QT1879. Dashed lines are the forward J-V for GaAs devices.

From Figure 4.11, it is seen that between the STC-3X devices, they are divided into two regions of current density. QW03 to QW40 show a similar range of dark current value. Another region is for QW54 and QW63 that show higher value of current density. From the graph, the dark current of QT1879 is between one and two orders of magnitude lower than those of QW05-QW40 at around 0.6 V; which is about $5.1 \times 10^{-7} \text{ A/cm}^2$ compared to between $2.1 - 9.0 \times 10^{-5} \text{ A/cm}^2$ at that voltage. These are, in turn, more than three orders of magnitude lower than those of QW54 and QW63 that have current density value of $7.7 \times 10^{-4} \text{ A/cm}^2$ and $1.2 \times 10^{-3} \text{ A/cm}^2$, respectively.

STF86 and STF87 show higher dark current compared to Kurtz et al. and has similar value with QT1879. It is suggested that the as-grown GaAs by the group is not as good as in other studies to begin with and therefore it gives some contributions to the high dark current in the STC-3X devices. In addition to that, the high dark currents exhibited by QW54 and QW63 are potentially due to higher dislocations densities formed during sample growth and they are attributed to strain relaxation. It is also seen that the strain level in QW20 and QW40 are enough to undergo dislocation propagation, whereas QW03-QW10 have lower level of strain.[8] As the dark currents of QW03-QW40 are all at similar values, it is concluded that strain related structural defects do not dominate these I-V curves and, therefore, QW03-QW40 are representative of the elastically strained GaAsBi material system whereas QW54 and QW63 are strain-relaxed GaAsBi material system.

From the ideal diode law, the Shockley equation can be presented as,

$$J_{diff} = J_o \left[\exp \left(\frac{qV}{kT} \right) - 1 \right] \quad (\text{Equation 4.7})$$

Where diffusion current, J_{diff} is the current created due to the electrons and holes diffusion with the consideration of Boltzmann relation. The term J_o which is the value of saturation current density can be used to compare electrical properties of a material system. The J_o term is dependent on temperature, related with value of the intrinsic carrier concentration of the semiconductor, n_i and is interpreted as shown in Equation 4.8 [11],

$$J_o = \frac{qD_p n_i^2}{L_p N_D} + \frac{qD_n n_i^2}{L_n N_A} \quad (\text{Equation 4.8})$$

Where the carrier diffusion coefficient (D_p for holes and D_n for electrons) is a parameter associated with mobility, and N_D and N_A are the concentration for donor and acceptor impurities, respectively. Diffusion length (L_p for holes and L_n for electrons) is another parameter related to mobility with expression of $L_p \equiv \sqrt{D_p \tau_p}$ and $L_n \equiv \sqrt{D_n \tau_n}$. Note that τ_p and τ_n are the minority carrier lifetime for holes and electrons, respectively.

At forward bias, recombination current, J_{re} is another capture process in addition to diffusion current. From Shockley-Read-Hall statistic, the dominant recombination process in the depletion region occurs with the activation energy of half of the bandgap and J_{re} can be expressed as,

$$J_{re} = \frac{qW_D n_i}{2\tau} \exp\left(\frac{qV}{2kT}\right) \quad (\text{Equation 4.9})$$

where W_D is the depletion layer width, τ is the carrier lifetime with relationship of $\tau = \frac{1}{\sigma v_{th} N_t}$ where σ is conductivity, v_{th} is thermal velocity and N_t is trap density. J_{re} can be created in the depletion region due to defects and impurities that cause the formation of energy states in forbidden gap.[11] Assuming a one-sided p⁺-n abrupt junction with N_D value, the forward current, $J_{forward}$ is the total forward current due to different mechanisms as shown in Equation 4.10,

$$J_{forward} = \frac{qD_p n_i^2}{L_p N_D} \exp\left(\frac{qV}{kT}\right) + \frac{qW_D n_i}{2\tau} \exp\left(\frac{qV}{2kT}\right) \quad (\text{Equation 4.10})$$

This in turn, gives the empirical form of $J_{forward}$ with the ideality factor, n .

$$J_{forward} \propto \exp\left(\frac{qV}{nkT}\right) \quad (\text{Equation 4.11})$$

where the value of n ranges between 1 and 2. If n is 1, the diffusion current is the dominant mechanism which is the value desired for opto-electronic devices. On the other hand, if n is 2, the forward current is dominated by recombination current. n can also be between 1 and 2 showing that both currents are comparable. If the value of n is greater than 2, this indicates that series resistance has started to dominate the forward current mechanism. The value of n can be calculated from the slope of the graph in Figure 4.11 and J_0 can be obtained by extrapolation

of the linear region from $\ln J$ to the y-intercept where $V = 0$. Table 4.1 summarises the value of J_0 and n for all STC-3X and QT1879 devices.

Devices	Saturation current density, J_0 (A/cm ²)	Ideality factor, n
QW03	2.63×10^{-9}	1.60
QW05	1.03×10^{-9}	1.55
QW10	6.37×10^{-9}	1.65
QW20	1.35×10^{-8}	1.77
QW40	1.91×10^{-8}	1.80
QW54	1.32×10^{-7}	1.70
QW63	2.80×10^{-7}	1.80
QT1879	8.87×10^{-11}	1.78

Table 4.1: Value of saturation current, J_0 and ideality factor, n extracted from the measured J-V data. The value of ideality factor for each device is valid between ~ 0.1 and 0.6 V forward bias.

It is shown that the ideality factor of all STC-3X and QT1879 devices is between 1.55 and 1.8, which indicates influence from both J_{diff} and J_{re} mechanisms, with J_{re} as the dominating factor at room temperature. This value is smaller compared to other work on GaAsBi MQWs that have n value of close to or more than 2 and it is independent of the number of wells.[5, 20, 21] At high bias, ideality factor may deviates from its calculated gradient value. The degree of deviation is different depending on how much the series resistance is affecting the measurements when high bias is applied. For example- QW54, roughly after 0.6 V; shows a non-exponential increase of current with bias with n value more than 2. The cause for high series resistance is unknown. Other devices do not show significant effects of series resistance and their n value is still < 2 at high voltages.

The strain-relaxed devices show higher values of J_0 compared to the strained devices. These values are expected because relaxed devices have a smaller energy bandgap as previously reported.[8] For a semiconductor material with larger bandgap, it is more difficult for carriers to escape through the forbidden gap, thermally. From Equation 4.8, J_0 is in relationship with n_i and it is also related to energy bandgap and temperature by the expression shown in Equation 4.12 [11],

$$n_i \propto \exp\left(-\frac{E_g}{2kT}\right) \quad (\text{Equation 4.12})$$

By comparing these two equations, it can be concluded that the value of n_i is higher when the energy bandgap is lower, and this increase the value of J_0 . The trend can be observed from Figure 4.12. At zero bias, three different ranges can be seen from the graphs showing different dark current density- bandgap energy groups. QW03 and QW05 are in the lower dark current density-large bandgap energy. QW10-QW40 show intermediate dark current density-bandgap energy. Meanwhile, QW54 and QW63 have the higher dark current density with smaller bandgap energy compared to others. These ranges indicate that the increase in number of wells for the same number of Bi contents increase the dark current due to the increase in defect levels. Besides that, the Bi inhomogeneity in the layer also causing different level of strains in the devices.

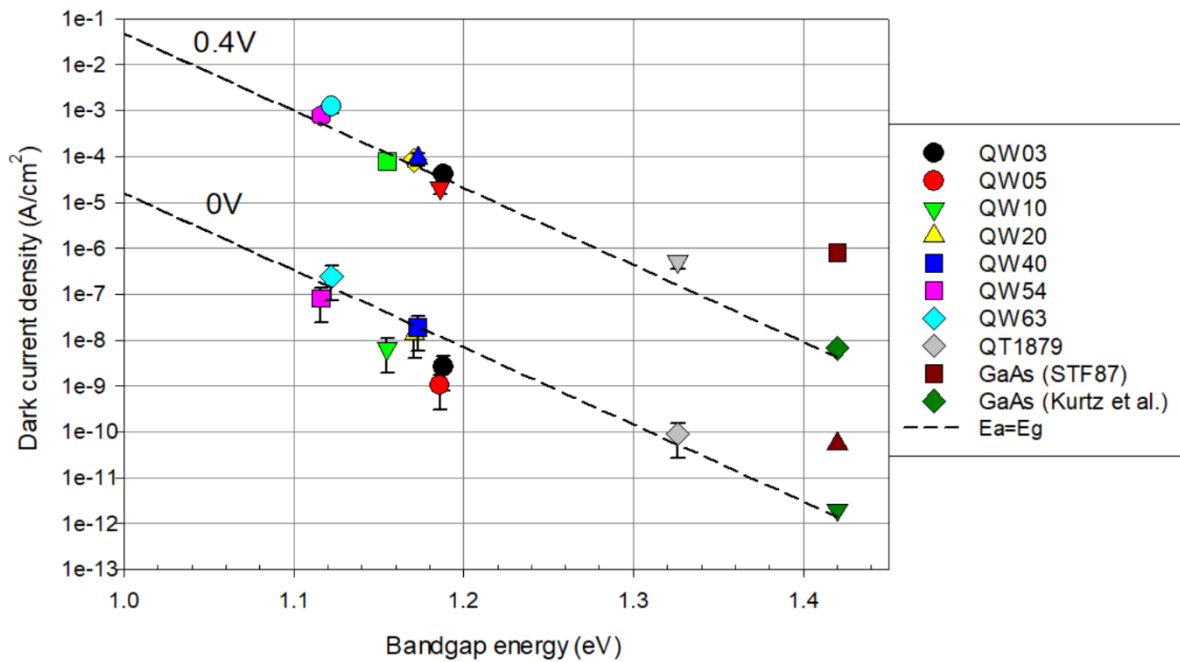


Figure 4.12: Dark current density at 0V and 0.4 V with respect to bandgap energy for STC-3X devices, QT1879 and GaAs reference devices.

Equation 4.13 can be used to fit the dark current values in Figure 4.12,

$$J = A \exp(-E_a/kT) \quad (\text{Equation 4.13})$$

where A is a constant, k is the Boltzmann constant, T is the temperature and E_a is the activation energy. It is shown that STC-3X devices dark current data is fitted to the expression at room temperature with E_a value to be equal to E_g at both 0 V and 0.4 V. The E_g values are taken from the PL peak estimated from previous work.[22] QT1879 and GaAs by Kurtz *et al.* also follows the $E_a = E_g$ fitting line. This indicates band-to-band generation current dominates the device mechanism which is expected because the devices have lower strain level. Meanwhile, GaAs STF87 does not follow the fitting as the dark current is higher than expected. This suggests a lower activation energy compared to its bandgap value and is possibly caused by the domination of generation process due to emission from deep-level traps instead of band-to-band generation current.

4.4.2 Reverse Dark (I-V) Measurement

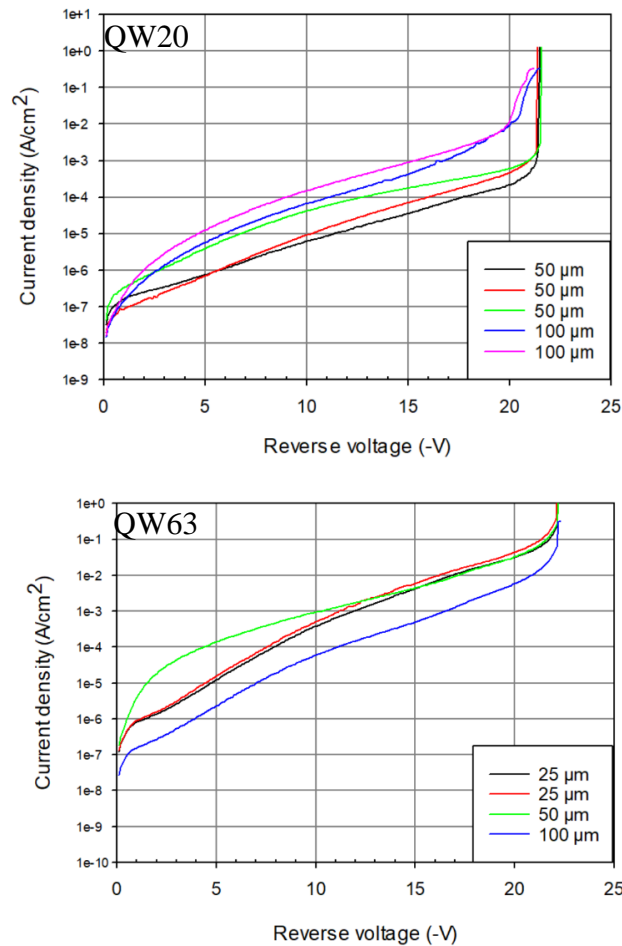


Figure 4.13: Reverse bias J-V of (a) QW20 and (b) QW63 taken from different sized-mesa cells. The sudden increase in current density at high reverse bias (>20 V) indicates that the device has reached its breakdown voltage.

It is seen that the values do not scale closely with area. The variation of current density for different cells also different for every device. From the figures, both devices show over one order of magnitude variation in the dark current values at -10V. This variation can be caused by the presence of surface leakage current that is affecting the overall density that is supposed to be dominated by bulk current. The surface leakage current can be determined by finding the perimeter current density of the devices. From the reverse perimeter current density graph (not shown in here), the reverse J-V also not quite scaling with perimeter. This suggests both surface and bulk leakage are present at reverse bias. The combination of these leakages is also seen in QT1879 where the reverse J-V data does not scale with area (refer appendix E).

Surface leakage current comes from the presence of charge outside the semiconductor layer which induce charge in the semiconductor. As the result, a surface depletion region is formed and it modifies the junction depletion region causing a current leakage. However, the current leakage seen in these devices is not a big issue if the structures are to be functioned as solar cells. This is because, solar cells operate at forward bias condition and the effect of surface leakage is very small. If the devices are to be used as photodiode applications, the surface leakage can be suppressed by the application of metal passivation to the devices.

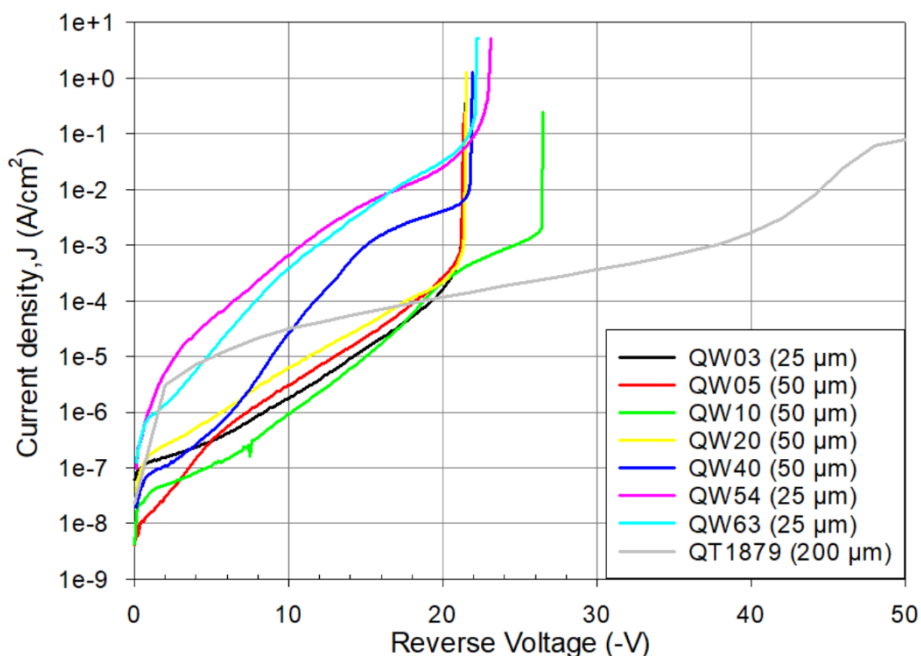


Figure 4.14: Reverse dark currents as a function of reverse voltage of STC-3X and QT1879. For all the devices, several slopes are identified at different voltage ranges, indicate that different domination of reverse bias mechanisms have occur.

The reverse dark current density as a function of reverse voltage at room temperature for all STC-3X and QT1879 devices are shown in Figure 4.14. Due to the inconsistency in current density value at reverse bias, the lowest dark current density value for each device is chosen for comparison in the figure. From the figure, the reverse dark current densities are similar for QW03 to QW20 which is at about 1×10^{-7} A/cm² at zero bias and the values increase a bit higher than an order of magnitude for QW40-QW63, roughly 3×10^{-6} A/cm². The increase in reverse leakage current can be caused by an increase in dislocation density in the devices as the number of wells increases, due to strain. QW10 shows a higher value of junction breakdown voltage which is roughly 26 V compared to the rest of devices that have breakdown voltages around 21-22 V. From the log-linear figure, it is seen that the reverse dark currents are made of a different combination of current mechanisms. The change in gradients of the dark current density for all devices at different reverse voltage show the change in dominating current mechanisms as bias is applied. The reverse dark current starts with rapid rise, followed by an exponential dependence on voltage before it hits the breakdown voltage.

Ideally, the current density for a diode at reverse bias is a constant value of J_o . However, it is not the case in real experimental measurements where other reverse bias mechanisms can contribute to the measured current. One of the reverse bias mechanisms that may contribute to the increase in reverse dark current with respect to voltage applied is the classic band to band tunneling current, J_{tun} . In a narrow bandgap semiconductor material, the electrons can tunnel from the valence band directly to the conduction band via the forbidden gap. This tunneling of electrons commonly occurs when the electric field is sufficiently high. Here, the forbidden gap acts as a potential barrier and this mechanism creates a band-to-band tunneling current.[23] Equation 4.14 shows the J_{tun} for a material,

$$J_{tun} = \frac{(2m_e)^{1/2} q^3 F_m V}{h^2 E_g^{1/2}} \exp\left(-\frac{2\pi\beta m_e^{1/2} E_g^{3/2}}{qhF_m}\right) \quad (\text{Equation 4.14})$$

where m_e is the effective mass of electron, q is the electronic charge, F_m is the maximum electric field obtained from C-V profiling, V is the voltage applied, h is Planck's constant, E_g is the bandgap energy and β is the tunneling barrier parameter. The value of m_e is taken from [24] which is $0.06m_o$ for the effective electron mass and m_o is the electronic charge mass. However, after the calculation of Equation 4.14, the dark current density value is not fitted to

the experimental result and the shape does not show a band-to-band tunneling-like curve. One of the examples for the non-fitted value can be seen from QW20 reverse bias data in Figure 4.15. This discounts the J_{tun} mechanism and implies the presence of another dark current mechanism for the devices.

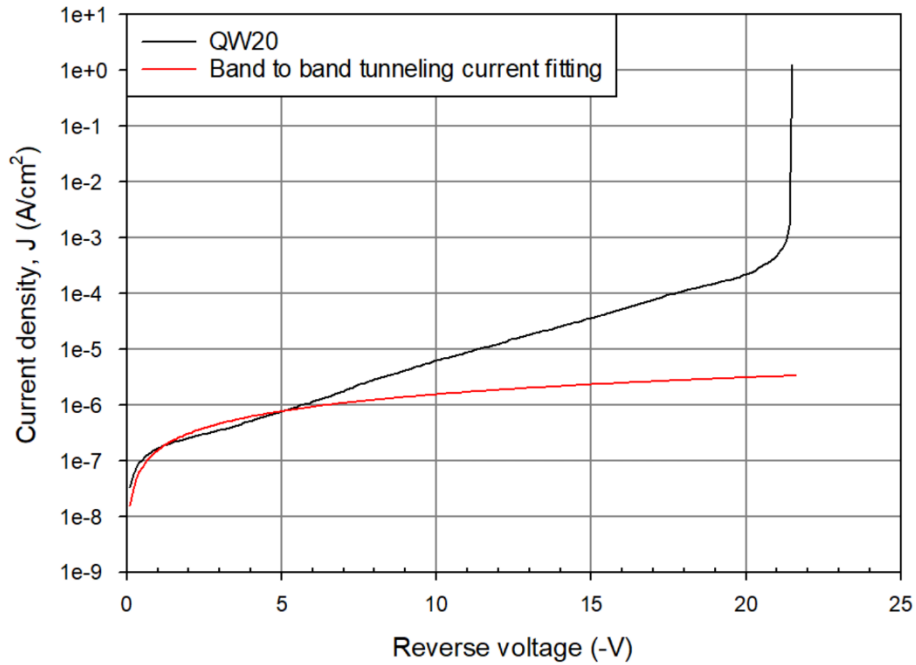


Figure 4.15: Reverse dark current density for QW20 with band to band tunneling current density, J_{tun} mechanism plotted on the same graph. J_{tun} calculated is not fitted to the experimental result.

Another dark current mechanism that may cause the increase in reverse dark current is the trap-assisted current mechanism, J_{TAT} . The movement of electron tunneling is different from the J_{tun} mechanism and its value depends on the trap energy and trap density. First, the electrons fill the traps in the bandgap, then move to the conduction band via the traps. Several works have proven the presence of J_{TAT} especially at the mid-voltage range dark current density.[25, 26]

J_{TAT} can be described as shown in Equation 4.15, taken from [27]

$$J_{TAT} = \frac{q^2 m_e V M^2 N_t}{8\pi \hbar^3} \exp\left(-\frac{4\sqrt{2m_T}(E_g - E_t)^3}{3e\hbar F(V)}\right) \quad (\text{Equation 4.15})$$

where V is the reverse bias voltage, M^2 is the matrix element related to the trap potential, N_t is the activated trap density, E_t is the trap potential within the bandgap. The modified one-dimensional model for J_{TAT} can be expressed as follows [28, 29]

$$J_{TAT} = qAN_tWT_{rate} \quad (\text{Equation 4.16})$$

where, T_{rate} is the tunneling rate of the carriers and other parameters follow the usual meaning. This expression also does not satisfy the reverse dark current obtained, considering the modified model is a constant value.

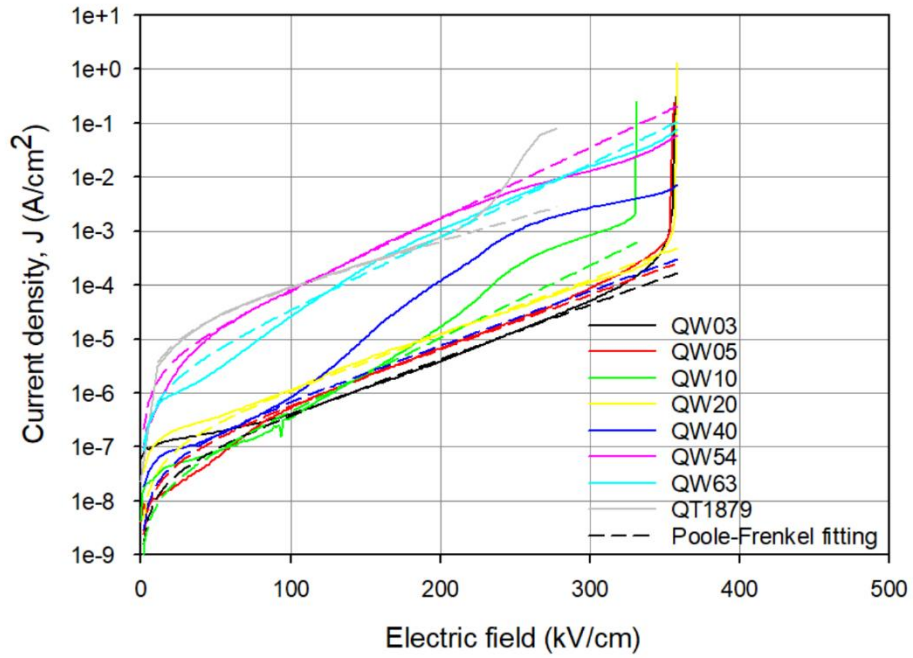


Figure 4.16: Poole-Frenkel equation fitted to the reverse bias J-V of the devices with respect to electric field.

In this work, the exponential dependence shown in Figure 4.16 can be fitted by a process called as Poole-Frenkel emission where the charge carriers escape from trap centres in electronic semiconductors and insulators with the assistance of an electric field. The three-dimensional Poole-Frenkel effect can be described as,[30]

$$J_{P-F} \approx \frac{\sigma_0 kT}{2qb} \left[\exp\left(\frac{qE_f b}{kT}\right) - 1 \right] \quad (\text{Equation 4.17})$$

where σ_0 , E_f , and b are the low-field conductivity, electric field and radius of the potential well, respectively and other symbols denote the usual parameters. The value of E is assumed to be the total voltage drop across the i-region width. Meanwhile, the value of σ_0 and b are varied to fit the magnitude and slope of the data, respectively.

The figure shows the reverse $J-E_f$ for all STC-3X and QT1879 devices with the Poole-Frenkel equation fitted to them. Except QW40, the Poole-Frenkel equation can be fitted to the reverse bias J-V data. It is suggested that QW40 shows anomalous fitting due to its condition of partial strain relaxation. There may be other mechanisms that are more dominant compared to Poole-Frenkel.

Devices	Low field conductivity, σ_0 (S/m)	Radius of the potential well, b (nm)
QW03	1.9×10^{-10}	6.0
QW05	2.9×10^{-10}	6.0
QW10	1.0×10^{-11}	6.0
QW20	5.5×10^{-10}	6.0
QW40	3.4×10^{-10}	6.0
QW54	2.5×10^{-8}	7.8
QW63	1.0×10^{-8}	8.0
QT1879	2.0×10^{-8}	1.6

Table 4.2: The fitting parameter values used to model Poole-Frenkel emission for STC-3X and QT1879 devices.

The parameters used to fit the Poole-Frenkel equation to the reverse bias J-V data are listed in 2. The values of low field conductivity and radius of the potential wells are distinct between the strained and strain-relaxed devices. This effect has also been reported for bulk GaAsBi [31] and InGaAsN lattice-matched to GaAs [32] material systems. For now, the physical significance in different regions of reverse bias is not clear yet for this set of devices. Different gradients from the reverse $J-E_f$ graphs may be caused by a different combination of the mechanisms and further study is needed to answer these questions. More in-depth study is beyond the scope of this work and will be the suggested as future work. Besides that, temperature dependent reverse bias measurements will be needed for modelling and to further study the possible mechanisms that dominate the J-V in these devices.

4.5 Summary

GaAsBi/GaAs MQW p-i-n diodes with different numbers of wells ranging from 3 to 63 quantum wells have been studied and compared with a strain-balanced InGaAs/GaAsP quantum well diodes. First, previous works on the STC-3X devices were presented including the PL data, TEM and Nomarski images. Then, the C-V measurements were performed on the STC-3X and QT1879 devices. It is shown that all STC-3X MQW devices are more than 90% depleted when zero bias is applied. The estimated i-region thicknesses for all devices are close to their nominal width which is 0.62 μm except QW10 where it shows thicker width, 0.74 μm . This is due to a thicker first barrier following an error during the growth process. Relatively high background doping values in the i-region compared to other material systems such as InGaAN are seen for all STC-3X devices with values $\sim 10^{16} \text{ cm}^{-3}$ and they are similar to values obtained from C-V by other research in Bi-based material.

A good agreement with the current density for each device at forward bias with different radii shows that the I-V results are dominated by bulk current mechanism. The value of dark currents for strained devices are within two orders of magnitude compared to InGaAs/GaAsP device. For relaxed devices, the value of dark current increases indicating strain relaxation occurrence. The dark current densities of the STC-3X devices also increase with the decreasing bandgap. From the gradient obtained by the energy fitting derivation, the activation energy is seen to be equal to the bandgap energy.

Besides that, reverse I-V characterisation was performed. The reverse leakage current seen when a reverse bias is applied indicates the dominance of leakage current during the reverse process. Several mechanisms are responsible for the reverse bias current with Poole-Frenkel emission mechanism fitted as the exponential dependence.

In conclusion, the STC-3X devices behave like conventional III-V semiconductor material, showing good rectifying diode-like characteristics with a reasonable ideality factor of between 1 and 2, with the recombination current mechanism dominating the process. The dark current densities for Bi-based devices can be improved by improving the growth conditions, reducing the strain levels and by more careful device fabrication.

4.6 References

- [1] T. Thomas *et al.*, "Requirements for a GaAsBi 1eV Sub-Cell in a GaAs-based Multi-Junction Solar Cell," *Semiconductor Science and Technology*, Article vol. 30, no. 9, p. 6, Sep 2015, Art no. 094010, doi: 10.1088/0268-1242/30/9/094010.
- [2] V. Bahrami-Yekta, T. Tiedje, and M. Masnadi-Shirazi, "MBE Growth Optimization for GaAs_{1-x}Bi_x and Dependence of Photoluminescence on Growth Temperature," *Semiconductor Science and Technology*, Article vol. 30, no. 9, p. 7, Sep 2015, Art no. 094007, doi: 10.1088/0268-1242/30/9/094007.
- [3] D. A. Beaton, R. B. Lewis, M. Masnadi-Shirazi, and T. Tiedje, "Temperature Dependence of Hole Mobility in GaAs_{1-x}Bi_x Alloys," *Journal of Applied Physics*, Article vol. 108, no. 8, p. 4, Oct 2010, Art no. 083708, doi: 10.1063/1.3493734.
- [4] S. Adachi, "Optical Dispersion-Relations for GaP, GaAs, GaSb, InP, InAs, InSb, Al_xGa_{1-x}As, and In_{1-x}Ga_xAs_yP_{1-y}," *Journal of Applied Physics*, Article vol. 66, no. 12, pp. 6030-6040, Dec 1989, doi: 10.1063/1.343580.
- [5] T. B. O. Rockett *et al.*, "Influence of Growth Conditions on the Structural and Opto-Electronic Quality of GaAsBi," *Journal of Crystal Growth*, Article; Proceedings Paper vol. 477, pp. 139-143, Nov 2017, doi: 10.1016/j.jcrysgr.2017.02.004.
- [6] Y. I. Mazur *et al.*, "Effects of AlGaAs Cladding Layers on the Luminescence of GaAs/GaAs_{1-x}Bi_x/GaAs Heterostructures," *Nanotechnology*, Article vol. 25, no. 3, p. 9, Jan 2014, Art no. 035702, doi: 10.1088/0957-4484/25/3/035702.
- [7] R. D. Richards *et al.*, "Molecular Beam Epitaxy Growth of GaAsBi using As-2 and As-4," *Journal of Crystal Growth*, vol. 390, pp. 120-124, Mar 15 2014, doi: 10.1016/j.jcrysgr.2013.12.008.
- [8] R. D. Richards, F. Bastiman, J. S. Roberts, R. Beanland, D. Walker, and J. P. R. David, "MBE Grown GaAsBi/GaAs Multiple Quantum Well Structures: Structural and Optical Characterization," *Journal of Crystal Growth*, Article; Proceedings Paper vol. 425, pp. 237-240, Sep 2015, doi: 10.1016/j.jcrysgr.2015.02.053.
- [9] R. Richards, "Molecular beam epitaxy growth and characterisation of GaAsBi for photovoltaic applications," ed, September 2014.
- [10] Z. Zhou, "Optimisation of GaAsBi Based Semiconductors," ed. The university of Sheffield, March 2017.
- [11] S. M. Sze and K. K. Ng, *Physics of Semiconductor Devices*, Third Edition ed. New Jersey: John Wiley & Sons, Inc, 2007.
- [12] M. O. Watanabe, J. Yoshida, M. Mashita, T. Nakanisi, and A. Hojo, "Band Discontinuity for GaAs AlGaAs Heterojunction Determined by C-V Profiling Technique," *Journal of Applied Physics*, Article vol. 57, no. 12, pp. 5340-5344, 1985, doi: 10.1063/1.334852.
- [13] I. R. Sellers, W. S. Tan, K. Smith, S. Hooper, S. Day, and M. Kauer, "Wide Depletion Width of 1 eV GaInNAs Solar Cells by Thermal Annealing," *Applied Physics Letters*, Article vol. 99, no. 15, p. 3, Oct 2011, Art no. 151111, doi: 10.1063/1.3648110.

- [14] Z. Z. Zhou, D. F. Mendes, R. D. Richards, F. Bastiman, and J. P. R. David, "Absorption Properties of GaAsBi based p-i-n Heterojunction Diodes," *Semiconductor Science and Technology*, Article vol. 30, no. 9, p. 6, Sep 2015, Art no. 094004, doi: 10.1088/0268-1242/30/9/094004.
- [15] C. J. Hunter *et al.*, "Absorption Characteristics of GaAs_{1-x}Bi_x/GaAs Diodes in the Near-Infrared," *Ieee Photonics Technology Letters*, vol. 24, no. 23, pp. 2191-2194, Dec 1 2012, doi: 10.1109/lpt.2012.2225420.
- [16] J. P. R. David, Y. H. Chen, R. Grey, G. Hill, P. N. Robson, and P. Kightley, "Effect of Misfit Dislocations on Leakage Currents in Strained Multiquantum-Well Structures," *Applied Physics Letters*, Article vol. 67, no. 7, pp. 906-908, Aug 1995, doi: 10.1063/1.114690.
- [17] S. Nargelas, K. Jarasiunas, K. Bertulis, and V. Pacebutas, "Hole Diffusivity in GaAsBi Alloys Measured by a Picosecond Transient Grating Technique," *Applied Physics Letters*, Article vol. 98, no. 8, p. 3, Feb 2011, Art no. 082115, doi: 10.1063/1.3557047.
- [18] G. Pettinari, A. Patane, A. Polimeni, M. Capizzi, X. F. Lu, and T. Tiedje, "Bi-induced p-type Conductivity in Nominally Undoped Ga(AsBi)," *Applied Physics Letters*, Article vol. 100, no. 9, p. 4, Feb 2012, Art no. 092109, doi: 10.1063/1.3690901.
- [19] S. R. Kurtz, J. M. Olson, A. Kibbler, and Ieee, "High-Efficiency GaAs Solar-Cells using GaInP₂ Window Layers," in *21st Ieee Photovoltaic Specialists Conf*, Kissimmee, FL, May 21-25 1990, NEW YORK: I E E E, in Ieee Photovoltaic Specialists Conference, 1990, pp. 138-140, doi: 10.1109/pvsc.1990.111605. [Online]. Available: <Go to ISI>://WOS:A1990BS39H00025
- [20] K. K, H. S, H. N. H, and Y. M, "Impact of a Small Change in Growth Temperature on the Tail States of GaAsBi," *Journal of Applied Physics*, 2019.
- [21] R. B. Lewis, D. A. Beaton, X. F. Lu, and T. Tiedje, "GaAs_{1-x}Bi_x Light Emitting Diodes," *Journal of Crystal Growth*, Article vol. 311, no. 7, pp. 1872-1875, Mar 2009, doi: 10.1016/j.jcrysgro.2008.11.093.
- [22] R. Richards *et al.*, "GaAsBi MQWs for Multi-Junction Photovoltaics," *2013 Ieee 39th Photovoltaic Specialists Conference (Pvsc)*, pp. 303-305, 2013 2013.
- [23] A. Zemel and M. Gallant, "Current-Voltage Characteristics of Metalorganic Chemical Vapor-Deposition InP/InGaAs P-I-N Photodiodes - The Influence of Finite Dimensions and Heterointerfaces," *Journal of Applied Physics*, Article vol. 64, no. 11, pp. 6552-6561, Dec 1988, doi: 10.1063/1.342026.
- [24] B. Fluegel, R. N. Kini, A. J. Ptak, D. Beaton, K. Alberi, and A. Mascarenhas, "Shubnikov-de Haas Measurement of Electron Effective Mass in GaAs_{1-x}Bi_x," *Applied Physics Letters*, Article vol. 99, no. 16, p. 3, Oct 2011, Art no. 162108, doi: 10.1063/1.3655198.
- [25] D. Rosenfeld and G. Bahir, "A Model for the Trap-Assisted Tunneling Mechanism in Diffused N-P and Implanted N+-P HgCdTe Photodiodes," *Ieee Transactions on Electron Devices*, Article vol. 39, no. 7, pp. 1638-1645, Jul 1992, doi: 10.1109/16.141229.

- [26] M. A. Kinch, "Electronic-Properties of HgCdTe," *Journal of Vacuum Science & Technology*, Article vol. 21, no. 1, pp. 215-219, 1982, doi: 10.1116/1.571719.
- [27] Q. K. Yang, F. Fuchs, J. Schmitz, and W. Pletschen, "Investigation of Trap-Assisted Tunneling Current in InAs/(GaIn)Sb Superlattice Long-Wavelength Photodiodes," *Applied Physics Letters*, Article vol. 81, no. 25, pp. 4757-4759, Dec 2002, doi: 10.1063/1.1529306.
- [28] V. Gopal, S. K. Singh, and R. M. Mehra, "Analysis of Dark Current Contributions in Mercury Cadmium Telluride Junction Diodes," *Infrared Physics & Technology*, Article vol. 43, no. 6, pp. 317-326, Dec 2002, Art no. Pii s1350-4495(02)00159-7, doi: 10.1016/s1350-4495(02)00159-7.
- [29] J. Y. Wong, "Effect of Trap Tunneling on the Performance of Long-Wavelength Hg_{1-x}Cd_xTe Photo-Diodes," *Ieee Transactions on Electron Devices*, Article vol. 27, no. 1, pp. 48-57, 1980, doi: 10.1109/t-ed.1980.19818.
- [30] J. L. Hartke, "3-Dimensional Poole-Frenkel Effect," *Journal of Applied Physics*, Note vol. 39, no. 10, pp. 4871-&, 1968, doi: 10.1063/1.1655871.
- [31] C. Hunter, "Growth and Characterization of Bulk GaAs_{1-x}Bi_x/GaAs Diodes," ed: University of Sheffield; 2014, 2014.
- [32] L. J. J. Tan, W. M. Soong, J. P. R. David, and J. S. Ng, "Dark Current Mechanism in Bulk GaInNAs Lattice Matched to GaAs," *Ieee Transactions on Electron Devices*, Article vol. 58, no. 1, pp. 103-106, Jan 2011, doi: 10.1109/ted.2010.2086061.

Chapter 5: Opto-Electronic Characterisation of GaAsBi/GaAs MQW Devices

5.1 Introduction

The opto-electronic characterisation presented in this chapter is important to further understand the GaAsBi/GaAs MQW material behaviour and to identify the potential of this Bi-based material specifically as a solar cell. So far, there are only a few reports of work done on GaAsBi for solar cell applications, such as on its absorption properties due to the research interest in other fields, especially in light emitting devices such as lasers and LEDs.[1-3]

5.2 Photocurrent Measurements

5.2.1 Measurement testing

Systematic photocurrent measurements as functions of wavelength were done for the STC-3X devices. The measurement setup has been explained in Section 3.5.1. First, the photocurrent measurements were done on STC-3X devices without any filter. Here, the photocurrents created by the device were due to the photon absorption from monochromatic light and the harmonic multiple-order light produced by the monochromator. Then, two types of filters were used: a 715nm long-pass filter and un-doped GaAs filter. The 715nm filter is used to filter out carrier excitation from the AlGaAs cladding layers in the device structures and to avoid any second order light absorption from the devices. Meanwhile, the GaAs wafer filter was used to exclude absorption from the GaAs barrier and at all shorter wavelengths. This is to allow current created due to the carrier excitation from the quantum well only, without stray effects from other sources. Different filters are used in measuring the photocurrent of the devices to ensure accuracy in obtaining the data and to identify the actual current created in the quantum wells when light falls onto the devices.

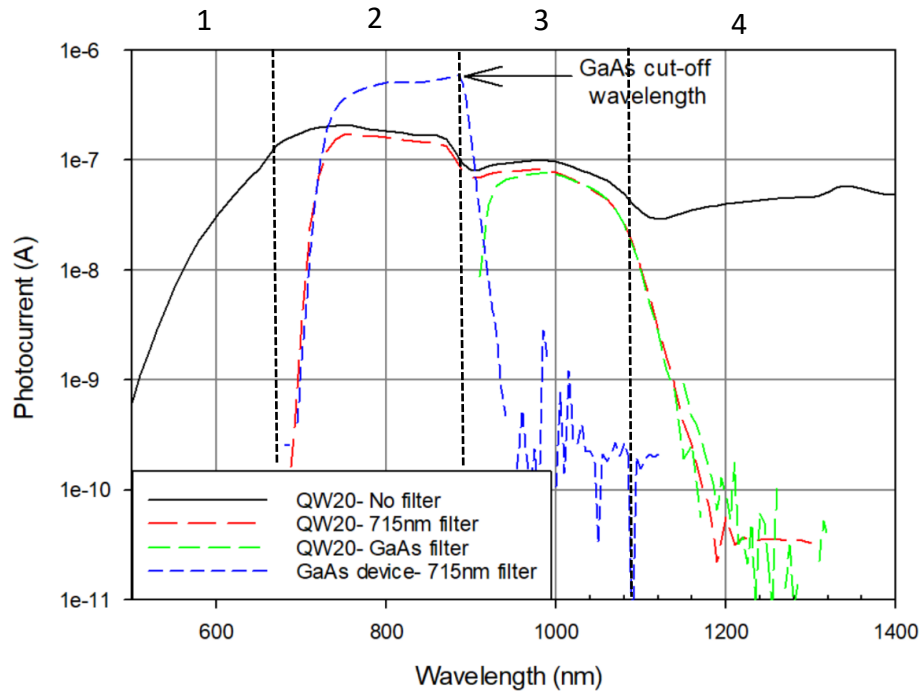


Figure 5.1: Photocurrent measurements of QW20 taken at 0V with no/different filter(s). GaAs control device (blue line) is shown for comparison. The graph is divided into 4 regions which are (1) AlGaAs cladding layer, (2) GaAs barriers, (3) GaAsBi quantum wells and (4) second order photons absorption.

Figure 5.1 shows the photocurrent spectra of QW20 from the STC-3X devices taken with no filters and two types of filters stated above. A measurement using the 715nm filter was also done for GaAs device for comparison. For this measurement, 200 μm -sized cells are used for all the devices because it has the biggest active window. Since the objective lens used in this experiment has a focused spot size of $\sim 1\text{mm}$ by 2mm , only a fraction of the incident beam is illuminating the cell mesa window. The power of illuminated light can be estimated as explained in Section 3.5. For the measurement of QW20 without filter, it is shown that the photocurrent spectrum is continuously high, including after the energy bandgap of QW20. Four parts can be seen from the spectrum indicating the carriers are created at different regions; (1) AlGaAs cladding layer, (2) GaAs barriers, (3) GaAsBi quantum wells and (4) second order photons absorption.

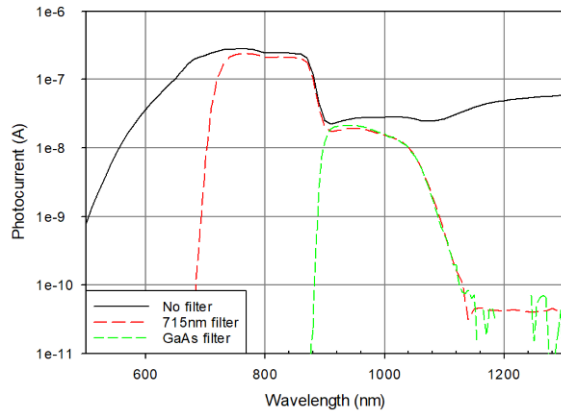
At the lower range wavelength at about 500-650 nm, a shoulder can be seen suggesting absorption in the AlGaAs cladding layer. This agrees with the AlGaAs with 30% aluminium bandgap, which has cut-off wavelength of 674 nm at room temperature.[4] The middle part of

the spectrum ranging between 680 nm and 880 nm is the photocurrent created due to GaAs barriers. Then, the spectrum range from 880 nm to 1,100 nm is the photocurrent from GaAsBi quantum wells and some of the second order diffraction light from the monochromator. After about 1,100 nm, the spectrum goes up again suggesting the second order diffraction light is absorbed by the device. This means that the photon absorption from the second order diffraction (of wavelength of 550 nm onwards) from the monochromator is the cause of carrier excitation and photocurrent seen from the device. It is unlikely that the photocurrent is due to the near infrared wavelengths because the bandgap of QW20 reported from PL measurement is 1,060 nm.[5]

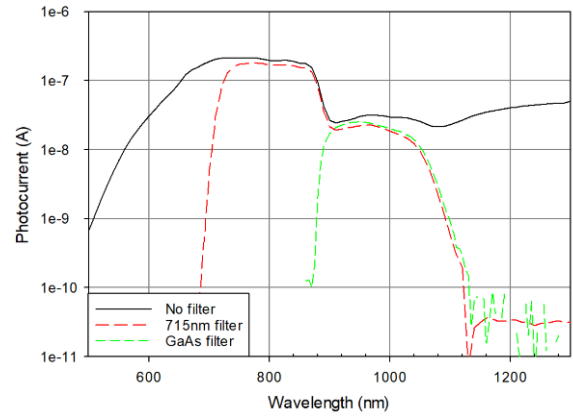
Next, a 715 nm long pass filter is used to measure the photocurrent of QW20. The aim of using this filter is to eliminate the second order diffraction. This is also to exclude the light absorption from the AlGaAs cladding layer. No photon absorption and associated carrier creation from the wavelengths below 715 nm. The spectrum shown consists of the photocurrent from the i-region only which contains GaAs barriers and GaAsBi quantum wells. A similar measurement was done on a GaAs device with the same filter. It is also clear that the GaAs photocurrent cuts off at its band edge around 873 nm. Therefore, it is confirmed that the photocurrents created with the use of a 715 nm filter arise from the specified wavelengths to about 1,300 nm without any interference.

After that, a photocurrent measurement was performed using a GaAs filter. The filter used was a double side polished un-doped GaAs wafer. The main reason for using this filter is to collect photocurrent due to the quantum wells only. Any wavelength below 873 nm did not contribute towards the total photocurrent value. The photocurrent roll-off of QW20 for both filters is similar in gradient showing that the cut-off wavelength of this device is independent of the filter. It is expected to see a very small photocurrent beyond the bandgap. Nevertheless, the photocurrent after the bandgap wavelength can still be measured down to almost three orders of magnitude (~tenth of pA).

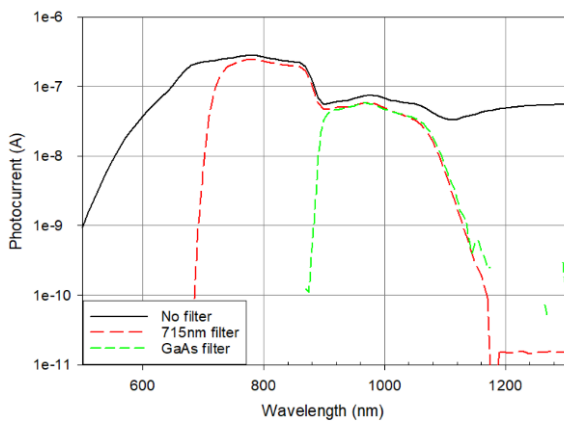
Figure 5.2 shows the photocurrent measurements for the rest of the STC-3X devices taken with no filter, the 715 nm filter and the GaAs filter. Larger-sized images are placed in Appendix F. From Figure 5.2 (a) to (f), it is shown that the spectra all agree with the discussion above.



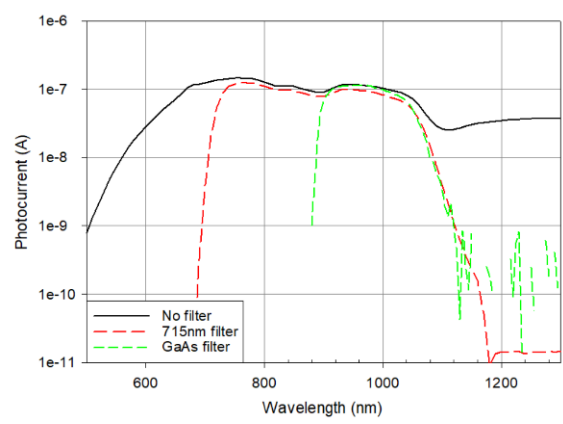
(a) QW03



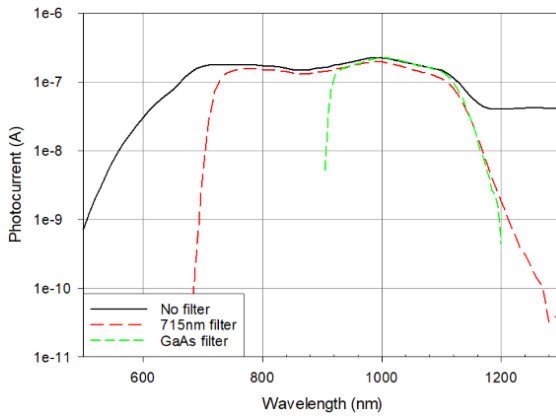
(b) QW05



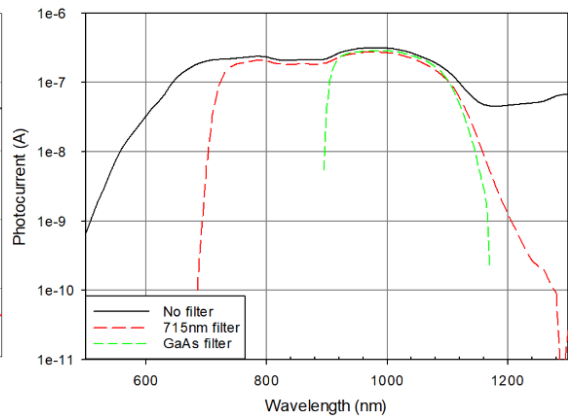
(c) QW10



(d) QW40



(e) QW54



(f) QW63

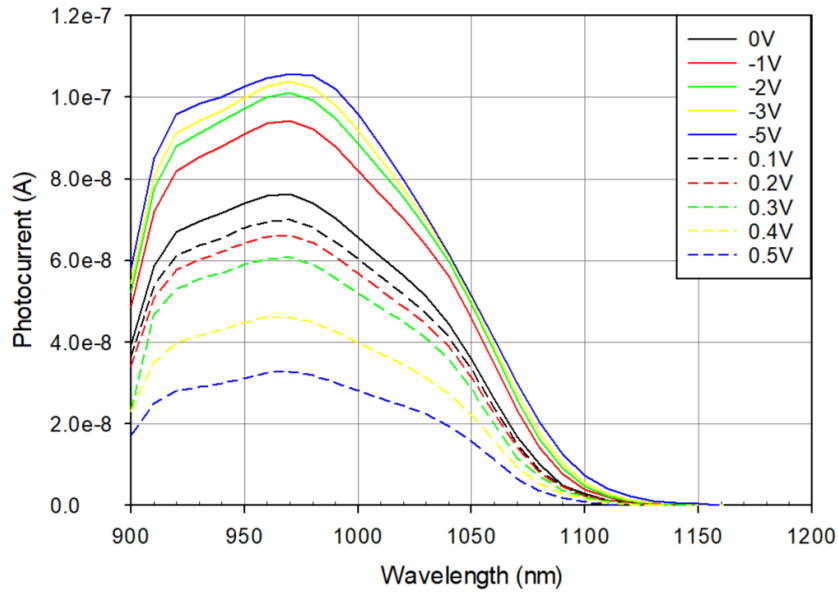
Figure 5.2: Photocurrent spectra of STC-3X devices taken at 0V with no/different filter(s) used.

In conclusion, it is important that careful measurements are taken to allow high accuracy in determining the device quality for future development. This is also to allow accurate bandgap measurements to be determined from the cut-off wavelength of the photocurrent. All photocurrent data shown after this used the GaAs filter to aid with the understanding of the Bi-based material system at a longer wavelength range.

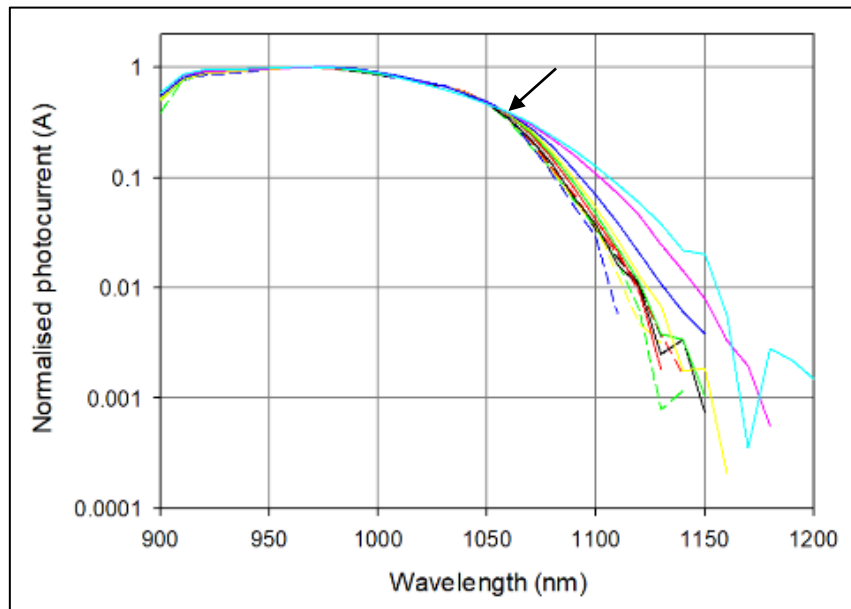
5.2.2 Photocurrent measurements

Firstly, photocurrent measurements were taken at zero bias to study the photocurrent created in the presence of the built-in voltage only. Then, a low reverse bias was applied to ensure full depletion of the i-region. Slight forward biases are also applied to see the effect of the forward diffusion current of the device on the total current while photocurrent measurements are taken. Careful measures need to be taken while applying the biases because dark currents may also arise and become comparable to the photocurrents during the measurement, especially at the absorption band-edge where the photocurrent drops to very low values.

Figure 5.3 shows the photocurrent data for QW20 taken at 0 V, reverse bias and slight forward bias at room temperature. Figure (a) has its y-axis plotted in linear scale and (b) is in normalised log scale, for easier comparison.



(a)



(b)

Figure 5.3: Photocurrent value at different bias for QW20 shown in (a) y-axis linear scale and (b) y-axis log scale normalised to unity. The arrow in figure (b) pointed at the pinch off of the spectra where the normalised photocurrent value is the same for all biases before the value disperse. This point indicates the cut-off wavelength of the device.

From Figure 5.3 (a), the photocurrent value for QW20 increases from the value at 0 V as reverse bias is applied until a saturation value is reached, which is at about -5 V. After about 1,000 nm, the photocurrent value starts to drop and its roll-off point is considered to be the absorption

band edge value or cut-off wavelength of the devices. About $41\pm 10\%$ carrier enhancement is seen when the bias goes from 0 to -5 V between 900-1,060 nm where the flat region is.

From Figure 5.3 (b), there is a clear pinch off (pointed with the black arrow) in the spectra at around 1,053 nm before the photocurrent spectra disperse. The wavelength where all the normalised photocurrents are the same before the cross-over denotes the energy bandgap value of QW20 and its value agrees with the room temperature PL peak emission reported with ± 10 nm difference.[6] The roll-off of the photocurrent after the band edge is the same for zero bias and when forward bias is applied except at 0.5 V where the roll-off deviates from the rest. The absorption after band edge is related to the tail states of the material and will be discussed later in this section.

The main cause for the incomplete carrier extraction at zero bias is carrier trapping in the wells. This incomplete extraction process from GaAsBi based devices also has been seen by Zhou et. al.[7] A similar case has been previously shown for GaInNAs/GaAs MQW p-i-n structures where electrons are trapped in the wells.[8] For GaAsBi based material, as opposed to N, the bandgap reduction of GaAs due to Bi incorporation is due to a raising of the valence band energy.[9, 10] Therefore, it is suggested that holes are being trapped in the wells instead of electrons. When a reverse bias is applied, the potential profile of the well changes. This allows the trapped carriers at the ground state of the well to escape with less energy. One method that could mitigate this is alloying the GaAsBi with In or N, so that the total band offset could be reduced to avoid carrier trapping in the material.

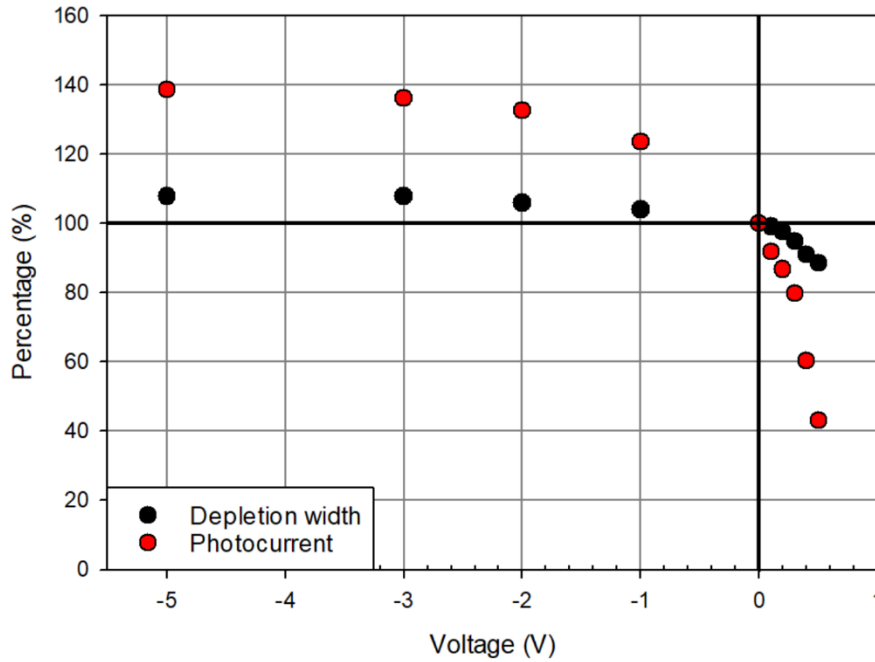


Figure 5.4: Percentage change in depletion width and photocurrent of QW20 relative to zero bias. The photocurrent value is taken from the spectrum peak at 970nm.

Figure 5.4 shows the data of the depletion width of QW20 at different voltages taken from its C-V measurements, compared with the bias dependent photocurrent value taken at 980nm. Both data sets are normalised to 100% at 0 V. From the graph, it is seen that both parameters increase in reverse bias and reduction in forward bias. From the C-V data, there is a small contribution from the increase in depletion width, about 4% increment when reverse bias is applied at -5 V. Meanwhile, from zero bias to -5 V, an increase in photocurrent of more than 40% can be seen. Therefore, it is likely that the increase in photocurrent with reverse bias is due to trapped carriers escaping with the aid of the electric field and not from the undepleted i-region of the device.

When a slight forward bias is applied, the photocurrent drops dramatically. The high dark current in the device dominates the total current and suppresses the photocurrent created in the i-region as forward bias is applied. As a result, photocurrent measurements cannot be conducted accurately unless a very high value resistor is used to suppress the dark current.

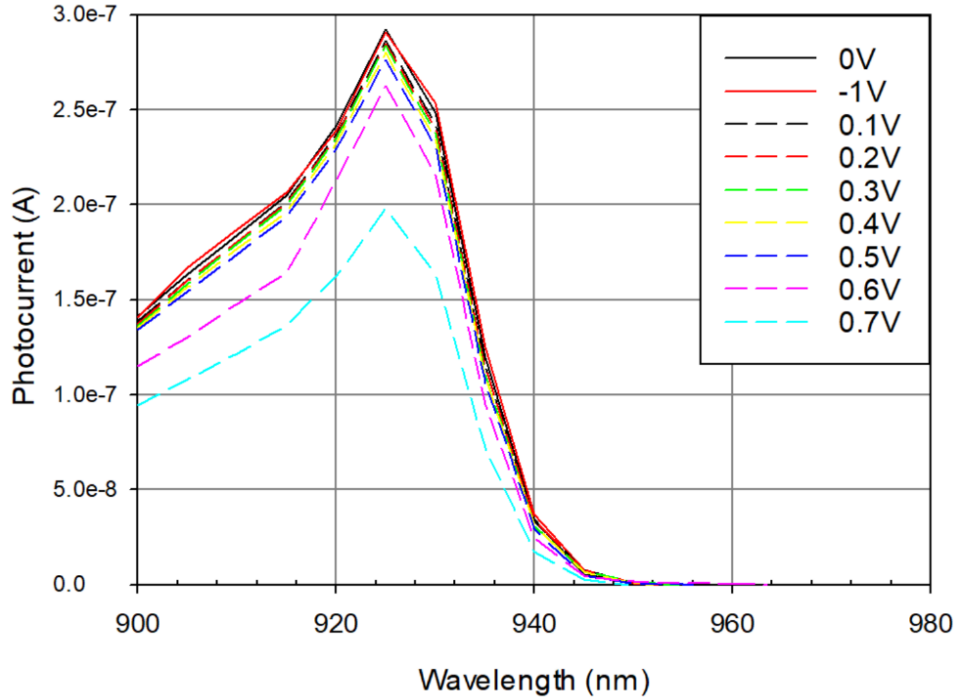
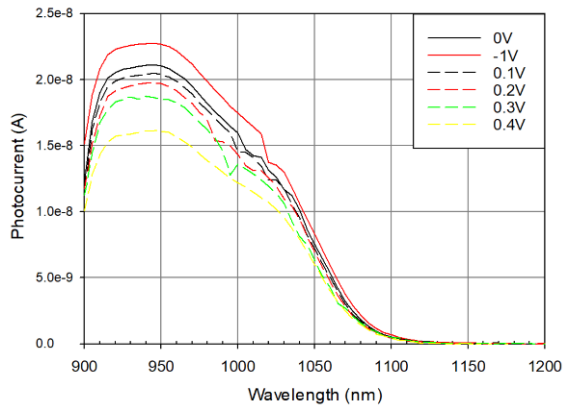


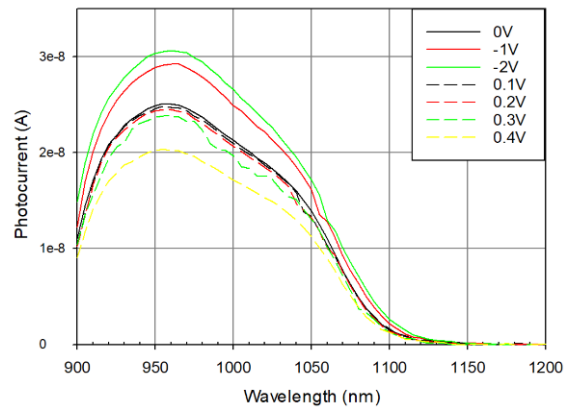
Figure 5.5: Photocurrent measurements of QT1879 at different biases.

For comparison, Figure 5.5 shows the zero, forward and reverse-biased photocurrent measurements taken on QT1879. It is seen that as a reverse bias is applied, the photocurrent value remains unchanged and complete carrier extraction is observed at 0 V. A reverse bias does not enhance the value of the photocurrent as no carriers are trapped in the wells. The drop in the photocurrent value in forward bias is also very small and can only be seen after 0.5 V, compared to QW20 here it is seen as soon as forward bias is applied. This is due to the lower forward dark current in this device and it allows constant generation of photocurrent at forward bias. This is consistent with other high quality MQW system such as GaAs/AlGaAs MQWs.[11].

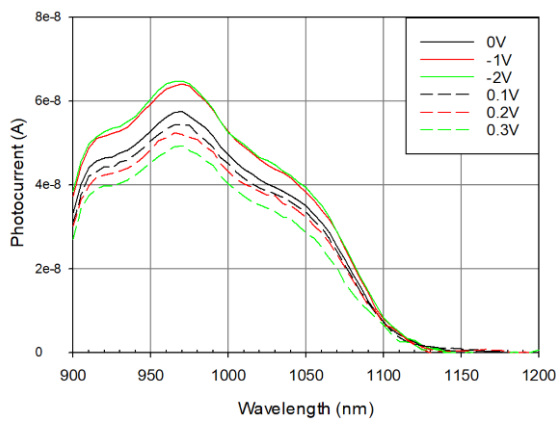
Photocurrent measurements taken for other STC-3X devices are shown in Figure 5.6. They all show a similar trend, with reverse bias needed to extract more carriers and slight forward bias causing a drop in photocurrent collection in the devices. The full-sized figures are placed in Appendix G.



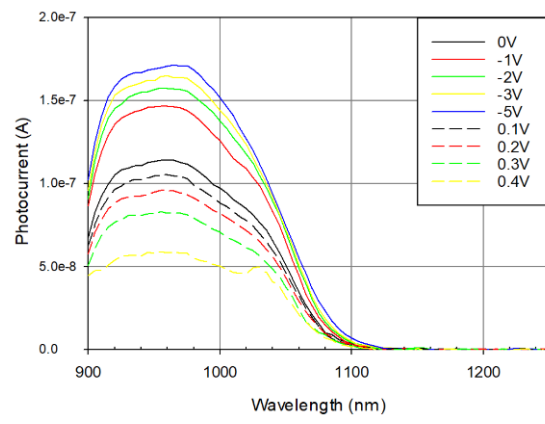
(a) QW03



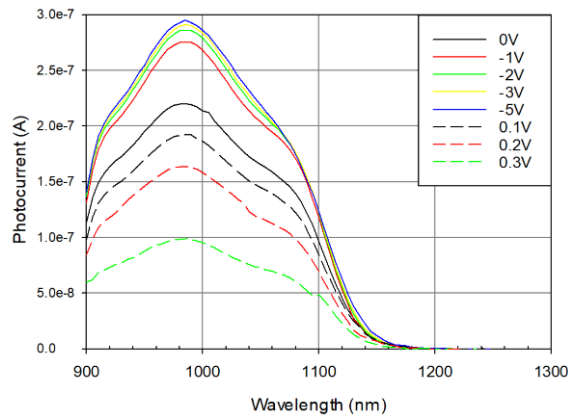
(b) QW05



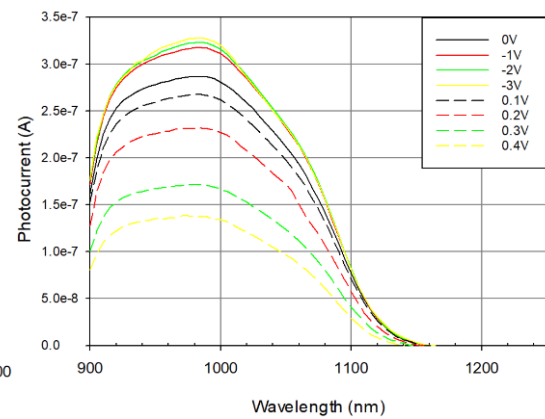
(c) QW10



(d) QW40



(e) QW54



(f) QW63

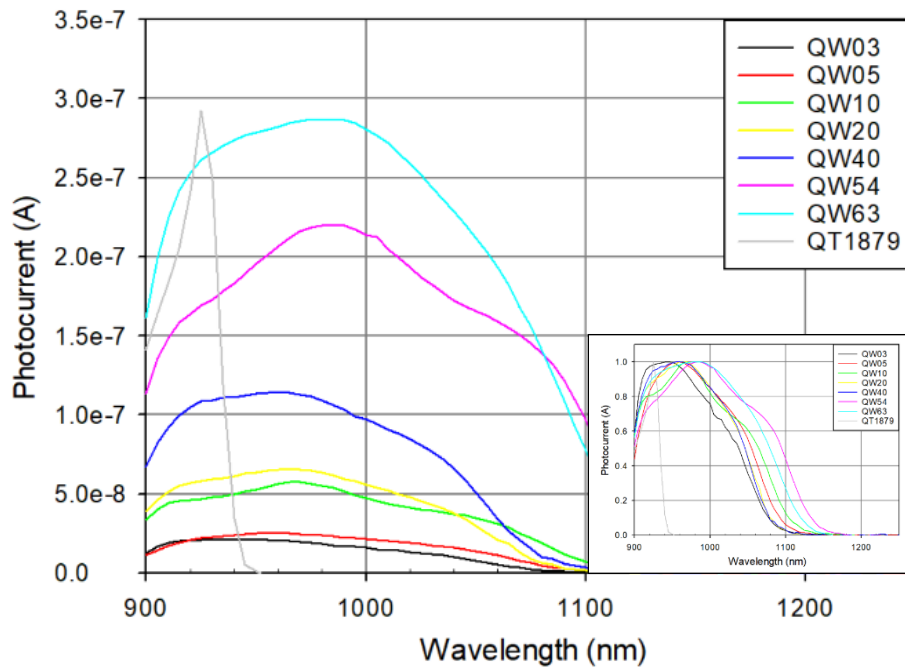
Figure 5.6: Photocurrent spectra at different biases for the rest of STC-3X devices. Different peaks seen from the photocurrent spectra are coming from the monochromator system response and they disappear after system response correction.

Different maximum reverse voltage are applied to the STC-3X devices to saturate the current collection, as shown in Table 5.1 together with the carrier enhancement percentages after that voltage is applied,

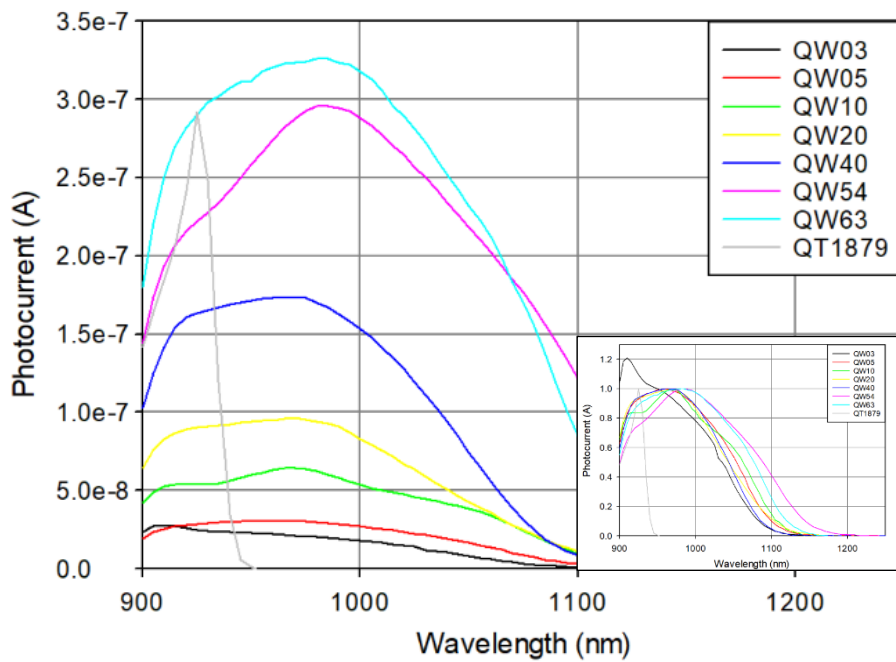
Device	QW03	QW05	QW10	QW20	QW40	QW54	QW63
Maximum reverse voltage (V)	-1	-2	-2	-5	-5	-5	-3
Carrier enhancement (%)	9.7	21.6	12.4	41.2	52.2	34.5	13.6
Estimated pinch-off wavelength (± 10 nm)	1040	1046	1080	1057	1048	1100	1096

Table 5.1: Maximum reverse voltage and carrier enhancement percentages for each of the STC-3X devices for maximum photocurrent collection.

Various reverse voltages are needed to enhance carrier collection in the devices, ranging between -1 V and -5 V. The photocurrent value in each device can increase up to roughly ~50% when bias is applied. The results are validated by data taken from Imperial College London, showing similar percentages.[12]



(a)



(b)

Figure 5.7: Photocurrent spectra for STC-3X devices and QT1879 at (a) 0V and (b) reverse voltage applied for maximum photocurrent collection. The inset is the normalised intensity of the photocurrent for roll-off comparison of photocurrent near its band edge.

Figure 5.7 (a) and (b) shows the photocurrent value for all STC-3X and QT1879 devices with respect to wavelength taken at zero bias and reverse bias for maximum photocurrent collection, respectively. Compared to figure (a), all devices in figure (b), except QT1879 show an increase in photocurrent suggesting more collection of current for STC-3X devices when carriers are aided by potential energy in escaping the wells.

It is seen that for the STC-3X devices, as the number of wells increases, the photocurrent value also increases. For QW03 – QW40, a similar roll off is seen showing that they share an absorption edge at $\sim 1,107$ nm (1.12eV). Meanwhile, QW54 and QW63 they show an absorption edge at about 1,180 nm (1.05eV). The red-shift that occurs from strained to strain-relaxed devices is fairly consistent between the photocurrent and room temperature PL data with a redshift of 69meV and 64meV for photocurrent and PL, respectively. The bandgap reduction is probably mainly caused by the loss of compressive strain in the structure. Besides that, the thinner barriers in QW54 and QW63 may allow the formation of mini-bands and at the same time could not maintain the effective quantum confinement causing a longer wavelength absorption. Photocurrent of QT1879 is showing limitation in its absorption edge at about 930 nm ($E_g = 1.33$ eV) due to its bandgap value.

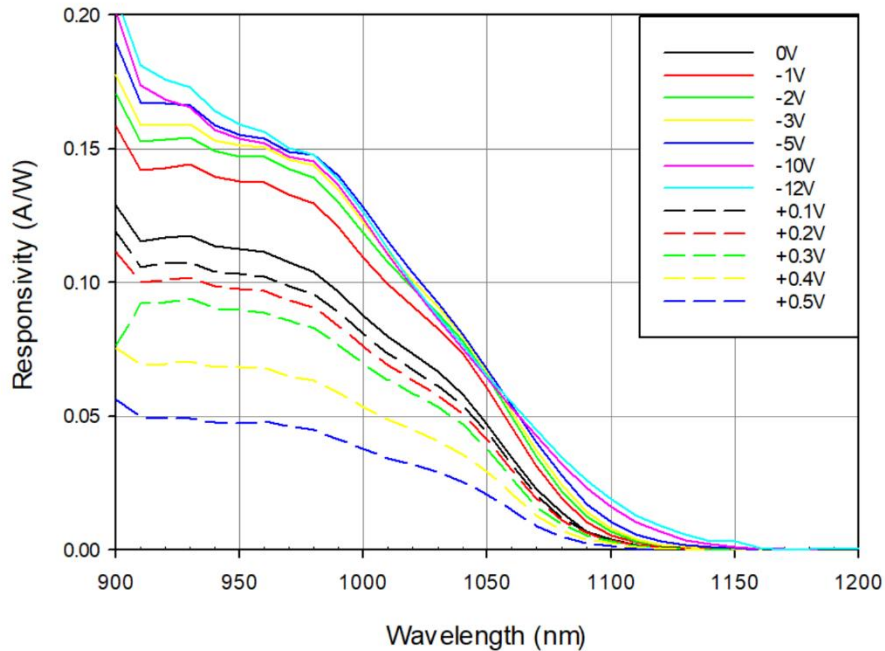


Figure 5.8: Responsivity spectra for QW20 at different biases.

From the photocurrent value and responsivity, R shown in Figure 5.8, the quantum efficiency can be calculated too. External quantum efficiency, EQE is another metric of detection efficiency of the devices and it is the ratio of the number of charge carriers produced from an incident photon.

$$EQE = R \times \frac{hc}{\lambda q} \quad (\text{Equation 5.1})$$

where h is Planck's constant, c is the speed of light, q is the electron charge and λ is the wavelength of the incident photon. Practically, it is not possible to achieve a unity in quantum efficiency value due to internal defect-caused phenomena such as surface recombination and minority carrier recombination. The EQE value can be improved by extending the depletion region of the device, thus increasing the number of swept carriers by the electric field and decreasing the recombination rate. The value can also be enhanced by including a layer of anti-reflection coating during the fabrication process. This is to reduce the reflection of the incident light at the device-air interface and maximise the photon absorption by the device. The absorption of light has been briefly mentioned in Section 2.3.1. Here, to determine the amount of light absorbed by a material as a function of material thickness, the Beer-Lambert law is applied, assuming that light reflection is negligible.[13] It can be described as,

$$A = A_0 \exp(-\alpha x) \quad (\text{Equation 5.2})$$

where A is the intensity of light after passing through the absorbing material, A_0 is the intensity of light incident on the material, α is the material absorption coefficient and x is the thickness of the material. Assuming that the value of $x = 1/\alpha$, the light intensity that get through the material is decreased by $1/e$, about ~63% from the number of absorbed photons. The EQE of a material is also related to the value of α by the equation,

$$EQE = (1 - R_p)[1 - \exp(-\alpha W)] \quad (\text{Equation 5.3})$$

where R_p is the reflection coefficient of a material and this value is considered while calculating the EQE due to a fraction of light that has been reflected from the sample surface. The value can be deduced by using Fresnel equation where the equation is able to describe the ratio of the reflected and transmitted incident light at the interface between two different media; in this case, between the air and the surface of the material as shown in Figure 5.9.

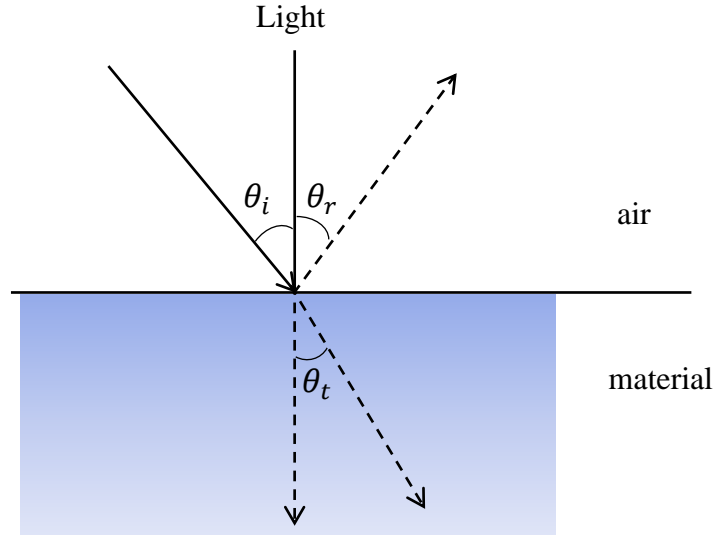


Figure 5.9: Transmission of light mechanism between air and material interface including the angle of incident, reflection and transmission.

From Equation 5.4, n_1 and n_2 are the refractive indices of first and second media, respectively, θ_i is the angle of incidence, θ_t is the angle of transmission and θ_r is the angle of reflection.

$$R_p = \left| \frac{n_1 \cos \theta_t - n_2 \cos \theta_i}{n_1 \cos \theta_t + n_2 \cos \theta_i} \right|^2 \quad (\text{Equation 5.4})$$

For interfaces between the surface of the device and the air, value of R_p can be simplified into Equation 5.5 assuming that both the incidence and transmission angles are normal to the surface of material ($\theta_i = \theta_t = 0^\circ$) and the refractive index of air is 1,

$$R_p = \left| \frac{1-n}{1+n} \right|^2 \quad (\text{Equation 5.5})$$

where n is the refractive index of the material. Note that value of n varies with wavelength and temperature. For example, at 300 K, n of GaAs at 885 nm and 1,064 nm are 3.6 and 3.48, respectively and the value of n for the same wavelengths stated reduce to 3.54 and 3.43, respectively at 103 K.[14] There is a report on value of n for GaAsBi with Bi percentage between 0 to 2.6% only and no report on value of n for Bi \geq 3% yet.[15] For this series, the value of n of GaAs from S. Adachi.[16] Rearranging Equation 5.1 and 5.3 into Equation 5.6, value of α can be obtained, 1 ----

$$\alpha = (-1/w) \ln \left[1 - \frac{Rhc}{(1 - R_p)\lambda q} \right] \quad (\text{Equation 5.6})$$

From the responsivity data in Figure 5.8, the α values for QW20 at 0V and -5V are extracted and plotted against energy as shown in Figure 5.10. The responsivity and α values for other STC-3X devices are placed in Appendix H.

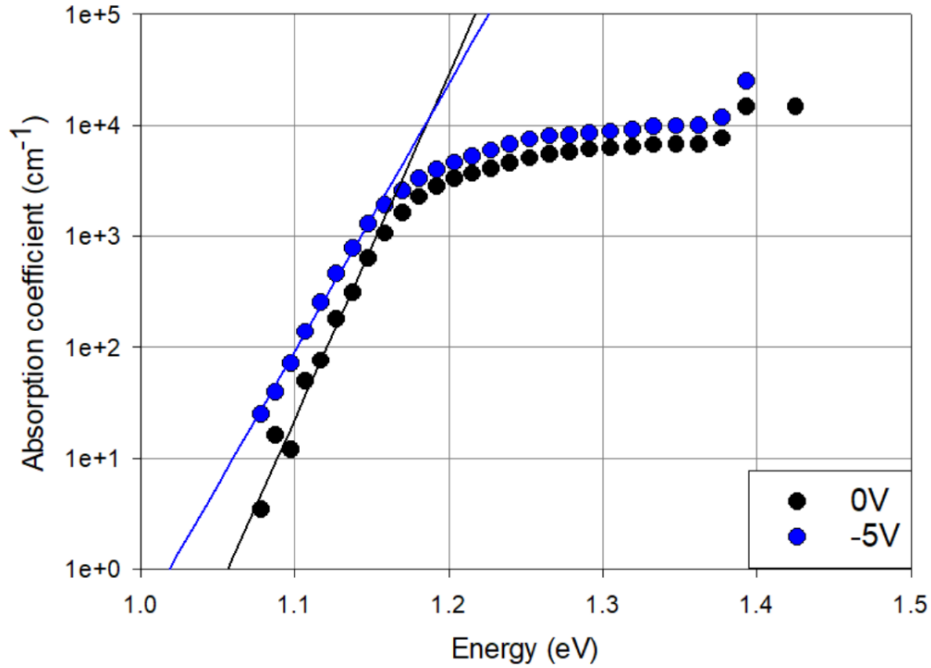


Figure 5.10: Absorption coefficients of QW20 at 0V and -5 V. The solid lines are the Urbach tails fitted to the data.

The estimated α values for QW20 shown in Figure 5.10 are plotted against energy instead of wavelength for better comparison and discussion. The room temperature absorption coefficients of QW20 at its energy bandgap taken from PL, 1.17 eV, are $1.64 \times 10^3 \text{ cm}^{-1}$ and $2.58 \times 10^3 \text{ cm}^{-1}$ for 0 V and -5 V, respectively. For the same photon energy, this device has a lower value of α compared to Ge ($\alpha = 1.45 \times 10^4 \text{ cm}^{-1}$)[17] and InGaAs ($\alpha = 2.18 \times 10^4 \text{ cm}^{-1}$).[16] Overall, the α value above the energy bandgap is within the 10^4 cm^{-1} which is within the estimated range for III-V semiconductor materials.

The exponential decay that occurs after the absorption edge can be describe by the Urbach effect and this slope is proportional to kT for temperatures above the Debye temperature.[18] It is an important characteristic because it indicates structural and/or thermal disorder in a

material system due to thermal fluctuations in the crystal lattice. Other work on Bi-based material systems have reported similar behaviour due to disorder of the material and the tail can be extended about <100 meV below the bandgap.[19-22]

The Urbach effect can be expressed as,[18, 23]

$$\alpha(h\nu) = \alpha_g \exp\left(\frac{h\nu - E_g}{E_o}\right) \quad (\text{Equation 5.7})$$

where $h\nu$ is the photon energy, α_g is the absorption coefficient when the photon energy is the same as the energy bandgap, E_g is the energy bandgap and E_o is the characteristic width of the absorption edge. The value of E_o indicates the material's state distribution caused by any of these conditions: lattice vibrations, structural disorders and impurities.

The values of E_o of QW20 fitted for 0 V and -5 V are 18 meV and 21 meV, respectively. A recent study by Kakuyama *et al.* shows that the E_o obtained is 18.4 meV, which is the same value as in this study.[24] This is expected due to the similarity in growth temperature value (380°C) and Bi percentage in the layer. The E_o values are also larger compared to the E_o of GaAs which is valued at 12.2 meV.[23] The reason for this increase may be due to the formation of Bi-clustering and increased disorder when Bi is introduced to GaAs.[25] The Urbach tailing that occurs after the band edge is consistent with the EL and PL emission after the band edge observed in other studies too.[26, 27]

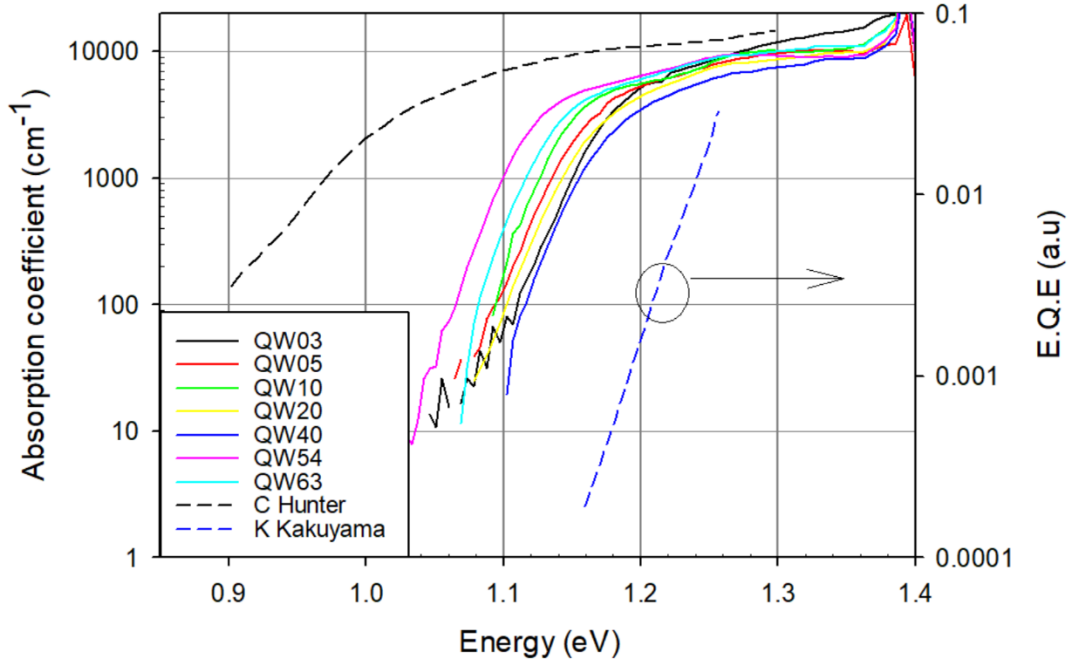


Figure 5.11: Absorption coefficients, α of STC-3X devices at 0V with comparison of α from other studies. (Data extrapolated from [24] and [28])

The α of all STC-3X devices are plotted together as shown in Figure 5.11. The results are compared with the α value from previous studies. Although the data taken from Kakuyama *et al.* is in terms of EQE , the line gradient shown in the figure is directly comparable with value of α of the devices. From the Urbach fitting, all STC-3X strained devices show as value of $E_o = 18$ meV, and the strain-relaxed devices show an E_o of 17 and 16 meV for QW54 and QW63, respectively. The calculated E_o from Hunter is slightly higher, which is 21 meV.

It is assumed that the more accurate value of α of STC-3X is from the photocurrent at 0 V, although higher extraction of carriers is obtained with reverse bias. This is due to the appearance of Franz-Keldysh electroabsorption when reverse bias is applied. This process, also known as the Franz Keldysh effect is a phenomenon where photons can be absorbed beyond the cut-off wavelength given by the bandgap when an electric field is applied.[29]

In the presence of an electric field, the electron and hole exponential wavefunctions ‘leak’ into the band-gap enabling absorption to occur at energies below the band-gap. The oscillations above the bandgap are due to the wavefunction interference. While small uncertainties may not matter in normal incidence devices where the absorption thickness is only up to a few microns thick, it can lead to significant errors in waveguide devices where the interaction

length is much longer. This effect also has been indentified in other materials such as Silicon and GaAs.[30, 31] The process can be expressed as shown in Figure 5.12.

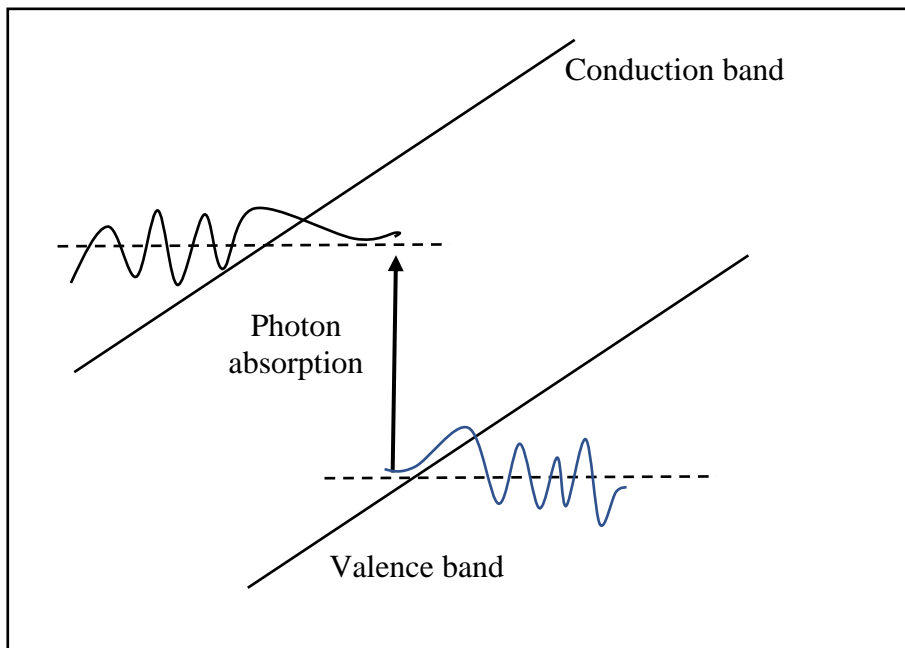


Figure 5.12: The schematic diagram of Franz-Keldysh effect in a material under applied electric field. Airy-like wavefunction is present in this effect.

Figure 5.13 shows the α for QW20 with bias from 0V to -5 V. The increase in α at 1.15 eV as a bias is applied are extracted and plotted in Figure 5.14. This photon energy is chosen due to its value being just under the bandgap of QW20. From the figure, it is confirmed that the Franz Keldysh effect is present in this material where the absorption varies with applied bias. However, this effect will not be discussed further as it is not in the area of interest for this research.

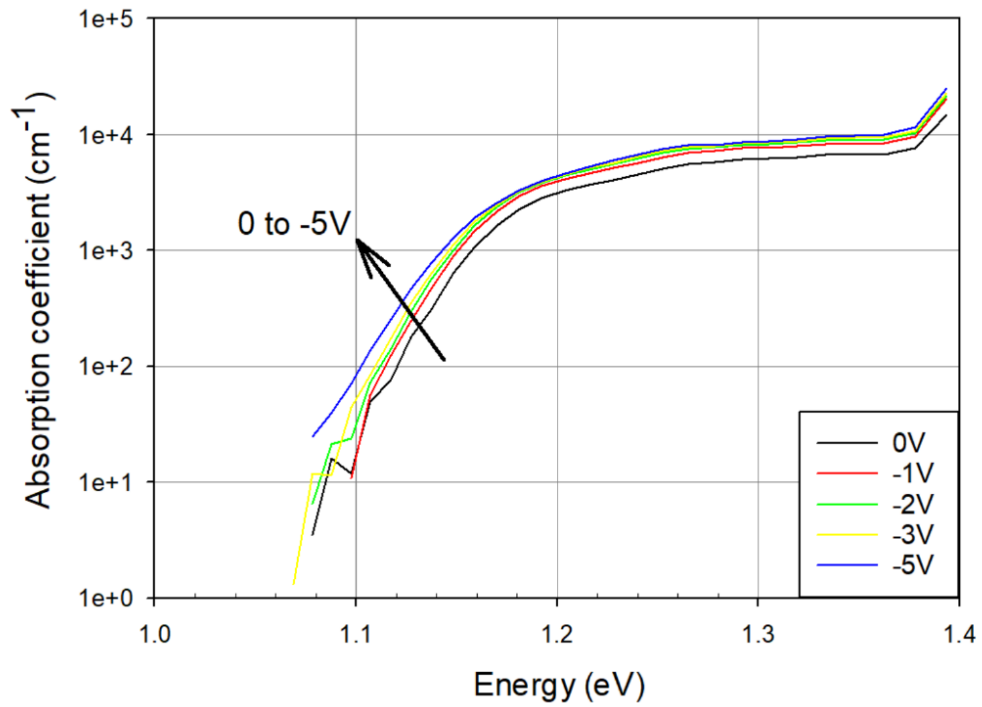


Figure 5.13: Absorption coefficients as a function of energy of QW20 at reverse biases.

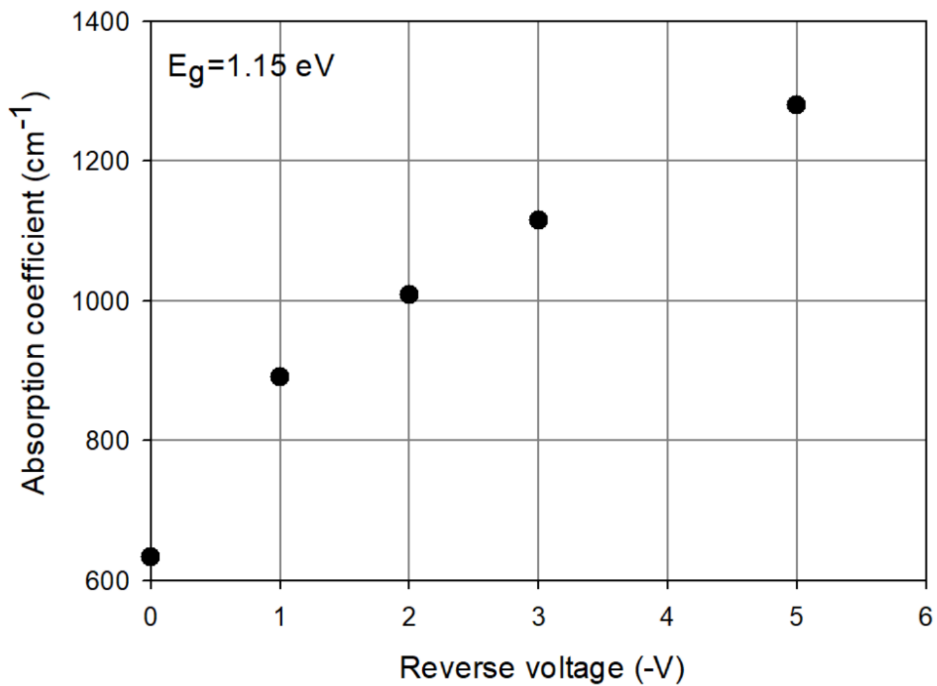


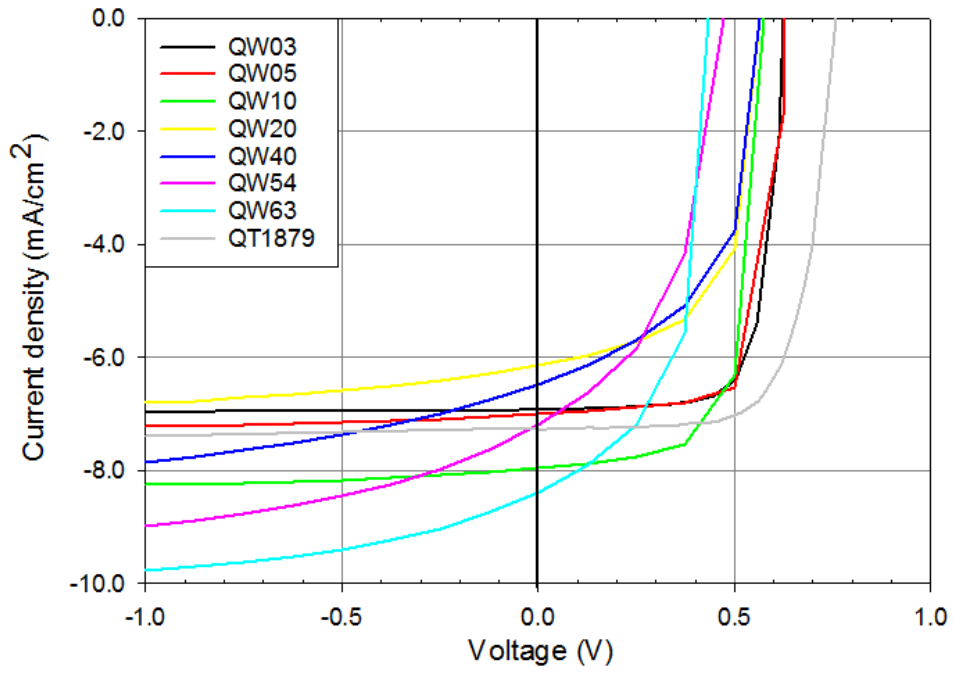
Figure 5.14: Absorption coefficients versus reverse bias for QW20 at a photon energy of 1.15 eV.

5.3 I-V under Illumination

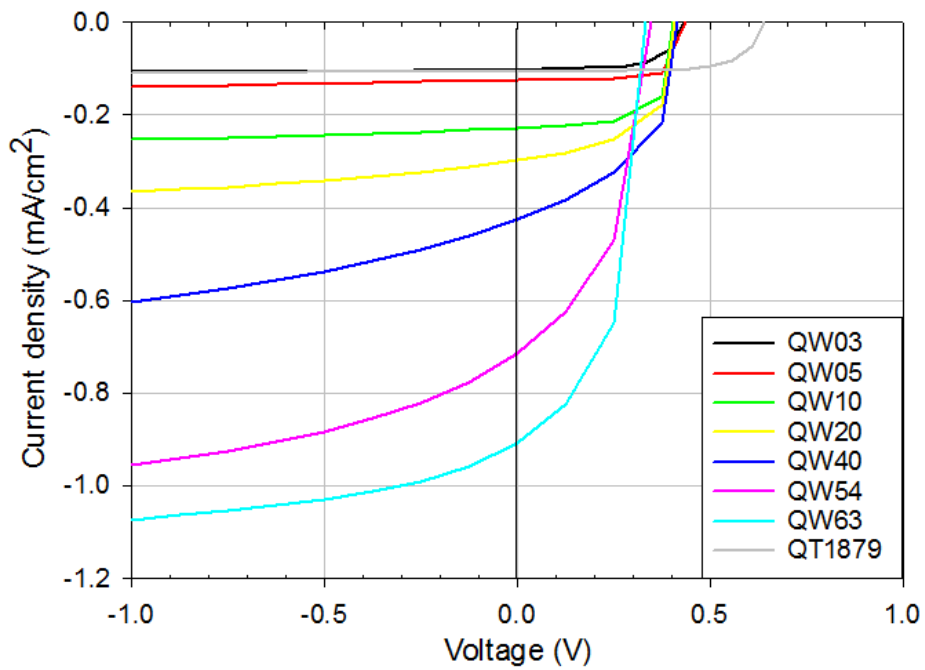
I-V under illumination for STC-3X devices and QT1879 were measured with a solar simulator as the light source. The photo-excitation in the devices is shown in the fourth I-V quadrant where there is positive bias and negative current. This is useful as it gives information about the potential for use in solar cells from its parameters; short-circuit current density, J_{SC} and open-circuit voltage, V_{OC} . J_{SC} is controlled by the quantum efficiency or absorption coefficient. This is also interrelated with the minority carrier diffusion lengths, the solar spectrum and device junction thickness. This is because the value of current collected under illumination is the sum of current created per unit wavelength integrated over the spectral range of interest at zero bias i.e the photocurrent. Meanwhile, V_{OC} is controlled by the value of J_0 , as shown by [32],

$$V_{OC} = \frac{kT}{q} \ln \left(\frac{J_{SC}}{J_0} \right) \quad (\text{Equation 5.8})$$

For this work, the light from the simulator was produced under two conditions, without filter and with an undoped GaAs wafer as a filter. The filter is placed above the device under examination to block all the wavelengths below the GaAs absorption edge from being absorbed by the device. Figure 5.15 (a) and (b) shows the I-V under illumination when no filter and GaAs filter were used, respectively. It is seen that the current collected when a GaAs filter is used are much lower compared to when measurements were done without the filter. The J_{SC} and V_{OC} values for all devices are relatively lower too. The main reason for these values reducing by almost ten times compared with the current values without filter is because all the wavelengths below 873 nm are not absorbed by the devices and not contributing to the total current collected.



(a)



(b)

Figure 5.15: I-V under illumination for STC-3X and QT1879 devices taken at room temperature, (a) without any filter and (b) with GaAs filter

From Figure 5.15 (b), the GaAsBi devices exhibit V_{OC} values between 0.40-0.45 V for the strained devices and 0.33-0.34 V for the strain-relaxed devices. Besides that, it can be seen that the J_{SC} increases as the number of wells increase. As the number of wells increases, the absorption of photons is increased and contributes to the value of J_{SC} . At reverse bias, the current densities appear to be sublinear with respect to the voltage. This suggests that poor carrier extraction causes the limitation in photocurrent collection as the number of wells increases. Although the C-V profile shows that the devices are more than 90% depleted at zero bias, there are still some carriers trapped in the wells and they require an electric field to escape. This is proven by photocurrent measurements taken at reverse bias, where higher collection of carriers is seen.

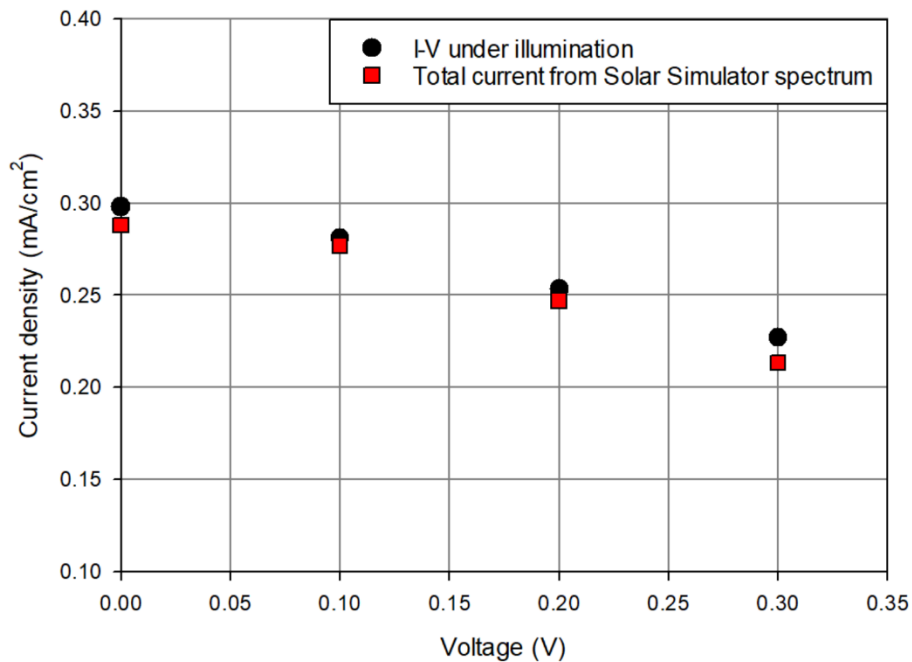


Figure 5.16: Comparison between I-V under illumination and total current calculated with the nominal solar simulator spectrum for QW20.

To validate the I-V under illumination result, the current created at each wavelength when the device absorbs the light from the solar simulator can be calculated. From the responsivity data in Figure 5.8 and the solar simulator spectrum from the equipment datasheet, the current produced is integrated as a function of wavelength and compared with the value from illuminated I-V. The solar simulator spectrum is placed in Appendix I. Figure 5.16 shows a very good agreement between the current density value extracted from Figure 5.15 (b) for QW20 at different biases compared to the total current density calculated from the responsivity

and solar simulator spectrum. The differences are less than 7% between these two data. The dark current is seen to be very low at low voltage and only becomes significant after 0.3 V. However, the photocurrent value is still dropping as the bias increases. This shows that the dark current is not causing the reduction in total current at forward bias at low voltage (as seen in Figure 5.15). If the data is interpolated, it is expected to yield a zero-photocurrent value after 0.55 V forward bias. One of the reasons for the photocurrent reduction is carriers being trapped in the deep wells or the localised states in the structures.

Another numerical expression representing the efficacy of a solar cell is its bandgap-voltage offset. This is determined by finding the difference between the bandgap voltage, (E_g/q) and the V_{OC} . Bandgap-voltage offset is a method to identify the material quality by looking at its non-ideal recombination properties. From Equation 5.8, the bandgap-voltage offset for the devices can be determined through the equations that follow,

$$J_o = qwBn_i^2 \quad (\text{Equation 5.9})$$

$$n_i^2 = N_C N_V e^{-E_g/kT} \quad (\text{Equation 5.10})$$

Where w is the thickness of the material, B is the radiative recombination coefficient, n_i is the intrinsic carrier concentration, N_C and N_V are the effective density of states in the conduction and valence bands, respectively, and other symbols have their usual meaning. This results in Equation 5.11,[33]

$$\frac{E_g}{q} - V_{OC} = \frac{kT}{q} \ln \left(\frac{qwBN_C N_V}{J_{SC}} \right) \quad (\text{Equation 5.11})$$

Due to the weak bandgap dependence of B , the offset can be treated as a constant value, and non-radiative recombination components can be estimated. A small value of offset is desired because the value indicates the closeness of the quasi-Fermi levels to the band edges. The offset value also shows the closeness of the voltage in approaching the fundamental radiative recombination limit. For a high-quality single-junction GaAs solar cell, the offset is about 0.4 V with radiative limit of 0.36 V. [33, 34]

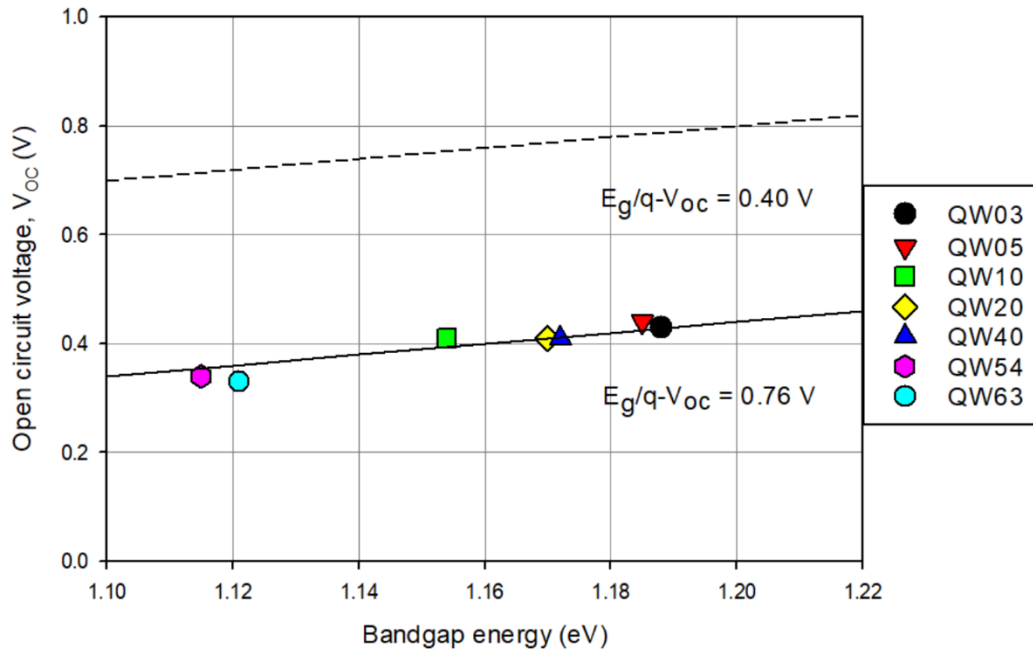


Figure 5.17: V_{OC} for all STC-3X devices with respect to its band gap energy value taken from PL. The solid line is the fitted voltage difference for STC-3X devices and the dashed line is bandgap offset limit for a high-quality single-junction GaAs solar cell, typically 0.4 V difference.[33]

From Figure 5.17, a linear dependence of V_{OC} with respect to the bandgap of the devices can be seen. The bandgap energy for the devices used in this diagram is taken from the bandgap determined from the PL peak energy.[6] The offset value is 0.76 V which is a bit higher compared to InGaAsN that has a value of ~ 0.7 V.[35] The large band offset can be related to the hole trapping in the valence band, as seen in InGaAsN where electron trapping occurs. [8, 36]

Parameter	QW03	QW05	QW10	QW20	QW40	QW54	QW63	QT1879
I_{SC} (mA/cm ²)	0.10	0.13	0.23	0.30	0.43	0.72	0.91	0.11
V_{OC} (V)	0.43	0.44	0.41	0.41	0.41	0.34	0.33	0.64
I_{max} (mA/cm ²)	0.09	0.11	0.16	0.18	0.22	0.47	0.65	0.10
V_{max} (V)	0.34	0.35	0.38	0.38	0.39	0.25	0.25	0.50
FF (%)	71	67	64	55	48	48	54	71

Table 5.2: Solar cell characteristics for all STC-3X devices and QT1879.

Table 5.2 summarises the solar cell characteristics for the STC-3X devices and QT1879. The values of I_{SC} , V_{OC} , I_{max} and V_{max} are extracted from Figure 5.15 (b) and the fill factor (FF) values are calculated. From the table, as the number of well increase, the I_{SC} value also increase. Meanwhile, the V_{OC} value are distinct between the strain-devices and strained-balanced devices where each category shows similar value. Besides that, the strained devices show a reduction in fill factor (FF) as the number of wells increases with QW03 shows a comparable value of FF to QT1879. The two strain-relaxed devices show a difference of 6% in FF value.

In summary, all the STC-3X devices show absorption of light and photocurrents are created at wavelengths longer than GaAs. The devices are divided into two categories, strained and strain-balanced devices, each category shows significant difference in dark current value and absorption properties. Although strained-balanced devices show higher dark current value, its short circuit current value are higher compared to strained-devices. If the open circuit voltage can be improved, it is expected to see higher value of fill factor indicating better solar cell performance.

A low background doping and long minority carrier diffusion length are the main keys in achieving highly efficient carrier collection in a solar cell. Although it is challenging for Bi-based material due to Bi impurities introduced to the layer, it is highly possible to produce high quality material with optimised and careful choices of growth parameters.

5.4 Summary

In this chapter, the photocurrent measurements and illuminated IV measurements were performed on the STC-3X and QT1879 devices to study the opto-electronic properties in a Bi-based material. Before real measurements were performed, preliminary checks were undertaken by using different long-pass filters when photocurrent measurements were taken. It is shown that the filters only allow the expected range of wavelengths to pass and accurate outputs are measured.

Photocurrent measurements were performed at different biases for all STC-3X and QT1879 devices. Carrier collection enhancement up to almost 53% can be seen when reverse bias is applied, while forward bias caused a reduction in carrier collection. Instead of incomplete depletion of the i-region of the devices, the carrier enhancement is expected to be caused by poor carrier extraction from the quantum wells at zero bias. The carrier trapping is the result of the large valence band offset in GaAsBi.

From the photocurrent value, the device's responsivity, QE and absorption coefficient can be deduced. Absorption coefficient values are comparable with other Bi-based studies. In addition to that, the effect of Franz Keldysh where the carriers leak into the range beyond the energy bandgap is seen in STC-3X devices. Overall, these devices demonstrate good properties and electro absorption up to its cut-off wavelength. This indicates good detectivity at the expected wavelength.

Besides that, illuminated IV measurements were performed at room temperature by using a solar simulator. Measurements without and with a GaAs filter show a large reduction in I_{SC} for devices with a low number of wells and the ratio becomes comparable at higher wells number. The bandgap offset calculated shows a high value of offset compared to GaAs and InGaAsN. This is caused by the carrier trapping specifically of holes in the valence band. The fill factors determined from the illuminated IV measurements show that the value drops as the number of wells increases. This is closely related to the strain levels that are present in the devices.

To acquire good carrier extraction and improve the absorption onset in GaAsBi based devices, growth optimisation is needed. The ongoing improvement in understanding of the growth of this material system will help GaAsBi to be competitive with existing technologies such as strained-balance InGaAs/GaAsP for device applications especially in solar cell industries.

5.5 References

- [1] P. K. Patil *et al.*, "GaAsBi/GaAs Multi-Quantum Well LED Grown by Molecular Beam Epitaxy using a Two-Substrate-Temperature Technique," *Nanotechnology*, Article vol. 28, no. 10, p. 8, Mar 2017, Art no. 105702, doi: 10.1088/1361-6528/aa596c.
- [2] S. J. Sweeney and S. R. Jin, "Bismide-Nitride Alloys: Promising for Efficient Light Emitting Devices in the Near- and Mid-Infrared," *Journal of Applied Physics*, Article vol. 113, no. 4, p. 6, Jan 2013, Art no. 043110, doi: 10.1063/1.4789624.
- [3] C. J. Hunter *et al.*, "Absorption Characteristics of GaAs_{1-x}Bi_x/GaAs Diodes in the Near-Infrared," *Ieee Photonics Technology Letters*, vol. 24, no. 23, pp. 2191-2194, Dec 1 2012, doi: 10.1109/lpt.2012.2225420.
- [4] M. Elallali, C. B. Sorensen, E. Veje, and P. Tidemandpetersson, "Experimental-Determination of the GaAs and Ga_{1-x}Al_xAs Band-Gap Energy-Dependence on Temperature and Aluminum Mole Fraction in the Direct-Band-Gap Region," *Physical Review B*, Article vol. 48, no. 7, pp. 4398-4404, Aug 1993, doi: 10.1103/PhysRevB.48.4398.
- [5] R. Richards, "Molecular Beam Epitaxy Growth and Characterisation of GaAsBi for Photovoltaic Applications," ed, September 2014.
- [6] R. Richards *et al.*, "GaAsBi MQWs for Multi-Junction Photovoltaics," *2013 Ieee 39th Photovoltaic Specialists Conference (Pvsc)*, pp. 303-305, 2013 2013.
- [7] Z. Zhou, "Optimisation of GaAsBi Based Semiconductors," ed. The university of Sheffield, March 2017.
- [8] H. M. Khalil, B. Royall, S. Mazzucato, and N. Balkan, "Photoconductivity and Photoluminescence under Bias in GaInNAs/GaAs MQW P-I-N Structures," *Nanoscale Research Letters*, vol. 7, Sep 2012, Art no. 539, doi: 10.1186/1556-276x-7-539.
- [9] A. R. Mohmad *et al.*, "Localization Effects and Band Gap of GaAsBi Alloys," *Physica Status Solidi B-Basic Solid State Physics*, Article vol. 251, no. 6, pp. 1276-1281, Jun 2014, doi: 10.1002/pssb.201350311.
- [10] R. Kudrawiec *et al.*, "Experimental and Theoretical Studies of Band Gap Alignment in GaAs_{1-x}Bi_x/GaAs Quantum Wells," *Journal of Applied Physics*, Article vol. 116, no. 23, p. 9, Dec 2014, Art no. 233508, doi: 10.1063/1.4904740.
- [11] M. Whitehead, G. Parry, K. Woodbridge, P. J. Dobson, and G. Duggan, "Experimental Confirmation of a Sum-Rule for Room-Temperature Electroabsorption in GaAs-AlGaAs Multiple Quantum Well Structures," *Applied Physics Letters*, Article vol. 52, no. 5, pp. 345-347, Feb 1988, doi: 10.1063/1.99459.
- [12] R. D. Richards *et al.*, "Photovoltaic Characterisation of GaAsBi/GaAs Multiple Quantum Well Devices," *Solar Energy Materials and Solar Cells*, Article vol. 172, pp. 238-243, Dec 2017, doi: 10.1016/j.solmat.2017.07.029.

- [13] R. W. Ricci, M. A. Ditzler, and L. P. Nestor, "Discovering the Beer-Lambert Law," *Journal of Chemical Education*, Article vol. 71, no. 11, pp. 983-985, Nov 1994, doi: 10.1021/ed071p983.
- [14] D. T. F. Marple, "Refractive Index of GaAs," *Journal of Applied Physics*, Article vol. 35, no. 4, pp. 1241-&, 1964, doi: 10.1063/1.1713601.
- [15] K. Yamashita, M. Yoshimoto, and K. Oe, "Temperature-Insensitive Refractive Index of GaAsBi Alloy for Laser Diode in WDM Optical Communication," *Physica Status Solidi C - Current Topics in Solid State Physics, Vol 3 No 3*, Proceedings Paper vol. 3, no. 3, pp. 693+, 2006, doi: 10.1002/pssc.200564110.
- [16] S. Adachi, "Optical Dispersion-Relations for GaP, GaAs, GaSb, InP, InAs, InSb, $Al_xGa_{1-x}As$, and $In_{1-x}Ga_xAs_yP_{1-y}$," *Journal of Applied Physics*, Article vol. 66, no. 12, pp. 6030-6040, Dec 1989, doi: 10.1063/1.343580.
- [17] S. M. Sze and K. K. Ng, *Physics of Semiconductor Devices*, Third Edition ed. New Jersey: John Wiley & Sons, Inc, 2007.
- [18] F. Urbach, "The Long-Wavelength Edge of Photographic Sensitivity and of the Electronic Absorption of Solids," *Physical Review*, Letter vol. 92, no. 5, pp. 1324-1324, 1953, doi: 10.1103/PhysRev.92.1324.
- [19] Z. Z. Zhou, D. F. Mendes, R. D. Richards, F. Bastiman, and J. P. R. David, "Absorption Properties of GaAsBi Based P-I-N Heterojunction Diodes," *Semiconductor Science and Technology*, Article vol. 30, no. 9, p. 6, Sep 2015, Art no. 094004, doi: 10.1088/0268-1242/30/9/094004.
- [20] C. Gogineni, N. A. Riordan, S. R. Johnson, X. F. Lu, and T. Tiedje, "Disorder and the Urbach Edge in Dilute Bismide GaAsBi," *Applied Physics Letters*, Article vol. 103, no. 4, p. 4, Jul 2013, Art no. 041110, doi: 10.1063/1.4816435.
- [21] M. Masnadi-Shirazi, R. B. Lewis, V. Bahrami-Yekta, T. Tiedje, M. Chicoine, and P. Servati, "Bandgap and Optical Absorption Edge of $GaAs_{1-x}Bi_x$ Alloys with $0 < x < 17.8\%$," *Journal of Applied Physics*, Article vol. 116, no. 22, p. 8, Dec 2014, Art no. 223506, doi: 10.1063/1.4904081.
- [22] R. D. Richards, C. J. Hunter, F. Bastiman, A. R. Mohmad, and J. P. R. David, "Telecommunication Wavelength GaAsBi Light Emitting Diodes," *Iet Optoelectronics*, Article; Proceedings Paper vol. 10, no. 2, pp. 34-38, Apr 2016, doi: 10.1049/iet-opt.2015.0051.
- [23] S. R. Johnson and T. Tiedje, "Temperature-Dependence of the Urbach Edge in GaAs," *Journal of Applied Physics*, Article vol. 78, no. 9, pp. 5609-5613, Nov 1995, doi: 10.1063/1.359683.
- [24] K. K. H. S, H. N. H, and Y. M, "Impact of a Small Change in Growth Temperature on the Tail States of GaAsBi," *Journal of Applied Physics*, 2019.
- [25] S. Imhof *et al.*, "Clustering Effects in Ga(AsBi)," *Applied Physics Letters*, Article vol. 96, no. 13, p. 3, Mar 2010, Art no. 131115, doi: 10.1063/1.3374884.

- [26] R. B. Lewis, D. A. Beaton, X. F. Lu, and T. Tiedje, "GaAs_{1-x}Bi_x Light Emitting Diodes," *Journal of Crystal Growth*, Article vol. 311, no. 7, pp. 1872-1875, Mar 2009, doi: 10.1016/j.jcrysgro.2008.11.093.
- [27] S. Francoeur, S. Tixier, E. Young, T. Tiedje, and A. Mascarenhas, "Bi Isoelectronic Impurities in GaAs," *Physical Review B*, Article vol. 77, no. 8, p. 5, Feb 2008, Art no. 085209, doi: 10.1103/PhysRevB.77.085209.
- [28] C. Hunter, "Growth and Characterization of Bulk GaAs_{1-x}Bi_x/GaAs Diodes," ed: University of Sheffield; 2014, 2014.
- [29] L. V. Keldysh, "Behavior of Non-Metallic Crystals in Strong Electric Fields," *Soviet Physics JETP-USSR*, Article vol. 6, no. 4, pp. 763-770, 1958.
- [30] B. R. Bennett and R. A. Soref, "Electrorefraction and Electroabsorption in InP, GaAs, GaSb, InAs, and InSb," *Ieee Journal of Quantum Electronics*, Article vol. 23, no. 12, pp. 2159-2166, Dec 1987, doi: 10.1109/jqe.1987.1073276.
- [31] A. Frova, P. Handler, F. A. Germano, and D. E. Aspnes, "Electro-Absorption Effects at Band Edges of Silicon and Germanium," *Physical Review*, Article vol. 145, no. 2, pp. 575-&, 1966, doi: 10.1103/PhysRev.145.575.
- [32] J. Nelson, *The Physics of Solar Cells*. Imperial College Press, 2003.
- [33] R. R. King *et al.*, "Bandgap Engineering in High-Efficiency Multijunction Concentrator Cells," in *International Conference on Solar Concentrators for the Generation of Electricity or Hydrogen*, Scottsdale, Arizona, May 2005.
- [34] K. Tanabe, D. Guimard, D. Bordel, and Y. Arakawa, "High-Efficiency InAs/GaAs Quantum Dot Solar Cells by Metalorganic Chemical Vapor Deposition," *Applied Physics Letters*, Article vol. 100, no. 19, p. 3, May 2012, Art no. 193905, doi: 10.1063/1.4714767.
- [35] L. J. J. Tan, W. M. Soong, J. P. R. David, and J. S. Ng, "Dark Current Mechanism in Bulk GaInNAs Lattice Matched to GaAs," *Ieee Transactions on Electron Devices*, Article vol. 58, no. 1, pp. 103-106, Jan 2011, doi: 10.1109/ted.2010.2086061.
- [36] D. B. Jackrel, S. R. Bank, H. B. Yuen, M. A. Wistey, and J. S. Harris, "Dilute Nitride GaInNAs and GaInNAsSb Solar Cells by Molecular Beam Epitaxy," *Journal of Applied Physics*, Article vol. 101, no. 11, p. 8, Jun 2007, Art no. 114916, doi: 10.1063/1.2744490.

Chapter 6: Conclusions and Future Work

6.1 Conclusions

In conclusions, a detailed study has been carried out to analyse the properties of a series of p-i-n GaAsBi/GaAs MQW diodes for the advancement of solar cell technology. The early chapters in this thesis explain the introductions of Sun's properties as renewable energy, the generations of solar cells and the importance of 1e V material system in a multiple-junction solar cell. Besides that, the III-V semiconductors and its lattice structure formation are discussed. Then, the application of multiple-quantum well (MQW) in a material system is explained with the effect of strains in the structure.

After that, the reports on photoluminescence characterisation, TEM and Nomarski imaging study have been summarised at the start of the result chapters. The devices were fabricated with metal contacts and have been used for electrical and opto-electronic characterisations.

From the electrical characterisations, the C-V measurements show that all MQW devices are almost fully depleted at zero bias. The doping density values in the i-region are about $\sim 10^{16}$ cm⁻³ which is within the reported range for Bi-based materials and is higher compared to other material systems. High dark current densities from I-V measurements are mainly due to dislocations arising from the increase in strain level in the higher well number structures. Another reason for the high dark current densities is the poor growth of GaAs-based in this work. Compared to the literature, the as-grown GaAs has higher dark current density. This in turn, increase the dark current when Bi is introduced to the layer. Reverse bias dark current measurements show that Poole-Frenkel emission may be the main cause for the leakage current exponential increase at reverse bias.

For opto-electronic characterisation involving photocurrent measurements and I-V under illuminations, the devices show incomplete carrier extraction at zero bias. This is due to hole trapping in the wells of the valence band. It is seen that slight reverse bias is needed to ensure complete carrier extraction for maximum photocurrent collection. Increases up to $\sim 53\%$ carrier enhancement from the MQW devices were obtained when reverse biases were applied. Besides that, the MQW devices in this study show better absorption coefficient values. In addition to that, absorption below the bandgap was observed, an effect known as the Franz-Keldysh effect. However, this effect was not further discussed. Comparing the bandgap values obtained from

PL peak and photocurrent cut-off wavelengths, it is concluded that both measurements show good agreements with each other.

Based on the results of I-V under illumination, the current produced was reduced by ten times when a GaAs filter was used. This is because the wavelengths below the GaAs absorption edgewavelength were filtered out and did not contribute to the current. The short circuit currents increase with the number of wells and open circuit voltages are similar for strained devices and dropped its value for strain-relaxed devices. Besides that, the fill factor that is accounted for the behaviour of the devices as solar cell shows decrement in value as the number of wells increase for strained devices. Meanwhile, QW63 shows a better fill factor value compared to QW54. Lastly, the bandgap offset calculated for the MQW devices show a linear dependency- of 0.76 V that is higher compared to GaAs and InGaAsN.

Overall, the introduction of bismuth into GaAs allows the extension to longer wavelength. The MQW structures also have been successfully employed up to 63 wells which is much higher than the number of wells from other study. The photocurrent collected increases as the number of wells increase too. It is seen that only devices with well number more than 40 show the strain-relaxation properties. However, the material quality of the devices is degraded due to high dark current and poor photocurrent collections at forward bias. Since the devices are neither fully strained nor fully strain-relaxed with different level of strains introduced to them, it is difficult to estimate the peak wavelength position to a high degree of accuracy. By identifying the source of dark current and improving the carrier collection components, a better-quality material with higher efficiency can be obtained.

6.2 Future Work

Several experimental works are recommended to further investigate the GaAsBi/GaAs MQW devices in this study. First, the electrical and opto-electronic temperature-dependent measurements on the devices could be performed. These include dark I-V measurements, photocurrent measurements and I-V under illumination measurements at below and above room temperatures. Low temperature dark I-V and photocurrent measurements can be done to identify operating capability and to figure out the activation energy of the material system.

For high temperature measurements, the dependency of the devices with temperature above room temperature can be used to study and investigate relevant properties for concentrator photovoltaic (CPV) applications. CPV units focus solar irradiance from a large area onto a relatively small solar cell, usually a multi-junction solar cell, reducing the impact of the solar cell cost on the total unit cost and improving the photovoltaic efficiency.[1, 2] High temperature measurements are of interest due to their matching to the CPV typical operating temperature which is about 100°C.[3]

It is also worth performing a systematic study of the atomic ordering in the material as another possible cause that could affect the material properties of GaAsBi/GaAs MQWs. This is because ordering has been observed in GaAsBi bulk layers and other standard III-V semiconductors such as GaAsSb and InAsSb.[4-6] To date, there is no report on the ordering of GaAsBi MQWs and its effect on the device performance.

A mixture of contributions toward the overall performance of GaAsBi/GaAs MQW devices include well thickness, Bi percentages and degree of strains. If these areas of interests can be developed and optimised to improve the electronic properties of GaAsBi devices, the photovoltaic performance of GaAsBi MQW will become increasingly competitive with InGaAs MQW photovoltaics especially for 1 eV junction solar cell.

6.3 References

- [1] C. Chukwuka and K. Folly, "Overview of Concentrated Photovoltaic (CPV) Cells," *Journal of Power and Energy Engineering*, 2014.
- [2] M. Yamaguchi and A. Luque, "High Efficiency and High Concentration in Photovoltaics," *Ieee Transactions on Electron Devices*, Article vol. 46, no. 10, pp. 2139-2144, Oct 1999, doi: 10.1109/16.792009.
- [3] R. R. King *et al.*, "Pathways to 40%-Efficient Concentrator Photovoltaics," presented at the 20th European Photovoltaic Solar Energy Conference and Exhibition, Barcelona, Spain, 2005.
- [4] A. G. Norman, R. France, and P. A. J., "Atomic Ordering and Phase Separation in MBE GaAs_[1-x]Bi_[x]" *J Vac Sci Technol B Microelectron Nanometer Struct Process Meas Phenom*, vol. 29, no. 03C121, 2011.
- [5] B. P. Gorman *et al.*, "Atomic Ordering-Induced Band Gap Reductions in GaAsSb Epilayers Grown by Molecular Beam Epitaxy," *Journal of Applied Physics*, Article vol. 97, no. 6, p. 7, Mar 2005, Art no. 063701, doi: 10.1063/1.1834983.
- [6] T. Y. Seong, G. R. Booker, A. G. Norman, and I. T. Ferguson, "Atomic Ordering in Molecular-Beam Epitaxial InAs_ySb_{1-y} Natural Strained-Layer Superlattices and Homogeneous Layers," *Applied Physics Letters*, Article vol. 64, no. 26, pp. 3593-3595, Jun 1994, doi: 10.1063/1.111208.

Appendices

Appendix A: FD05D Responsivity Graph

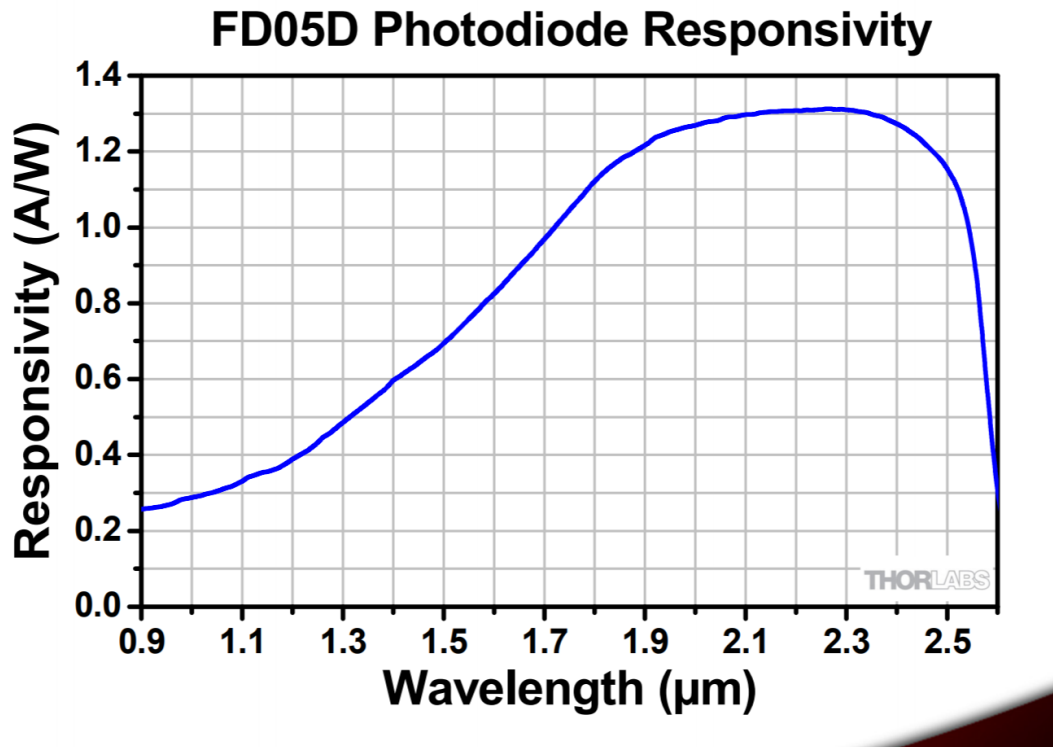
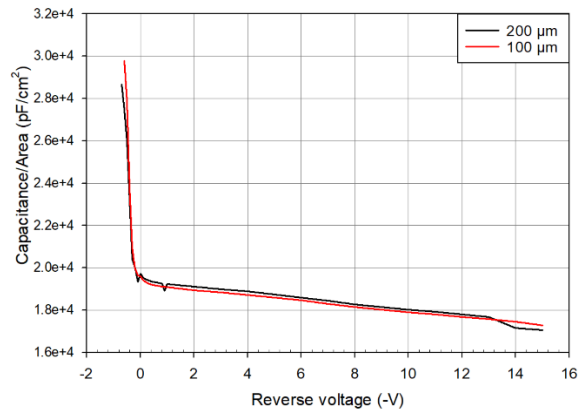
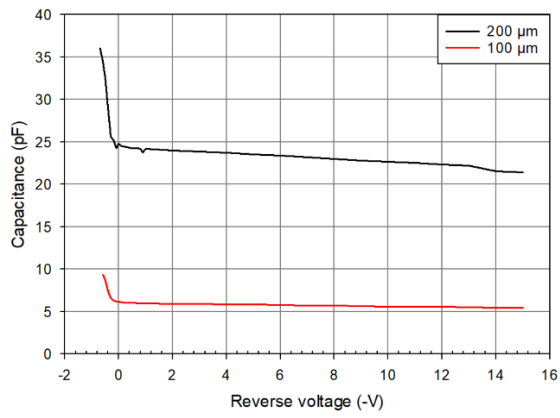


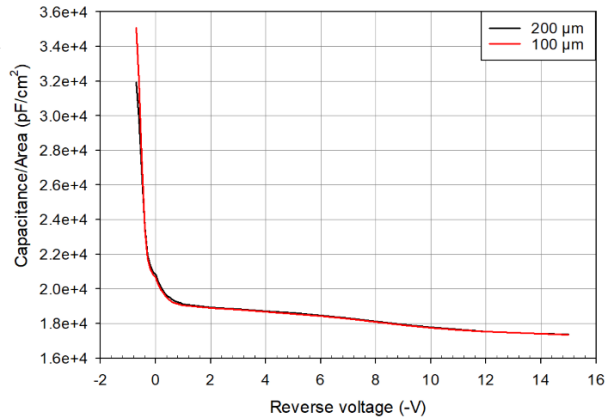
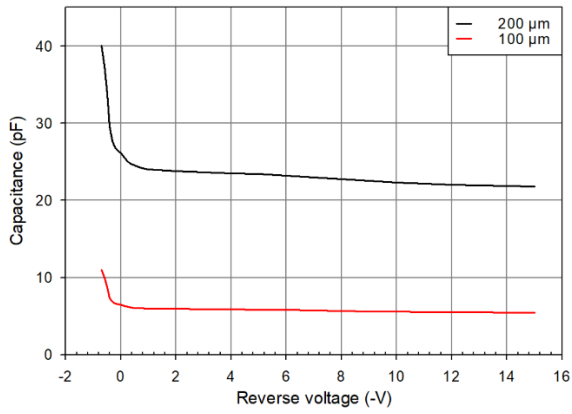
Figure A.1: The graph is taken from InGaAs FD05D specification sheet from Thorlab Inc website, Thorlab's FD05D InGaAs photodiode specification sheet numbered as TTN035395-S01, Rev D; Oct 10, 2017)

Appendix B: C-V and CA-V for STC-3X and QT1879 devices

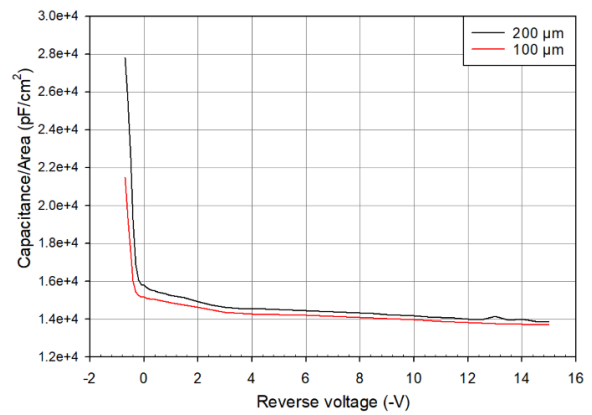
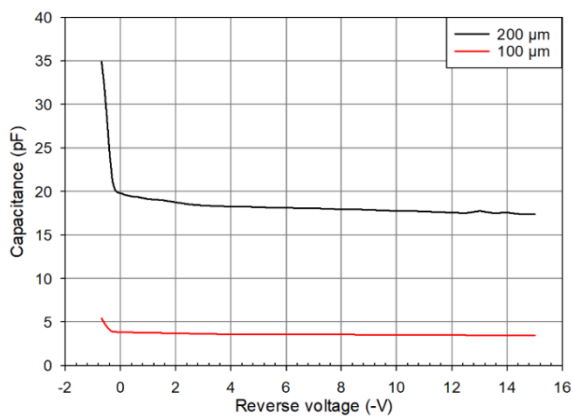
QW03



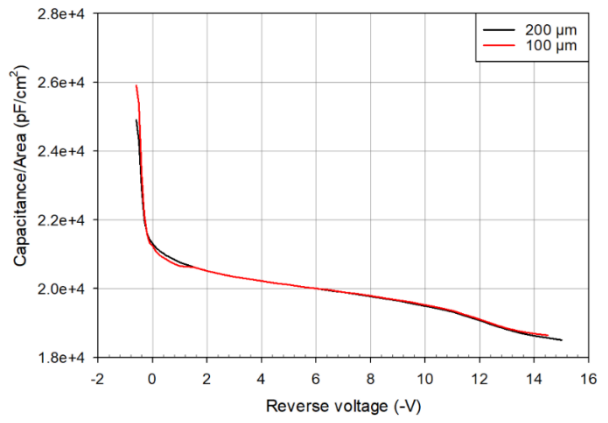
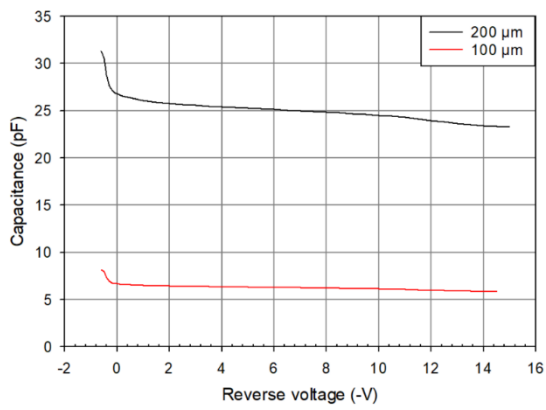
QW05



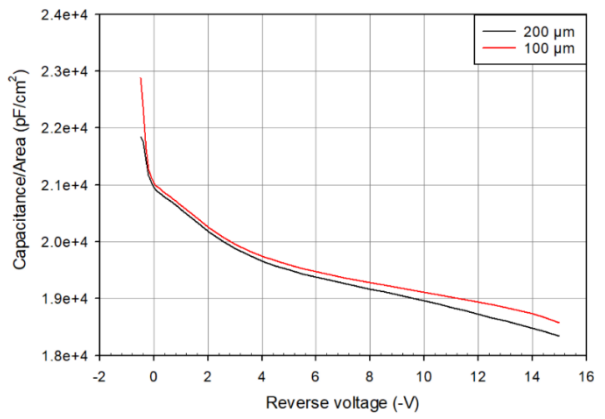
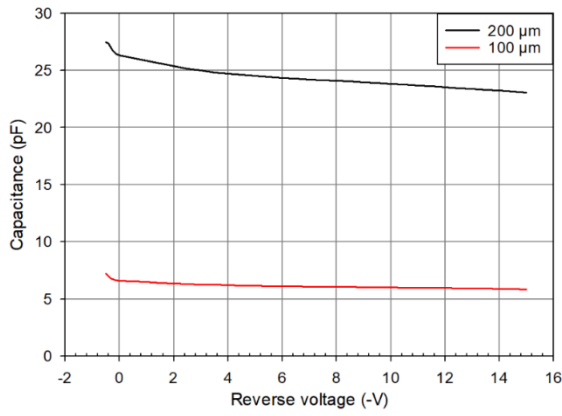
QW10



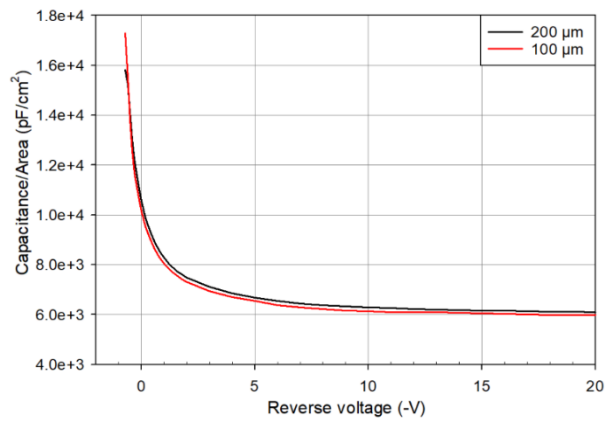
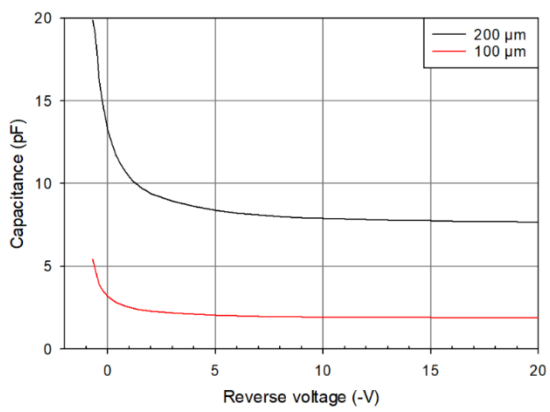
QW40



QW54

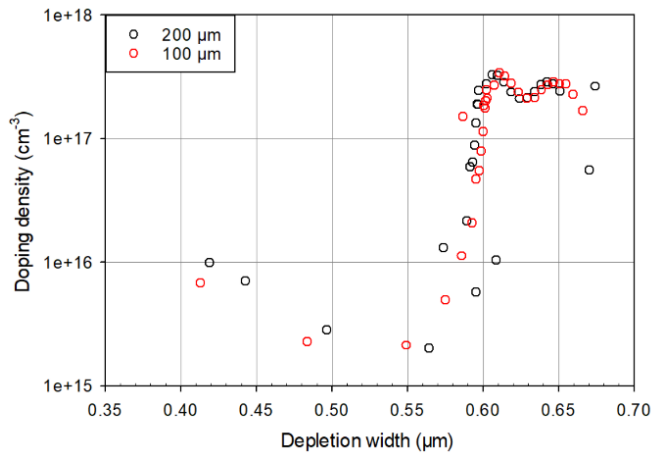


QT1879

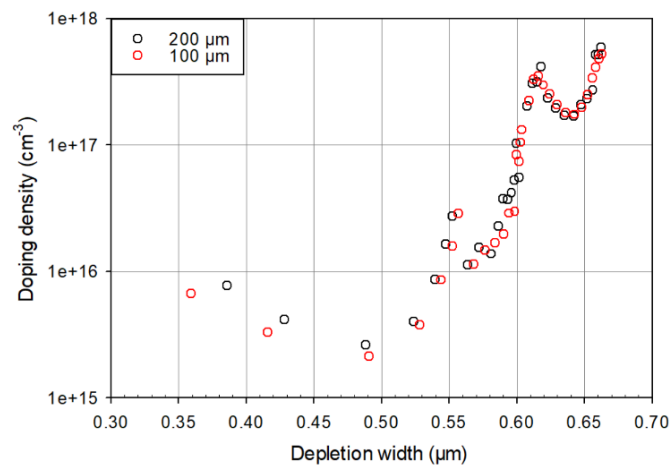


Appendix C: Doping profile for STC-3X and QT1879 devices

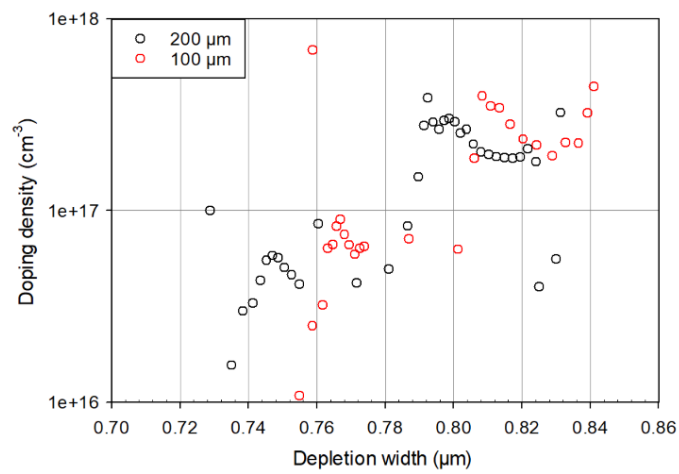
QW03



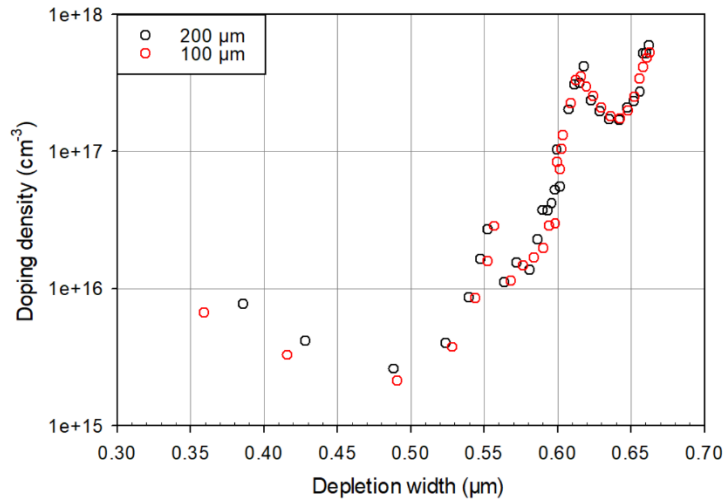
QW05



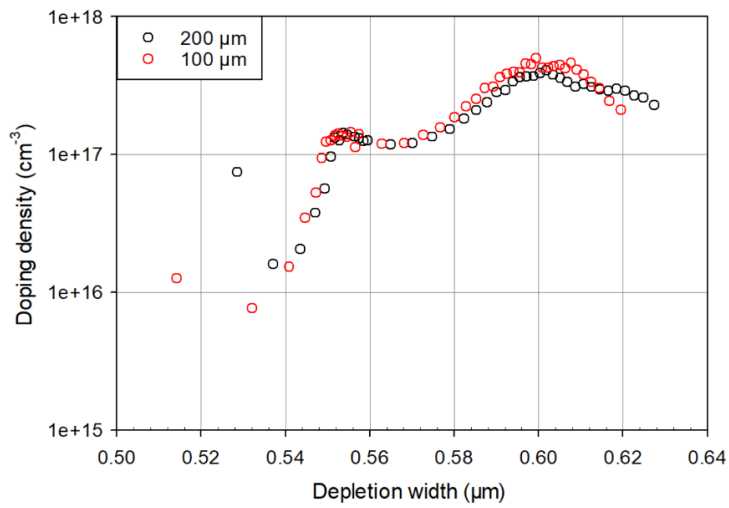
QW10



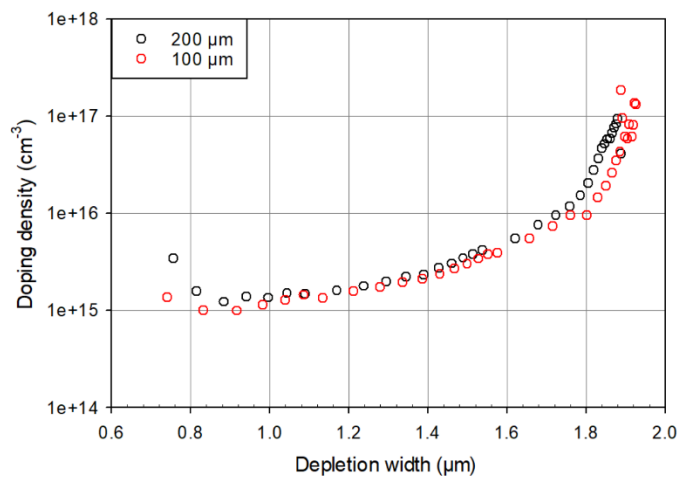
QW40



QW54

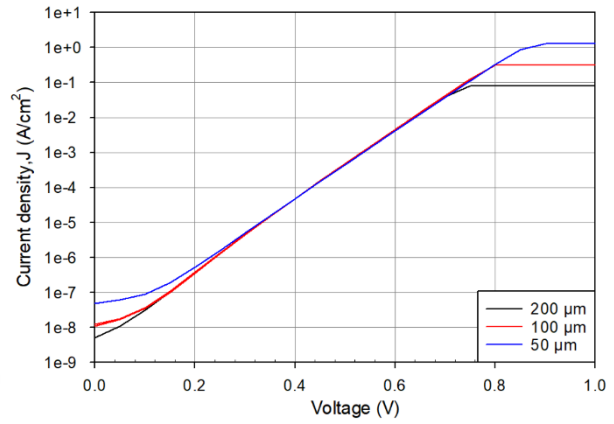
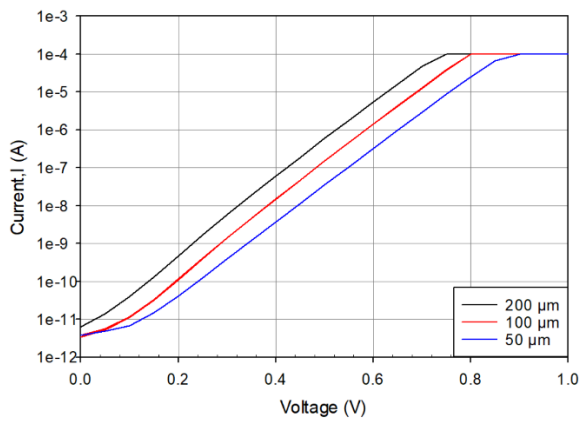


QT1879

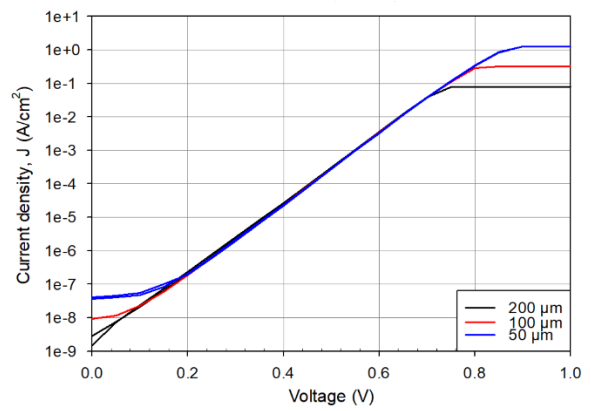
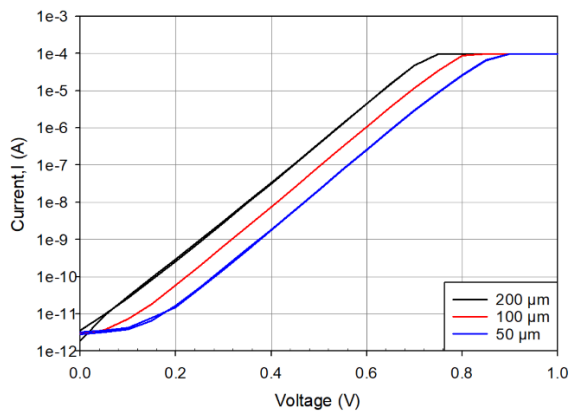


Appendix D: Forward bias I-V and J-V for STC-3X devices

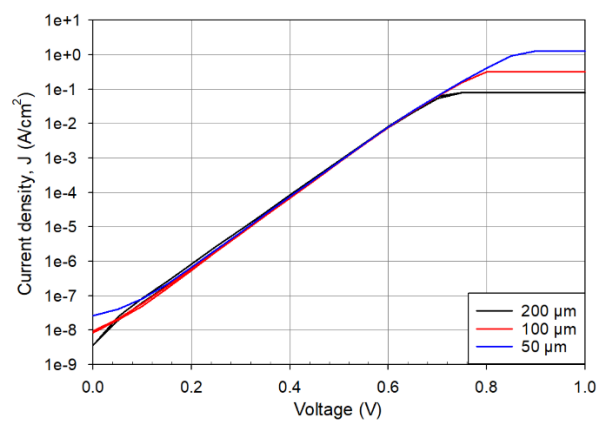
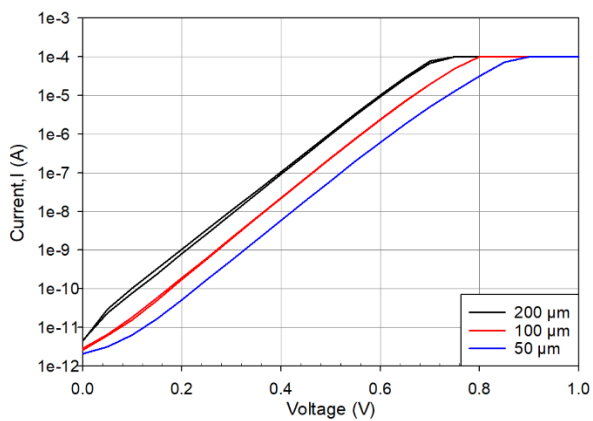
QW03



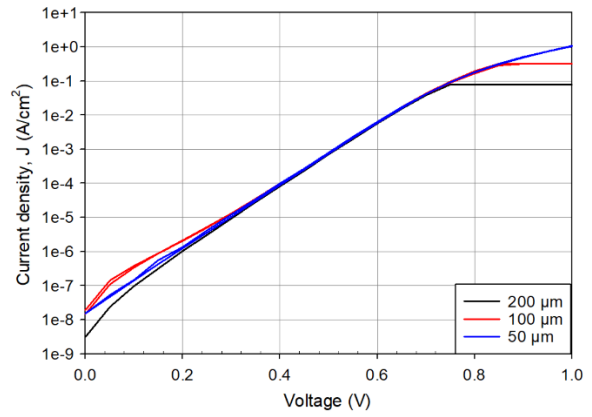
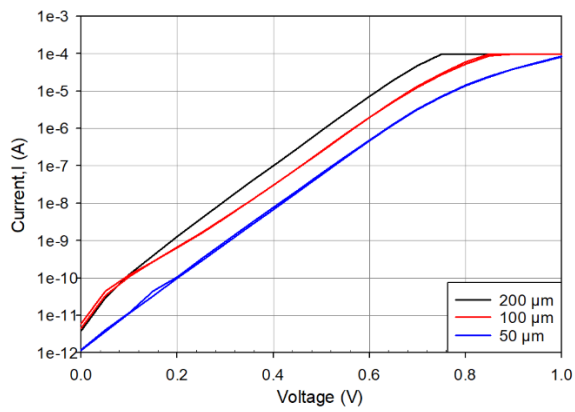
QW05



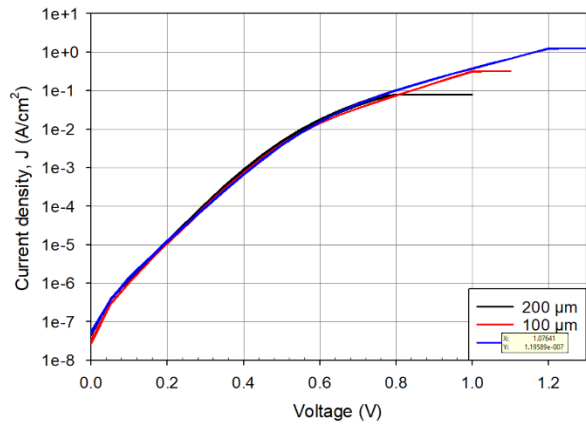
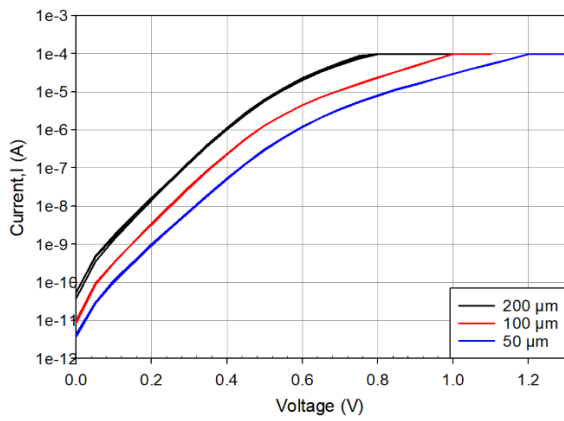
QW10



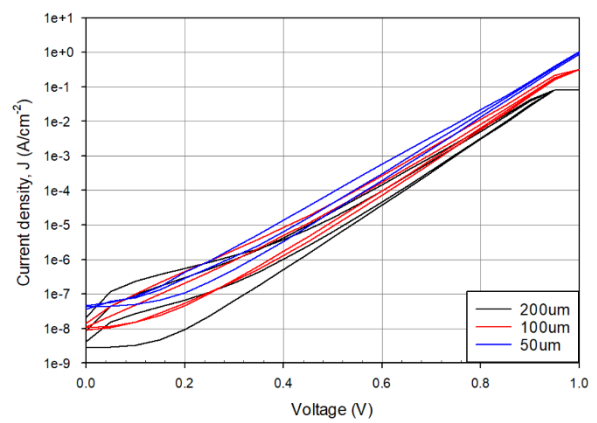
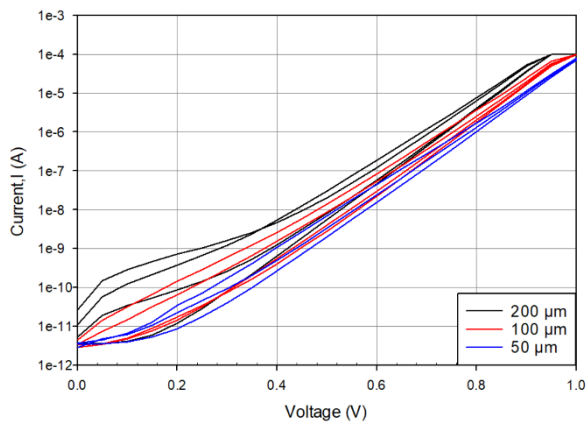
QW40



QW54

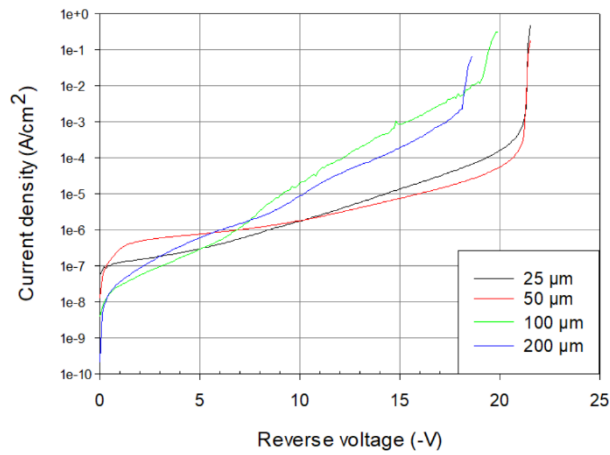


QT1879

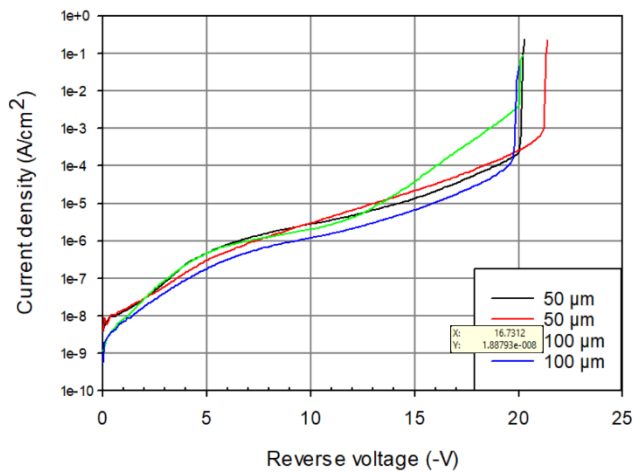


Appendix E: Reverse bias J-V for STC-3X devices

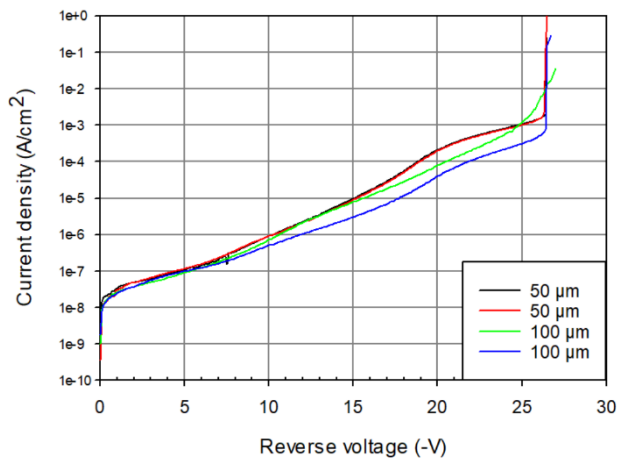
QW03



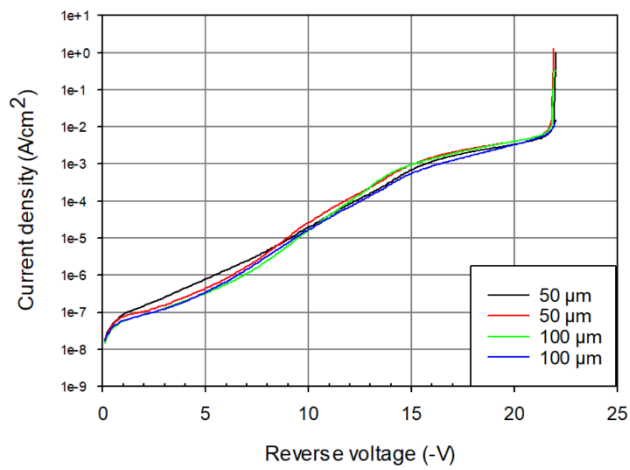
QW05



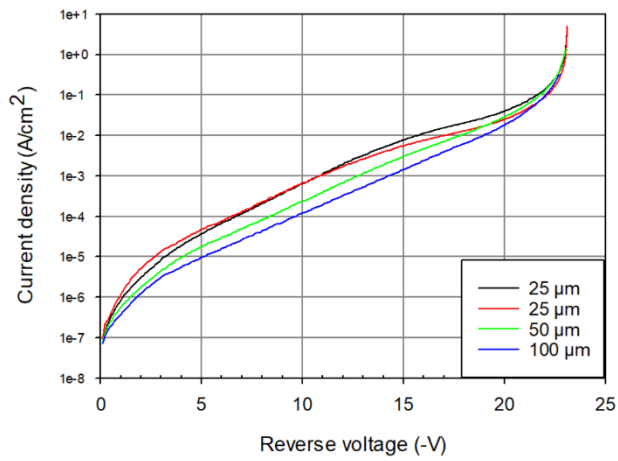
QW10



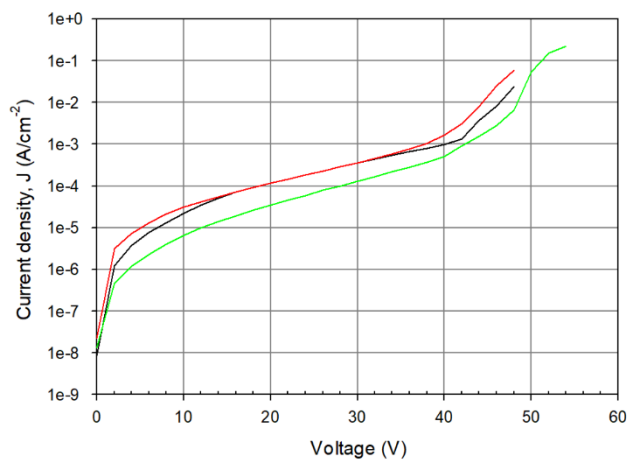
QW40



QW54

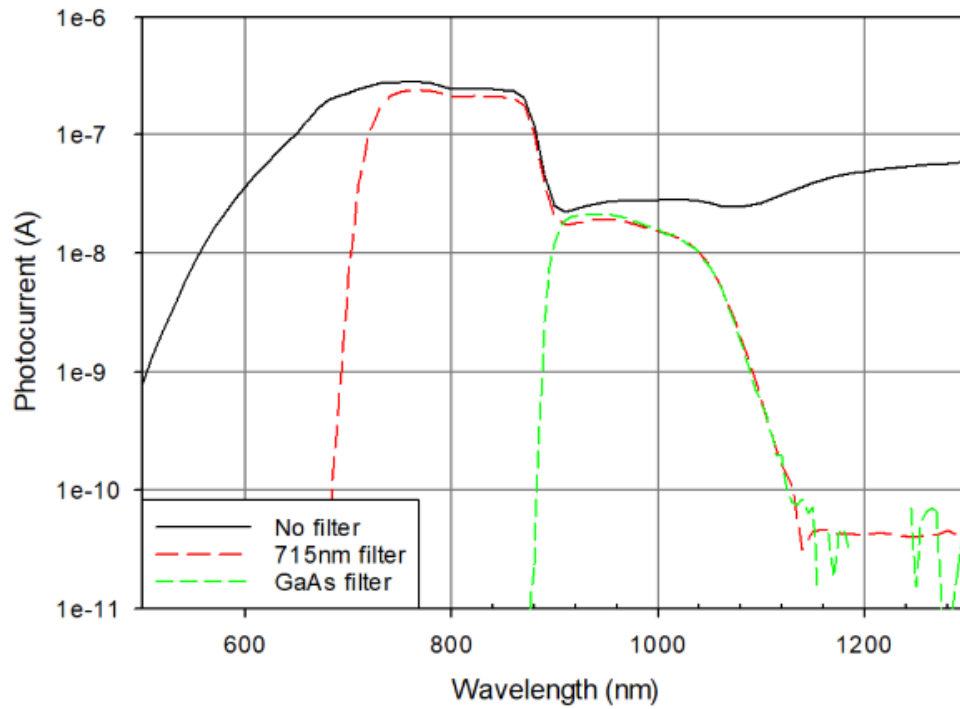


QT1879

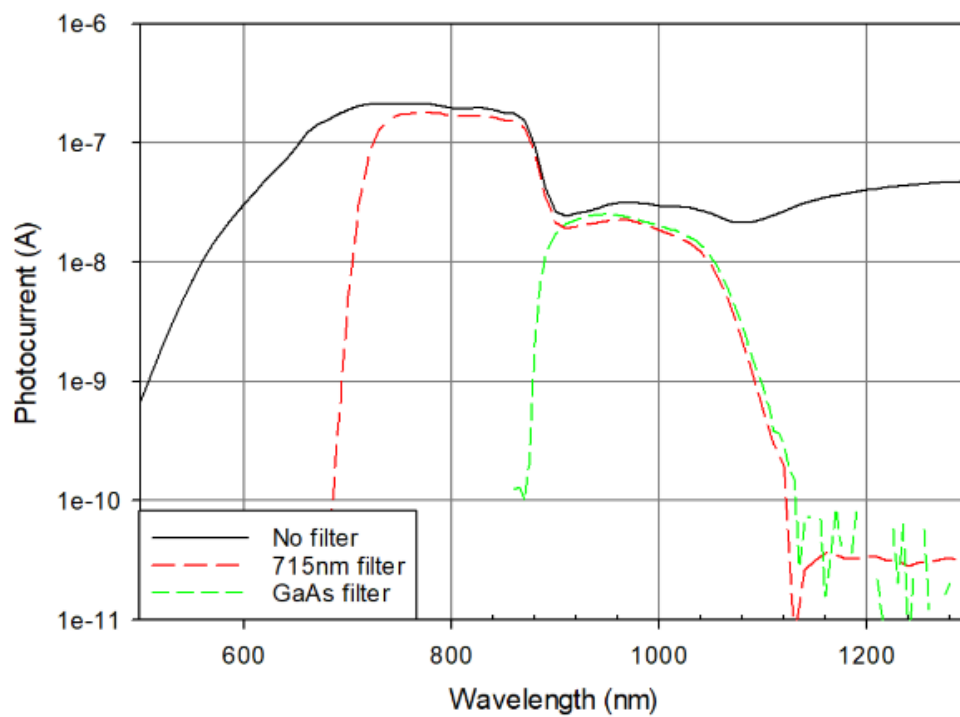


Appendix F: Photocurrent of STC-3X devices taken with different filters

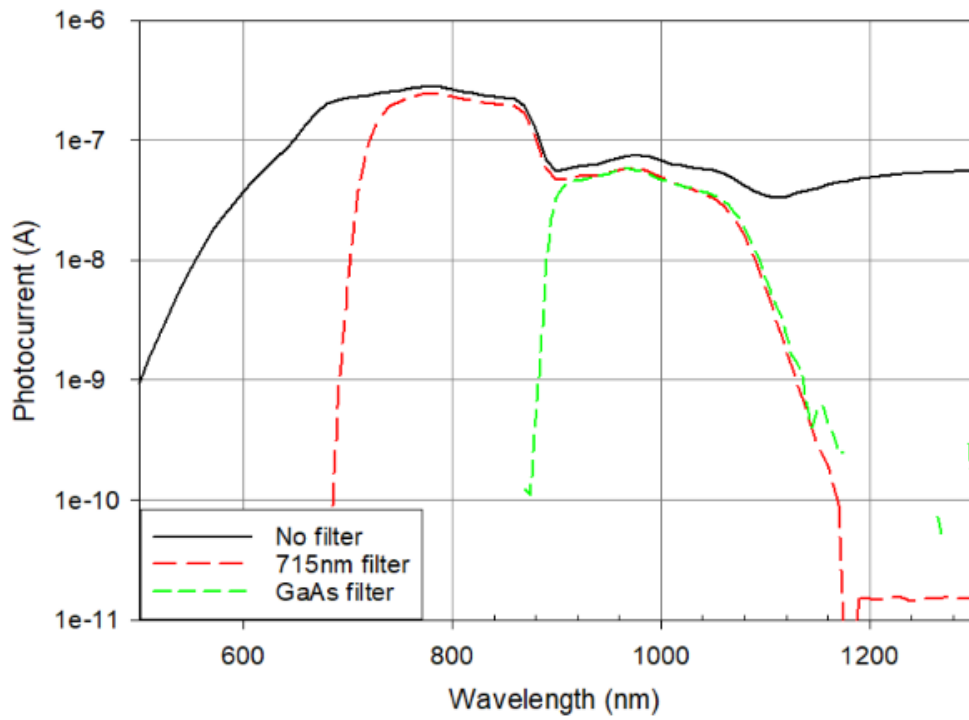
QW03



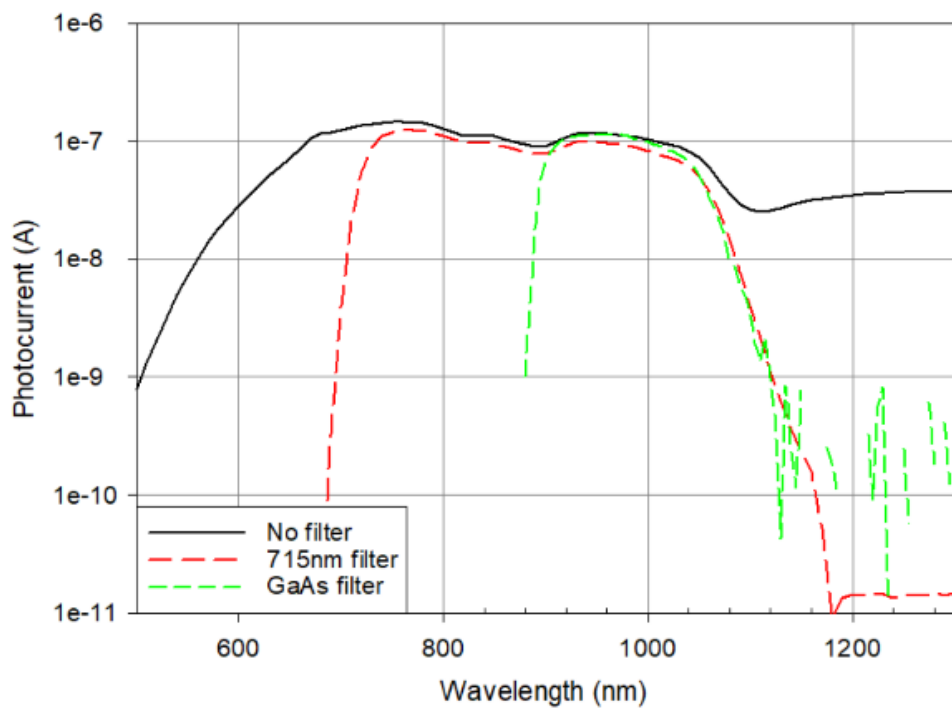
QW05



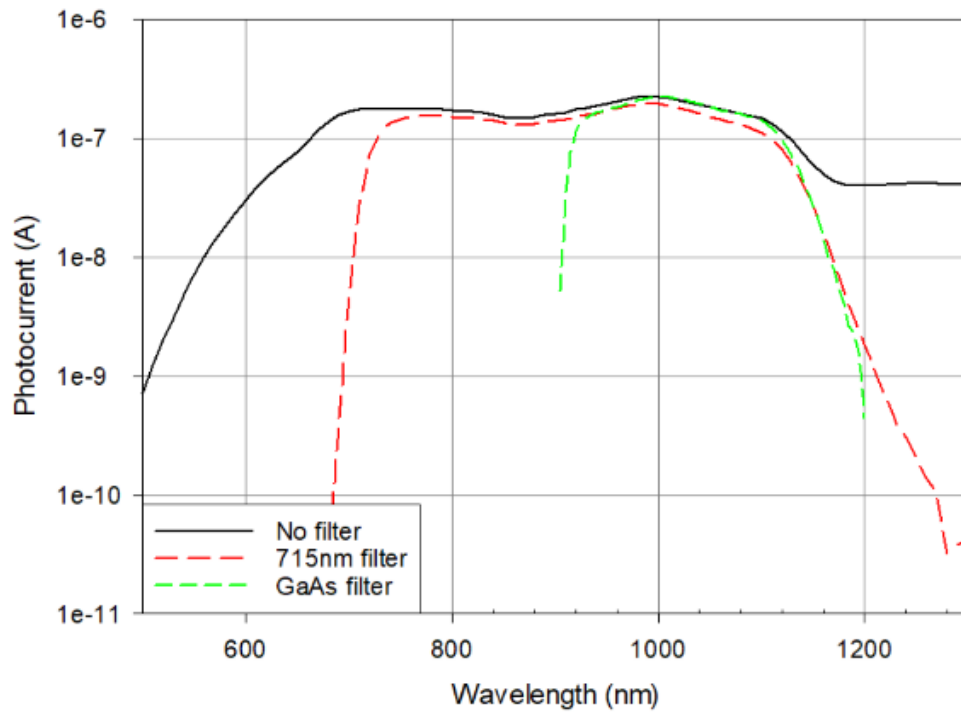
QW10



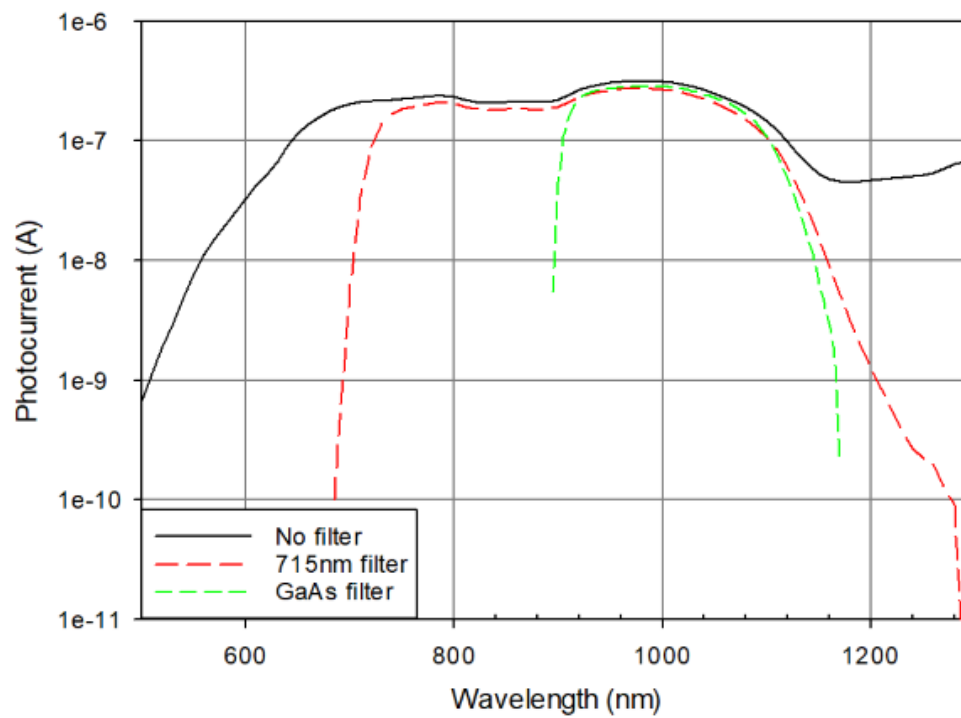
QW40



QW54

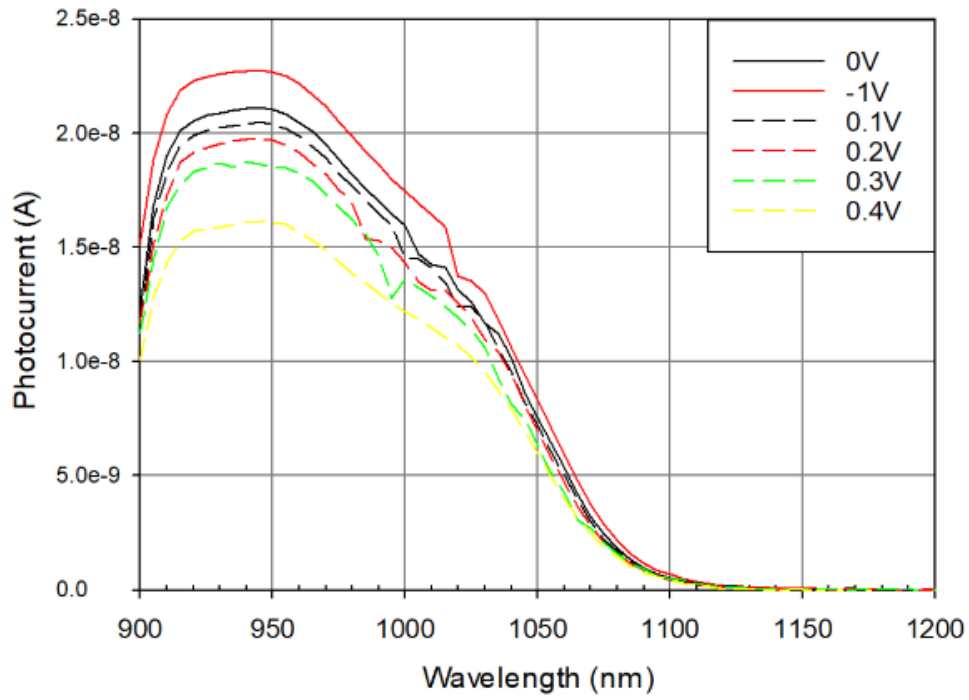


QW63

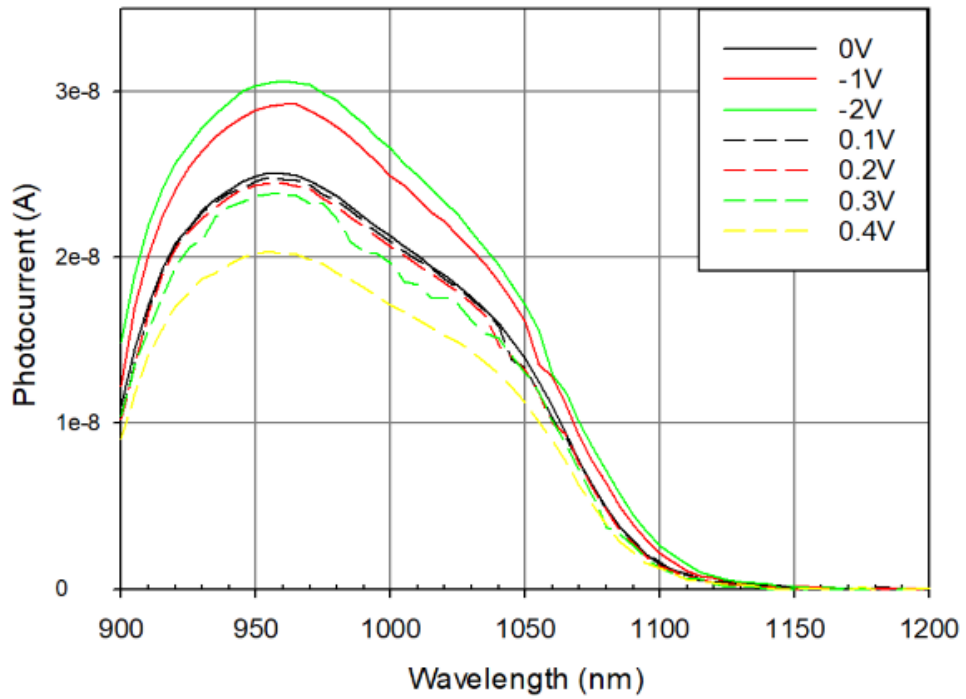


Appendix G: Photocurrent of STC-3X devices taken at different biases

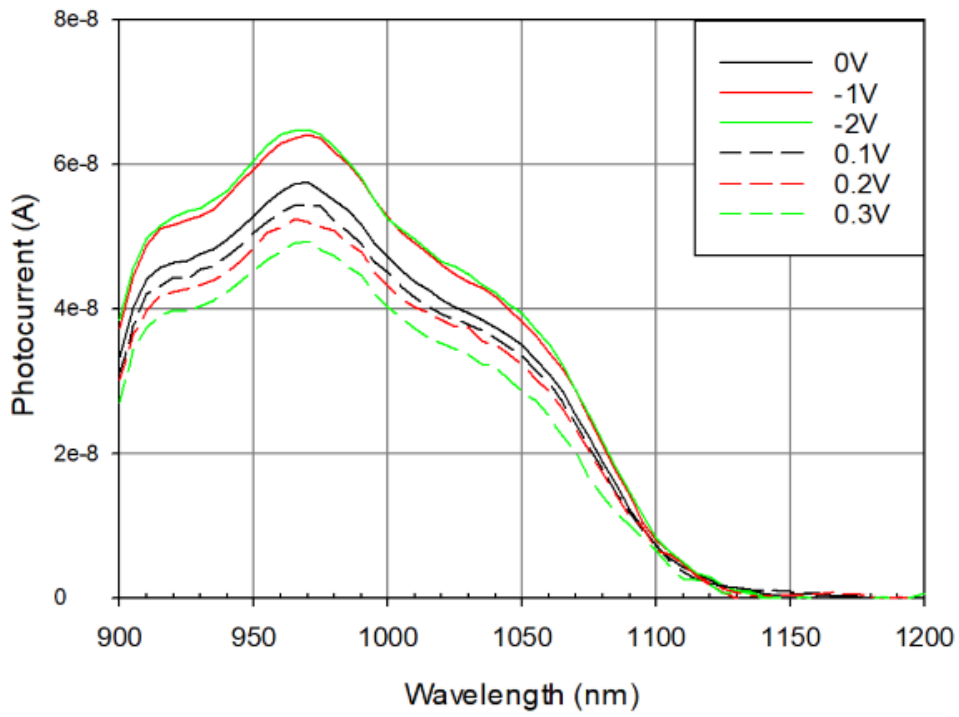
QW03



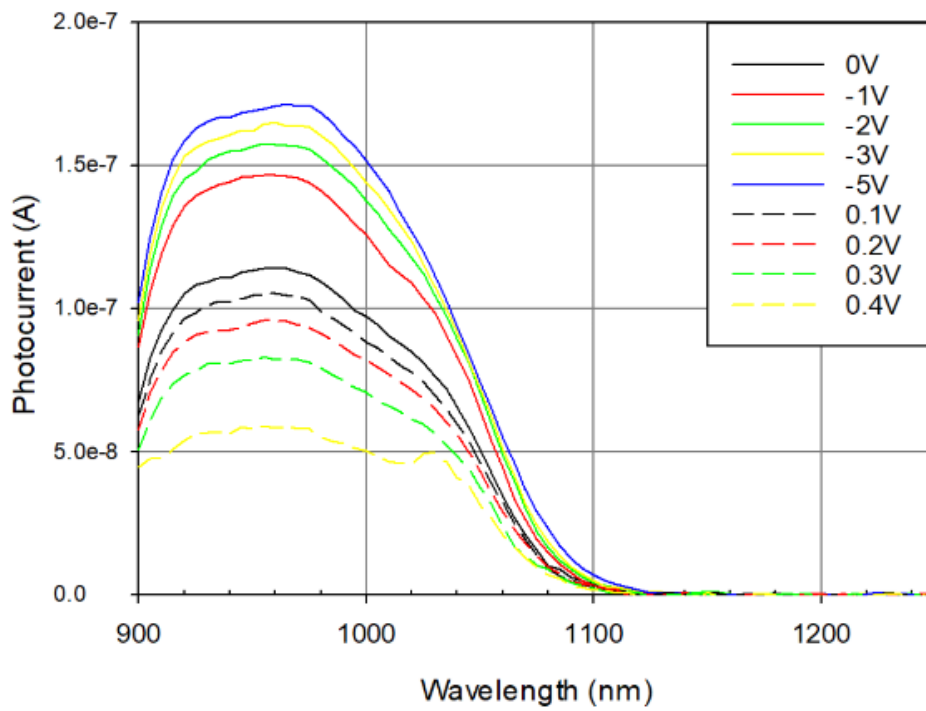
QW05



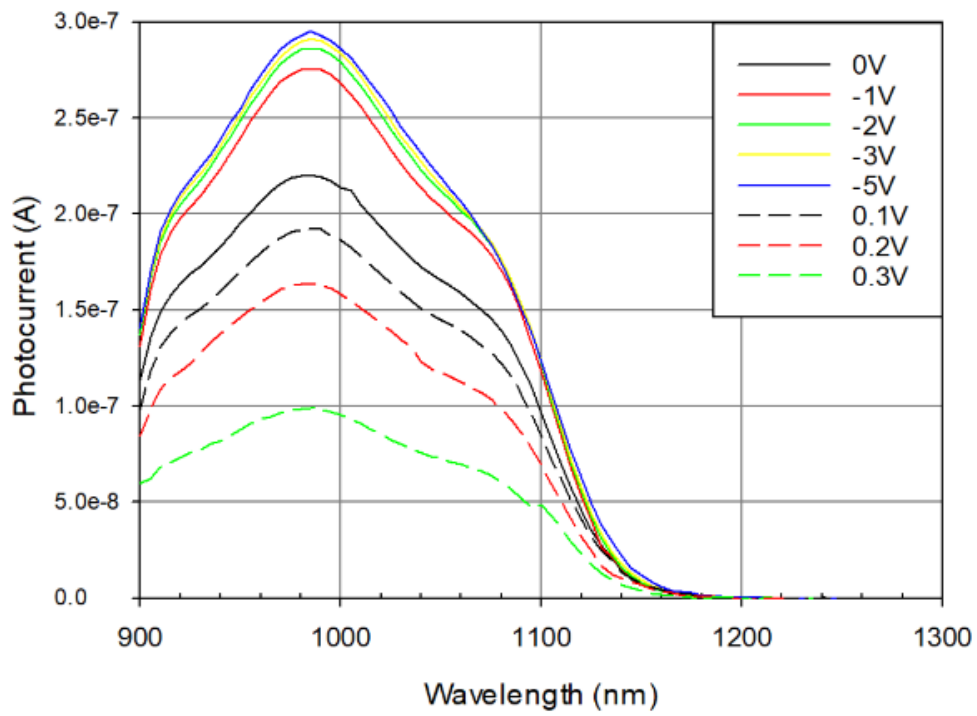
QW10



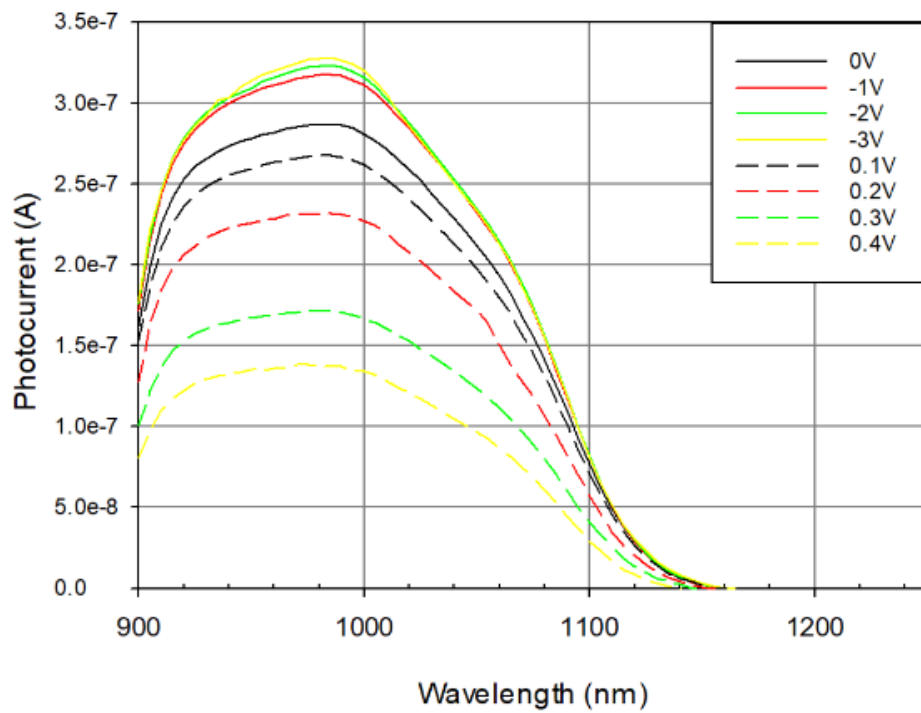
QW40



QW54

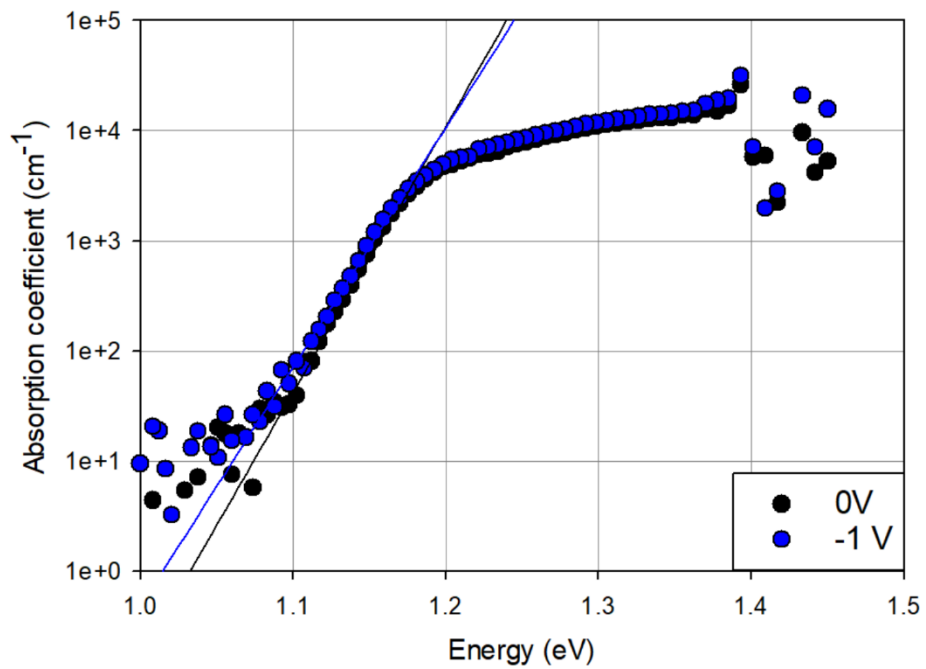
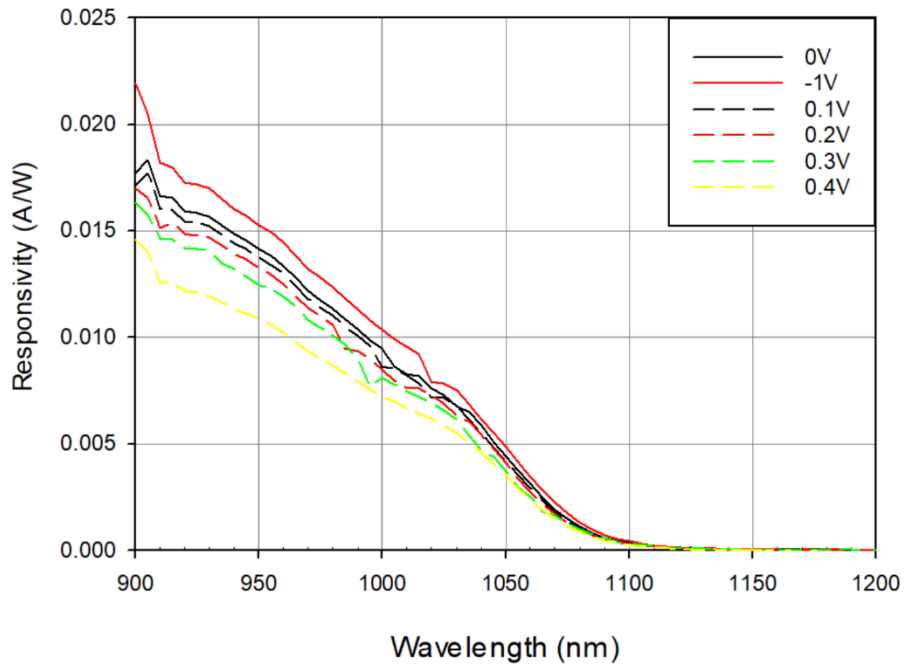


QW63

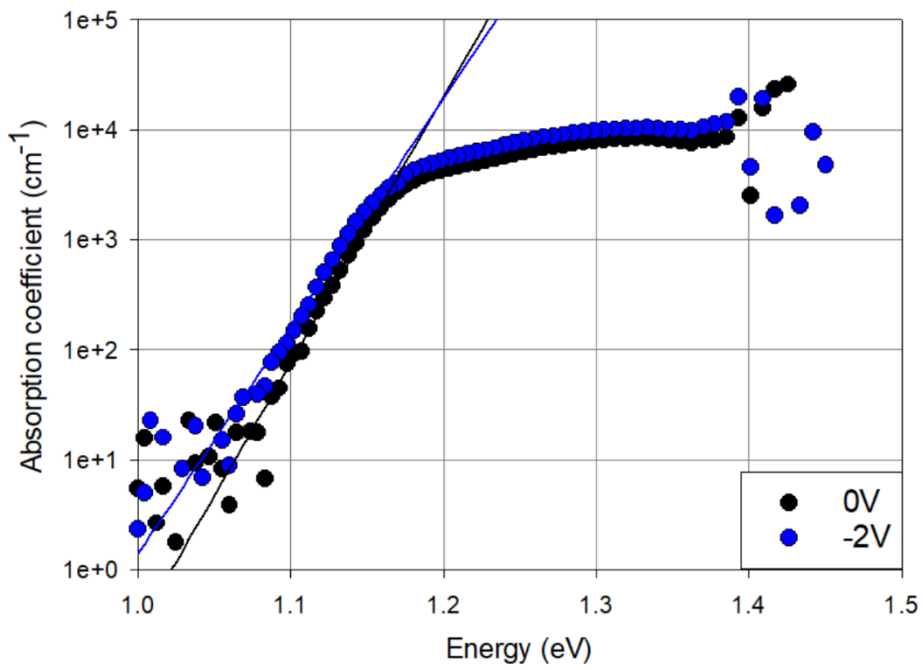
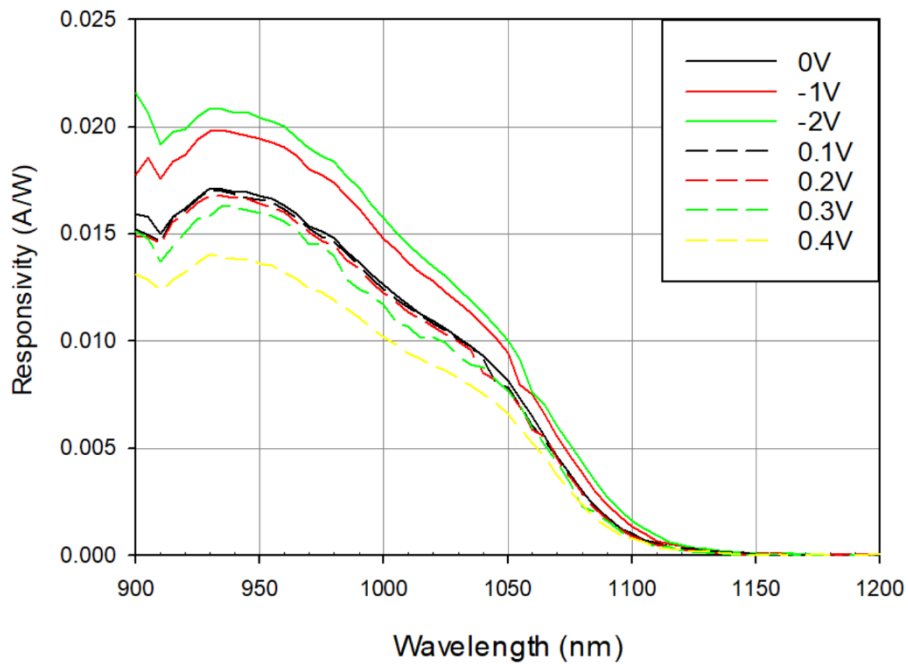


Appendix H: Responsivity and absorption coefficient (with Urbach fitting) of STC-3X devices

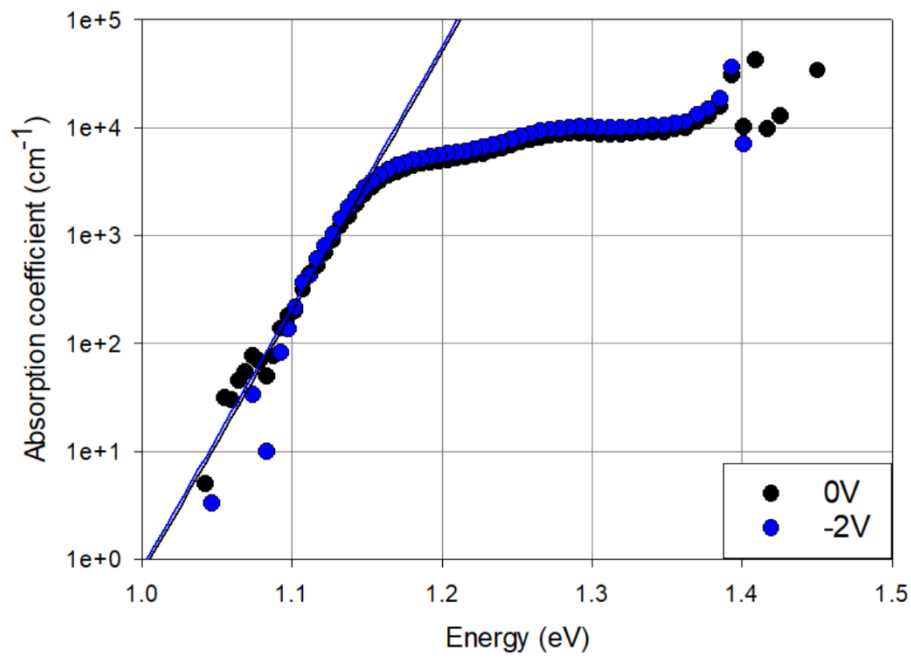
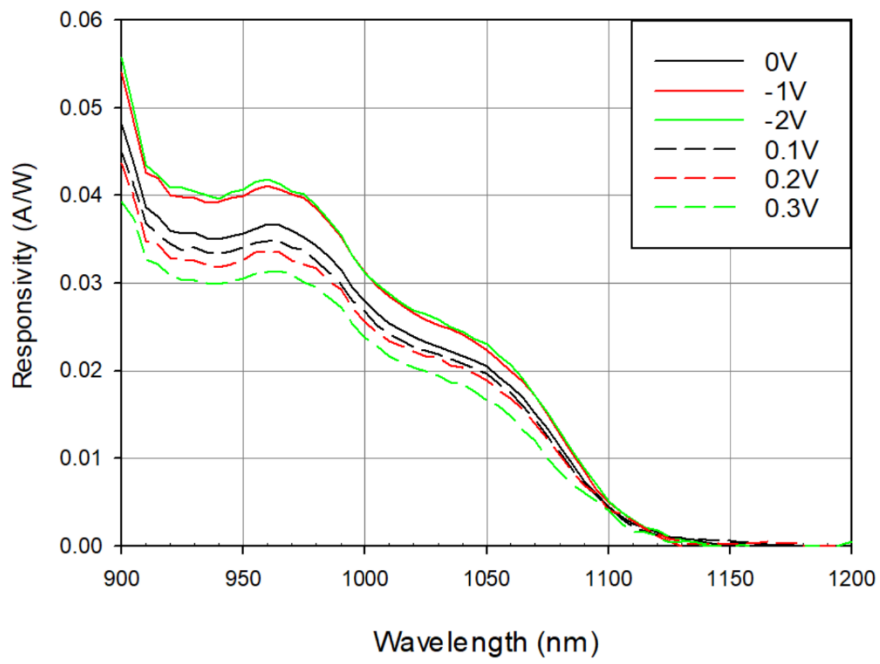
QW03



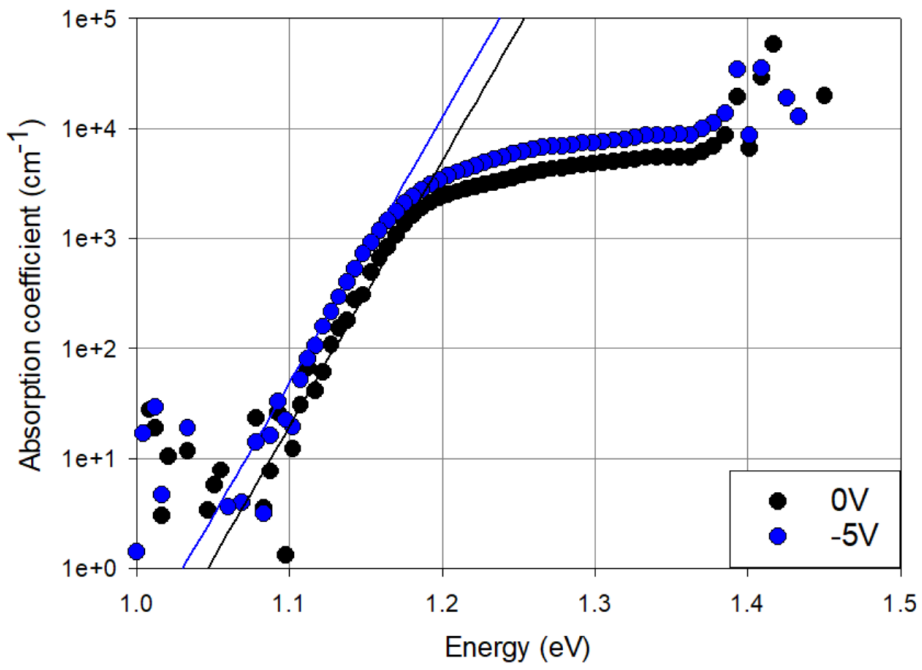
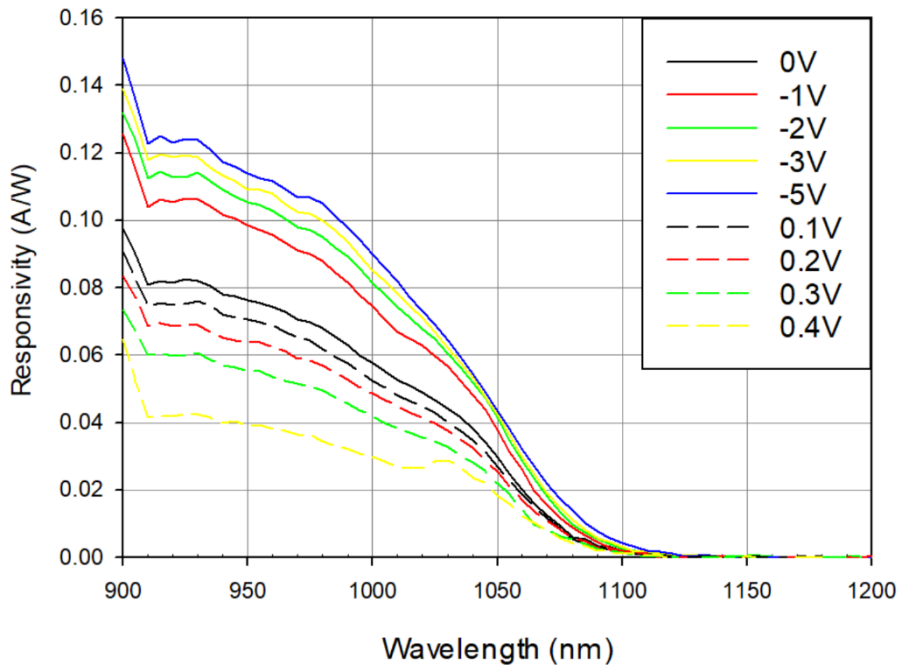
QW05



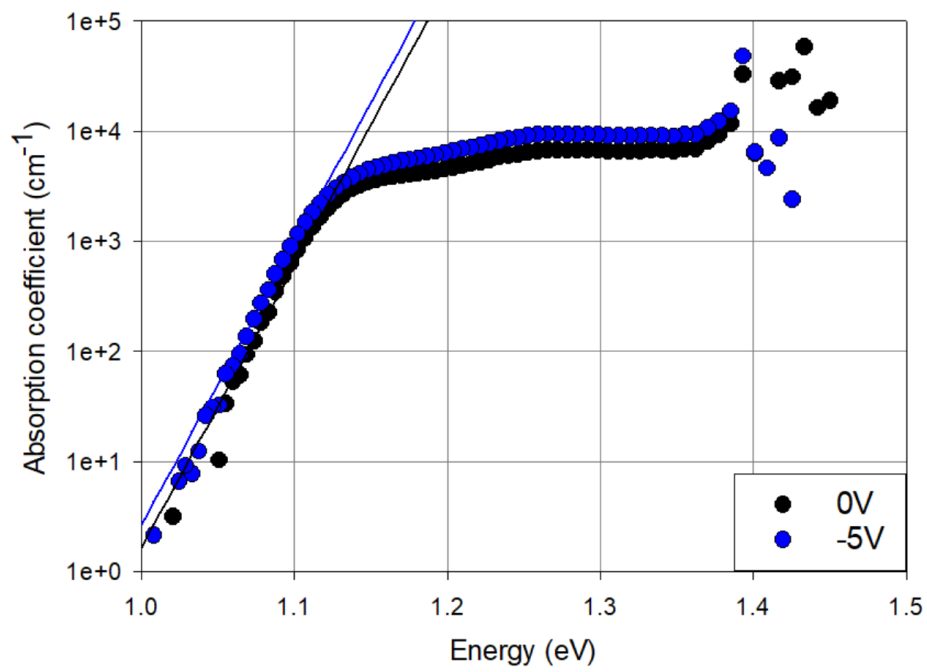
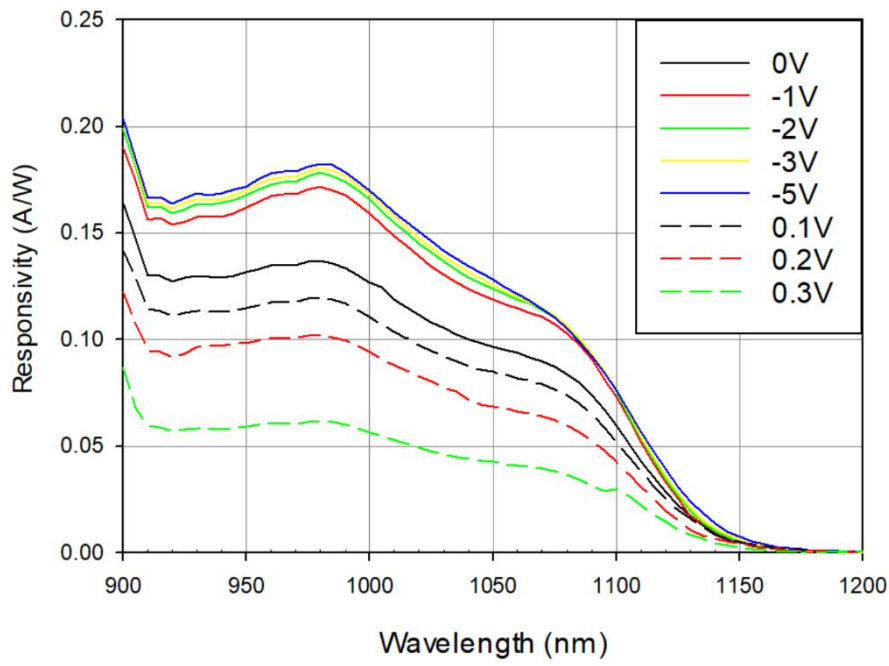
QW10



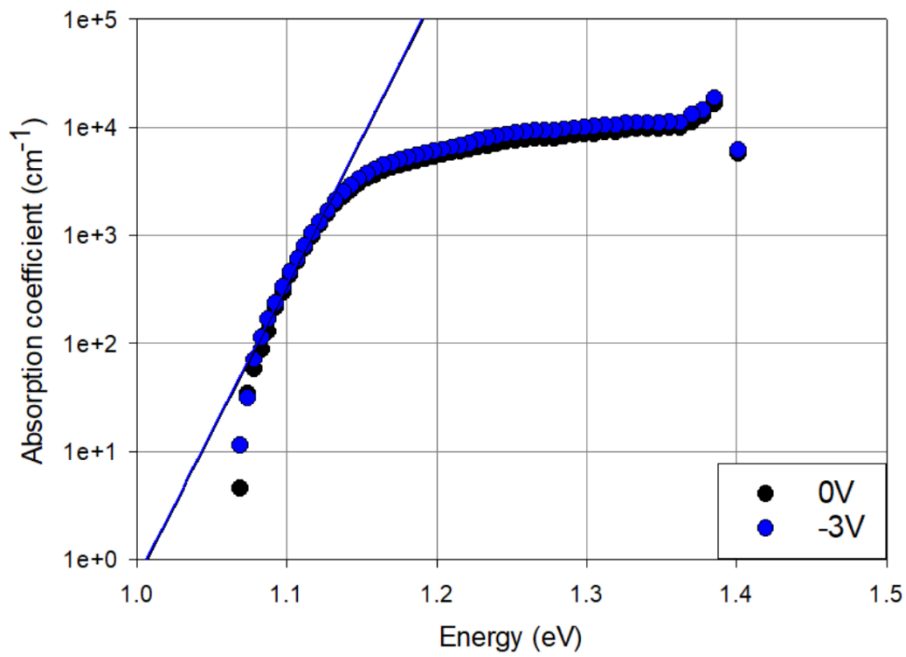
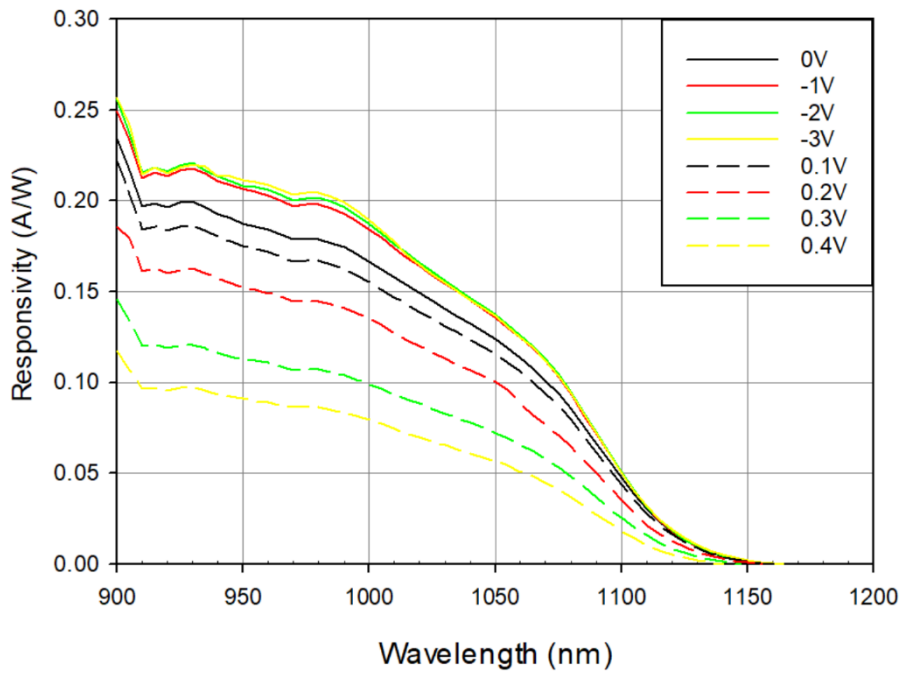
QW40



QW54



QW63



Appendix I: Solar Simulator Spectrum

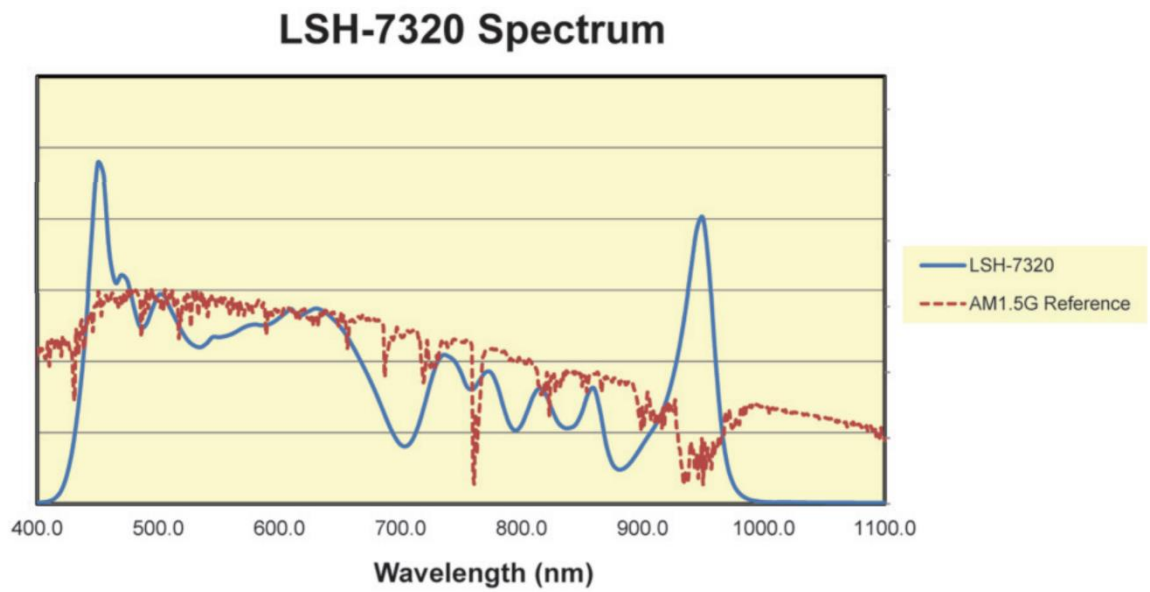


Figure I.1: The figure is taken from LSH-7320 LED Solar Simulator Spectrum specification sheet from Oriel Instruments, Newport Corp. website, specification sheet numbered as LSH-7320 REV07 110414